EXPLORING THE MECHANISM FOR THE ELECTROCATALYTIC REDUCTION OF CO_2 TO CO AND THE INDUSTRIAL INTEGRATION OF A BISMUTH-BASED ELECTROCATALYST

by

Stephanie M. Velardo

A dissertation submitted to the Faculty of the University of Delaware in partial fulfillment of the requirements for the degree of Doctor of Philosophy in Chemistry and Biochemistry

Fall 2017

EXPLORING THE MECHANISM

FOR THE ELECTROCATALYTIC REDUCTION OF CO_2 TO CO

AND THE INDUSTRIAL INTEGRATION OF

A BISMUTH-BASED ELECTROCATALYST

by

Stephanie M. Velardo

Approved: _____

Brian J. Bahnson, Ph.D.
Chair of the Department of Chemistry and Biochemistry

Approved: _____

George H. Watson, Ph.D.
Dean of the College of Arts and Sciences

Approved: _____

Ann L. Ardis, Ph.D.
Senior Vice Provost for Graduate and Professional Education

I certify that I have read this dissertation and that in my opinion it meets the academic and professional standard required by the University as a dissertation for the degree of Doctor of Philosophy.

Signed: _____

Joel Rosenthal, Ph.D.
Professor in charge of dissertation

I certify that I have read this dissertation and that in my opinion it meets the academic and professional standard required by the University as a dissertation for the degree of Doctor of Philosophy.

Signed: _____

Svilen Bobev, Ph.D.
Member of dissertation committee

I certify that I have read this dissertation and that in my opinion it meets the academic and professional standard required by the University as a dissertation for the degree of Doctor of Philosophy.

Signed: _____

Mary Watson, Ph.D.
Member of dissertation committee

I certify that I have read this dissertation and that in my opinion it meets the academic and professional standard required by the University as a dissertation for the degree of Doctor of Philosophy.

Signed: _____

Robert Opila, Ph.D.
Member of dissertation committee

ACKNOWLEDGMENTS

I would sincerely like to thank my committee members and research advisor for their guidance, criticisms, and advice throughout my graduate school career. Their guidance provided me with a strong background in scientific fields that would prepare me for my future career endeavors. My graduate school experiences have been a treasured journey that helped me grow intellectually and professionally.

As with any long journey, these past few years were filled with difficult times and rewarding times. For that reason, I owe a very special thank you to my parents, Marilyn and Frank Velardo, my siblings, Elizabeth and Frankie Velardo, and my boyfriend, Gabriel Andrade. Their confidence in me gave me the strength they knew I had to accomplish my educational goal; this turned out to be one of my most rewarding life events.

The following chapters describe a few of the projects that I have been fortunate to work on as a graduate student. All projects that I have developed, contributed to, or continued, were executed with great passion, scrutiny, and enthusiasm. Graduate school helped me learn that there is no failed experiment. Experiments can have unexpected outcomes that can create new approaches to your studies or perspective. Even when events do not go as planned, there will always be new opportunities. During tough times, one simply must continue performing admirably.

TABLE OF CONTENTS

LIST OF TABLES

LIST OF FIGURES

LIST OF SCHEMES

ABSTRACT

Global energy demand has historically been provided for by fossil fuels. As energy demand continues to rise in response to increasing population and industrialization, the use in fossil fuels will also rise. This rise is anticipated to have negative impacts on our global environment in the form of environmental risk factors. Therefore, a switch in energy dependency from fossil fuels to clean renewable energy is necessary to mitigate these risk factors. To make this transition, we envision a zero-emission pathway by harnessing energy from the sun in the form of solar fuels. By harnessing solar energy via a photovoltaic, electrons will be provided to reduce CO_2 to CO. The well-known Fischer-Tropsch process will then use CO as the C1 feedstock to produce the solar fuels.

For the initial transformation, the Rosenthal Research Lab developed a bismuth carbon monoxide evolving catalyst (Bi-CMEC), prepared by an acid aqueous electrodeposition bath. Its ability to selectively (>90 %) and efficiently (83 %) electrocatalytically transform CO_2 to CO with the incorporation of imidazolium-based ionic liquids (ILs) was demonstrated. Bi relates to the historic Ag and Au cathodes in the ability to selectively evolve CO, but is not impeded by the cost of material when used on an industrial scale.

To further encourage industrial integration of Bi-CMEC and to enhance these impressive metrics, I helped with the development of a 3D-printed flow electrolysis assembly for the electrocatalytic reduction of CO_2 to CO. 3D printing allows for rapid and cost effective prototyping with high precision and accuracy. The flow cell is a sealed

system which does not require constant operation or system re-optimization. Importantly, the flow cell recycles electrolyte and encourages faster mass transport from the constant flow of fresh electrolyte across the electrode surface. Here, we have modified existing drop casting techniques to screen a slew of inexpensive and commercially available Bi^{3+} salt precursors. We also took advantage of inexpensive carbon supports to further the likelihood of transitioning this chemistry into industry. Our progress with Bi-CMEC preparation and industrial cell design truly highlights the feasibility of integrating a Bi-based CO_2 electrolyzer into industry.

Mechanistic insights for Bi-CMEC to facilitate this transformation were studied with Tafel analysis and MD calculations performed in a collaborative effort with the University of Minnesota and co-workers of the Rosenthal Research Lab. Specifically, Tafel analysis suggested that the rate determining step (RDS) for Bi-CMEC is the first electron transfer (ET) to yield the surface bound $CO_2^{\bullet-}$. MD simulations agreed with the first ET being rate limiting and highlighted the role of surface bound IL and IL in the solution bulk. Upon developing an organic plating procedure, in situ studies were performed which offered additional insight for the catalytic behavior of Bi-CMEC. The organic electrodeposition procedure was general and allowed for materials other than Bi (Sn, Pb, and Sb) to be studied. The ability of these p-block metals to reduce CO_2 to CO was explored and ultimately revealed unique electrochemical behaviors. Despite Sb showing poor activity for CO_2 reduction, Bi, Sn, and Pb demonstrated high CO selectivity (~80 %) with current densities for CO generation ranging from 5–8 mA/cm^2. While Bi and Sn both showed impressive electrochemical behaviors, Pb demonstrated film passivation and CO_2 activation occurred at a larger overpotential. These initial

studies inspired curiosity as to why these materials, when prepared in a similar manner, demonstrated unique catalysis.

To understand why Pb becomes passivated, I performed extensive studies on the RDS, electrochemical events, and surface adsorbate interactions for the Bi, Sn, and Pb cathodes. Tafel studies performed on the Pb cathode suggested that an adsorbate forms on the surface to block charge transfer events. Surface studies were subsequently performed to identify the evolution of adsorbates for the Bi, Sn, and Pb cathodes. While Bi and Sn were nearly identical, Pb demonstrated an additional impurity adsorption component. This component was later identified as an imidazolium-carboxylate adduct. This adduct was found to exist both on the surface and in solution for Pb, but was not identified in either medium for Bi or Sn.

Imidazolium-carboxylate is highlighted in the literature to be an essential intermediate for the stabilization of $CO_2^{\bullet-}$ to lower the activation energy of this redox reaction. Because this theory disagrees with our previous experimental results, I performed thorough studies on the adduct itself. Here, direct information on its electrochemical behavior and participation in catalysis were observed. It was revealed that the adduct formation is irreversible, such that it creates a thermodynamic sink upon formation during electrolysis. When the adduct exists in solution, it was found to interfere with the diffusion of reactants and products migrating to and from the electrode surface to negatively impact the current density. For Bi and Sn specifically, the adduct interferes with the cathode/IL interaction at the surface without formally adsorbing. The IL monolayer becomes loosely adsorbed and no longer suppresses hydrogen production to selectively favor CO evolution.

IL serves multiple purposes during catalysis including stabilizing the electrode bias, providing protons for the $2H^+/2e^-$ redox reaction, and functioning as electrolyte. Therefore, I was interested in observing how neat IL systems would compare to the organic system with dilute IL. Additionally, ILs are a greener solvent compared to organics and would further help with industrial integration. For these studies, the essential cathode/IL interface remained, but the inherent physical properties of the IL electrolyte became more prevalent, i.e. viscosity, symmetry, intermolecular interactions. The higher solution viscosity was shown to drastically reduce mass transport. Poor diffusion was remedied with temperature enhancement. Here, it was found that Sn-CMEC was more durable than Bi-CMEC for extreme reaction conditions. Thus, temperature studies were continued with Sn-CMEC. Temperature studies were performed with 1-butyl-3-methylimidazolium hexafluorophosphate ([BMIM]PF_6) and 1-butyl-3-methylimidazolium trifluoromethanesulfonate ([BMIM]OTf). Interestingly, the durability of these ILs were found to be highly dependent on the anion. [BMIM]OTf demonstrated high selectivity and current density up to 100 ºC, whereas [BMIM]PF_6 showed no positive correlation to any temperature range. These differences were due to the durability (decomposition temperature) of each IL.

To enhance mass transport for [BMIM]PF_6 without sacrificing the durability of the IL during catalysis, admixtures of acetonitrile were added. This revealed fascinating chemistry, such that there is now a switch in catalytic dependency. Remarkably, the electronic behavior became less resistive to facilitate charge transfer, mass transport, and CO selectivity. Importantly, the IL did not show evidence for significant decomposition. These IL studies highlight electrochemical behavior of IL during electrolysis.

Chapter 1

INSPIRATION AND HISTORICAL IMPORTANCE FOR THE DEVELOPMENT OF ENERGY STORAGE DEVICES

1.1 Introduction

Global energy consumption has been rising over several decades due to economic growth and industrialization.[1,2,3] China alone has achieved the reputation of being the greatest energy consumer, and consequently the greatest CO_2 emitter in the world.[3,4] Atmospheric CO_2 levels resided at 278 ppm in 1975 and now doubled (>400 ppm) in 2016.[5] In 2015 alone, 17 TW of energy were consumed globally (Figure 1.1a), where nearly 86 % of that energy was supplied by fossil fuels.[6] Fossil fuels have historically been our primary energy source, highlighted in Figure 1.1b, and truly dominate our energy profile. If our dependency on fossil fuels continues, such that they continue to provide for our projected energy demand by 2050, our atmospheric CO_2 contribution will continue to rise at alarming rates.[7]

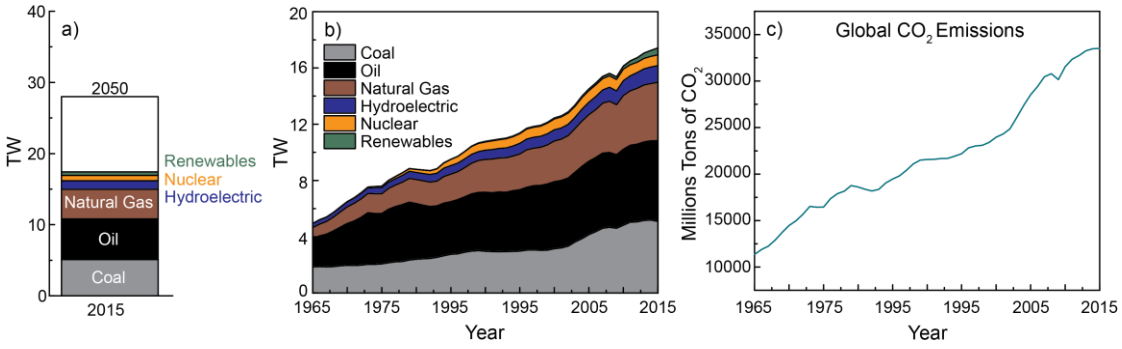

Figure 1.1. Energy profile for 2015 and projected energy consumption by 2050 is featured in a). The energy profile over a series of decades is featured in b). Global CO_2 emissions with respect to year is shown in c).

CO_2 resides in two reservoirs; the atmosphere and the deep ocean. CO_2 concentrations between the two reservoirs naturally fluctuate, but the recent jump in atmospheric CO_2 levels (Figure 1.1c) resulted in a CO_2 flux that requires equilibria to be reestablished.[8] This CO_2 flux has resulted in global reasons for concern (RFC) and are prevalent in our global economy by environmental warning signs, i.e. extreme weather, encroaching seas, ocean acidification, and climate change.[9,10] To mitigate these RFCs, decreasing our contribution to CO_2 emissions is critical. This stresses the need for establishing a new dependence on renewable energy sources.

Renewable energy has shown a slight emergence over the past couple decades (Figure 1.1b, green trace).[6] Renewables provide carbon neutral energy from naturally occurring and inexhaustible means. Of the renewable energy sources, solar is the only one that scales to match our future energy demand, such that more energy from the sun strikes the earth's surface in one hour than is used in one year.[8] Because of its intermittency, however, the development of an efficient solar energy storage device is needed. The ability of a material to store energy is measured by its energy density. Table

1.1 summarizes the energy density for three energy storage methods; kinetic (flywheel), potential (compressed air), and chemical energy (batteries, carbon based fuels).[11]

Table 1.1. Energy sources and their respective energy density in kJ/ kg.[11]

energy source	energy density (kJ/ kg)
Crude oil	42 000
Coal	32 000
Methanol	21 000
Lithium-ion batteries	700
Compressed air	400
Flywheel, composite materials	> 200

Of the three methods, carbon based fuels (chemical energy) are the most energy dense. Additionally, hydrocarbon fuels can easily be stored and transported to where the energy is needed.[5] Due to the economics for transcontinental distribution of liquid fuels, hydrocarbons are an efficient method for storing energy. Seeing as our economy relies heavily on liquid fuels for energy, incorporating solar fuels may significantly decrease contributions of atmospheric CO_2 emissions.[12] Here, if solar energy drives the production of liquid fuels, energy from the sun would be stored through chemical bonds.

One way solar fuels can be produced is through the reduction of CO_2. A current challenge faced with CO_2 reduction is the high thermodynamic energy barrier to reverse the exergonic combustion reaction as shown in equation 1.1.

$$C_xH_y + zO_2 \rightarrow xCO_2 + \frac{y}{2}H_2O \qquad (1.1)$$

Depending on the amount of energy provided, different reduced carbon species will be produced (Figure 1.2). Competitive proton reduction must also be considered (–0.42 (V) vs. SHE). This is only a 100—200 mV difference from CO_2 reduction reactions.

Competitive reduction leads to poor product selectivity. Therefore, a catalyst that can suppress hydrogen (H_2) evolution to selectively favor one product is desired.

Reaction:	$E°_{eq}$ (V) vs. SHE
$CO_{2\,(g)} + 2\,H^+ + 2\,e^- \longrightarrow CO_{(g)} + H_2O_{(l)}$	–0.52
$CO_{2\,(g)} + 2\,H^+ + 2\,e^- \longrightarrow HCOOH_{(aq)}$	–0.61
$CO_{2\,(g)} + 6\,H^+ + 6\,e^- \longrightarrow CH_3OH_{(aq)} + H_2O_{(l)}$	–0.38
$CO_{2\,(g)} + 8\,H^+ + 8\,e^- \longrightarrow CH_{4\,(g)} + 2\,H_2O_{(l)}$	–0.38

Figure 1.2**.** Equilibrium potentials for CO_2 reduction to CO, formic acid, methanol, and methane. E_{eq} are obtained at pH 7 and referenced to the standard hydrogen electrode (SHE).

The thermodynamic theory for multiple e^-/H^+ transfer processes predicts that for two electrons transferred, catalysis will function efficiently in both the forward and reverse direction with the use of a catalyst.[13] The reversibility of two electron transfer (ET) events is satisfied by the Sabatier principle.[14] This states that the intermediate formed will bind optimally to the catalyst, such that the intermediate will not bind too strongly to poison catalysis, but not too weakly to prevent further transformation. For reactions with more than two electrons transferred, such as for methanol or methane, the transformation becomes more complicated due to more than one reaction intermediate. This leads to an irreversible reaction.

Understanding that two step ET mechanisms are more kinetically accessible than multiple ET events, the production of CO is a promising redox reaction for producing solar fuels. CO is a commodity chemical for industrial processes, such that it is the C1 feed stock for hydroformylation, the Monsanto process, and the water-gas shift

(WGS) reaction.[15,16,17] Notably, CO is a precursor for synthetic fuel production via the Fischer-Tropsch process.[18] The challenge for CO evolution, however, is the high kinetic barrier. This redox reaction therefore requires a catalyst.

Heterogeneous catalysis, where the catalyst is in a different phase than the reactants or products, are commonly used in industry.[19] An advantage of heterogeneous catalysis over homogeneous catalysis, where the reactants and products are in the same phase as the catalyst, is the inability to dimerize into stable bimetallic compounds and create a thermodynamic sink.[19] Additionally, homogeneous catalysis is accompanied with large costs for catalyst production and product separation.[20] Transition metal heterogeneous catalysts have been studied for CO_2 reduction and were shown to produce either CO or formate (Table 1.2).[13] Under aqueous conditions, Sn and Pb have been shown to be highly quantitative for formate production, while Ag and Au are highly selective towards CO evolution. When considering the cost of Ag and Au materials, however, its price greatly outweighs its catalytic capabilities, ~$700/ kg and ~$45 000/ kg respectively.

Table 1.2. Metrics for common heterogeneous CO_2 reducing catalysts under aqueous conditions.[13]

catalyst	(V) vs. SCE	FE_{CO} (%)	FE_{H2} (%)	FE_{HCOO-} (%)	j_{tot} (mA cm^{-2})
Silver	–1.4	82	12	---	12
Gold	–1.1	87	10	---	10
Lead	–1.6	---	5	97	5
Tin	–1.5	2	5	88	5

In shifting from transition metal catalysts to p-block metal catalysts, Bi has remained relatively unexplored in its CO_2 reduction capabilities. It is the by-product of Pb, Cu, and Sn refining and has little to no environmental impact. Due to having few

industrial applications, its price is more accommodating than the noble metal cathodes, ~$18/ kg. Until recently, there was only one electrocatalytic study showing Bi's ability to reduce CO_2, which did not describe CO evolution.[21] Because Bi had not yet been demonstrated to produce CO, it would be a significant contribution towards CO_2 electrocatalytic reduction studies to develop an inexpensive Bi-based cathode to drive the evolution of this high energy storing small molecule.

In preliminary work with exploring the electrocatalytic CO_2 reduction capabilities of Bi, it was demonstrated that Bi could be electrodeposited onto an inert glassy carbon electrode (GCE, 3.0 mm diameter). Detailed electrochemical studies were later performed to understand why Bi possessed high and impressive activity towards CO_2 reduction.[22] This Bi-modified electrode came to be the first reported Bi carbon monoxide evolving catalyst (Bi-CMEC) and truly pioneered subsequent electrocatalytic discoveries. Since these initial studies, The Rosenthal Research Lab developed various electrodeposition methods that involved either an acid aqueous or organic baths for ex situ or in situ studies respectively.[23] Upon developing a general organic electrodeposition procedure, other inexpensive p-block metals were studied for CO_2 to CO catalysis (Sn, Pb, and Sb).[24] Additionally, the essential interplay between the metal cathodes and 1,3-dialkylimidazolium ionic liquids (IL) to promote CO_2 to CO catalysis was highlighted.

1.2 Results and Discussions

1.2.1 Bismuth Carbon Monoxide Evolving Catalyst (Bi-CMEC)

Previous Rosenthal Group co-workers studied the preparation of a Bi electrocatalyst. Specifically, initial work with Bi involved the modification of current

electrodeposition techniques to develop a concentrated HCl acid aqueous bath with a bismuth nitrate ($Bi(NO_3)_3$) precursor and electrolyte (KBr). Upon polarizing an inert GCE at the potential at which $Bi(NO_3)_3$ is reduced, shown by the cathodic peak in the cyclic voltammogram (CV) in Figure 1.3a, they successfully modified the electrode surface, seen visually by a dark gray film. The morphology, elemental surface composition, and the composition of the film were analyzed with secondary electron microscopy (SEM), X-ray photoelectron spectroscopy (XPS), energy dispersive X-ray spectroscopy (EDX), and powder X-ray diffraction (PXRD) respectively.

Figure 1.3b features an SEM image of the electrodeposited film. This image revealed micrometer-sized clusters on the surface that are reminiscent of rosebuds. These microstructures overwhelm the surface and provide information on the porosity of the film. Having a porous film with enhanced depth provides additional active sites for the reactants (CO_2) to bind to during catalysis.[25]

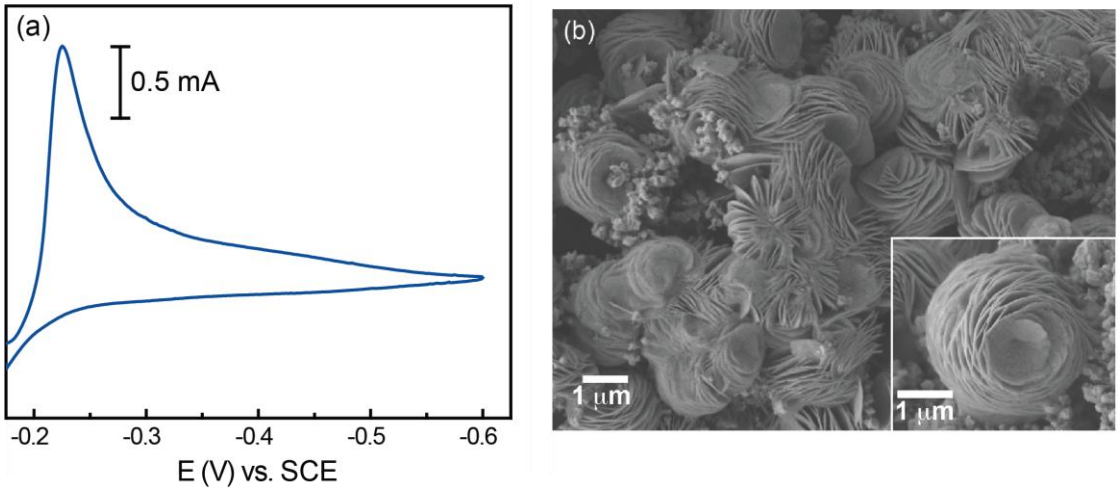

Figure 1.3. Cyclic voltammogram in a) describes the cathodic behavior for $Bi(NO_3)_3$ when conditioning the GCE in an acid aqueous bath. The secondary electron microscopy image of the Bi-modified GCE is illustrated in b).

EDX detected Bi, K, C, Br, and Cl in the film bulk (Figure 1.4a). Upon qualitative analysis, Bi was found to be the main component. The presence of Br and Cl on the surface were believed to be contaminants from the electrodeposition. They appear necessary for neutralizing the Bi^{3+} charge, but show no evidence towards encouraging CO_2 reduction. XPS complimented EDX by providing quantitative elemental analysis of the surface. Figure 1.4b shows the Bi 4*f* high resolution XPS spectrum which detected two components: metallic bismuth (Bi^0) and oxidized bismuth (Bi^{3+}) at 157.0 and 159.9 eV respectively. PXRD characterized the Bi^{3+} component as being bismuth(III) oxychloride (BiOCl), shown in Figure 1.4c where the electrodeposited Bi diffraction (black trace) overlaid nicely with Bi^0 (orange trace) and BiOCl (green trace) standards.[22]

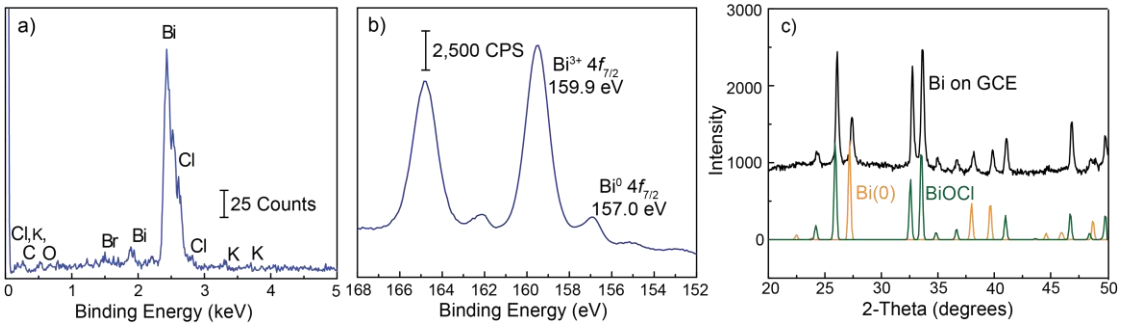

Figure 1.4. Electrodeposited Bi-CMEC film characterized by a) EDX, b) XPS, and c) PXRD.

Electrochemical studies were subsequently performed on the modified surface to observe CO_2 reduction activity. Specifically, CV was used to monitor current responses. Current, in Amps (C s^{-1}), is a measure charge (Q) passed per time (t) (equation 1.2). Current is linked to the rate of reaction, such that if the current (flow of electrons) is high, then the rate of catalysis is also high. Dividing by the electrode area

normalizes the current to allow for comparisons between systems with varying surface sizes to be made. This results in the total current density (j_{tot}), measured in mA/cm^2.

$$i = \frac{Q}{t} \qquad (1.2)$$

For this study, the electrolyte solution consisted of acetonitrile (MeCN) and supporting electrolyte (100 mM tetrabutylammonium hexafluorophosphate ($TBAPF_6$)). The solution was first saturated with nitrogen (N_2) to observe if Bi-CMEC was stable under potentials ranging from –0.25 to –2.25 (V) vs. SCE (all potentials will be reported to this reference). A flat current response was observed (Figure 1.5b, black trace), which signified a strong ohmic contact between the film and electrode surface. When saturated with CO_2, a rise in current was observed with an onset potential of –2.0 V (Figure 1.5b, blue trace). Despite showing modest activity towards CO_2 reduction, small aliquots of ionic liquid (IL), 1-ethyl-3-methylimidazolium tetrafluoroborate ([EMIM]BF_4), were titrated into the CO_2 saturated electrolyte solution with the intention of further enhancing the observed activity (Figure 1.5a). A significant current enhancement was observed after the first few additions of IL. Further additions (reaching 100 mM) demonstrated a substantial current enhancement greatly surpassing the initial current response without IL. Additionally, the onset potential became less negative implying a more thermodynamically favorable redox reaction.

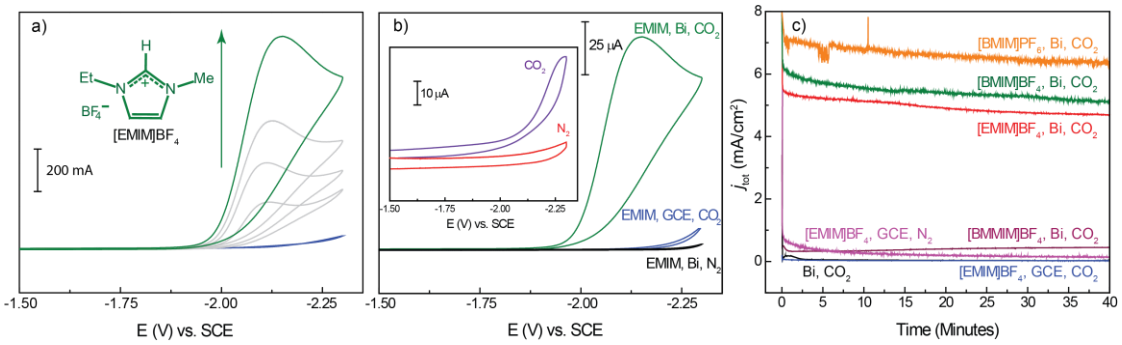

Figure 1.5. Cyclic voltammograms in a) show an IL titration into CO_2 sat. MeCN. Cyclic voltammograms in b) show the polarization curves for IL/Bi/CO_2 (green trace), IL/Bi/N_2 (black trace), and IL/CO_2 (blue trace). The inset magnifies the polarization curves for Bi under CO_2 and N_2 without IL (purple and red traces respectively). The current density plot in c) illustrates the kinetic comparisons between [BMIM]PF_6, [BMIM]BF_4, [EMIM]BF_4, and [BMMIM]BF_4, in orange, green, red, and purple traces respectively.

The significance of incorporating IL was further highlighted when performing controlled potential electrolysis (CPE) at –1.95 V on a variety of ILs. CPE was performed in a sealed two-compartment electrochemical cell equipped with CO_2 saturated electrolyte solution. The headspace of the cell was analyzed with gas chromatography (GC) to monitor CO production reported in Faradaic efficiencies (FEs). Like the yield of a synthetic reaction, the FE of electrochemical catalysis is a measure of moles of product formed divided by the theoretical moles amount of product (equation 1.3). Catalytic systems associated with high FEs are systems that have high product selectivity.

$$\text{FE} = \frac{mol\ product\ formed}{theoretical\ mol\ product} \text{ x } 100 \qquad (1.3)$$

The ILs studied varied in cation and anion combinations: 1-ethyl-3-methylimidazolium tetrafluoroborate ([EMIM]BF_4), 1-butyl-3-methylimidazolium

tetrafluoroborate ([BMIM]BF_4), 1-butyl-3-methylimidazolium hexafluorophosphate ([BMIM]PF_6), and 1-butyl-2,3-dimethylimidazolium tetrafluoroborate ([BMMIM]BF_4). The structures for these imidazolium-based ionic liquids are shown below in Figure 1.6. The IL's behavior during electrolysis are summarized in the current density plot in Figure 1.5c. Control experiments were when either IL or Bi-CMEC were not incorporated (Figure 1.5c, black and blue traces respectively).

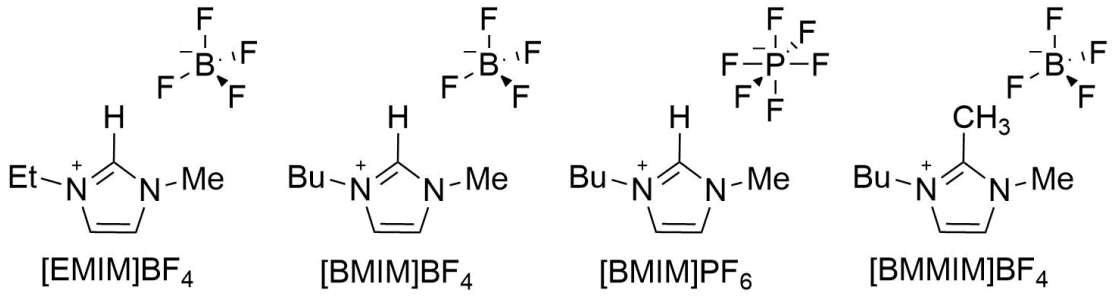

Figure 1.6. Structures for imidazolium-based ionic liquids.

The current density plot showed a large enhancement in current density for the Bi/1,3-dialyklimidazolium IL interfaces compared to when the Bi/IL interface did not exist. This was found true regardless of the anion (BF_4^-, PF_6^-) or C1 alkyl substitution ($[BMIM]^+$, $[EMIM]^+$).

Table 1.3 shows that the Bi/IL interface produced high CO efficiencies exceeding 90 %. The impressive metrics were suggested to not be the result of IL or solvent decomposition, as observed when performing CPE under N_2; negligible current and no CO evolution. If Bi-CMEC was absent in the CO_2 saturated MeCN/IL solution, the current density was negligible with trace amounts of CO produced. Conversely, when Bi was present without IL, CO production was halved. This further supports that

this is not a homogeneous system mediated by the IL. If this were true, then the absence of Bi would have minimal effects on the metrics. Lastly, a significant IL characterization was revealed when the C2 proton was substituted by a methyl group, [BMMIM]BF_4. When [BMMIM]BF_4 was used in catalysis, the current density was comparable to when IL was absent from the electrolyte solution. Further, CO production was sacrificed by nearly 20 %. This highlights the importance of the acidic C2 proton.

Table 1.3. CPE metrics for Bi-CMEC at –1.95 (V) vs. SCE.[22]

electrode	IL	FE_{CO} (%)	j_{CO} (mA cm^{-2})
GCE	[EMIM]BF_4	trace	<0.03†
Bi-CMEC	[EMIM]BF_4	93 ± 7	3.77 ± 0.7
Bi-CMEC	none	48 ± 13	0.11 ± 0.1
Bi-CMEC	[BMIM]BF_4	95 ± 6	5.51 ± 1.2
Bi-CMEC	[BMIM]PF_6	90 ± 9	4.82 ± 0.7
Bi-CMEC	[BMMIM]BF_4	76 ± 6	0.67 ± 0.5

† Total current density

The energy efficiency (ε) of Bi-CMEC was calculated by equation 1.4. E_{app} is the applied potential for CPE and $E^0_{CO_2/CO}$ is the standard reduction potential for the CO_2 to CO reduction.

$$\text{Energy efficiency } (\varepsilon) = \frac{E^0\,(CO2/CO)}{Eapp} \text{ x FE} \qquad (1.4)$$

This equation requires the estimation of $E^0_{CO_2/CO}$ and overpotential. $E^0_{CO_2/CO}$ is dependent on the electrolyte's ability to proton donate. For our system, this is likely influenced by IL.[26] Overpotential (η) is a measure of the additional energy required (energy cost) for an electrocatalytic reaction to overcome the kinetic barrier (equation 1.5), where E_{eq} is the equilibrium potential. A lower η implies a lower energy cost, thus a more efficient system.

$$\eta = E_{app} - E_{eq} \qquad (1.5)$$

The Bi/IL interface experimentally demonstrated a lower overpotential of 0.165 V. The C2 acidic proton of 1,3-dialkylimidazolium cations have a reported p*K*a of ~32 in MeCN and an observed experimental redox couple of –1.78 V.[27] Applying these values to equation 1.4, ε exceeded 85 %. These catalytic properties further highlight the potential of Bi-CMEC acting as a heterogeneous platform for CO_2 reduction to CO.

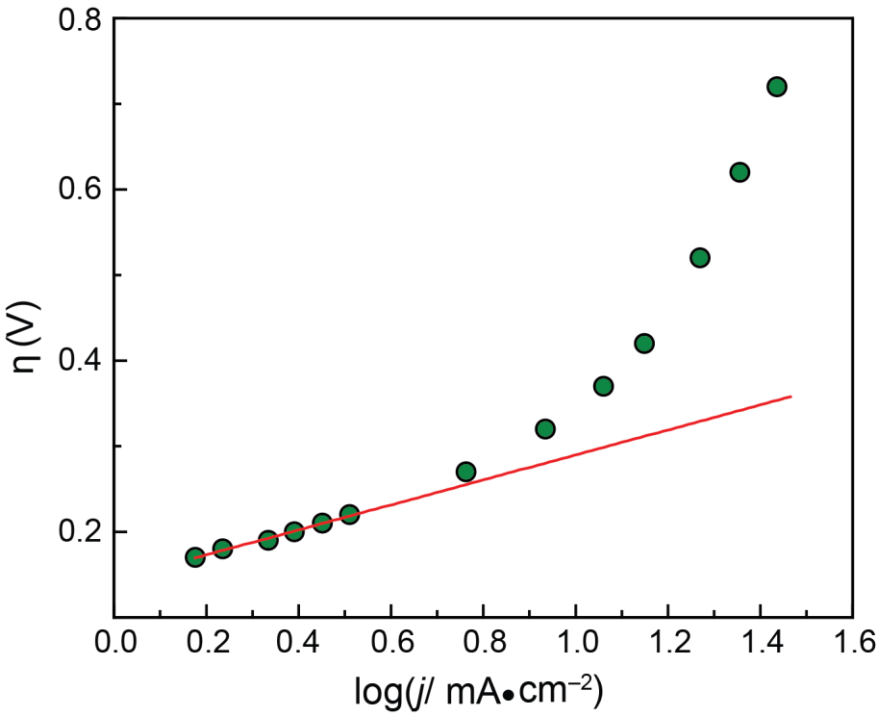

Figure 1.7. Tafel plot for Bi-CMEC via step potential electrolysis.

The mechanism for this redox reaction was studied with Tafel analysis. As described by the Butler-Volmer equation (equation 1.6), Tafel analysis provides mechanistic information on the rate determining step (RDS). When expressed for a large overpotential (>100 mV), equation 1.7 is obtained, where i is current, i_o is the exchange

current, α is a symmetry factor, and f is a combination of constants (equation 1.9, F is faradays number, R is a gas constant, and T is temperature in K).[28]

$$i = i_o[\exp(-\alpha f\eta) - \exp((1-\alpha)f\eta)] \qquad (1.6)$$

$$i = i_o\exp((1-\alpha)f\eta) \qquad (1.7)$$

$$\eta = -b \log (i) + a \qquad (1.8)$$

$$f = F/RT \qquad (1.9)$$

Rearranging equation 1.7 by solving for η, equation 1.8 is obtained, which shows a linear relationship between η and log i. When this relationship is described in a Tafel plot, the slope of this linear region provides information on the rate limiting ET event. Theoretical slopes have been derived to helped elucidate mechanistic information for the RDS.[29,30] For Bi-CMEC specifically, its Tafel plot (Figure 1.7) suggested a Tafel slope of 118 mV dec^{-1}. This slope correlates to the first ET being rate determining for the formation of surface adsorbed $CO_2^{\bullet-}$.[30]

This RDS has been suggested for a variety of heterogeneous electrodes,[13] but has recently been supported by potential dependent density functional theory (DFT) calculations performed in collaboration with the University of Minnesota. This was based on a higher calculated kinetic energy barrier for the first ET from the Bi/IL interface to the adsorbed CO_2 in comparison to subsequent H^+/e^- transfer events. Interestingly, an even larger kinetic barrier was calculated in the absence of IL. The acidic C2 proton on the IL likely interacts with the $CO_2^{\bullet-}$ to stabilize this intermediate and lower the energy barrier. The simulation also suggested that proton transfer is not from the adsorbed IL, despite it acting as a Lewis acid to stabilize $CO_2^{\bullet-}$. The pKa of adsorbed IL is increased significantly, such that IL in the bulk is likely providing the protons towards catalysis. When bulk IL delivers a proton to $CO_2^{\bullet-}$ it produces carboxyl

(COOH) and carbene. The second H^+/e^- transfer events are faster in comparison and are theorized to be similar to the first H^+/e^- transfer to yield water and loosely bound CO (Scheme 1.1).

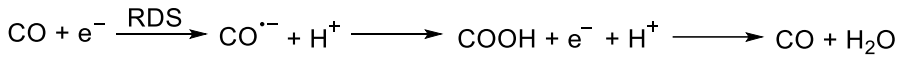

Scheme 1.1. Mechanistic depiction of the $2H^+/2e^-$ transfer for CO_2 to CO electrocatalysis.

Initial Bi-CMEC studies highlighted an impressive platform for CO_2 conversion to CO which marked the first example of Bi functioning as a carbon monoxide evolving catalyst. The Bi/IL interface demonstrated current densities reaching 9 mA/cm^2 and CO FEs exceeding 90 % that rival the historic silver and gold cathodes. Bi-CMEC remained robust during electrolysis (>12 hours) and demonstrated no decay in rate. XPS showed that the surface material that drives these high rates and CO selectivity was a Bi^0/Bi^{3+} assembly. The utility of this composition was initially unclear, i.e. if Bi^{3+} assists in stabilizing intermediates or if Bi^0/Bi^{3+} was the result of in situ reduction. To clarify its significance, in situ electrodeposition of Bi-CMEC was of interest. This required the development of a new organic electrodeposition procedure for the preparation of Bi-CMEC. Additionally, we hoped to achieve even faster rates by either strengthening ohmic contact, or by changing cathode material itself.

1.2.2 Advancements in the Bi-CMEC Platform

The previous ex situ acid aqueous plating procedure is incompatible with organic electrolysis conditions. Therefore, previous co-workers in the Rosenthal

Research Lab developed an in situ electrodeposition procedure based directly from the organic electrolysis conditions.[23] Additionally, the extent to which the catholyte anion effects CO_2 catalysis, and if the expensive $TBAPF_6$ supporting electrolyte can be eliminated without sacrificing CO production or current density, were also studied.

In situ electrodeposition streamlines an alternative method for modifying electrodes. Switching from a concentrated HCl acid aqueous electrodeposition to an organic electrodeposition allowed for the incorporation of more gentle substrates that are sensitive to corrosion or too reactive to remain inert under acidic conditions. The in situ plating deposition required the Bi material to be reduced at potentials more positive than the CO_2 reduction potential and for the Bi complex to be soluble in organics. Most Bi complexes are insoluble in organics. Some Bi complexes that are soluble in organics are reduced at potentials more negative than the CO_2 reduction potential, i.e. $Bi(Ph)_3$. Fortunately, $Bi(OTf)_3$ was found to fit these criteria. Importantly, OTf^- was previously demonstrated to be inert towards CO_2 catalysis.

Now having an attractive precursor, in situ electrodeposition was performed with 1.0 mM $Bi(OTf)_3$ and CO_2 saturated electrolyte solution via CV. The electrolyte solution consisted of 0.1 mM $TBAPF_6$ and 0.1 mM[BMIM]OTf in MeCN. Upon scanning through a range of potentials, a cathodic feature was shown at –1.2 V (Figure 1.8a, inset) and a larger current response was shown at –1.8 V, (Figure 1.8a, red trace). This is representative of Bi precipitating onto the GCE followed by CO_2 reduction respectively. The intense current enhancement at –1.8 V is analogous to cathodic rise for Bi when prepared with the acid aqueous ex situ electrodeposition. When in situ studies were performed under N_2, the current enhancement was suppressed,

representing no CO_2 reduction activity. Likewise, negligible current was observed under CO_2 when either Bi or IL were absent.

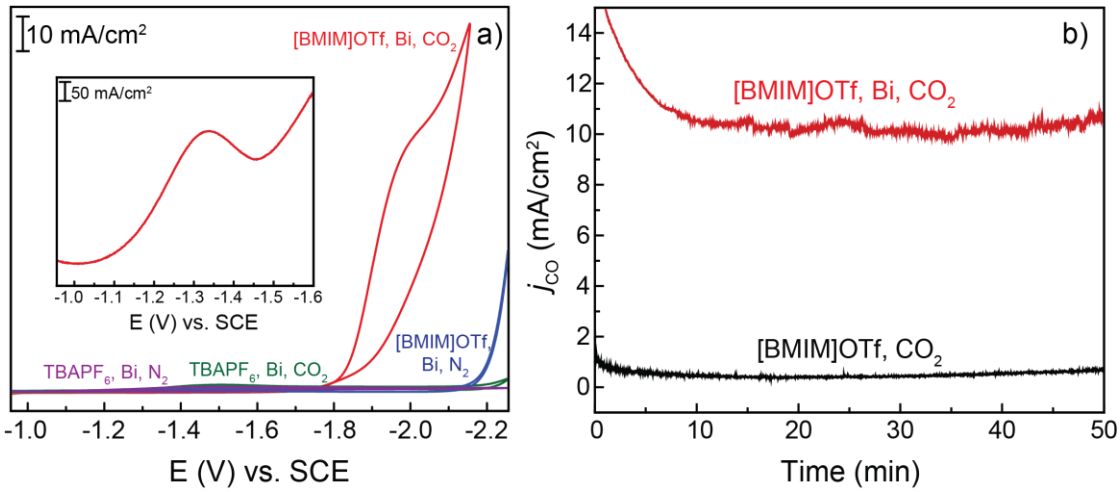

Figure 1.8. Cyclic voltammograms in a) illustrate in situ electrodeposited $Bi(OTf)_3$ in MeCN/IL. The inset shows the reduction of $Bi(OTf)_3$. Current density plot in b) shows in situ electrolysis for Bi/GCE/IL (red trace) and GCE/IL without Bi (black trace).

In situ capabilities were studied further via CPE (–2.0 V) when monitoring CO evolution and current density (Figure 1.8b). When the electrocatalytic cell consisted of just an unmodified GCE submersed in a CO_2 saturated MeCN/IL solution, no CO was quantified and the current density was negligible. When 1.0 mM $Bi(OTf)_3$ was added to the cathode, high current densities were achieved (~12 mA/cm^2) and surpassed what was observed previously with ex situ acid aqueous baths. CO was the only gaseous product detected and the catholyte showed no detection of formate, oxalate, or glyoxalate, other common production from CO_2 reduction.[31,32] Additionally, the

electrode at the end of electrolysis possessed a dark film representing the in situ modified Bi film.

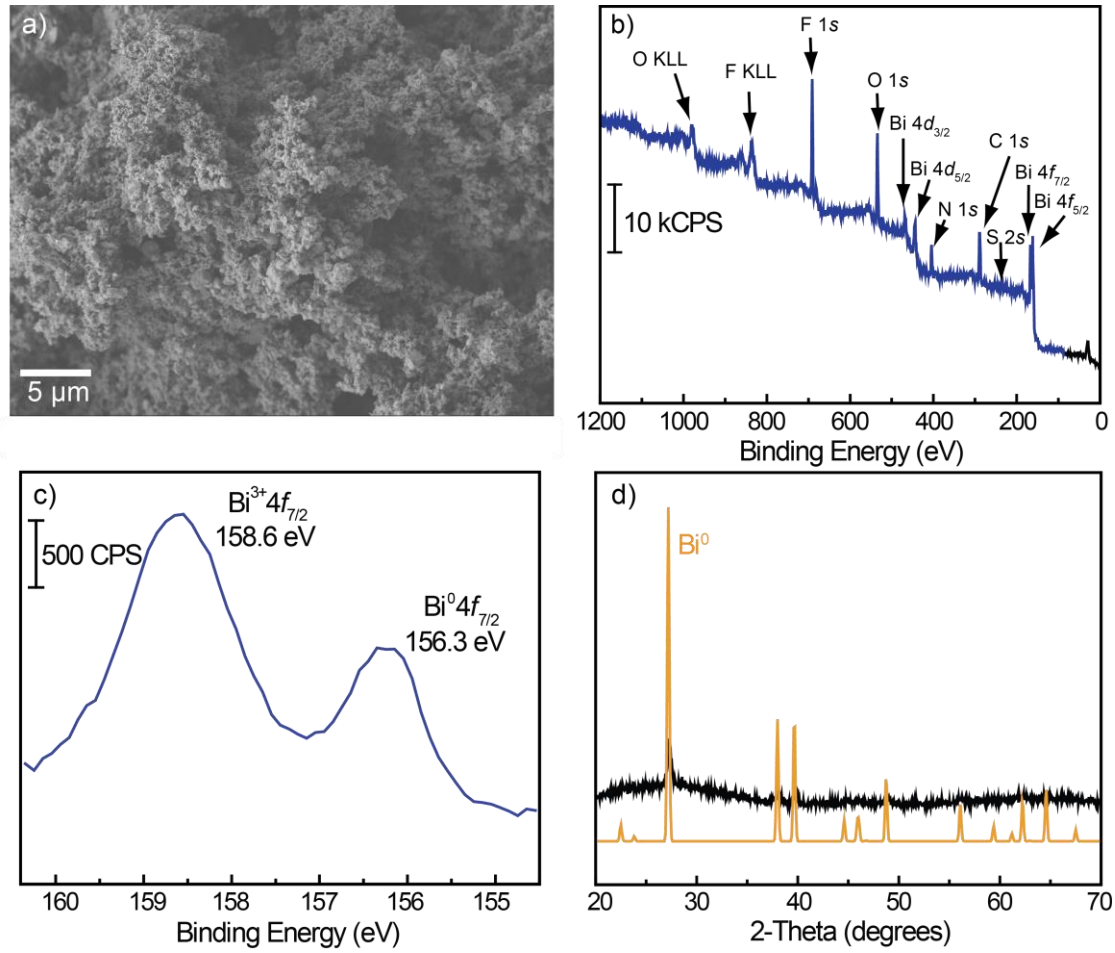

Figure 1.9. Secondary electron microscopy image in a) shows the surface morphology of the film in a 40 x 40 µm^2 window. The XPS survey spectrum and the Bi 4*f* high resolution spectrum are shown in b) and c) respectively. PXRD for the Bi-CMEC film (black trace) and the Bi^0 standard (orange trace) are shown in d).

The film was analyzed with SEM, XPS, and PXRD to probe for morphological information and film composition. SEM imaging (Figure 1.9a) revealed submicrometer-sized particles arranged with much depth and porosity to give a sponge-like appearance. The XPS survey spectrum (Figure 1.9b) suggested that Bi, in addition to residual triflate from the initial $Bi(OTf)_3$ starting complex, is present on the surface. Analogous to the Bi 4*f* high resolution spectrum for acid aqueous ex situ electrodeposition for Bi-CMEC, the in situ Bi 4*f* high resolution spectrum revealed a component at 157.1 and 159.5 eV representing Bi^0 and Bi^{3+} respectively (Figure 1.9c). PXRD demonstrated that the Bi^{3+} species is amorphous, such that the only peak observed represents Bi^0 (Figure 1.9d). This suggested that the main difference between the acid aqueous and organic electrodepositions is the crystalline vs amorphous morphology respectively.

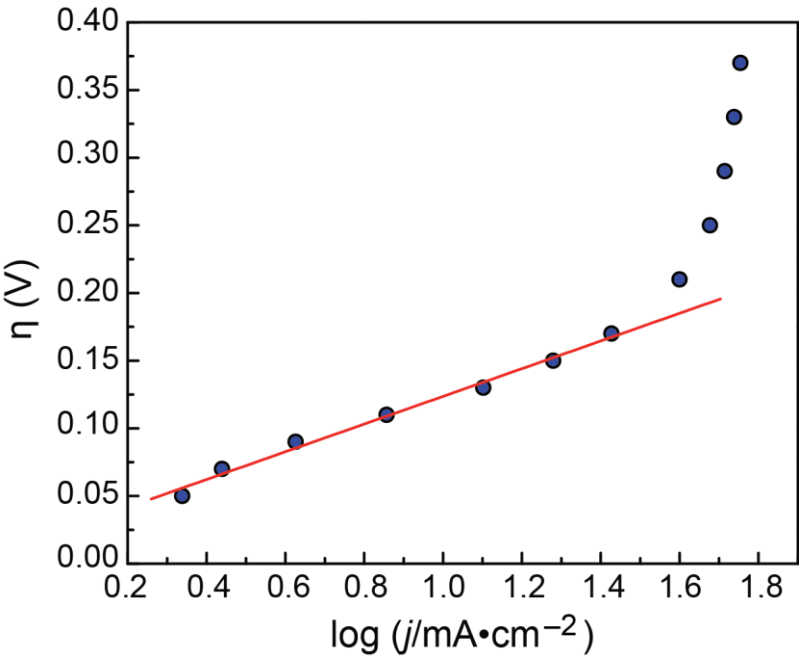

Figure 1.10. Tafel analysis performed using rotating ring electrode techniques at 1000 rpm.

Tafel studies were performed via rotating disc electrode (RDE). The Tafel plot slope was found to be 135 mV dec^{-1} which suggests that the RDS is the first ET to reduce the linear CO_2 species to generate the bent $CO_2^{\bullet-}$ (Figure 1.10). This parallels the RDS for Bi film prepared with acid aqueous conditions. Therefore, it was concluded that regardless of the acid aqueous electrodeposition or the organic electrodeposition, the mechanism for CO_2 reduction to CO is analogous.

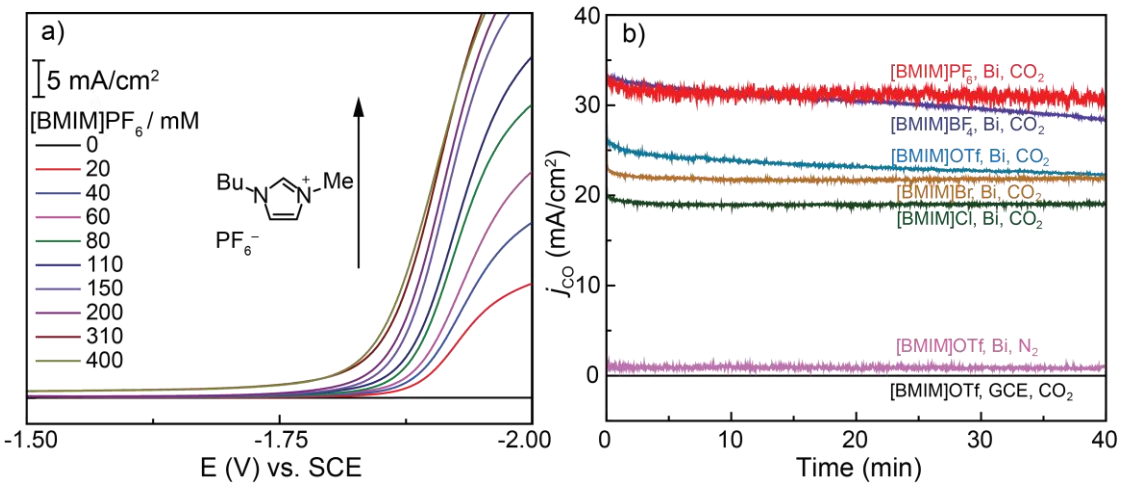

Figure 1.11. Cyclic voltammograms in a) show the $[BMIM]PF_6$ titration into CO_2 sat. MeCN with an ex situ Bi-modified GCE via organic electrodeposition. The current density plot in b) shows the comparisons between $[BMIM]^+$ ILs with PF_6^-, BF_4^-, OTf^-, Br^-, and Cl^- anions in the red, purple, blue, orange, and green traces respectively.

Because IL is known to act as electrolyte, it was of interest to observe if catalysis can be as effective with the elimination of $TBAPF_6$ supporting electrolyte.[33] To determine if $TBAPF_6$ can be removed, LSV studies were performed with ex situ organic electrodeposited Bi-CMEC/GCE in CO_2 saturated MeCN (Figure 1.11a) without

electrolyte. [BMIM]PF_6 was titrated into MeCN, which resulted in polarization curves resembling previously shown CVs that incorporated electrolyte (Figure 1.5b). With additions of IL, the current responses increased until a plateau at ~300 mM.

Now knowing that impressive CO_2 reduction activity is achieved with IL in lieu of incorporating supporting electrolyte, more robust ILs were explored. This was prompted from the previously studied ILs ([BMIM]PF_6 and [BMIM]BF_4) slowly hydrolyzing during long electrolysis. Keeping with the $[BMIM]^+$ cation, the anions studied included BF_4^-, Cl^-, Br^-, and OTf^-. CO_2 reduction activity for these ILs were studied similarly with LSV IL titrations. The resulting polarization curves were found to be nearly identical to the PF_6^- derivative. The current also plateaued at ~ 300 mM IL and demonstrated an onset potential of –1.78 V. Additionally, the onset potential relates well to $E^o_{CO2/CO}$ seen previously with the acid aqueous electrodeposition of Bi.

The screened $[BMIM]^+$ ILs were then studied via CPE with an applied potential of –2.0 V (η = of 220 mV) and an elevated concentration (300 mM) in CO_2 saturated MeCN in the absence of supporting electrolyte. As summarized in Table 1.4, all $[BMIM]^+$ ILs selectively evolved CO with FEs nearly reaching 90 %. The partial current densities associated with CO generation (j_{CO}) ranged from 17 to 30 mA/cm^2, affording higher rates than reported with 100 mM $TBAPF_6$ and IL. Additionally, the Bi film was not found to become passivated upon increasing amounts of IL. A robust film was demonstrated by steady current densities (Figure 1.11b). It is important to note, that when either Bi or IL was absent, there was no CO evolution.

Table 1.4. CPE metrics for Bi-CMEC with 300 mM $[BMIM]^+$ ILs at –2.0 (V) vs. SCE.

Electrode	IL	solvent	FE_{CO} (%)	ϕ_{CO} (%)	j_{CO} (mA cm^{-2})
Bi-CMEC	[BMIM]PF_6	MeCN	82 ± 12	73	31 ± 2

Bi-CMEC	[BMIM]BF_4	MeCN	82 ± 11	73	26 ± 4
Bi-CMEC	[BMIM]Cl	MeCN	79 ± 12	70	17 ± 2
Bi-CMEC	[BMIM]Br	MeCN	74 ± 4	65	20 ± 2
Bi-CMEC	[BMIM]OTf	MeCN	87 ± 8	77	25 ± 2
GCE	[BMIM]OTf	MeCN	None		0.4†

† Total current density

CO was produced in excellent yields in the absence of supporting electrolyte. The halide derivatives had the lowest CO generation likely from the additional water content from being more hydroscopic. The ε surpassed 70 % for all ILs, except for Br^- (demonstrating the lowest CO FE). OTf^- had the highest CO FE and ε (80 %). Discovering that [BMIM]OTf could yield these impressive metrics was beneficial towards the continuation of this study. [BMIM]OTf is one of the least expensive commercially available ILs, $2/ g, and previously to date, only the expensive noble metal Ag and Au cathodes could achieve these efficiencies.

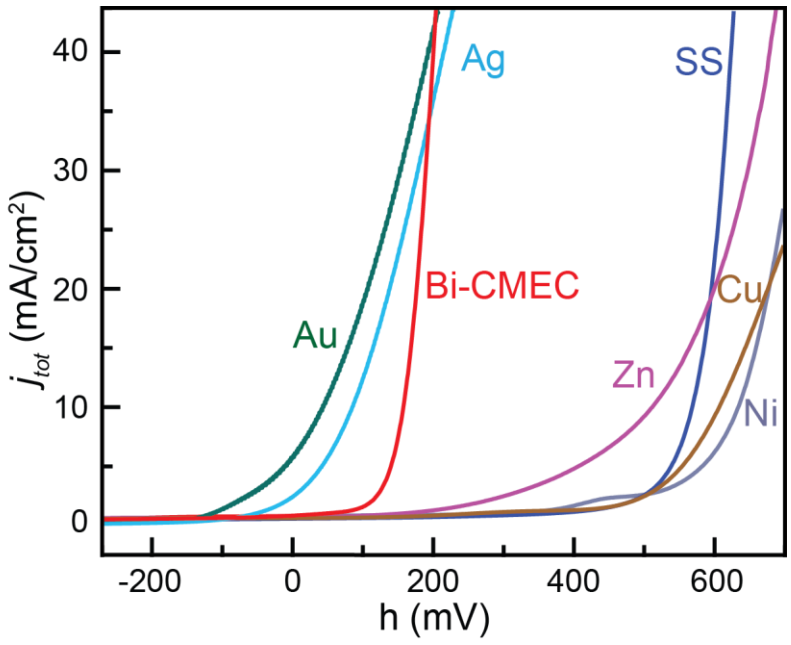

Figure 1.12. Linear sweep voltammograms for Bi, Au, Ag, SS, Zn, Cu, and Ni in red, green, blue, navy, purple, gold, and gray traces respectively.

These studied highlighted the versatility of the electrolyte solution and the electrode modification methods for Bi-CMEC to afford substantial current densities and CO efficiencies at low overpotentials (~200 mV). This demonstrated much promise in the advancement of energy conversion devices due its low energy input. Further, having the ability to screen various substrates via the recently developed organic electrodeposition method, future study for improving ohmic contact to create a more robust electrocatalyst was of interest. The impressive capabilities of the Bi-CMEC platform was highlighted when directly comparing its polarization curve to the historic Ag and Ag cathodes and other inexpensive cathode materials including Cu, Zn, stainless steel (SS), and Ni (Figure 1.12). Seeing that many metal cathodes have larger overpotentials for CO_2 reduction, it was curious if other inexpensive p-block metals near Bi on the periodic table promote similar catalysis to Bi. In doing so, it was of interest to observe if the cathode/IL interface is as essential for other cathodes as it is for Bi-CMEC.

1.2.3 Investigation of p-block Metal Cathodes

The p-block metal complexes studied were $Sn(OTf)_2$, $Pb(OTf)_2$, and $Sb(OTf)_3$. Triflate complexes were pursued because of their solubility in organics and for direct comparisons with $Bi(OTf)_3$. The triflate complexes were either commercially available (Sn) or easily synthesized (Pb and Sb). Organic ex situ electrodeposition resulted in a dark gray film which was later characterized with surface techniques to determine its morphology and elemental composition.

SEM imagining revealed similarities in film depth and porosity, however, unique microstructures were identified. Bi and Sb illustrated amorphous granular structures (Figures 1.13a and d respectively), whereas Pb showed striated clusters of

platelets and Sn showed micrometer crystallites that resembled ferns (Figures 1.13b and c respectively). EDX identified the p-block metal, along with O, F, and P. XPS also identified the respective metal, O, and F along with trace amounts of S, N, and P. These elements are likely from the electrodeposition solution (Bu_4N^+ and PF_6^-) and the triflate anion ($CF_3SO_3^-$).

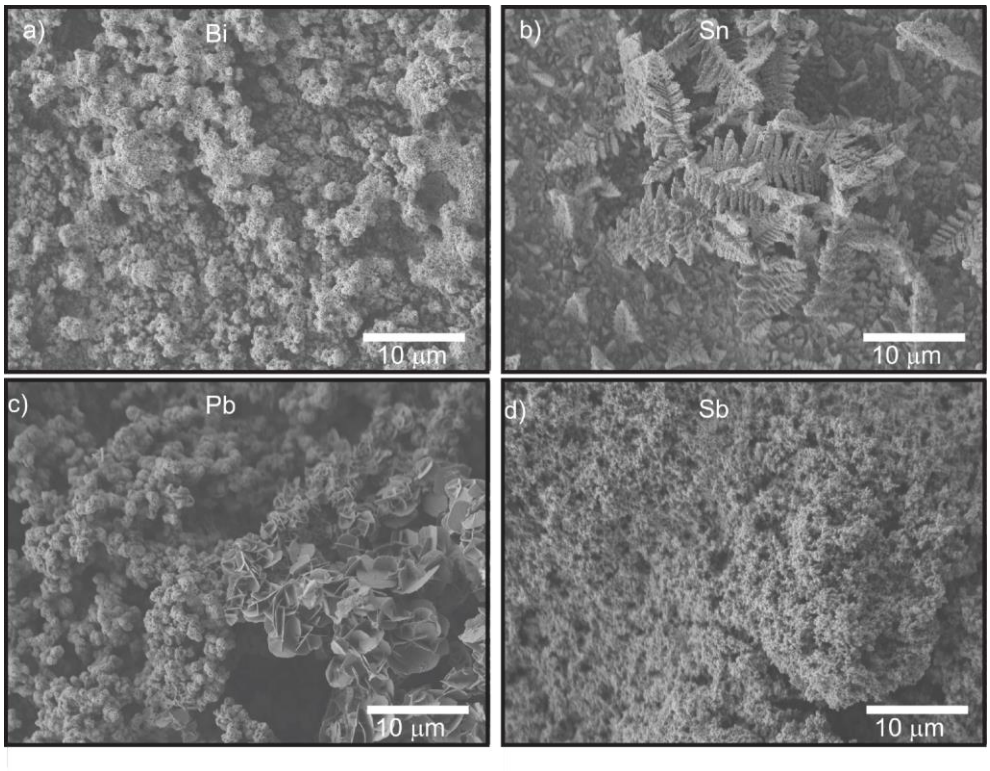

Figure 1.13. Secondary electron microscopy images of a) Bi, b) Sn, c) Pb, and d) Sb via ex situ organic electrodeposition.

The high resolution spectra for the p-block metals all revealed an overwhelming contribution of metal oxides on the surface (Figure 1.14). Bi $4f_{7/2}$ was fit to two components, 157.6 and 159.4 eV corresponding to Bi^0 and Bi^{3+} respectively in a 6:96

ratio (Figure 1.14a). Sn $3d_{5/2}$ was also fit to two components at 484.9 and 487.0 eV for Sn^0 and $Sn^{2+/4+}$ respectively in a 14:86 ratio (Figure 1.14b). Sb $3d_{5/2}$ was in a 19:81 ratio for Sb^0 to Sb^{3+}at 528.1 and 530.5 eV respectively (Figure 14d). Interestingly, Pb showed only a single component at 139.0 eV in the Pb $4f_{7/2}$ high resolution region indicative of $Pb^{2+/4+}$ (Figure 1.14c).

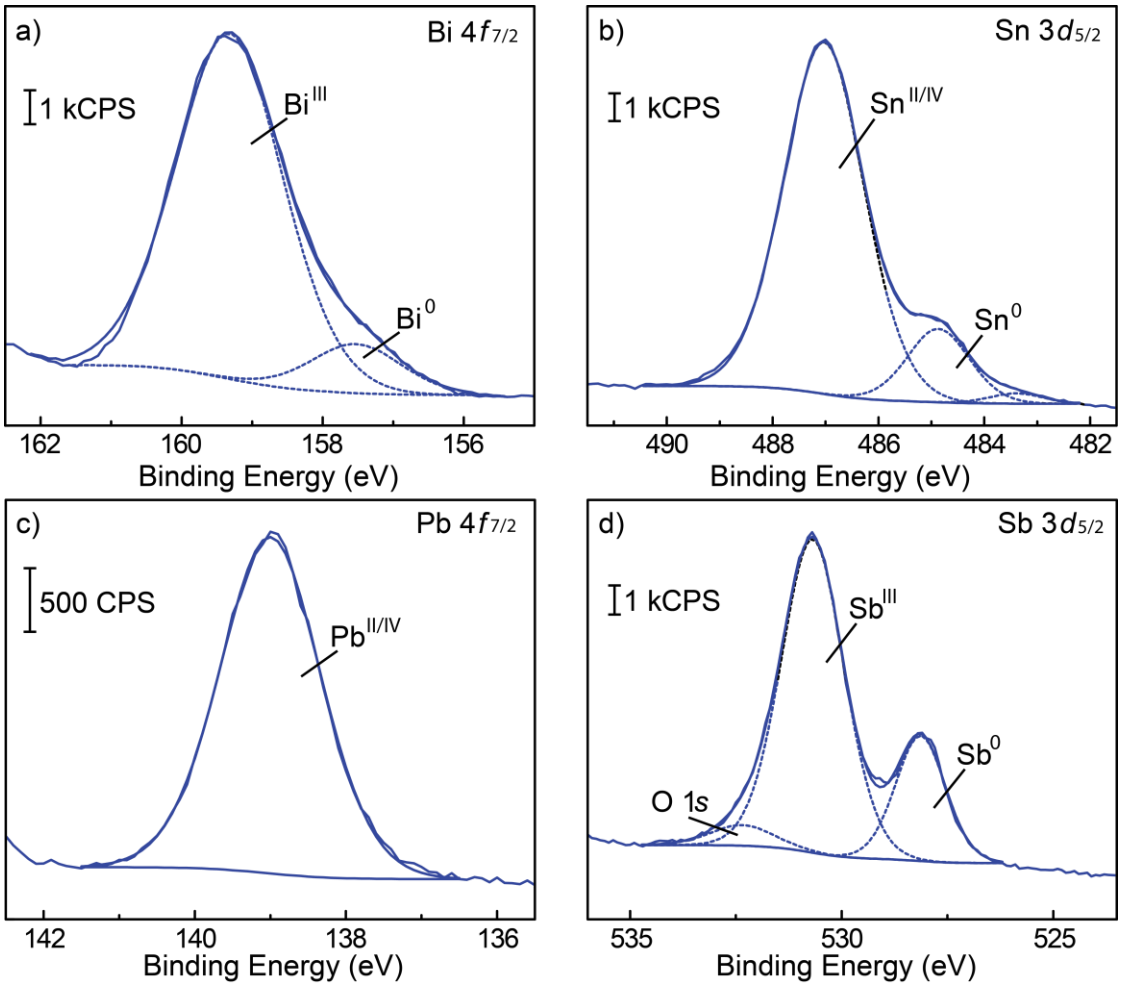

Figure 1.14. XPS high resolution spectra for a) Bi $4f_{7/2}$, b) Sn $3d_{5/2}$, c) Pb $4f_{7/2}$, and d) Sb $3d_{5/2}$.

After uncovering their unique surface compositions, their activity for CO_2 reduction was studied via LSV with 100 mM [BMIM]OTf and $TBAPF_6$ in CO_2 saturated MeCN with either a GCE (Bi, Pb, and Sb) or Ni electrode (Sn). Bi was found to have the earliest onset potential, –1.80 V, closely followed by Sn and Sb. Pb had the latest onset potential of ~ –1.95 V (Figure 1.15a), suggesting that Pb has the largest kinetic barrier. When performed under N_2, there was negligible current for all cathodes. Interestingly, Sb was the only material to show no current enhancement even under CO_2, implying no activity towards CO_2 reduction. Bi and Sn both showed similar polarization curves, whereas Pb demonstrated a less intense rise in current.

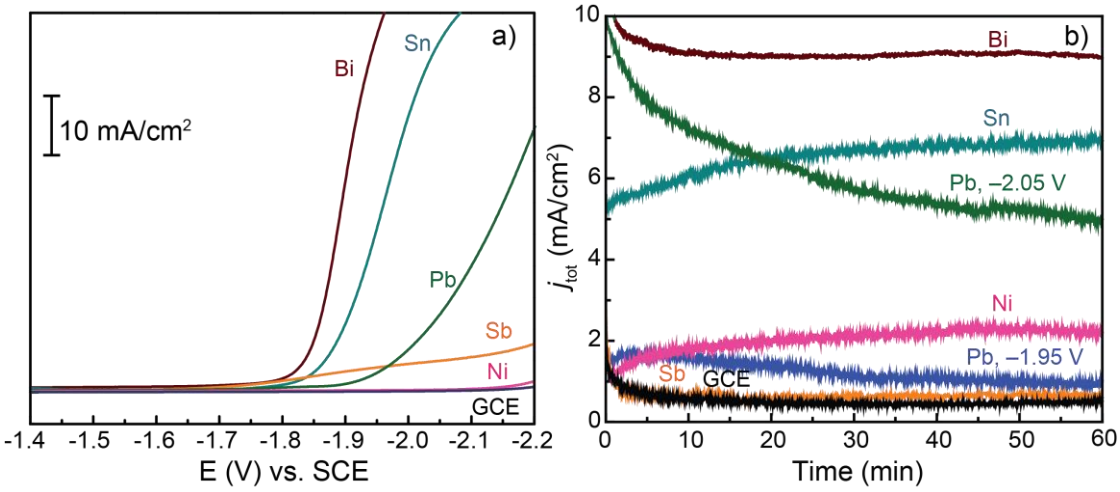

Figure 1.15. Linear sweep voltammograms in a) for Bi (marron trace), Sn (cyan trace), Pb (green trace), Sb (yellow trace), and their respective inert substrates (Ni (pink trace) and GCE (black trace)). The current density plot is illustrated in b).

The product distribution for CO_2 reduction was studied via CPE. Specifically, it was curious if the greater O or F content affects catalysis. Because Bi, Sn, and Sb

demonstrated similar onset potentials, electrolysis was performed at –1.95 V. Pb was performed at –1.95 and –2.05 V due to having a more negative onset potential. The current density plot from CPE (Figure 1.15b) showed Bi and Sn having high and steady currents affording no contribution from the inert substrate. Pb began electrolysis (–2.05 V) with an equally high rate, but decreased over time. Even when –1.95 V was applied to the Pb cathode, its current density did not exceed 2 mA/cm^2 and decrease further just 10 minutes into electrolysis. The final current density was no higher than the bare GCE. Similarly, the current density for Sb was comparable to the unmodified GCE.

As shown in Table 1.5, Bi, Sn, and Pb (–2.05 V) were ~ 80 % selective for CO evolution with no H_2, methane, or other small hydrocarbon production. The uncompensated 20 % of charge is likely attributed to nonvolatile CO_2 reduction products that are not detectible within our GC detection limits. Sb showed no selectivity for CO and produced an equivalent amount of H_2 and formic acid (HCOOH). At –1.95 V for Pb, CO selectivity was halved (40 %) and it now produced HCOOH (31 %) and H_2 (11 %). When performed under N_2, the current densities for Bi, Sn, and Pb were negligible. When IL was removed from the electrolyte solution under CO_2, the current density and CO production dropped significantly. This highlights that the cathode/IL interface is not only essential for Bi, but for Sn and Pb as well.

Table 1.5. CPE metrics for the Bi, Sn, Pb, and Sb cathodes.

electrode	E_{appl} (η)	j_{tot} (mA cm^{-2})	FE_{CO} (%)	FE_{H2} (%)	FE_{FA} (%)	j_{CO} (mA cm^{-2})
Bi	–1.95 V (~200 mV)	10.1 ± 2.1	78 ± 5			8.4 ± 1.7
Sn	–1.95 V (~200 mV)	7.2 ± 1.9	77 ± 5		5 ± 1	5.0 ± 1.8
Sb	–1.95 V (~200 mV)	0.5 ± 0.1		30 ± 20	29 ± 21	
Pb	–1.95 V (~200 mV)	1.0 ± 0.4	40 ± 12	11 ± 6	31 ± 17	0.4 ± 0.2
Pb	–2.05 V (~300 mV)	5.0 ± 1.0	81 ± 5			4.1 ± 0.9

Of the four p-block metals, only Bi, Sn, and Pb demonstrated the ability to reduce CO_2 with impressive metrics. The Pb cathode, however, became passivated with current densities reaching below 4 mA/cm^2 and CO evolution steadying at ~10 %. Sn demonstrated catalytic behaviors that resembled Bi (CO selectivity, onset potential, and kinetics) and therefore modeled a promising platform for organic electrolysis for the rapid conversion of CO_2 to CO. Sn also demonstrated the same essential cathode/IL interface, highlighted in Figure 1.15a via CV. A desire to further optimize Sn was prompted by its ability to be prepared via in situ techniques. Sn is a good candidate for in situ catalysis because $Sn(OTf)_2$ is soluble in organics and has a reduction potential lower than the CO_2 reduction potential.

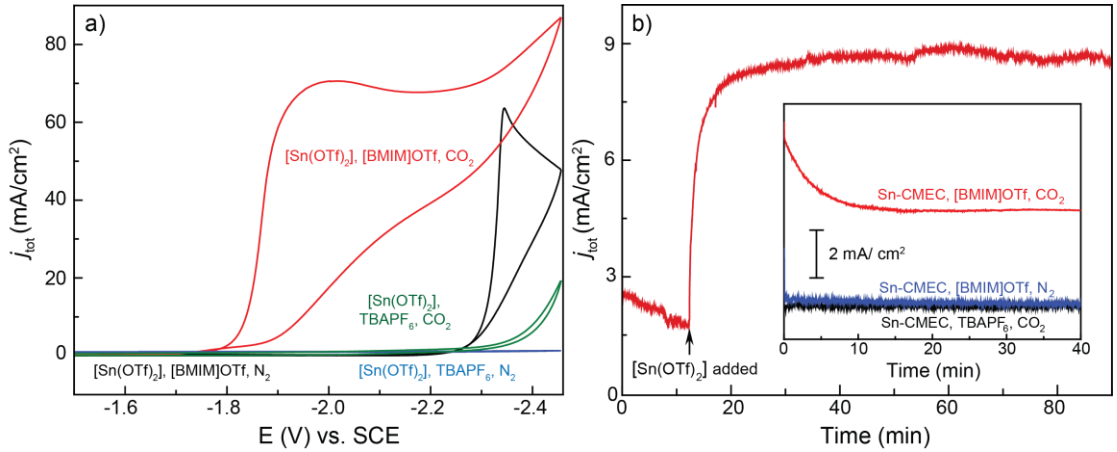

Figure 1.16. Cyclic voltammograms in a) show the current response for Sn in MeCN/IL/$TBAPF_6$ under CO_2 (red trace) and N_2 (black trace), and for MeCN/$TBAPF_6$ under CO_2 (green trace) and N_2 (blue trace). The current density plot in b) shows 0.1 M $Sn(OTf)_2$ added in situ to the catholyte during CPE. The inset describes the current density for Sn in CO_2 sat. MeCN/IL (red trace), N_2 sat. MeCN/IL (blue trace), and CO_2 sat. MeCN/$TBAPF_6$ (black trace).

The in situ capabilities for Sn were highlighted during CPE when a bare Ni disc electrode was submersed in CO_2 saturated MeCN/IL (Figure 1.16b). The current density was negligible until 1.0 mM $Sn(OTf)_2$ was added to the catholyte where a sharp rise in current density was observed, reaching ~9 mA/cm^2. Paired with GC analysis, CO was the sole product detected only after Sn was added (~75 %).

These studies demonstrated that there are other inexpensive earth abundant materials that are capable of electrochemically transforming CO_2 to CO, highlighting that these materials can be prepared via ex situ and in situ techniques. Of the additional p-block metals studied, Sn stands out as a promising platform for CO evolution. Additionally, the IL interface for Bi and Sn was demonstrated to be an essential component for establishing high CO selectivity, appreciable rates, and low energy costs.

1.3 Conclusions and Future Directions

In summary, the Rosenthal Research Lab was the first to explore the electrocatalytic capabilities of Bi; an inexpensive and earth abundant material that can electrochemically transform CO_2 to CO with high selectivity, appreciable current densities, and low energy cost. Bi-CMEC is comparable to the historic noble metal cathodes, but it is not impeded by the cost of material for industrial scaling. Industrial integration can be promoted further upon redesigning our two-compartment electrochemical cell into a flow cell. This may also encourage enhanced mass transport.

Already demonstrating impressive metrics, the versatility of Bi-CMEC was further demonstrated upon developing an organic plating procedure for in situ studies. The organic electrodeposition tolerated delicate substrates that are reactive under acidic conditions. The organic electrodeposition is easily modified and allowed for materials other than Bi (Sn, Pb, and Sb) to be studied. Despite Sb showing poor CO_2 reduction

activity, Sn and Pb demonstrated high activity towards CO_2 reduction and selective CO evolution. The Sn cathode demonstrated the greatest resemblance to Bi. Pb, however, was not robust during CPE and instills curiosity as to why this film becomes passivated. It was of interest to perform additional studies on Pb to investigate this behavior.

An essential cathode/IL interface was revealed and was suggested to play a critical role in stabilizing the electrode bias, suppressing H_2 evolution, and stabilizing the $CO_2^{\bullet-}$. It was curious to observe how neat IL systems (the absence of solvent) would behave during catalysis. Additionally, their physical properties (viscosity and T_{onset}) would provide valuable insight on diffusional effects and IL structural durability.

REFERENCES

(1) Richels, R. G. *Energy Journal*. **1991**, *12*, 211—212.

(2) Worrell, E.; Price, L.; Martin, N.; Hendriks, C.; Meida, L. O. *Annual Review of Energy and the Environment*. **2001**, *26*, 303—329.

(3) Wang, S.; Li, Q.; Fang, C.; Zhou, C. T. *Science Direct*. **2016**, *542*, 360—371.

(4) Zhang, X.; Cheng, X. *Ecological Economics*. **2009**, *68*, 2706—2712.

(5) Chu, S.; Cui, Y.; Liu, N. *Nature Materials*. **2017**, *16*, 16—22.

(6) BP Statistical Review of World Energy, 2016.

(7) Lewis, N. S.; Nocera, D. G. *Proceedings of the National Academy of Sciences.* **2006**, *103*, 15729.

(8) Crabtree, G.; Lewis, N.; Tsao, J. Solar FAQs, 2016.

(9) Solomon, S.; Plattner, G.; Knutti, R.; Friedlingstein, P. *Proceedings of the National Academy of Sciences.* **2009**, *106*, 1704.

(10) Drijfhout, S.; Bathiany, S.; Beaulieu, C.; Brovkin, V.; Claussen, M.; Huntingford, C. *Proceedings of the National Academy of Sciences.* **2015**, *112*, 5777.

(11) Luo, X.; Wang, J.; Dooner, M.; Clarke, J. *Applied Energy.* **2015**, *137*, 511.

(12) van Vliet, O. P. R.; Faaij, A. P. C.; Turkenburg, W. C. *Energy Conversion and Management*. **2009**, *50*, 855—876.

(13) Kortlever, R.; Shen, J.; Schouten, K. J. P.; Vallejo, F. C.; Koper, M. T. M. *Journal Physical Chemistry Letters*. **2015**, *6*, 4073—4082.

(14) Huddleston, J. G.; Visser, A. E.; Reichert, M.; Willauer, H. D.; Broker, G. A.; Rogers, R. D. *Green Chemistry*, **2001**, *3*, 156—164.

(15) Beller, M.; Cornils, B.; Frohning, C. D.; Kohlpaintner, C. W. *Journal of Molecular Catalysis A.* **1995**, *104*, 17—85.

(16) Sano, K.; Uchida, H.; Wakabayshi, S. *Catalysis Surveys from Japan*. **1999**, *3*, 55—60.

(17) Fu, Q.; Saltsburg, H.; Flytzani-Stephanopoulos. *Science*. **2003**, *301*, 935—938.

(18) Rofer-DePoorter, C. K. *Chemical Reviews*. **1981**, *81*, 447—474.

(19) Liu, C.; Cundari, T. R.; Wilson, A. K. *Journal of Physical Chemistry C*. **2012**, *116*, 5681—5688.

(20) Zhang, Y.; Yin, S.; Luo, S.; Au, C. T. *Industrial and Engineering Chemistry Research.* **2012**, *51*, 3951—3957.

(21) Komatsu, S.; Yanagihara, T.; Hiraga, Y.; Tanaka, M.; Kunugi, A. *Denki Kagaku*. **1995**, *63*, 217–224.

(22) DiMeglio, J. L.; Rosenthal, J. *Journal of the American Chemical Society*. **2013**, *135*, 8798–8801.

(23) Medina-Ramos, J.; DiMeglio, J. L.; Rosenthal, J. *Journal of the American Chemical Society*. **2014**, *136*, 8361–8367.

(24) Medina-Ramos, J.; Pupillo, R. C. Keane, T. P.; DiMeglio, J. L.; Rosenthal, J. *Journal of the American Chemical Society.* **2015**, 137, 5021—5027.

(25) de Souza, J. P.; Iwasita, T.; Nart, F. C.; Vielstich, W. *Journal of Applied Electrochemistry*. **2000**, *30*, 43—48.

(26) Costentin, C.; Drouet, S.; Robert, M.; Saveant, J. M. *Science* **2012**, *338*, 90−94.

(27) Magill, A. M.; Cavell, K. J.; Yates, B. F. *Journal of the American Chemical Society*. **2004**, *126*, 8717−8724.

(28) Bard, A. J.; Faulkner, L. R. *Electrochemical Methods Fundamentals and Applications*; second edi.; John Wiley & Sons: Hoboken, New Jersey, 2001.

(29) Guidelli, R.; Compton, R. G.; Feliu, J. M.; Gileadi, E.; Lipkowski, J.; Schmickler,W.; Trasatti, S. *Pure and Applied Chemistry.* **2014**, *86*, 245.

(30) Noel, M.; Vasu, K. I. *Cyclic Voltammetry and the Frontiers of Electrochemistry*; Oxford & IBH: Janpath, New Delhi, 1990.

(31) Eggins, B. R.; Ennis, C.; McConnell, R.; Spence, M. *Journal of Applied Electrochemistry*. **1997**, *27*, 706.

(32) Amatore, C.; Saveant, J. M.́ *Journal of the American Chemical Society*. **1981**, *103*, 5021.

(33) Salen, N.; Nicodemou, L.; Abu-Lebdeh, Y. *Journal of The Electrochemical Society*. **2012**, *159*, A172—A176.

Chapter 2

Bi-CMEC ASSIMILATION INTO INDUSTRY VIA A 3D-PRINTED FLOW ELECTROLYSIS ASSEMBLY

2.1 Introduction

The fossil fuel industry has been implemented for decades and has optimized their fuel production to easily adapt to fluctuations in energy demand.[1] Solar energy, however, currently faces a challenge with meeting supply and demand of its global consumers due to its intermittency and lack of a long-term energy storage mechanism.[2] When sunlight emits solar energy via high power energy irradiation, it is not guaranteed that it will be during the peak energy demand. Because of this, the development of inexpensive solar energy storing devices remains essential. If energy-storage devices can provide energy during seasonal changes and unexpected weather, renewable energy could displace facilities that are less efficient and more expensive. The ability to provide for sudden demands in energy may also encourage an energy dependency switch to renewables. This can ultimately suppress environmental damages from fossil fuel combustion (CO_2) from the fossil fuel industry.[1] Additionally, solar energy electrical storage devices offer benefit during off energy peaks by pumping/ charging to further optimize operations.[3]

One proposed solar energy storing devise is through the chemical bonds in solar fuels.[4,5] Chemical bonds in hydrocarbons, i.e. methanol, are amongst the highest energy dense materials, greatly surpassing other energy storage devices, i.e. lithium-ion batteries (chemical energy) and flywheels powered by wind turbines (kinetic energy).[2,6]

If the proposed solar energy storage device can be manufactured in a cost effective and efficient manner, then solar fuels would act as an efficient platform to provide clean renewable energy to the consumer during the low and high energy peaks. This would mark a critical transition of energy dependency from fossil fuels to solar energy. This demonstrates high potential for a switch in energy dependency, in that solar energy utilization has been increasing yearly by approximately 60 %.[7]

Implementing solar fuel production is envisioned by coupling solar energy to a photovoltaic to drive the reduction of CO_2 to CO. CO will then undergo the well-known Fischer-Tropsch process, as it is the C1 feedstock, to produce hydrocarbon solar fuels. There are two key challenges associated with the anticipated production of solar fuels; (1) the development of an inexpensive catalyst for the initial reduction of CO_2 to the high-energy CO molecule and (2) designing an electrolysis assembly that matches industrial requirements while encouraging optimal CO production.

In recent work, co-workers in the Rosenthal Research Lab developed a bismuth carbon monoxide evolving catalyst (Bi-CMEC) that can undergo the initial transformation from CO_2 to CO. Bi-CMEC was identified with high selectivity for CO evolution (90%), high energy efficiency (ε, ~83 %), sufficient current density (~5 mA/cm^2), and low energy cost (~200 mV). These metrics rivaled the historic noble metal cathodes, Ag and Au, for CO_2 to CO heterogeneous electrocatalysis. Comparing the cost of Ag and Au ($700 and $45 000/ kg respectively) to the cost of Bi (~ $18/ g), however, Bi-CMEC was more attractive for industrial scaling.

Bi showed promise in the advancement of solar energy storage by acting as an inexpensive material to catalyze CO production. To further this advancement and overcome the second challenge associated with implementing solar fuel production via

a solar energy storage device, the two-compartment electrochemical cell architecture used previously for electrocatalysis was redesigned to encourage integration into industry. Specifically, the fragile glass cell was transformed into a robust 3D printed electrolysis flow cell assembly. The flow cell incorporated inexpensive nylon material, low-costing carbon supports that can easily be scaled, and commercially available and inexpensive Bi^{3+} complexes. Further, 3D printing the redox cell offered rapid and cost effective prototyping for easily optimizing the cell design with high precision and accuracy. Additionally, the constant flow of recycled electrolyte over the catalyst surface showed a substantial enhancement in mass transport.

2.2 Experimental Method

2.2.1 Materials and Methods

Reagents and solvents were purchased from Sigma Aldrich, Alfa Aesar, Acros or Fisher. Imidazolium ionic liquid 1-butyl-3-methylimidazolium trifluoromethanesulfonate ([BMIM]OTf), Nafion perfluorinated ion-exchange resin (5 wt.% solution in lower aliphatic alcohols/H_2O mix), bismuth(III) carbonate, bismuth(III) nitrate, and bismuth(III) subsalicylate were purchased from Sigma Aldrich. Tetrabutylammonium hexafluorophosphate ($TBAPF_6$) was purchased from TCI America and purified by recrystallization with ethanol. Multiwall carbon nanotubes (MWCNTs) were purchased from Fuel Cell Earth. Carbon dioxide (CO_2) was purchased from Keen Compressed Gas Company.

Platinum gauze (99 %) was purchased from Sigma Aldrich. The bare glassy carbon disc electrode and the Ag/AgCl reference electrode were purchased from CHI

Instruments. Carbon paper, carbon cloth, and 10 % Pt on Carbon Cloth were purchased from Fuel Cell Earth.

2.2.2 Bismuth Slurry Procedure

The solution was prepared by suspending a Bi^{3+} complex in tetrahydrofuran (THF, 10 mL) where it was immobilized on multiwall carbon nanotubes (MWCNTs) in a 40:1 wt.% ratio in the presence of 5% Nafion (1.1% of slurry). The suspension was sonicated for 20 minutes before drop casting. Drop casting involved applying 500 μL of the slurry onto carbon paper, carbon cloth, or a GCE using an automated pipet (100/1000). The Bi^{3+} complex was either bismuth(III) carbonate, bismuth(III) nitrate, or bismuth(III) subsalicylate.

2.2.3 Instrumentation

2.2.3.1 Electrochemical Measurements

Electrochemical studies were conducted using a CHI-620D potentiostat/galvanostat or a CHI-720D bipotentiostat. Electrochemical apparatus consisted of a three-electrode system; working (bare glassy carbon disc (3.0 mm diameter), carbon paper (1.0 cm x 2.2 cm), carbon cloth (1.0 cm x 2.2 cm)), counter (platinum gauze (1.0 cm x 2.2 cm)), and a reference (Ag/AgCl, (1.0 M HCl)) or pseudo reference (Ag wire)). Cyclic voltammetry and linear voltammetry experiments were performed with iR drop compensation with 100 mV s^{-1} scan rate. Ag/AgCl reference was converted to SCE referencing by the equation, $E_{SCE} = E_{Ag/AgCl} + 0.044$ V.

2.2.3.2 X-ray Photoelectron Spectroscopy

XPS analysis was performed using a Thermo Scientific K-alpha^{+} spectrometer with monochromatic Al Kα X-ray (1486.7 eV) and 72 W of power (12 kV, 6 mA) equipped with a 128 CCD detector plate. Operating vacuum pressure in the main chamber was less than $1x10^{-8}$ torr. XPS survey scans were collected with a step size of 1.0 eV and a pass energy of 100 eV. High resolution spectra were collected with a step size of 0.1 eV and a pass energy of 20 eV. The X-ray spot size was an elliptical shape with a semi-major axis of approximately 400 μm.

2.2.3.3 SEM and EDX

Secondary electron microscopy (SEM) and energy dispersive X-ray (EDX) were performed on a JEOL JSM 7400F scanning electron microscope. Data was collected in a 40 x 40 μm^2 window.

2.2.3.4 CO_2 Reduction Electrolysis and Headspace Analysis

Current densities were obtained by performing controlled potential electrolysis (CPE) on a nylon 3D printed cell. The electrolyte solution contained 50 mL of CO_2 saturated acetonitrile with dissolved ionic liquid and/or 0.1 M $TBAPF_6$. The solution was sparged for 30 minutes prior to electrolysis.

During CPE, the electrolyte solution was continuously mixed by the peristaltic pump (100 mL min^{-1}) with a continuous flow of CO_2 into the headspace (30 mL min^{-1}). The single cell head space was vented directly into a flow gas chromatograph (SRI Instruments, SRI-8610C). A chromatograph was obtained every 15 min throughout the duration of electrolysis by placing the sampling loop in line with a packed HayeSep D column and a packed mole Sieve 13X column. The columns led directly to a thermal conductivity detector (TCD) and a flame ionization detector (FID) equipped with a

methanizer to quantify hydrogen and carbon monoxide production respectively. The gas carrier was Argon (Keen, 99.999 %).

2.2.3.5 Solvent Suppression ^{1}H NMR

Solvent suppression ^{1}H NMR was performed with aliquots from the electrolyte solution to detect any solution products from electrolysis and/or decomposition of electrolyte solution. The acetonitrile resonance was suppressed at 1.96 ppm. Formic acid production was monitored at 8.1 ppm.

2.3 Results and Discussions

2.3.1 Flow Cell Inspiration for Energy Storage

A variety of electrolyzer architectures have been designed and implemented in industry since the 1920s and 1930s.[8] Commercial electrolyzers have demonstrated the ability to store electrical energy for extended periods of time, such as for redox flow batteries (RFB) for hydrogen (H_2) fuel production.[9] Manufacturing electrolyzers for large-scale production, however, is costly. Even when constructed, the capital cost for implementing them into industry is high.[3] From an industrial standpoint, using low costing hydrocarbons is a more attractive alternative to electricity-based energy.[8] Energy storage devices typically require frequent maintenance and are heavy, which places additional limitations on profit and transportability.[10] Altering the design and method of manufacturing existing bulky electrolyzers may greatly lessen the price and may ultimately make industrial integration desirable. 3D printed flow assemblies help to negate these costs and also offers desirable assets for industrial corporations; rapid and cost effective prototyping for facile design optimization, assemblies can be

constructed with intricate designs and flow ports with high precision and accuracy, and the weight is reduced considerably.[11] It has an adaptable design that results in maintenance and manufacturing costs to be less than other electrical storage methods stated previously.[10] 3D printing also allows for the quick fabrication of multiple electrolyzers to test different design architectures, i.e. channel width and flow path, that were once difficult, time consuming, and expensive to screen.[3] Flow cells are sealed systems that are not affected or influenced by the surrounding environment. This results in little need to re-optimize existing systems while also offering a safer environment for industry workers.

Flow technologies have also shown promise for other chemical systems, such as continuous-flow organic synthesis and water electrolyzers. These systems used 3D printing technologies that took advantage of design schemes with inline analytics to observe results in real time.[11,12] Redox flow cells have been designed for the purpose of storing and dispensing electrical energy for Fe/Cr, V(II)/V(III), or V(IV)/ V(V) systems, but they lacked the industrial advantages of 3D printing technologies.[13,14] For the encouragement of solar fuel production specifically, our redox electrochemical cell was designed with appropriate dimensions to encourage the flow of electrolyte over the catalyst to swiftly bring CO_2 to the electrode surface and ultimately diffuse away CO. In doing so, we anticipated an enhancement in mass transport (rate) in addition to making our system more industrially feasible.

2.3.2 Flow Cell Design

As stated previously, our electrochemical flow cell was manufactured using nylon 3D printing technologies to prepare the central flow body and the exterior flow plates. The design was modeled on computer aided design (CAD) software and

ultimately constructed layer by layer by a 3D printer. The architecture for the electrochemical flow cell is displayed in Figure 2.1a. Structural support was added to the flow cell by incorporating stainless steel (SS) plates adjacent to the exterior nylon plates. Two sets of silicon strips, one with a central window and one without, sandwiched the auxiliary (Pt/ C cloth) and working electrode (inert carbon substrate) individually. The silicone strips encouraged a sealed system thus to prevent leaking and contamination from the surrounding environment. The working and auxiliary electrodes were placed on either side of the central flow plate (silicone window facing the central flow plate). Because the auxiliary and working electrode are trapped inside the cell, SS conducting strips (3.0 cm x 1.0 cm) were used to extend these terminals to the potentiostat leads. The complete layering of the various components to the cell are secured together with screw and bolt clamping pressure at each of the four corners.

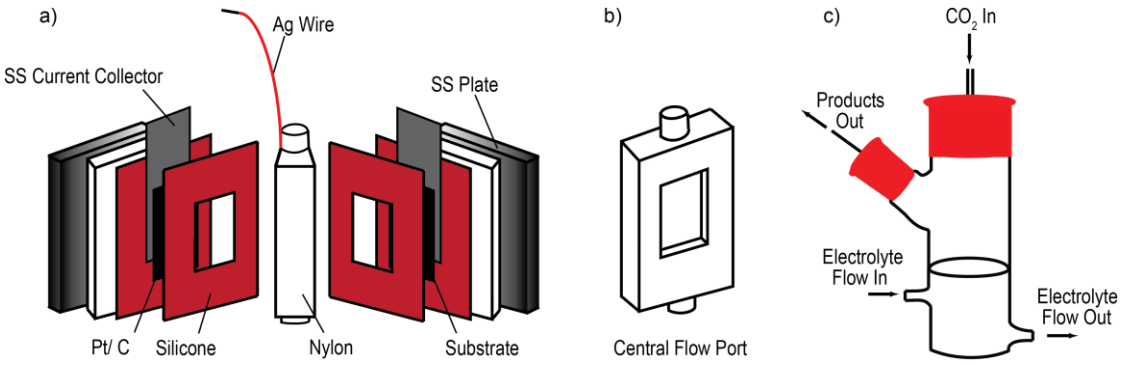

Figure 2.1. Flow cell design, central flow port architecture, and single cell reservoir are illustrated in a, b, and c respectively.

The central flow plate was designed with an internal window (1.0 cm x 2.2 cm), as illustrated in Figure 2.1b. This allows for the flowing electrolyte solution to interact

simultaneously with the anode and cathode. As the solution flows out of the exit channel of the central flow plate, it comes into contact with the pseudo reference electrode (Ag wire) and is collected in a single cell reservoir (Figure 2.1c). Here, any gaseous products will migrate out of solution and fill the single-cell headspace which is tethered with inline analytics to a flow gas chromatograph (GC). Gaseous products could now be detected in real time during the duration of the electrolysis. The final flow device when assembled is shown in Figure 2.2.

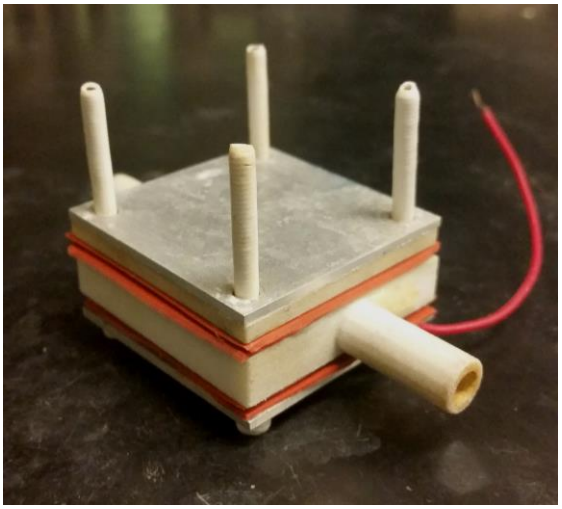

Figure 2.2. Assembled 3D printed electrocatalytic flow cell.

Although flow systems have been successful for heterogeneous systems with a liquid/solid interfaces, they were previously restricted to steady state conditions.[15] Here, we demonstrated channel widths that were optimized (4 mm diameter) to encourage nonrestrictive electrolyte flow for the $2H^+/2e^-$ redox reaction. To further enhance the industrial use of our flow cell, the substrate material (GCE) and substrate modification method (electrodeposition) were also modified.

2.3.3 Substrate and Catalyst Modification Assessment

Bi-CMEC was previously prepared by electrodeposition techniques onto a glassy carbon plate (GCP) from an acid aqueous or organic bath. The time needed to pass 3 C cm^{-2} of charge to precipitate Bi onto the substrate was not adequate for the fast pace of industry. Additionally, if the Bi-modified GCP were to be equipped in the flow cell, the GCP would not guarantee a sure seal for the flow cell. The GCP would unequally displace the clamping pressure and result in leaking. Furthermore, the flow cell promotes an enhanced surface area that is nearly 12x larger than the GCP. Scaling GCPs would be expensive (\$16/ cm^2, pricing from Sigma Aldrich) and not ideal. To encourage substrate compatibility with the flow cell and rapid catalyst preparation, alternate substrates and modification methods were explored.

2.3.3.1 Substrate Evaluation

Two common substrates that have been used for flow systems are carbon paper and carbon cloth.[16] Both are inexpensive pliable materials that are capable of being compressed and scaled (\$0.12/ cm^2 and \$0.05/ cm^2 for carbon paper and carbon cloth respectively, pricing from Fuel Cell Earth). These substrates differ merely in morphological arrangement of carbon fibers; carbon paper has an arrangement of compressed carbon fibers (Figure 2.3a) and carbon cloth has interwoven carbon fibers (Figure 2.3b). This arrangement becomes significant when considering the resistivity and intrusion of the flow cell. These properties are unique for specific systems and flow cell designs.

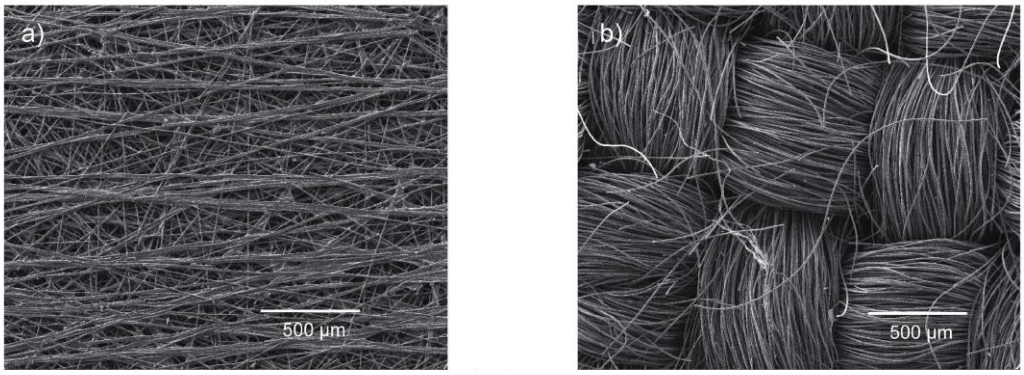

Figure 2.3. Secondary electron microscopy images of a) carbon paper and b) carbon cloth.

When materials are compressed, resistivity is reduced and the flow of electrons become more favorable.[16] Carbon paper is already a characteristically compressed material. This results in carbon paper reaching its resistivity limit sooner than carbon cloth. Carbon cloth is an overall thicker material and can show more intrusion into the central flow port and interrupt the flow path. Intrusion becomes significant when channel widths of 2 and 3 mms are reached. The channel width for our electrochemical cell is 4 mm. The difference in physical structures between the two substrates suggests that the redox chemistry at the surface will be different for each material. Because reduced resistivity and less intrusion were suggested to occur with carbon paper, carbon paper was the substrate chosen for our flow cell. Despite carbon paper being a more fragile material, the flow cell would provide structural support to prevent fracture.

2.3.3.2 Optimizing Drop Casting Method for Bi-Modified Surface

Drop casting is a common surface modification technique featured in the literature to strongly adhere catalysts, or materials, to inert substrates.[17] Drop casting,

as the name implies, drops the catalyst onto a substrate where it is set (cast) within a matter of minutes prior to its use. This technique highlights ease in solution preparation and substrate modification. Unlike the necessary skill set required by electrodeposition methods, drop casting does not require technical training. This reduces the external cost for training employees. Additionally, this film may ultimately be prepared via a spray gun with constant slurry convection to coat very large surface areas. This would afford reduced catalyst preparation time for large scale productions. One of the attractive features for Bi, and what sets it apart from the historic Ag and Au catalysts, is its cost. Remarkably, the overall cost for Bi-CMEC was further reduced with the incorporation of multiwalled carbon nanotubes (MWCNTs) in the drop casting slurry, such that MWCNTs encourage lower catalyst loading.[18,19]

Previously, bismuth(III) nitrite ($Bi(NO_3)_3$) was the precursor for Bi-CMEC acid aqueous electrodeposition. Initial Bi-CMEC surface studies revealed that there was a significant contribution of Bi^{3+}. Therefore, when optimizing the drop casting slurry, a sampling of inexpensive and commercially available Bi^{3+} complexes were studied. Screening the different Bi^{3+}complexes could ultimately provide information on if the specific Bi^{3+} complex structure influences the outcome of CO_2 to CO catalysis.

The Bi^{3+} complexes studied were $Bi(NO_3)_3$, bismuth(III) carbonate ($(BiO)_2CO_3$), and bismuth(III) subsalicylate ($C_7H_5BiO_4$). These Bi^{3+} materials are insoluble in organics (MeCN) and well suited for organic electrolysis. Their respective structures are illustrated in Figure 2.4, along with their respective cost per mole of Bi.

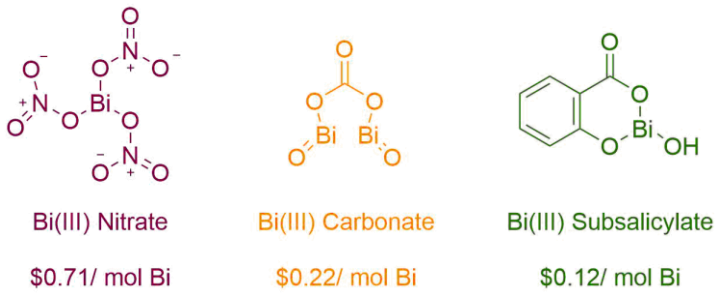

Figure 2.4. Structures for bismuth(III) nitrate (purple), bismuth(III) carbonate (orange), and bismuth(III) subsalicylate (green) with their respective commercial cost per mole of bismuth.

Per one mole of Bi, each Bi^{3+} complex is <$1 to purchase via chemical retailors. Specifically, $Bi(NO_3)_3$ was of interest because, as stated previously, it is the precursor for the acid aqueous electrodeposition. This would allow for significant comparisons to be made between modification techniques. $(BiO)_2CO_3$ and $C_7H_5BiO_4$ are both currently used in industry. $(BiO)_2CO_3$ has production in recreation use, specifically in fireworks, but also in health care to offer antibacterial properties towards peptic ulcers and gastritis.[20] $C_7H_5BiO_4$ also finds benefits in health care as it is an essential component in the commercially produced medication for indigestion relief, Pepto-Bismol.

Once the slurries were prepared for each Bi^{3+} complex, their films were cast onto carbon paper and characterized with surface techniques to obtain information on film morphology and elemental compositions. Electrochemical methods were used to observe CO_2 reduction activity for the Bi^{3+} catalysts. When equipped in the newly designed flow cell, current densities and product distributions were monitored. Specifically, it was of great interest to observe how the flow cell impacts mass transport for the $2H^+/2e^-$ redox reaction to evolve CO.

2.3.4 Surface Analysis of Drop Cast Bismuth Modification

Drop casting was facile surface modification method to produce a dark gray film for all Bi^{3+} complexes. The surface morphology and elemental composition for the Bi-modified carbon paper (for $(BiO)_2CO_3$, $Bi(NO_3)_3$, and $C_7H_5BiO_4$) were then analyzed with secondary electron microscopy (SEM), energy dispersive X-ray spectroscopy (EDX), and X-ray photoelectron spectroscopy (XPS) respectively.

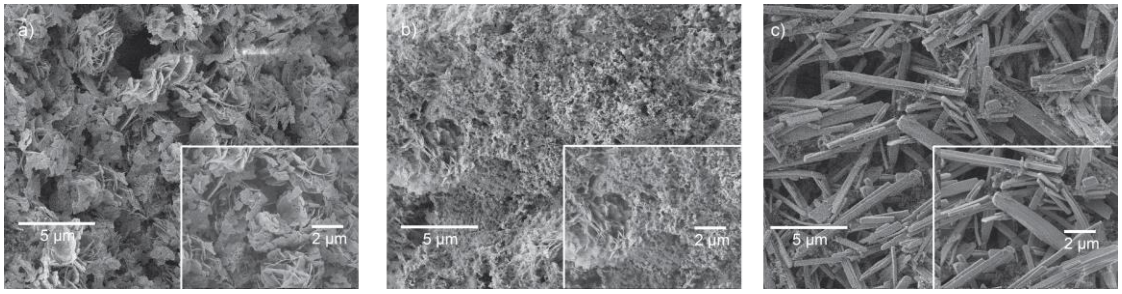

Figure 2.5. Secondary electron microscopy images of a) bismuth(III) carbonate, b) bismuth(III) nitrate, and bismuth(III) subsalicylate at magnifications of 5 K and 10 K (inset).

The SEM images (Figure 2.5) revealed morphologies resembling the electrodeposited Bi surface in terms of depth and porosity. Enhanced porosity is desirable because it encourages more available active sites for the binding of reagents or adsorbates. The porosity is likely encouraged by gentle solvent evaporation from THF, such that Bi loaded on MWCNTs can settle into optimal sites with maximum stability. Unlike electrodeposited Bi surface modifications, the drop cast Bi^{3+} complexes do not undergo a chemical transformation, such that there is no applied reduction potential to precipitate Bi onto the surface. The cast Bi^{3+} complex retains its starting composition. Therefore, the observed microstructures for $Bi(NO_3)_3$, $(BiO)_2CO_3$, and

$C_7H_5BiO_4$ each portray their characteristic architectural identities; $(BiO)_2CO_3$ demonstrates clusters of platelets (Figure 2.5a), $Bi(NO_3)_3$ appears as an amorphous sponge-like material (Figure 2.5b), and $C_7H_5BiO_4$ shows stick-like striations spanning across the surface of the film (Figure 2.5c).

The characteristic identities for the Bi^{3+} complexes were further illustrated with XPS when analyzing the Bi 4*f* high resolution region for each Bi^{3+} surface. Characteristic binding energies (BEs) were revealed for $(BiO)_2CO_3$ (Figure 2.6a), $Bi(NO_3)_3$ (Figure 2.6b), and $C_7H_5BiO_4$ (Figure 2.6c) at 159.0, 159.9, and 159.5 eV respectively. Unlike the electrodeposited Bi surface, there was no metallic Bi (Bi^0) component (157.0 eV). It is curious to observe how catalysis will differ when there is no starting Bi^0 on the electrode surface.

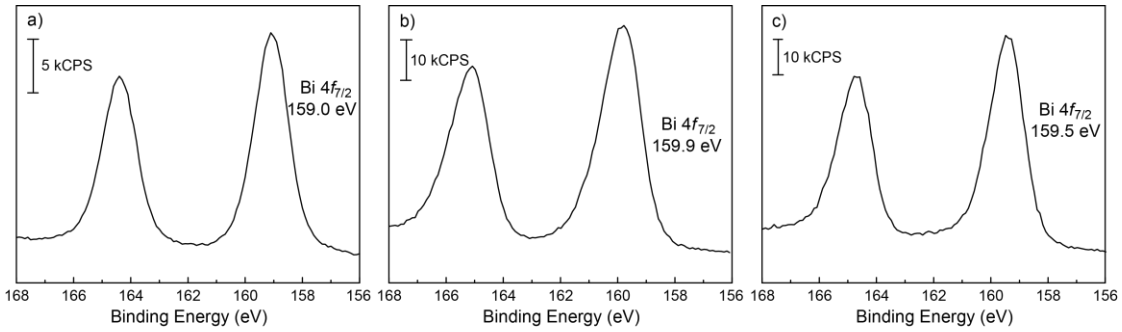

Figure 2.6. Bi 4*f* high resolution spectra for a) bismuth(III) carbonate, b) bismuth(III) nitrate, and c) bismuth(III) subsalicylate modified carbon paper.

The survey spectra for these prepared films identified F, S, O, C, and Bi. The presence of F, S, and O are likely from the Nafion binder. Appropriately, the survey spectrum for $Bi(NO_3)_3$ showed the incorporation of N.

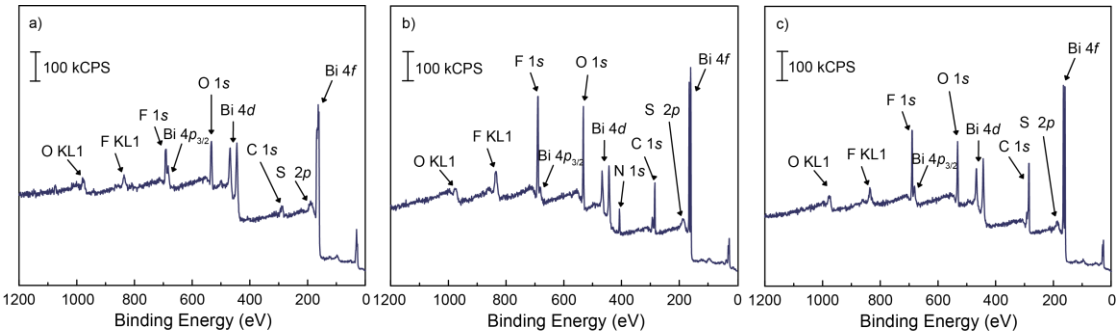

Figure 2.7. XPS survey spectra for a) bismuth(III) carbonate, b) bismuth(III) nitrate, and c) bismuth(III) subsalicylate modified carbon paper.

Bi, C, F, S, and O were also identified by EDX in the film bulk. F and S appeared in trace amounts, whereas the greatest elemental contribution was from C, Bi, and O. The abundance of carbon is likely due to the incorporation of MWCNTs and not from penetration into the carbon paper support. Drop casting provides a robust film microns in thickness which makes the detection of carbon paper unlikely. When Bi-CMEC was prepared by organic electrodeposition, an overwhelming amount of oxygen was also observed.[21,22] Comparatively, the oxygen contribution was less significant, such that the ratio of Bi to O for $Bi(NO_3)_3$, $(BiO)_2CO_3$, and $C_7H_5BiO_4$ were 1:6, 1:5, and 1:3 respectively. These ratios resemble what would be expected for each Bi^{3+} complex. This suggests that once the surface is modified, Bi does not become further oxidized.

The organic electrodeposition for Bi-CMEC also identified F, S, and O on the film surface from either residual supporting electrolyte ($TBAPF_6$) or residual triflate ($CF_3SO_3^-$).[21] These elements did not demonstrate negative correlations toward the efficacy of catalysis (CO evolution, current density, energy cost). This suggests that these elements will remain inert during catalysis, however, this will be investigated in greater depth upon performing electrochemical studies.

Noting the resemblances to previously prepared electrodeposited Bi materials, the drop casting method appeared promising for preparing a Bi platform for industrial CO_2 reduction to CO. Importantly, it was curious to observe if these films demonstrate resemblances in CO_2 reduction activity and CO selectivity to the analogous Bi-CMEC system. Because these films no longer show Bi^0 on the prepared surface, it will be a significant contribution towards CO_2 to CO electrocatalysis to observe if it is necessary to have this component present on the surface to initiate catalysis. Additionally, it was of interest to observe the durability of the drop cast films once equipped in the flow cell. If high CO selectivity and enhanced mass transport are achieved, the designed redox flow cell would be a significant contribution to the advancement of energy-storage devices.

2.3.5 Activity Towards CO_2 Reduction and CO Evolution

It was encouraging to observe similarities in surface structure and composition to previously studied electrodeposited Bi surfaces. To observe if there were also resemblances in the CO_2 reduction activity, the film itself (in the absence of the flow cell) was first studied with cyclic voltammetry (CV). Once the activity and peak potential have been identified, controlled potential electrolysis (CPE) was performed with the Bi-cast modified surface equipped in the flow cell and tethered to a GC to monitor the evolution of CO, H_2, or methane (CH_4). To support that carbon paper is the optimal substrate for the redox flow cell, CPE was also performed with Bi-modified carbon cloth where CO evolution was monitored. This is expected to highlight their unique resistivity and intrusion properties as suggested in the literature.[16]

2.3.5.1 CO_2 Activation Demonstrated by Cyclic Voltammetry

CVs were performed by suspending the modified substrate in electrolyte consisting of supporting electrolyte (100 mM $TBAPF_6$) and 1-butyl-3-methylimidazolium trifluoromethanesulfonate (100 mM [BMIM]OTf) in either CO_2 or N_2 saturated MeCN. In lieu of using carbon paper, the Bi^{3+} slurries were cast onto a glassy carbon disc electrode (GCE, 3.0 mm diameter) due to the current limitation on the potentiostat. Carbon paper has a larger surface area which would result in the current limits of the potentiosat being maxed at potentials where you would expect to see the cathodic rise for CO_2 reduction. Additionally, preparing carbon paper with a smaller surface areas may result in fracture. Any of these outcomes would result in unreliable voltammogram readings.

A GCE and carbon paper demonstrate different ohmic interactions based on their unique microstructures and ultimately encourage different surface chemistries for the $2H^+/2e^-$ redox reaction. Therefore, direct comparisons between the Bi^{3+} complexes are not encouraged. CV analysis aimed to observe if the Bi^{3+} complexes demonstrate the ability to reduce CO_2.

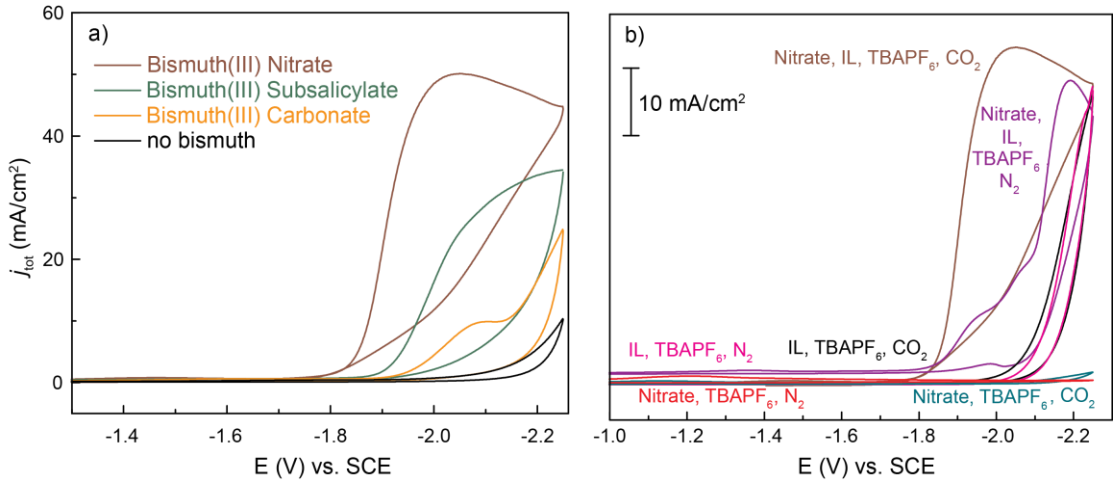

Figure 2.8. Cyclic voltammograms a) for bismuth(III) nitrate (brown), bismuth(III) subsalicylate (cyan), bismuth(III) carbonate (yellow), and no bismuth (black) drop cast on GCE submersed in 100 mM IL and 100 mM $TBAPF_6$ in CO_2 saturated MeCN. Cyclic voltammograms for b) control studies are shown with bismuth(III) nitrate.

The overlaid CVs in Figure 2.8a suggesed that regardless of the Bi^{3+} complex, the slurry was active towards CO_2 reduction. $Bi(NO_3)_3$ demonstrated the earliest onset potential, ~ –1.75 (V) vs. SCE (all potentials will be referred to this reference), followed by $C_7H_5BiO_4$ (cyan trace) and $(BiO)_2CO_3$ (yellow trace). Each Bi^{3+} complex showed a cathodic peak maxima at ~2.0 V. To highlight that the Bi^{3+} complex is responsible for CO_2 reduction, the slurry was prepared with only the MWCNTs and Nafion. The resulting polarization curve (Figure 2.8a, black trace) revealed negligible activity towards CO_2 reduction suggesting that the Nafion and MWCNTs are not responsible for the cathodic feature. Further, the Bi^{3+} films demonstrated a similar potential for the CO_2 redox event. This observation was significant because it is analogous to the electrodeposited Bi-CMEC systems.

$Bi(NO_3)_3$/GCE demonstrated the greatest enhancement in CO_2 reduction activity and demonstrated a stronger ohmic contact to glassy carbon compared to $(BiO)_2CO_3$ and $C_7H_5BiO_4$. Because the current response was substantial and the film was robust under these conditions, $Bi(NO_3)_3$ was ideal for executing control studies (Figure 2.8b). Specifically, it was of interest to observe the stability of the film and the IL, in addition to observing if there is still an essential Bi/IL interface that encourages CO_2 reduction, as demonstrated from previous electrolysis with electrodeposited Bi-CMEC.[21,23]

The stability of the film and IL were studied upon saturating the electrolyte solution with N_2 (Figure 2.8b, purple trace). The polarization curve was flat until an observed cathodic feature at –2.15 V. This is the observed reduction potential for 1,3-dialkylimidazolium ILs. This observation suggests that the film is stable under these applied potentials. Furthermore, the negligible current response discredits the possibility for the breakdown of IL or solvent to result in a feature at –2.0 V. The absence of a cathodic feature under N_2 supports that Bi is responsible for the CO_2 redox reaction under CO_2 saturated conditions.

To highlight the essential interplay between Bi and IL, separate CVs were performed in the absence of IL under CO_2 and N_2 (Figure 2.8b, black and pink traces respectively), and in the absence of a Bi-modified electrode under CO_2 and N_2 (Figure 2.8b, cyan and red traces respectively). The polarization curve in the absence of IL demonstrated no activity under CO_2 or N_2. With just the bare GCE submersed in MeCN/IL, the only cathodic feature was IL reduction. Appreciable current enhancements were only observed for the Bi/IL interface under CO_2. These results support initial electrodeposited Bi-CMEC studies which highlighted the significance of incorporating both components to mediate the CO_2 to CO redox reaction.

2.3.5.2 Product Distribution Elucidation

More direct comparisons in electrochemical behavior were made by performing CPE with the Bi-modified carbon paper equipped in the flow cell. These conditions now incorporated the appropriate substrate (carbon paper) to reveal the true durability of the catalyst. Here, the ability to catalyze CO_2 was monitored by current density and product distribution. Gaseous products were monitored by GC (CO, CH_4, H_2) and solution phase solvents (formic acid (HCOOH)) were monitored by ^{1}H NMR. CPE was performed at –1.95 V with CO_2 saturated electrolyte solution(100 mM IL, 100 mM $TBAPF_6$).

Table 2.1. CPE metrics for Bi-modified carbon paper at –1.95 (V) vs. SCE.

Bi^{3+}	IL	IL conc.	FE_{CO} (%)	j_{CO} (mA cm^{-2})	j_{tot} (mA cm^{-2})
nitrate	[BMIM]OTf	100 mM	45 ± 8	5.6 ± 1.9	12.6 ± 4.5
subsalicylate	[BMIM]OTf	100 mM	50 ± 6	3.3 ± 2.1	6.9 ± 4.3
carbonate	[BMIM]OTf	100 mM	54 ± 3	12.5 ± 1.3	23.0 ± 1.5

As demonstrated in Table 2.1, the Bi^{3+} complexes produced CO with comparable efficiencies and suggests that Bi^0 does not need to be present to initiate catalysis. $(BiO)_2CO_3$ demonstrated the highest CO efficiency and current density which suggests that it is an ideal platform for industry. Surprisingly, $Bi(NO_3)_3$ evolved the least amount of CO. This is the precursor for Bi-CMEC prepared by acid aqueous electrodeposition which evolved CO with >90 % Faradaic efficiencies (FEs). Without experiencing a chemical change, $Bi(NO_3)_3$ demonstrated less impressive metrics. Electroreduction of NO_3^- anions can produce side products such as ammonia or hydroxylamine.[24] Additionally, some metal-N bonds experience stronger binding interactions which result in film passivation for cathodic processes. In analyzing the current density plot for in $Bi(NO_3)_3$ (Figure 2.9, maroon trace), passivation is unlikely

due to the observed steady rates over time. Therefore, the NO_3^- reduction products are likely interfering with CO selectivity.

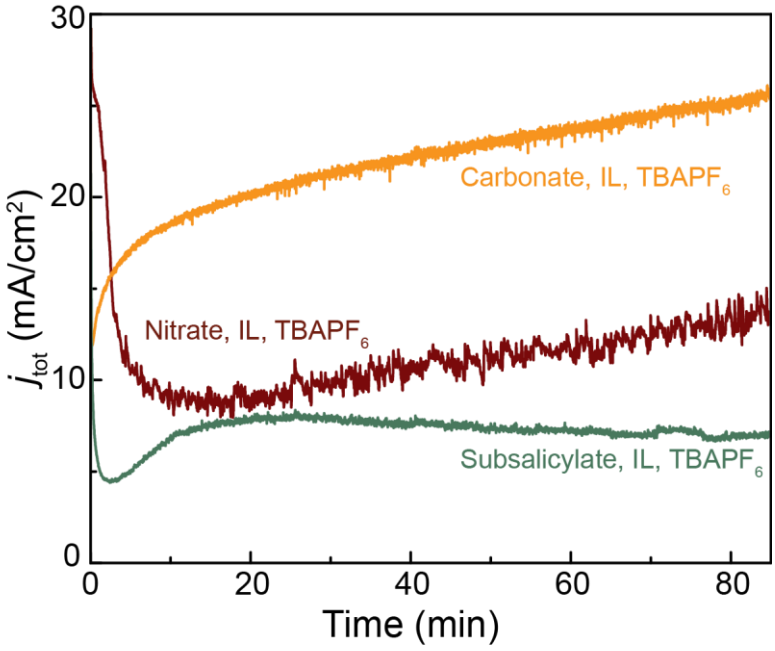

Figure 2.9. Current density plot for the Bi(III) carbonate (yellow trace), nitrate (maroon trace), and subsalicylate (green trace).

The current density for $(BiO)_2CO_3$ exceeded 20 mA/cm^2 which greatly surpassed electrolysis performed in a two-compartment electrolytic cell where convection was controlled by vigorous catholyte stirring. $C_7H_5BiO_4$, not showing as high of rates, still demonstrated comparable current densities to the ex situ acid aqueous electrodeposition.[21,23] Despite $(BiO)_2CO_3$ and $C_7H_5BiO_4$ evolving CO with similar selectivity (~60 %), their rate for the $2H^+/2e^-$ redox reaction varied by nearly 18 mA/cm^2. This is highlighted in the current density plot in Figure 2.9, yellow and green

traces respectively. It was curious if the difference in rate was the result of the Bi^{3+} molar dependence for catalysis, or the complex structure itself. The moles of Bi^{3+} used in the drop casting slurry for $(BiO)_2CO_3$ and $C_7H_5BiO_4$ were 1.57 mmol and 1.10 mmol Bi^{3+} respectively. These amounts were calculated based on the 40:1 wt.% ratio of Bi^{3+} to MWCNTs for preparing the slurry. To determine if the higher rates were the result of slightly elevated Bi^{3+} loadings (+0.47 mmol for $(BiO)_2CO_3$), CPE was performed where the moles of Bi^{3+} were switched for $(BiO)_2CO_3$ and $C_7H_5BiO_4$: $(BiO)_2CO_3$ would now have 1.10 mmol Bi^{3+} and $C_7H_5BiO_4$would have 1.57 mmol Bi^{3+}.

2.3.5.2.1 Bi^{3+} Molar Dependence for Catalysis

Switching the catalyst loadings for $(BiO)_2CO_3$ and $C_7H_5BiO_4$ will reveal if the specific Bi^{3+} architecture or if the moles of Bi^{3+} incorporated in the slurry have a greater influence on CO_2 to CO catalysis. The new wt.% ratios for $(BiO)_2CO_3$ and $C_7H_5BiO_4$ are 28:1 and 56:1 respectively. CPE was performed with the same electrochemical apparatus where product distribution and current density were monitored. The current density plot for $(BiO)_2CO_3$ and $C_7H_5BiO_4$ is illustrated in Figure 2.10, yellow and green traces respectively.

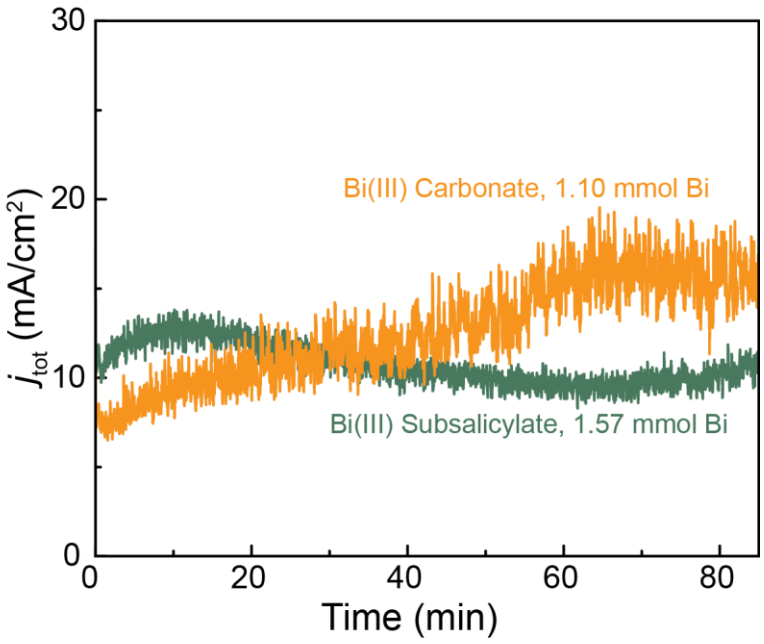

Figure 2.10. Current density plot of Bi(III) carbonate (yellow trace) and subsalicylate (green trace) with 1.10 and 1.57 mmol Bi respectively.

Regardless of exchanging the mmoles of Bi^{3+}, $(BiO)_2CO_3$ still demonstrated higher current densities than $C_7H_5BiO_4$ by ~5 mA/cm^2. Because the current density for $C_7H_5BiO_4$ was only slightly elevated by the 0.47 mmol Bi^{3+} increase, the rate is suggested to be less affected by Bi^{3+} loading and more affected by the architecture for the Bi^{3+} complex. The local bonding for $(BiO)_2CO_3$ and $C_7H_5BiO_4$ are unique, as illustrated by their oxidative environments from XPS (Figure 2.6a and c respectively), and may ultimately interact with intermediates differently. This is likely to play a more significant role in the progression of CO_2 to CO catalysis.

Table 2.2. CPE metrics for Bi(III) carbonate and Bi(III) subsalicylate mole dependent study.

Bi^{3+}	IL	IL conc.	FE_{CO} (%)	j_{CO} (mA cm^{-2})	j_{tot} (mA cm^{-2})
carbonate	[BMIM]OTf	100 mM	43 ± 6	5.6 ± 1.6	15.8 ± 5.1
subsalicylate	[BMIM]OTf	100 mM	48 ± 8	4.5 ± 0.2	9.6 ± 1.8

Table 2.2 summarizes the metrics for the mole dependent CPE study. The selectivity for CO is comparable, in that the efficiency is still within the standard deviations of the previously reported metrics (Table 2.1). These results suggest that slightly lower catalyst loadings will not jeopardize efficient CO_2 to CO catalysis. This observation was significant in furthering the progression of industrial integration, such that catalyst loading can be reduced further to result in a greater industrial profit.

Because the complex structure appears to play a significant role in catalysis, observing the structural durability of the $(BiO)_2CO_3$ and $C_7H_5BiO_4$ was of interest. If the architecture is durable, minor surface deviations would be expected after electrolysis. If the morphology demonstrates significant deviations from the starting composition, the film durability would be poor and the changes in architecture may likely alter the CO_2 to CO redox reaction. To analyze the durability and evolution of the Bi film, the film morphology after CPE was studied via SEM. EDX and XPS were used to study the elemental composition of the surfaces after CPE.

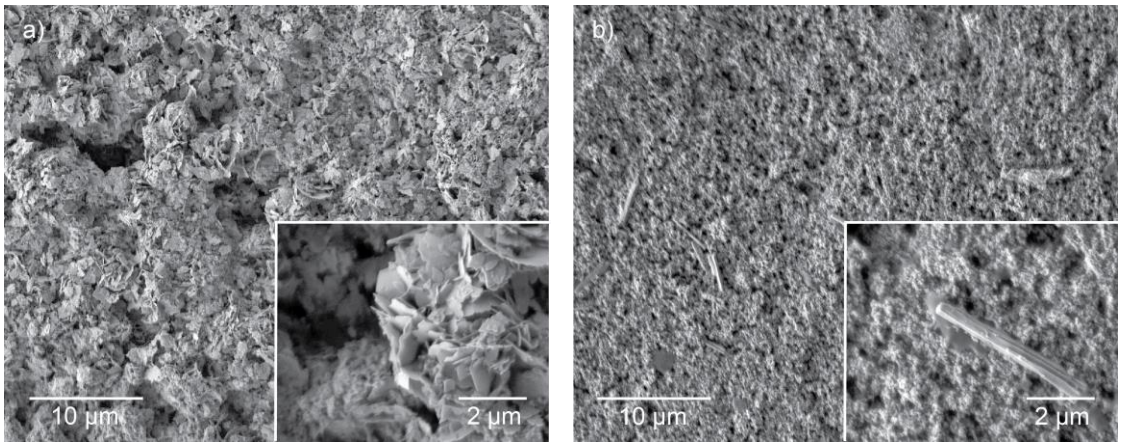

Figure 2.11. Secondary electron microscopy images of a) Bi(III) carbonate and b) Bi(III) subsalicylate after electrolysis at –1.95 (V) vs. SCE. Magnifications of 2.5K and 15K (inset).

It was fascinating to observe how $(BiO)_2CO_3$ and $C_7H_5BiO_4$, when prepared in the same manner and enduring identical electrolysis conditions, demonstrated unique surface deviations after electrolysis. The morphology for $(BiO)_2CO_3$ (Figure 2.11a) after electrolysis was nearly identical to the prepared surface. The morphology for $C_7H_5BiO_4$ after electrolysis, however, barely resembled the initial surface architecture. The stick-like striations were sparse and a majority of the surface demonstrated a more rugged morphology. Interesting, the new surface microstructure showed similarities to $(BiO)_2CO_3$.

Because the surface for $C_7H_5BiO_4$ showed similarities in surface structure to $(BiO)_2CO_3$, it was curious to identify if $C_7H_5BiO_4$ underwent a compositional change during electrolysis. Elemental analysis was performed to observe possible transformations. First, EDX revealed that the oxygen content for $(BiO)_2CO_3$ which suggested that $(BiO)_2CO_3$ was robust and did not become further oxidized. The oxygen content for $C_7H_5BiO_4$ increased to a 1:5 Bi to O ratio. $C_7H_5BiO_4$ is likely becoming

more oxidized during electrolysis and may experience a new oxidative environment. To clarify this observation, XPS complimented EDX by identifying the elemental composition of the Bi^{3+} species specifically. The Bi 4*f* high resolution spectra for $(BiO)_2CO_3$ and $C_7H_5BiO_4$ are illustrated in Figure 2.12a and b respectively.

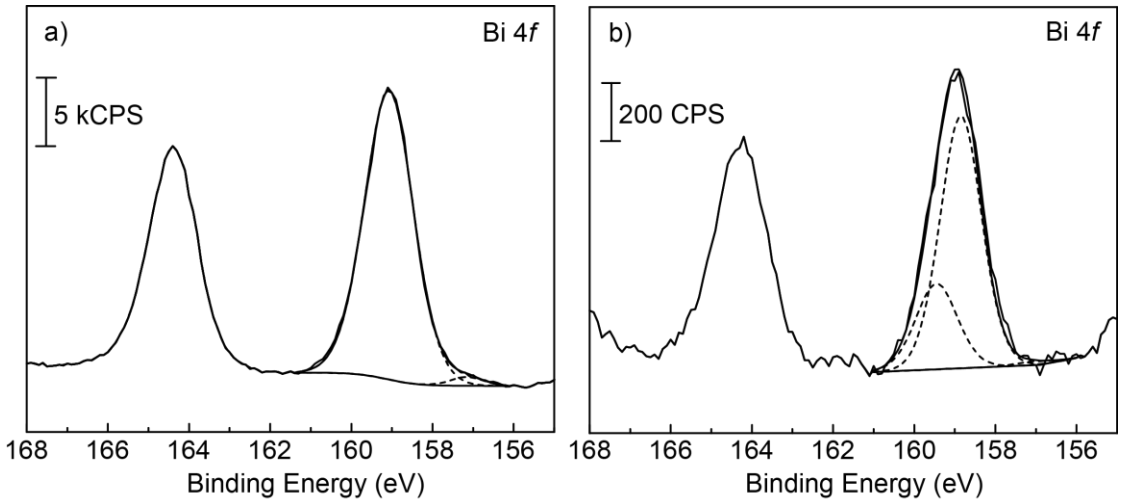

Figure 2.12. Bi 4*f* high resolution spectra for a) Bi(III) carbonate and b) Bi(III) subsalicylate.

XPS revealed a slight change in the Bi^{3+} oxidative environment for $C_7H_5BiO_4$. Specifically, the Bi $4f_{7/2}$ component for $C_7H_5BiO_4$ demonstrated a shift to lower BE. Here, the spectrum was optimally fit to two components, 158.9 and 159.5 eV. Interestingly, these BEs represent $(BiO)_2CO_3$ and $C_7H_5BiO_4$ respectively. Having both components present corresponds to the observed SEM image (Figure 2.10b), such that stick- and sponge-like morphologies were identified. As supported by SEM (Figure 2.11a), XPS demonstrated that the oxidative environment for $(BiO)_2CO_3$ remained idle and suggested no compositional changes.

Observing that the final Bi^{3+} compositions after CPE was $(BiO)_2CO_3$ was a significant observation for understanding the evolution of the active species during catalysis. Further, this correlates to the Bi composition after electrolysis when prepared via acid aqueous electrodeposition. This suggests that despite the $2H^+/2e^-$ redox reaction occurring in a different electrochemical apparatus and Bi-CMEC being prepared by a different surface modification method, the pathway for catalysis appears analogous.

2.3.5.3 Energy Efficiency for the Redox Flow Cell

The Bi^{3+} complexes demonstrated CO selectivity with high current densities and a low overpotential (η ~200 mV). The FE for CO and η ($E_{eq} - E_{app}$) effect the energy efficiency (ε) for the redox event, which is calculated by equation 2.1. Despite demonstrating a low energy cost, roughly ~40 % of charge was unaccounted for. The low selectivity significantly affected the ε. $(BiO)_2CO_3$ demonstrated the greatest ε with a maximum of 53.1 % (considering upper end of standard deviation). This is a ~30% drop in efficiency from the two-compartment electrochemical assembly.

$$\varepsilon = \frac{Eeq}{Eapp} \text{ x FE} \qquad (2.1)$$

The Bi film was robust during CPE and demonstrated no signs of passivation. Only trace amounts of H_2 were produced (<5 %) with no CH_4 or oxalate detected. HCOOH was only detected for $(BiO)_2CO_3$ (<2 %). It is likely that part of the charge goes towards stabilizing the larger electrode surface area, such that altered efficiencies are not uncommon for larger electrodes. Additionally, the production of small reduced hydrocarbons that are not detectable with the GC detection limits may also occur. Lastly, it is possible that lower selectivity may be the result of re-oxidation of evolved CO. The flow path for CO_2 to leave the electrolyte solution and enter the headspace is

longer for the flow cell than it is for the two-compartment cell. This may encourage additional interactions with the reactants and products to re-oxidize CO to CO_2.

2.3.5.4 Detection of the Bismuth/IL Interface

The Bi/IL interface was highlighted when performing CPE without either IL or the Bi-modification. CV studies demonstrated that CO_2 reduction activity was sacrificed without this interface. CPE will investigate this behavior further by understanding catalytic effects on product distribution and current density (rate). Additionally, it was of interest to observe if the supporting electrolyte can be removed from the electrolyte solution completely. IL has been reported to possess multi-functional properties, which involves promoting ion conductivity.[25] It would be advantageous for promoting industrial integration if the expensive supporting electrolyte can be eliminated.

[BMIM]OTf was shown to be robust during catalysis and demonstrated a highly energy efficient system (~87 %) when used at slightly elevated concentrations (300 mM) without electrolyte.[21] This efficiency had only been seen previously with noble metals (Ag and Au).[26] Additionally, [BMIM]OTf is among the least expensive ILs ($2/ g). It is curious to observe if IL still demonstrates these multifunctional properties when flowing continuously in the redox cell.

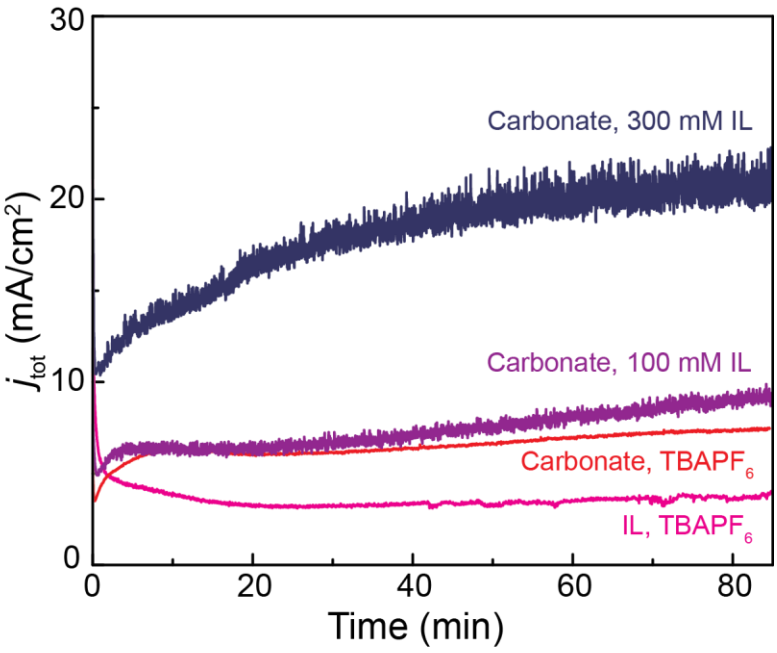

Figure 2.13. Current density plot for 300 mM IL/MeCN/Bi, 100 mM IL/MeCN/Bi, $TBAPF_6$/MeCN/Bi, and IL/$TBAPF_6$/MeCN in the navy, purple, red, and pink traces respectively

The control studies were performed with $(BiO)_2CO_3$ because it has higher current densities and CO efficiencies compared to $Bi(NO_3)_3$ or $C_7H_5BiO_4$. To demonstrate the Bi/IL interplay, separate CPE studies were performed where either Bi or IL were not included in electrolysis (Figure 2.13, pink and red trace respectively). When Bi was absent, the slurry was only composed of MWCNTs and Nafion. Lastly, to determine if supporting electrolyte can be eliminated, CPE was performed with 100 and 300 mM IL (Figure 2.13, purple and navy traces respectively). The metrics are summarized in Table 2.3

Table 2.3.CPE metrics for Bi(III) carbonate and variable IL conditions at –1.95 (V) vs. SCE.

Bi^{3+}	ionic liquid	IL conc.	FE_{CO} (%)	j_{CO} (mA cm^{-2})	j_{tot} (mA cm^{-2})
none	[BMIM]OTf	100 mM	1 ± 1	trace	4.3 ± 1.3†
carbonate	none		4 ± 2	0.3 ± 0.2	5.9 ± 1.4
carbonate*	[BMIM]OTf	100 mM	57 ± 6	6.7 ± 3.9	12.1 ± 3.8
carbonate*	[BMIM]OTf	300 mM	57 ± 7	11.3 ± 1.4	19.8 ± 1

† Total current density
* No $TBAPF_6$ supporting electrolyte

These metrics compliment previous Bi-CMEC studies describing the relationship between Bi and IL.[21,23] These metrics also compliment the CV traces presented in Figure 2.7b, such that current density is reduced significantly without the Bi/IL interface. Despite being reduced, the current densities were still slightly higher than expected for these two controls studies. Previously, the current densities for an unmodified GCE or for Bi-CMEC without IL were <1 mA/cm^2. This may result from the enhanced surface area and mass transport effects from the flow cell. The enhanced surface area is not only due to the size of the substrate, but also in part with the incorporation of MWCNTs. MWCNTs have been shown to lower the resistance of charge transfer for the reaction occurring at the cathode.[18]

These studies highlighted the multifunctionality for imidazolium donating protons for the $2H^+/2e^-$ redox reaction, neutralizing surface charge from bias, stabilizing radical intermediates ($CO_2^{\bullet-}$), and functioning as electrolyte. Comparable selectivity for CO evolution was observed with only 100 mM IL and no electrolyte, however, the current density was slightly reduced. Increasing the IL concentration to 300 mM, the selectivity for CO evolution and current density now matched the metrics for the $TBAPF_6$/IL electrolyte. These electrolyte conditions are identical to previous Bi studies

in the absence of electrolyte, and demonstrated an analogous dependency on 1,3-dialkylimidazolium IL.[21,23]

2.3.5.5 Elucidating the Significance of the Modified Substrate Material

It was previously suggested that carbon cloth would demonstrate greater intrusion and resistivity than carbon paper when equipped in the flow cell. Intrusion would interrupt the flowing electrolyte and would likely accumulate pressure from the restricted flow. Added resistivity would interfere with facile electron transfer (ET) events and further increase the kinetic barrier for the rate determining step (RDS). For these reason, carbon paper was pursued. It was of interest, however, to observe these properties experimentally and to compare the differences in electrolysis between the two carbon substrates. The influence that the substrate has over the outcome of electrolysis was studied by performing CPE on the Bi^{3+} modified surfaces for carbon cloth and carbon paper when equipped in the flow cell. The effects on CO evolution is highlighted in Figure 2.14.

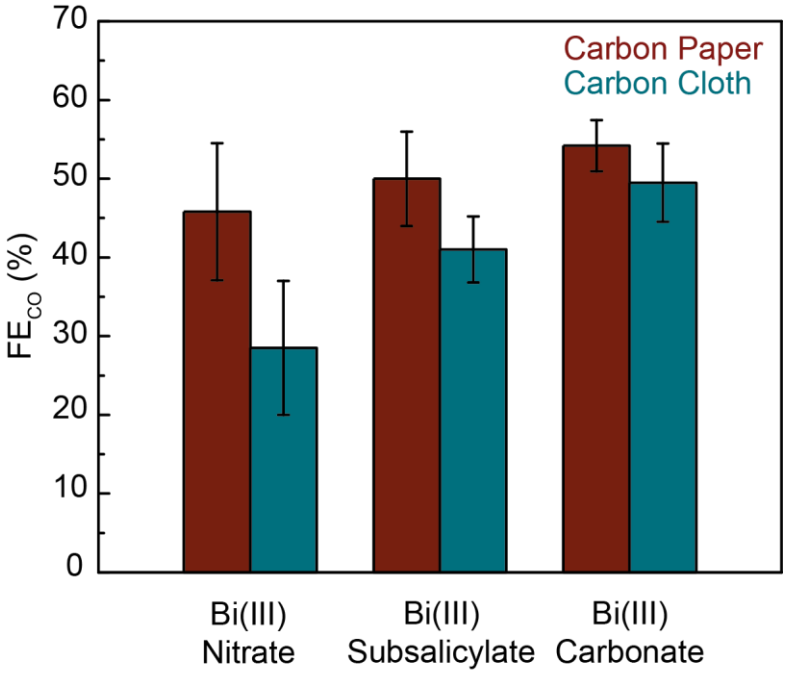

Figure 2.14. Bar graph describes the CO Faradaic efficiencies for carbon paper (maroon) and carbon cloth (blue) substrates. Substrates were modified with Bi(III) nitrate, Bi(III) subsalicylate, and Bi(III) carbonate.

Regardless of the Bi^{3+} complex, carbon cloth demonstrated lower selectivity for CO than carbon paper. Because the substrate is the only variable changing in these electrolysis experiments, it is likely that the surface chemistry deviates due to the unique microstructures. Therefore, these results suggested that the compressed fibers in carbon paper encourage ideal binding for the adsorption and desorption of CO_2 and CO respectively. Carbon cloth demonstrates 50-70 % of charge unaccounted for (no H_2, CH_4, or HCOOH production). It is possible that intermediates may become trapped in carbon cloth and become further reduced to small hydrocarbon species. This may result from restricted flow to allow a longer interaction times between intermediates and the

Bi-modified surface. Further, electrolysis efficiencies have been demonstrated to have a strong dependence on the substrate pore size (porosity/architecture).[27]

Table 2.4. CPE metrics for Bi-modified carbon paper at –1.95 (V) vs. SCE.

Bi^{3+}	ionic liquid	IL conc.	FE_{CO} (%)	j_{CO} (mA cm^{-2})	j_{tot} (mA cm^{-2})
nitrate	[BMIM]OTf	100 mM	29 ± 8	4.3 ± 1.1	15.0 ± 1.5
subsalicylate	[BMIM]OTf	100 mM	41 ± 4	5.5 ± 1.6	13.2 ± 2.7
carbonate	[BMIM]OTf	100 mM	50 ± 5	8.8 ± 1.0	17.9 ± 0.3

Interestingly, Table 2.4 describes current densities that do not deviate significantly from carbon paper (Table 2.1), within standard deviation limitations. It was expected to observe an increase in current density with increased surface area. The anticipated increase in rate may have been offset by the added resistivity from carbon cloth.

These studies highlight the intrusion and resistive properties for carbon paper and carbon cloth. It was fascinating to observe how different microstructures of the same elemental material influence different surface interactions. Additionally, these CPE results afford confidence in selecting carbon paper as the substrate for the redox flow cell.

2.4 Conclusions

In transitioning our energy dependency from the combustion of fossil fuels to renewable solar power, challenges are faced when matching energy demands for spontaneous weather and seasonal changes.[6] This is largely attributed to solar energy lacking an efficient energy storage device to provide energy during high and low energy peaks. An energy storage method that has received much attention in the literature is

solar fuel, in that they are among the most energy dense storage devices.[28] In producing these fuels, we have successfully developed a bismuth carbon monoxide evolving catalyst (Bi-CMEC) capable of producing the C1 feedstock (CO) for the well known Fischer-Tropsch process. In this work, we modified our Bi-CMEC system to function optimally in an industrial setting to encourage integration of energy storage devices.

The modifications that were necessary to encourage industrial integration included redesigning the electrochemical cell, exploring a new surface modification method, and exploring more cost-efficient materials. First, the architecture of the previous fragile two-compartment electrochemical cell was redesigned into a robust, compact, and cost efficient 3D printed electrolysis assembly. The flow cell encouraged a sealed environment for the redox event to take place that reduces the need for constant re-optimization of reaction conditions. The technical and time consuming electrodeposition technique was replaced by drop casting methods. Slurry conditions were adapted from the literature and incorporated inexpensive commercially available Bi^{3+} salts (<$1/ mol Bi). When cast on inexpensive carbon supports, a strong ohmic contact was demonstrated from high and steady current densities. The current densities were also found to greatly surpass published values for Bi-CMEC in the two-compartment cell. The enhancement in mass transport is likely due to the continuous flow of recycled electrolyte refreshing the catalyst support.

It was also discovered that expensive supporting electrolyte can be eliminated with the incorporation of IL ([BMIM]OTf, 300 mM). [BMIM]OTf is one of the least expensive commercially available 1,3-dialkylimidazolium ILs. Furthermore, ILs can also be recycled which would further enhance industrial profit.[29,30,31] [BMIM]OTf demonstrated appreciable rates that were steady during electrolysis, except for when

there was no Bi-modified surface. An essential interaction between IL and Bi was revealed and complimented previous Bi-CMEC studies. The Bi/IL interface proves to be critical for the outcome of CO_2 to CO electrolysis; current density, product distribution, and selectivity. If either Bi or IL is removed, these metrics were sacrificed.

The ease in cell modification encourages further advancements in cell design. The cell architecture can be screened easily and quickly from the ability to 3D print. This allows the cell to easily adapt to the ever-changing demands of industry to fit specific criteria or goals. This feature further highlights the significance of our proposed electrolysis assembly. A potential modification in cell design would be through stacking multiple flow cells (Figure 2.15a). This involves more than one flow plate incorporated in the architecture. Multiple flow plates require multiple catalyst supports which would result in enhanced CO production. The stacking design has shown interest in the literature for energy storing devices, but could further be improved upon by this lightweight and robust material.[3]

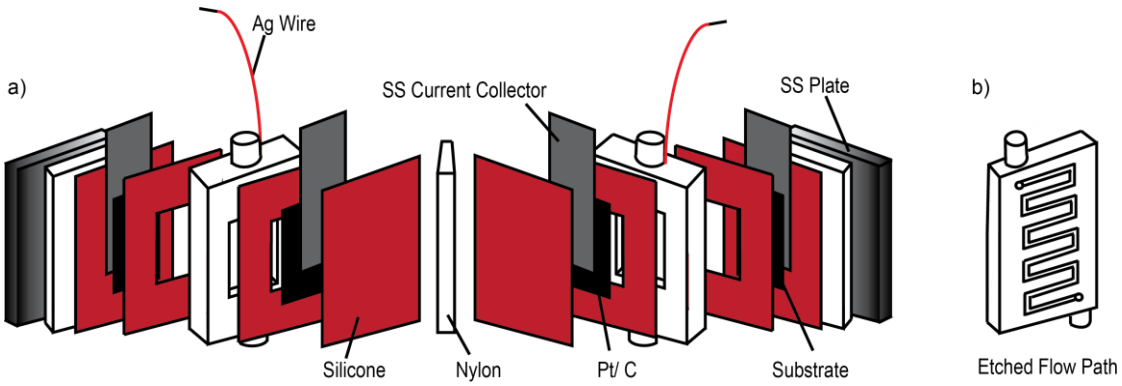

Figure 2.15. Stacked flow cell design is featured in a). Illustration in (b) shows etched engravings for gas flow systems.

An additional modification involves the redesign on the flow cell into a gas flow system. A flow plate can be designed with etched grooves with high precision to direct the flow path for gasses (Figure 2.15b). The grooves encourage direct interaction with the gas reactants and catalyst support. Depending on the length of the flow path, short or long interaction times can be achieved. In lieu of constant electrolyte flow, gas flow systems would involve an IL bath suspended below the Bi-modified surface (Bi/IL interface remains). The elimination of supporting electrolyte and organic solvent both reduces the cost and encourages greener solvents.[32]

Additionally, the IL would be used in 1.5 mL volume. This is a small volume that does not result in a costly supply of IL. However, implementing neat IL alters our previously explored dilute IL electrolyte conditions. It would be curious to observe if the physical properties of IL alter the outcome of electrolysis. ILs are highly viscous, which would provide valuable insight on diffusional effects despite having the multi-functionality of IL being an electrolyte and proton donor. (See Chapter 5).

REFERENCES

(1) Díaz, R. *Journal of Energy and Power Engineering*. **2014**, *5*, 794—804.

(2) Cook, T. R.; Dogutan, D. K.; Reece, S. Y.; Surendranath, Y.; Teets, T. S.; Nocera, D. G. *Chemical Reviews*. **2010**, *110*, 6474.

(3) Hudkins, J. R.; Wheeler, D. G.; Pena, B.; Berlinguette, C. P. *Energy and Environmental Science*. **2016**, *9*, 3417—3423.

(4) Gu, X.; Carneiro, J. S. A.; Nikolla, E. *Catalysis*. **2017**, *29*, 94—121.

(5) Whipple, D. T.; Kenis, P. J. A. *Journal of Physical Chemistry Letters*. **2010**, *1*, 3451—3458.

(6) Luo, X.; Wang, J.; Dooner, M.; Clarke, J. *Journal of Applied Energy*. **2015**, *137*, 511.

(7) Soloveichik, G. L. *Chemical Reviews*. **2015**, *115*, 11533—11558.

(8) LeRoy, R. L. *International Journal of Hydrogen Energy*. **1983**, *8*, 401—417.

(9) Cho, K. T.; Tucker, M. C.; Weber, A. Z. *Energy Technology*. **2016**, *4*, 655—678.

(10) León, C. P.; Frías-Ferrer, A.; González-Garcia, J.; Szánto, D. A.; Walsh, F. C. *Journal of Power Sources*. **2006**, *160*, 716—732.

(11) Dragone, V.; Sans, V.; Rosnes, M. H.; Kitson, P. J.; Cronin, L. Beilstein *Journal of Organic Chemistry*. **2013**, *9*, 951—959.

(12) Chisholm, G.; Kitson, P. J.; Kirkaldy, N. D.; Bloor, L. G.; Cronin, L. *Energy & Environmental Science*. **2014**, *7*, 3026—3032.

(13) Sahu, S. K. Redox flow cell. 2008. US 20100003586 A1.

(14) Skyllas-Kazacos, M.; Rychcik, M.; Robins, R. G.; Fane, A. G. *Journal of the Electrochemical Society*. **1986**, *133*, 1057—1058.

(15) Gooding, J. J.; Brennan, C. M.; Atherton, J. H.; Coles, B. A.; Compton, R. G. *Journal of Physical Chemistry B*. **1997**, *101*, 182—188.

(16) Radhakrishnan, V.; Haridoss, P. *Materials and Design*. **2011**, *32*, 861—868.

(17) McGuire Jr. R.; Dogutan, D. K.; Teets, T. S.; Suntivich, J.; Shao-Horn, Y.; Nocera, D.G. *Chemical Science*. **2010**, *1*, 411—414.

(18) Pu, L.; Zou, L.; Zhou, Y.; Zou, Z.; Yang, H. *RSC Advances*. **2017**, *7*, 12329—12335.

(19) Zhang, X.; Wu, Z.; Zhang, X.; Li, L.; Li, Y.; Xu, H.; Xu, H.; Li, X.; Yu, X.; Zhang, Z.; Liang, Y.; Wang, H. *Nature Communications*. **2017**, *8*, 1—8.

(20) Chen, R.; Ho So, M.; Yang, J.; Deng, F.; Che, C. M.; Sun, H. *Chemical Communications.* **2006**, *21*, 2265—2267.

(21) Medina-Ramos, J.; DiMeglio, J. L.; Rosenthal, J. *Journal of the American Chemical Society*. **2014**, *136*, 8361–8367.

(22) Medina-Ramos, J.; Pupillo, R. C. Keane, T. P.; DiMeglio, J. L.; Rosenthal, J. *Journal of the American Chemical Society*. **2015**, *137*, 5021—5027.

(23) DiMeglio, J. L.; Rosenthal, J. *Journal of the American Chemical Society*. **2013**, *135*, 8798–8801.

(24) Mishra, D.; Farrell, J. *Environmental Science and Technology*. **2005**, *39*, 645—650.

(25) Montalban, M. G.; Bolivar, C. L.; Banos, G. C.; Villora, G. *Journal of Chemical Engineering Data*. **2015**, *60*, 1986—1996.

(26) Hori, Y.; Wakebe, H.; Tsukamoto, T.; Koga, O. *Electrochimica Acta*. **1994**, *39*, 1833—1839.

(27) Dutta, A.; Rahaman, M.; Luedi, N. C.; Mohos, M.; Broekmann, P. *ACS Catalysis*. **2016**, *6*, 3804—3814.

(28) Chu, S.; Cui. J.; Liu, N. *Nature Materials*. **2017**, *16*, 16—22.

(29) Abu-Eishah, S. I. *Ionic Liquids Recycling for Reuse*. Intech: open science, open mind.

(30) Valdés Vergara, M. A.; Lijanova, I. V.; Likhanova, N. V.; Olivares, Xometl, O.; Jaramillo Vigueras, D.; Morales Ramirez, A. J. *Separation and Purification Technology*. **2015**, *155*, 110—117.

(31) Sklavounos, E. Helminen, J. K. J.; Kyllönen, L.; Kilpeläinen, I.; King, A. W. T. *Encyclopedia of Inorganic and Bioinorganic Chemistry*. 15 Sep 2016.

(32) P. Wasserscheid and T. Welton. Wiley-VCH, Weinheim, Germany, 2003.

Chapter 3

INVESTIGATING THE CATALYTIC DISCREPANCIES BETWEEN THE BISMUTH AND TIN PLATFORMS TO THE LEAD PLATFORM FOR THE ELECTROCATALYTIC REDUCTION OF CO_2 to CO

3.1 Introduction

With energy consumption and the atmospheric concentration of CO_2 rapidly increasing, electrochemical conversion of CO_2 to reduced carbon species has grown in interest to mitigate CO_2 emissions.[1,2,3] Specifically, reducing CO_2 to CO has received much attention because CO is the C1 feedstock for producing liquid fuels via the Fischer-Tropsch process. Recycling CO_2 by storing electrical energy in chemical bonds is a promising route for decreasing our contributions to rising atmospheric CO_2 levels; a carbon-neutral system.[2,4] This reduction, however, is kinetically challenging due to high CO_2 stability and therefore requires a catalyst. There is continued research devoted towards discovering noble metal heterogeneous electrocatalysts that can facilitate this reduction with high efficacy with the intent of developing more energy efficient systems.[5] Additionally, by studying a slew of potential platforms, this research would also help to further understand the currently unclear mechanistic pathway.[1] Unfortunately these noble metal platforms are expensive and even if they are found to demonstrate the ability to selectively and efficiently transform CO_2 to CO, the price would make the systems impractical for further applications.

Thus, when deviating from the expensive noble metal cathodes, Bi was found to possess analogous metrics at a much lower cost. Because the Bi carbon monoxide

evolving catalysts (Bi-CMEC) was a promising platform for the heterogeneous reduction of CO_2 to CO, other p-block metals were explored near Bi on the periodic table to determine if they also have high electrocatalyticic activity towards this reduction. To explore the CO_2 reduction capabilities of a library of p-block materials, a general organic electrodeposition method was developed.[6,7] This deposition bath was no longer acidic and could accommodate a slew of materials and sensitive substrate supports that were once hindered from electrochemical analysis due to being reactive under acidic conditions. Incorporating these substrates aided in enhancing the ohmic contact for certain materials to strengthen its durability as a catalyst; greater CO_2 reduction activity, CO selectivity, and current density. Specifically, the expanded p-block metal library included Sn, Pb, and Sb on either a glassy carbon electrode (GCE) or Ni supports. Here, the variety of inexpensive materials allowed further discovery of more efficient catalytic systems and enabled additional mechanistic insights for the CO_2 to CO reduction pathway.

Of the variety of heterogeneous p-block metals studied, Sn and Bi demonstrated the greatest potential of being a CO evolving catalyst. Regardless of the substrate material, however, Sb was not active towards CO_2 reduction and Pb did not demonstrate film durability as high as Bi or Sn. The Pb cathode initially produced CO with selectivity exceeding 80 % Faradaic efficiencies (FEs) with current densities of ~10 mA/cm^2, but became passivated during electrolysis within a matter of minutes.

Passivation of the Pb cathode inspired a series of investigations to understand why the Pb-modified surface demonstrated different metrics and catalytic behaviors than the Bi and Sn platforms. It was possible that Pb endured a unique pathway if 20 % of unaccounted charge is going towards the evolution of a counter species. Reports have

suggested that Pb foil electrodes are prone to producing an imidazolium-carboxylate adduct (Figure 3.1) upon polarization at very negative applied potentials in a $[BMIM]^+$ and CO_2 environment.[4]

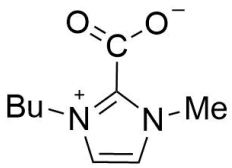

Figure 3.1. Structure of imidazolium-carboxylate adduct.

This electrolyte environment parallels the electrolyte solution used in these studies with Bi, Sn, and Pb. Therefore, the formation of this adduct may be forming and thermodynamically stabilizing on the Pb surface to result in passivation and subsequent loss of CO production due to competing pathways.[8] Bi and Sn can activate CO_2 at a less negative applied potential and may circumvent the formation of this adduct as a side product, thus, to be selective towards one product, CO.

If this theory represents the surface chemistry occurring at the Pb cathode, it would be a significant discovery towards the continued mechanistic research for the heterogeneous electroreduction of CO_2 to CO. Currently, the adduct is believed to encourage catalysis and the production of CO, not poison the transformation.[9,10] Interestingly, despite these statements, there has been no evidence to support the mechanistic interaction of the adduct.[11,12]

3.2 Experimental Method

3.2.1 Materials and Methods

Reagents and solvents were purchased from Sigma Aldrich, Alfa Aesar, Acros or Fisher. Bismuth(III) trifluoromethanesulfonate ($Bi(OTf_3)$) and imidazolium ionic liquid 1-butyl-3-methylimidazolium trifluoromethanesulfonate ([BMIM]OTf) were purchased from Sigma Aldrich. Tin(II) trifluoromethanesulfonate ($Sn(OTf)_2$), lead(II) oxide (PbO) 99.999 % puratrem, and potassium superoxide (KO_2) were purchased from Strem Chemicals. Electrochemistry grade hydrochloric acid (36.5—38.0 % in H_2O) was purchased from Sigma Aldrich. Tetrabutylammonium hexafluorophosphate ($TBAPF_6$) was purchased from TCI America and purified by recrystallization with ethanol. Carbon dioxide (CO_2) was purchased from Keen Compressed Gas Company.

Platinum gauze (99 %) was purchased from Sigma Aldrich. The bare glassy carbon disc electrode, bare Ni disc electrode, and the Ag/AgCl reference electrode were purchased from CHI Instruments. Graphite plates were purchased from Ohio Carbon and Ni foil was purchased from Sigma Aldrich.

3.2.2 Instrumentation

3.2.2.1 Electrochemical Measurements

Electrochemical studies were conducted using a CHI-620D potentiostat/galvanostat or a CHI-720D bipotentiostat. Electrochemical apparatus consisted of a three-electrode system; working (bare glassy carbon disc (3.0 mm diameter), bare Ni disc (3.0 mm diameter)), counter (platinum gauze), and a reference electrode (Ag/AgCl (1.0 M KCl)). Cyclic voltammetry and linear voltammetry experiments were performed with iR drop compensation with 100 mV s^{-1} scan rate.

Ag/AgCl reference was converted to SCE referencing by the equation, $E_{SCE} = E_{Ag/AgCl} + 0.044$ V.

3.2.2.2 Electrochemical Impedance Spectroscopy

Electrochemical impedance spectroscopy (EIS) was performed using a CHI-720D bipotentiostat. Electrochemical apparatus consisted of a three-electrode system; working (bare glassy carbon disc (3.0 mm diameter), bare Ni disc (3.0 mm diameter), Ni foil (~1 cm x 1.0 cm x 0.00125 cm), or graphite plate (~1 cm x 1.0 cm x 0.1 cm)), counter (platinum gauze), and a reference electrode (Ag/AgCl (1.0 KCl)). Frequency ranged from 0.1 Hz to 100 000 Hz. The electrolyte solution consisted of 0.1 M [BMIM]OTf and 0.1 M $TBAPF_6$ in CO_2 saturated MeCN.

3.2.2.3 Rotating Disc Electrode

Rotating disc electrode (RDE) was performed using a CHI-720D bipotentiostat. Electrochemical apparatus consisted of a three-electrode system; working (glassy carbon disc (5.0 mm diameter)), counter (platinum gauze), and a reference electrode (Ag/AgCl (1.0 KCl)). Linear sweep voltammograms (LSVs) were obtained between scanned potentials ranging from –1.45 to –2.95 V. Rotation rate was performed at 1000 rpm and scan rate of 100 mV sec^{-1}. The electrolyte solution consisted of 0.02 M [BMIM]OTf and 0.1 M $TBAPF_6$ in CO_2 saturated MeCN (80 mL).

3.2.2.4 X-ray Photoelectron Spectroscopy

XPS analysis was performed using a Thermo Scientific K-alpha$^+$ spectrometer with monochromatic Al Kα X-ray (1486.7 eV) and 72 W of power (12 kV, 6 mA) equipped with a 128 CCD detector plate. Operating vacuum pressure in the main chamber was less than $1x10^{-8}$ torr. XPS survey scans were collected with a step size of

1.0 eV and a pass energy of 100 eV. High resolution spectra were collected with a step size of 0.1 eV and a pass energy of 20 eV. The X-ray spot size was an elliptical shape with a semi-major axis of approximately 400 μm.

3.2.2.5 CO_2 Reduction Electrolysis and Headspace Analysis

Current densities were obtained by performing controlled potential electrolysis (CPE) on a sealed two-compartment electrochemical cell with the cathode and anode separated by a proton permeable Nafion membrane (NRE-212). The anode and cathode compartment both contained 20 mL of electrolyte solution; 0.1 M ionic liquid ([BMIM]OTf) and 0.1 M $TBAPF_6$ that was dissolved in CO_2 saturated MeCN. The solution was sparged for 30 minutes before the start of electrolysis.

During CPE, the cathode was stirred at a steady rate while there was a continuous flow of CO_2 into the headspace (5 mL/min). The cathode was vented directly into a flow gas chromatograph (SRI Instruments, SRI-8610C). A chromatograph was obtained every 15 min throughout the duration of electrolysis by placing the sampling loop in line with a packed HayeSep D column and a packed mole Sieve 13X column. The columns led directly to a thermal conductivity detector (TCD) and a flame ionization detector (FID) equipped with a methanizer to quantify hydrogen and carbon monoxide production respectively. The gas carrier was Argon (Keen, 99.999 %).

3.2.2.6 NMR

Solvent suppression ^1H NMR was performed with aliquots from the cathode solution to detect any solution products from electrolysis and/or decomposition of electrolyte solution. The acetonitrile resonance was suppressed at 1.96 ppm. Formic

acid production was monitored at 8.1 ppm and imidazolium-carboxylate adduct was monitored at 7.17 and 7.13 ppm.

Synthetic products were characterized with ^{13}C and ^{1}H NMR. ^{13}C NMR was performed as an attached proton test (APT) experiment with 2048 scans. ^{1}H NMR was performed with 8 scans. The samples were solvated in deuterated-MeCN.

3.2.2.7 Lead (II) trifluoromethansulfonate

Lead(II) oxide was reacted with excess triflic acid in correspondence to a modified literature procedure.[13] A Schlenk flask, equipped with lead oxide (2.00 g), triflic acid (4 mL) and 40 mL dry toluene. The mixture was heated at 110 ºC under N_2 for 5 hrs. The Schlenk flask was transferred to a N_2-filled glove box upon the removal of solvent and a slightly reduced pressure. The crude material was dissolved in acetonitrile and filtered through celite. The filtrate was then concentrated under vacuum to yield an off-white powder in a 62 % yield. ^{19}F NMR (376 MHz, CD_3CN, 25 ºC) δ/ ppm= –78.67.

3.2.2.8 1-butyl-3-methylimidazolium-carboxylate

In a N_2-filled glove box, was suspended 1-methyl-3-butylimidazolium bromide ([BMIM]Br; purchased from Alfa Aesar) in dried toluene and let it react with sodium hexamethyldisilizane (NaHMDS; purchased from Sigma Aldrich) for 2 hrs. This solution was filtered through celite and the filtrate, carbene, was sparged with CO_2 gas for 0.5 hr. This solution underwent a second filtration step where the product was collected as a white precipitate in a 78 % yield.

3.2.2.9 1-butyl-3-methyl-2-imidazolone

In a N_2-filled glove box, 1-butyl-3-methylimidazolium bromide (1.0 M, 0.4382 g) was solvated in dry dimethylsulfoxide (DMSO, 2 mL) in a 20 mL conical vial equipped with a stir bar. 1 eq. potassium superoxide (KO_2, 0.1422 g) was added to the round bottom and let react overnight with vigorous stirring. The round bottom was removed from the glove box and washed with water and dichloromethane (DCM). The DCM layer was collected and dried with magnesium sulfate. DCM was then removed under reduced pressure. The product was a viscous liquid collected in a 25 % yield. Product was analyzed via ^{1}H NMR, ^{13}C NMR, and XPS.

3.2.3 Electrodeposition of Bi, Sn, and Pb Electrodes

Prior to electrodeposition, the Ni disc electrode (3.0 mm diameter), carbon disc electrode (3.0 mm diameter), or graphite plate (~1 cm x 1.0 cm x 0.1 cm) was polished with 0.05 micron alumina powder in Millipore water and then sonicated in Millipore water for five minutes to remove residual powder. If starting with Ni foil (~1 cm x 1.0 cm x 0.00125 cm), it was sonicated in water, acetone, and lastly acetonitrile for 20 minutes for each step to remove excess oils. The substrate was then submersed in an acetonitrile organic electrolyte solution containing 0.02 M of the respective triflate metal and 0.1 M $TBAPF_6$ saturated with N_2. A series of cyclic voltammetry sweeps (10 cycles, 100 mV s^{-1}) were performed with applied potentials ranging from –0.25 to –2.25 (V) vs. SCE. Following the electrode conditioning, the GCE/Ni disc was agitated to remove exfoliated material formed on the electrode surface. Using the same electrolyte solution, controlled potential electrolysis (CPE) applied a constant potential of –1.35 for $Bi(OTf)_3$, –0.55 V for $Sn(OTf)_2$, and –1.35 (V) vs. SCE for Pb until a total of ~1 C cm

$^{-2}$ was passed. The modified electrode was rinsed with acetonitrile followed by a drying step consisting of a gentle N_2 flow over the modified surface.

3.3 Results and Discussions

3.3.1 Identifying Surface Impurities

Literature has openly stated that the imidazolium-carboxylate adduct is an essential intermediate for the heterogeneous electroreduction of CO_2 to CO.[14,15] Therefore, there is apprehension in confidently stating that the adsorption of this species leads to film passivation, despite the likely thermodynamic formation for Pb surfaces as discussed previously. Because of this, careful and vigorous studies were performed to first support that there is an impurity adsorption event for Pb. This should also support that film passivation is not simply due to film thinning, which was further demonstrated by a sleek gray film existing on the electrode surface after electrolysis.

Further, understanding how surface adsorbates interact with the specific cathode is critical towards gaining clarity on the mechanism for CO evolution. Detecting a difference in adsorbate interactions would be a key insight for understanding why the mechanism for Pb leads to film passivation. Importantly, because impurity adsorption likely alters the pathway that catalysis proceeds, it was therefore critical to first identify if the mechanism for Pb is analogous to Bi. Tafel analysis was used to elucidate this mechanism based on the rate determining step (RDS). To monitor impurity adsorption events specifically, the cathode surface before and after controlled potential electrolysis (CPE) was monitored via X-ray photoelectron spectroscopy (XPS) to observe how the adsorbates evolve. Because impurities can complicate charge transfer events, the

resistivity of these events were investigated with electrochemical impedance spectroscopy (EIS).

3.3.1.1 Tafel analysis

Tafel analysis, as described by the Butler-Volmer equation (equation 3.1), provides information on the type of rate determining electron transfer (ET) event occurring in an electrocatalytic redox reaction.[16] For a simple irreversible two-electron redox reaction, such as for Bi-CMEC, the Butler-Volmer equation can be manipulated to provide the Tafel equation (equation 3.2) which affords a linear relationship between overpotential (η) and the log of current (log(*i*)).

$$i = nFAk^{o}\,(C_A(0,t)\exp(-\alpha f(E-E^{o}) - C_B(0,t)\exp((1-\alpha)f(E-E^{o})) \qquad (3.1)$$

$$\eta = -b\,\log(i) + a \qquad (3.2)$$

A is the area of the electrode, F is faraday's constant, k^{o} is a gas constant, n is the number of electrons transferred, α is the transfer coefficient (symmetry factor), $E-E^{o}$ represents the overpotential (η), and $C_A(0,t)$ and $C_B(0,t)$ are the concentrations of the oxidized and reduced species at the surface respectively. In equation 3.2, b represents the Tafel slope. Slopes for this equation have been theoretically derived with an absolute maximum of 120 mV dec^{-1}.

Tafel analysis for Bi revealed Tafel slopes of ~120 mV dec^{-1}, [6,17] which suggested that the first ET event is rate determining for the reduction of CO_2.[8] This results in the formation of a CO_2 radical anion ($CO_2^{\bullet-}$) after the first ET event, which is common for many heterogeneous catalysts for CO_2 reduction.[18] To observe if Pb experiences a similar mechanism to Bi based on the RDS, Tafel experiments were performed via rotating disc electrode (RDE) studies. Steady-state Tafel analysis is beneficial for minimizing diffusional effects, which is important for Pb.[19] Specifically,

poor diffusion of the co-catalyst (imidazolium), reactant (CO_2), or product (CO) may complicate adsorption events and result in non-ideal adsorbates (impurities).

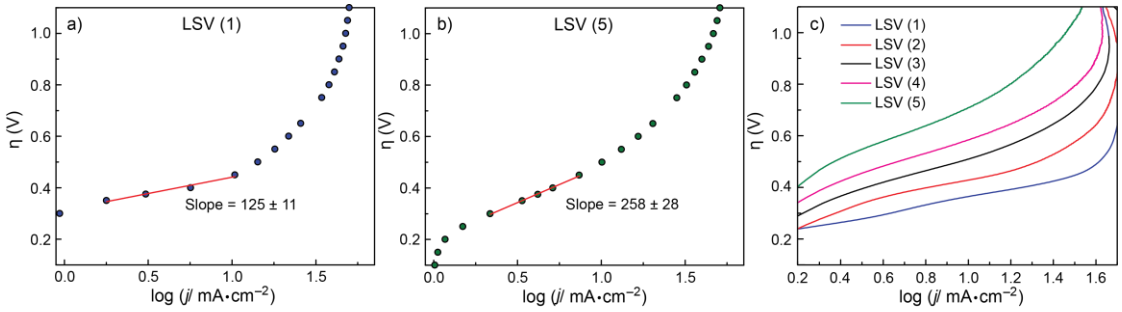

Figure 3.2. Linear sweep voltammogram in a) and b) show the Tafel plots for the Pb-modified electrode for the first (LSV (1), blue trace) and fifth (LSV (5), green trace) sweep respectively. Plot c) overlays five Tafel plots. LSVs obtained at 1000 rpm and scan rate of 100 mV sec^{-1}.

Upon multiple executions, a Tafel slope of 125 ± 11 mV dec^{-1} was obtained (Figure 3.2a). This value correlates to the RDS being the first ET to yield $CO_2^{\bullet-}$. This suggested that Pb undergoes a similar mechanism to Bi. Interestingly, upon sequential sweeps using the same Pb-modified electrode (without re-plating the Pb surface), the Tafel slope became larger and exceeded the maximum 120 mV dec^{-1} for a two-step ET mechanism. This feature is unlike what was observed for Bi.

When the Tafel slope exceeds 120 mV dec^{-1}, often it is the result of non-ideal charge transfer conditions, such as for when $\alpha \neq 0.5$.[8] Specifically, high Tafel slopes have been observed for when $\alpha << 0.5$. As shown in equation 3.1, α is the symmetry factor for the distribution of electrons going towards oxidation or reduction. When $\alpha<<0.5$, there are fewer electrons going towards oxidation and more going towards reduction. This leads to an irreversible redox reaction to favor product formation. An

explanation for this event has been attributed to impurity adsorption to hinder charge transfer.[8] Once formed, the impurity is stable and can be displaced by either solvent (MeCN) or reagent (CO_2) itself. This results in additional energy required to remove the impurity to make available active sites to continue charge transfer events. The extra energy required to remove the impurity, in addition to the already high potential barrier, is representative of the higher Tafel slope (>120 mV dec^{-1}). Therefore, the increasing Tafel slope upon sequential sweeps (Figure 3.2c) supports the theory that an impurity is thermodynamically formed and adsorbed to the Pb cathode.

The higher potential barrier from the surface impurity is also highlighted in Figure 3.3a. Here, the overpotential becomes more negative upon additional LSV sweep segments using the same Pb-modified electrode. Additionally, Figure 3.3b suggested that the shift to more negative overpotentials is not a function of rotation rate because the change in overpotential shifts accordingly for the two separate RDE studies.

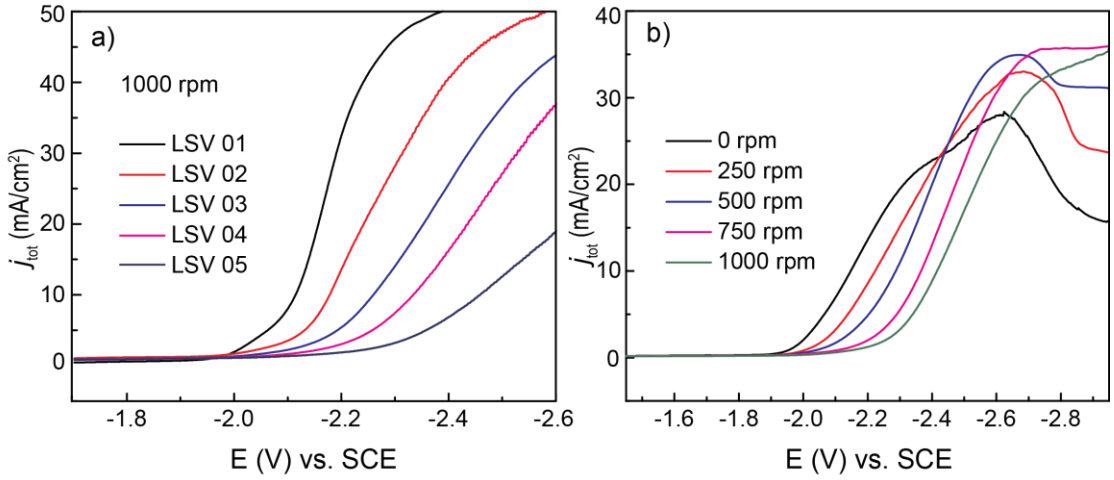

Figure 3.3. Linear sweep voltammograms are overlaid in a) using the same Pb-modified electrode using RDE. Overlaid voltammograms in b) illustrate a rotation rate study performed with the same Pb-modified electrode for all rpms.

These Tafel studies suggested that there is an adsorbate that forms on the Pb cathode. This results in active sites being occupied by the impurity and not by the reactant to undergo the $2H^+/2e^-$ redox reaction. The formation of the adsorbate appears to be thermodynamically favored for the Pb cathode because of the lower apparent charge transfer coefficient and higher Tafel slopes for continuous LSV sweep segments. Understanding that the Tafel slope for Bi does not change upon multiple LSV sweep segments, in that it does not demonstrate impurity adsorption, it was curious to see how the active metal species for the Bi-, Sn-, and Pb-modified surfaces evolve during electrolysis. Specifically, it was curious to observe if the surface evolution for the Pb cathode is unique from Bi and Sn due to demonstrating a surface impurity.

3.3.1.2 Evolution of Surface Composition

Elemental surface changes of the metal cathodes were analyzed with XPS for the Bi 4*f*, Sn 3*d*, and Pb 4*f* high resolution regions. High resolution spectra for O 1*s*, C 1*s*, S 2*p*, and F 1*s*, in addition to Bi, Sn, and Pb standards, were also acquired to support component labeling for the active metals (Appendix B.1—3). The type of components identified for the active species can provide significant information on how adsorbates may interact with the oxidative environments. This was highlighted by analyzing the stability of the metal catalyst components on the surface from Gibbs free energy values (ΔG), which are summarized in Table 3.1 for Bi and Sn and Table 3.2 for Pb.

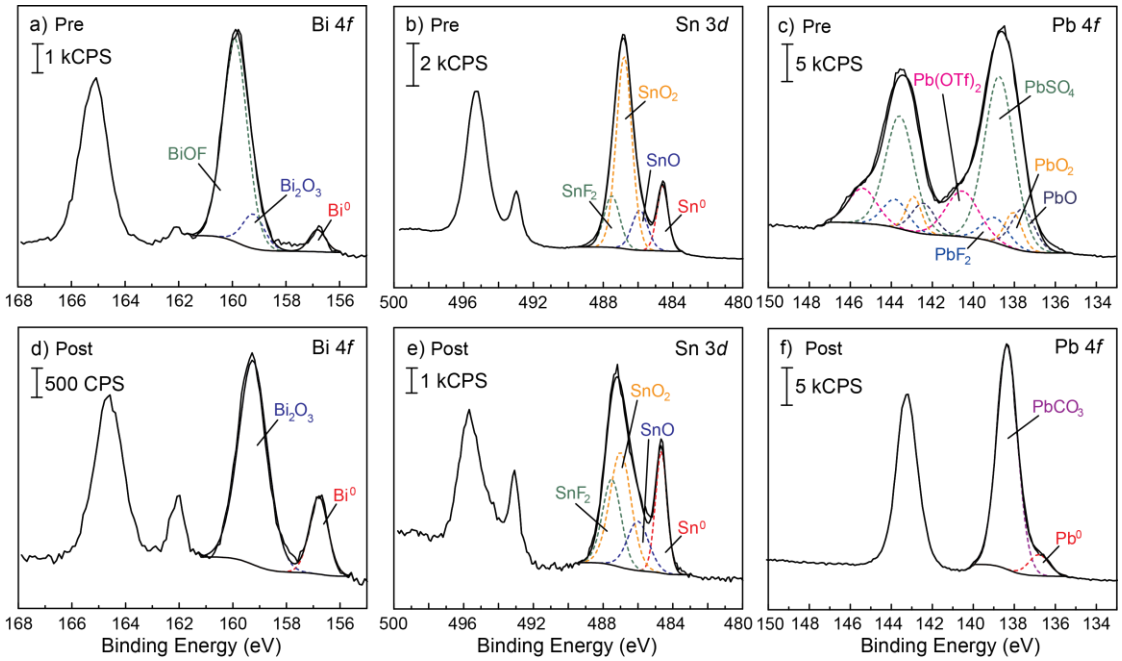

Figure 3.4. XPS spectra showing the Bi 4*f*, Sn 3*d*, and Pb 4*f* high resolution region for their respective cathodes as plated (pre, a, b, and c respectively) and after electrolysis (post, d, e, and f respectively).

Bi and Sn showed similar surface compositions via organic electrodeposition (Figure 3.4a and b respectively). Interestingly, these surface compositions also relate to the surface composition of the acid aqueous electrodeposited Bi-CMEC, such that there is a metallic and metal halide component.[17] Specifically, organic electrodeposition of $Bi(OTf)_3$ shows metallic bismuth (Bi^0, red trace), bismuth oxide (Bi_2O_3, blue trace), and bismuth oxyfluoride (BiOF, green trace). In this case, Bi_2O_3 is the result of ex situ oxidation of Bi^0, not from electrochemical formation. The same conclusions were found for electrodeposited $Sn(OTf)_2$, which showed metallic Sn (Sn^0, red trace), tin(II/IV) oxide (SnO (blue trace) and SnO_2 (yellow trace) respectively), and tin(II) fluoride (SnF_2,

green trace). The thermodynamic stabilities of these species are roughly similar and do not exceed ~500 kJ mol^{-1}. Similar ΔG values correspond to the analogous onset potential for Bi and Sn; neither requiring a significant overpotential.

Table 3.1. Gibbs free energy values for Bi and Sn components detected in the Bi 4*f* and Sn 3*d* high resolution regions.[20]

Bi components	ΔG (kJ mol^{-1})	Sn components	ΔG (kJ mol^{-1})
Bi(0)	0	Sn(0)	0
Bi(III) oxide	–494	Sn(II) oxide	–252
Bi(III) oxyfluoride	N/A	Sn(II) fluoride	–316
		Sn(IV) oxide	–516

Unlike Bi and Sn, Pb showd no evidence for a metallic component. Pb was composed primarily of lead(II) sulfate ($PbSO_4$, green trace) with slight contribution from Pb(II/IV) oxide (PbO (navy trace) and PbO_2 (yellow trace) respectively) and lead fluoride (PbF_2, blue trace). Significant $PbSO_4$ contribution is rationalized by its thermodynamic stability compared to PbO (Table 3.2). Such a high contribution may result in the more negative onset potential to reduce the thermodynamically stable Pb active species. More negative applied potentials commonly bind intermediates more strongly,[21] thus slowing the rate of catalysis. Slower rates can have negative effects on proton availability and result in intermediate rearrangement on the surface. This can negatively impact catalysis for Pb significantly.

Table 3.2. Gibbs free energy values for Pb components detected in the Pb 4*f* high resolution region.[22]

Pb components	ΔG (kJ mol^{-1})
Pb(0)	0

Pb(II) oxide	–188
Pb(IV) oxide	–217
Pb(II) fluoride	–617
Pb(II) carbonate	–626
Pb(II) sulfate	–814

The surface compositions post electrolysis demonstrated a common trend; a metallic component for all cathodes. For Bi and Sn, this component nearly double in atomic percent. After electrolysis Bi was composed primarily of Bi_2O_3, Sn showed greatest contribution from SnO and SnO_2 with slight contribution still from SnF_2 (more thermodynamically stable, Table 3.1), and Pb favored lead(II) carbonate ($PbCO_3$, purple trace). Here, Pb now deviated from what was observed for the highly efficient Bi and Sn cathodes; no metal oxides were present. $PbCO_3$ is highly stable at room temperature (–625.9 kJ mol^{-1})[22] which may therefore not be readily reduced to Pb^0 during catalysis. Carbonate likely forms at the electrode surface when there is limited proton availability. The local pH at the cathode surface is typically higher than in the bulk, especially with a more negative applied potential.[12] This can result in CO_2 reacting with OH^- to yield CO_3^{2-}, which would then favorably bind to Pb^{2+}. Here, the active Pb component is >100 kJ mol^{-1} more stable than the Bi and Sn active species. This likely contributes to the greater energy cost for Pb to perform the CO_2 to CO redox reaction.

3.3.1.3 Impedance Studies

Once understanding the composition of the cathodes before and after electrolysis, it was curious to observe how these materials interact with the catalyst support by analyzing ohmic resistance (R_{ohmic}). R_{ohmic} is a measure of the resistance between the electrode surface and the electrodeposited film to facilitate ET events. EIS is a highly sensitive technique for measuring the electronic behavior for the rate

determining ET event. In particular, EIS is highly beneficial for catalyst electrodes for CO_2 reduction because it provides capacitance and resistance values for charge transfer and mass transport events upon detailed analysis.[23] Therefore, this is a highly reliable method for measuring the resistivity associated with the rate determining electron migrating through the film for the different p-block materials.

3.3.1.3.1 Elucidating the Ohmic Strength for Bi, Sn, and Pb Platforms

Electrochemical responses are generated from alternating potential signals that output different frequencies. The system's impedance response to those frequencies are summarized in a Nyquist plot (complex plane plot) to describe current/ voltage relationships. For monitoring the ohmic strength specifically, high frequency and short time intervals were applied (Figure 3.4) This high frequency region carefully detects the electrochemical response of applied input frequencies for the measured interaction between the film and substrate. For an ohmic response specifically, an "elbow" (or "L") is featured. This feature highlights the capacitive and resistive contributions of R_{ohmic}: suppressed elbow signifies a more resistive system and a pronounced elbow suggests an electronic distribution between capacitive and resistive components.

The electrolyte solution for the EIS studies mimicked electrolysis conditions. A potential range was studied (–1.80 to –2.20 (V) vs. SCE (all potentials will be referred to this reference)) to observe how robust the film is not only at the applied potential for catalysis, but also for a slew of reaction conditions.

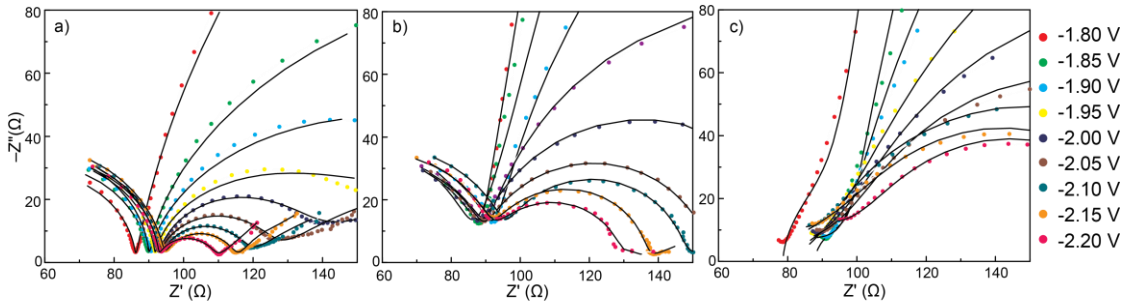

Figure 3.5. Nyquist plots (high frequency region) for a) Bi, b) Sn, and c) Pb are shown for potentials ranging from –1.80 to –2.20 (V) vs. SCE.

Bi and Sn both show a significant feature (elbow) at high frequencies (Figure 3.5a and b respectively). This elbow is not dominant in the responses for Pb (Figure 3.5c). This suggests that Bi and Sn have a less resistive ohmic interaction than Pb to facilitate charge transfer. Resistivity is measured by the x-axis (Z´, real) and capacitance is measure by the y-axis (–Z″, imaginary). The ohmic response for Pb remains near Z´ with minimal contribution from –Z″. Bi and Sn both have an ohmic response along the Z´ and –Z″ axis, suggesting a combination of capacitive and resistive properties which is ideal for electrocatalysis;[24] not completely energy storing or resistive such as to prevent charge transfer events.

The Nyquist plot for Pb complimented the previous Tafel results, in that a surface impurity for Pb may complicate charge transfer events, thus becoming more resistive. Complicated charge transfer events result in greater difficulty (resistance) for transferring electrons through the substrate to reduce CO_2.

Interestingly, Bi and Sn maintained impressive ohmic contact with the substrate even at more negative applied potentials. This further highlights these impressive and durable platforms for efficient CO_2 to CO electrocatalysis.

3.3.1.3.2 Resistivity Comparisons for Bi, Sn, and Pb Cathodes

In expanding the impedance window to include lower frequencies obtained at longer time intervals, information on diffusion effects and the resistance to charge transfer (R_{CT}) was revealed. R_{CT} provides information on how easily the rate determining ET step occurs. Minimal R_{CT} values are ideal, such that a smaller R_{CT} implies a less resistive and more favorable ET event.

As illustrated in Figure 3.6a, the R_{CT} value is obtained by taking the difference between the sum of R_{CT} and solution resistance (R_{sol}) (orange trace) and just R_{sol} (green trace). This yields the resistance (Ω) for the diameter of the semicircle.

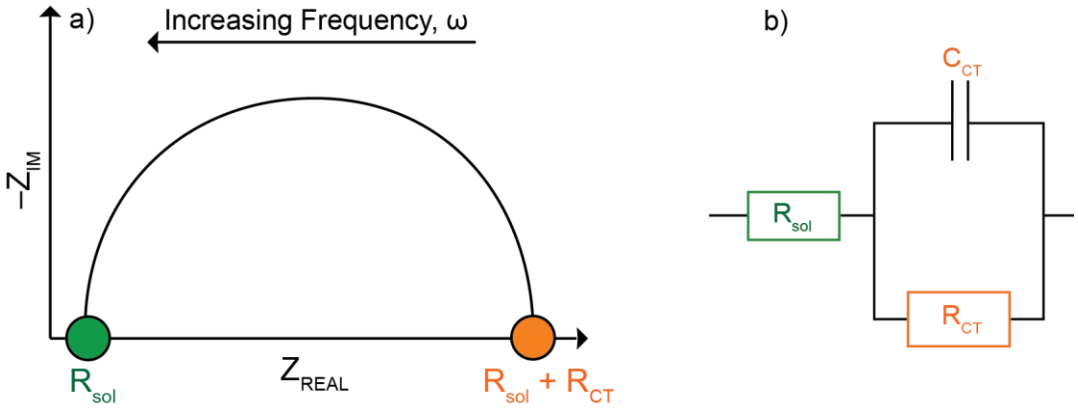

Figure 3.6. The Nyquist plot in a) features a simple Randles impedance response for a one ET event. The circuit in b) shows the Randles circuit to describe the mechanism shown in a). C_{CT} is the charge transfer capacitance.

These EIS studies for lower frequencies were performed under identical electrolyte conditions as used previously, but were performed with a constant applied potential of –1.95 V. Pb was also performed at –2.05 V because this is the optimal potential for Pb catalysis. Performing EIS at both applied potentials allowed for direct

comparisons to be made between the various cathodes. Here, the objective was to elucidate mechanistic information under optimal catalytic conditions based on the RDS. In addition to R_{CT}, adsorption phenomenon (R_{AD}) were monitored and the impedance responses were simulated with circuit analysis (example in Figure 3.6b).

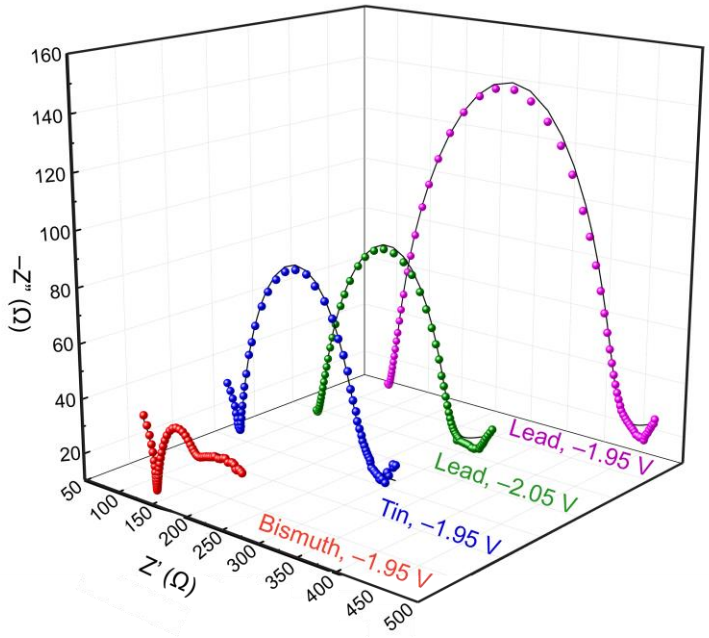

Figure 3.7. Nyquist plot for the Bi (red trace), Sn (blue trace), and Pb cathodes (green trace, –2.05 V; purple trace, –1.95 V). Black lines represented 3RC simulated data.

Figure 3.7 summarizes the impedance responses in overlaid 3D-Nyquist plots for Bi (red trace), Sn (blue trace), and Pb (–2.05 V (green trace), –1.95 V (purple trace)). Upon comparison of the p-block metal cathodes, Bi was found to have the smallest R_{CT}, followed by Sn and Pb (–2.05 V) respectively. Interestingly, Pb (–2.05 V) and Sn demonstrate comparable R_{CT} values. When Pb was exposed to the same applied

potential as Bi and Sn (–1.95 V), however, its R_{CT} nearly doubled. This supports initial CPE studies and Tafel studies, that at higher applied potentials, Pb is initially capable of reducing CO_2.

When looking more closely at the Nyquist plot in Figure 3.7, Bi showed a more complex impedance response. Bi demonstrated two fused-semicircles opposed to one. In EIS, a fused-semicircle suggests an adsorption phenomenon, which could likely be due to the adsorption of imidazolium on the surface to facilitate the RDS. This is based on the essential cathode/IL interface. Without this interface, the $2H^+/2e^-$ redox reaction is jeopardized significantly.[6,17]

In comparison to Sn and Pb, neither showed a defined fused-semicircle. The possibility for an adsorption phenomenon is not eliminated, however, because this could be the result of two semicircles overlapping to give the appearance of one more broad semicircle. Because it is unclear if an adsorption phenomenon exists for Sn and Pb, circuit analysis will be beneficial for elucidating their mechanism.

3.3.1.3.3 Circuit Analysis for Detection of Adsorption Phenomenon

Circuit analysis involves the strategic arrangement of basic elements into a network of connected resistors and capacitors. The different values for the resistor and capacitor, based on the path of the electrons, gives information on the kinetics and mechanism for the catalytic system.[23] For example, a simple Randles circuit is featured in Figure 3.6b to describe an ideal impedance response (Figure 3.6a) for a perfect semicircle. This circuit is designed with one resistor (R) and one capacitor (C) in parallel, which represents a time constant (RC). When designing circuits, the first resistor typically represents R_{sol}. A time constant is implemented for each subsequent event leading up to the ET event. For simple impedance responses, such as the Randles

impedance response (Figure 3.6a), one time constant is sufficient in describing the electrochemical event. The more complex the ET event is, such as for the $2H^+/2e^-$ redox reaction, more time constants will likely be required to describe the complex electrochemical behavior; no longer demonstrating a perfect semicircle.[25]

Two circuits were designed to represent possible electrochemical events for the Bi, Sn, and Pb cathodes, the 3RC and 2RC. As the name implies, the 3RC has three time constants, whereas the 2RC is less complex and has only two time constants. The 3RC and 2RC circuits are illustrated in Figure 3.8a and b respectively.

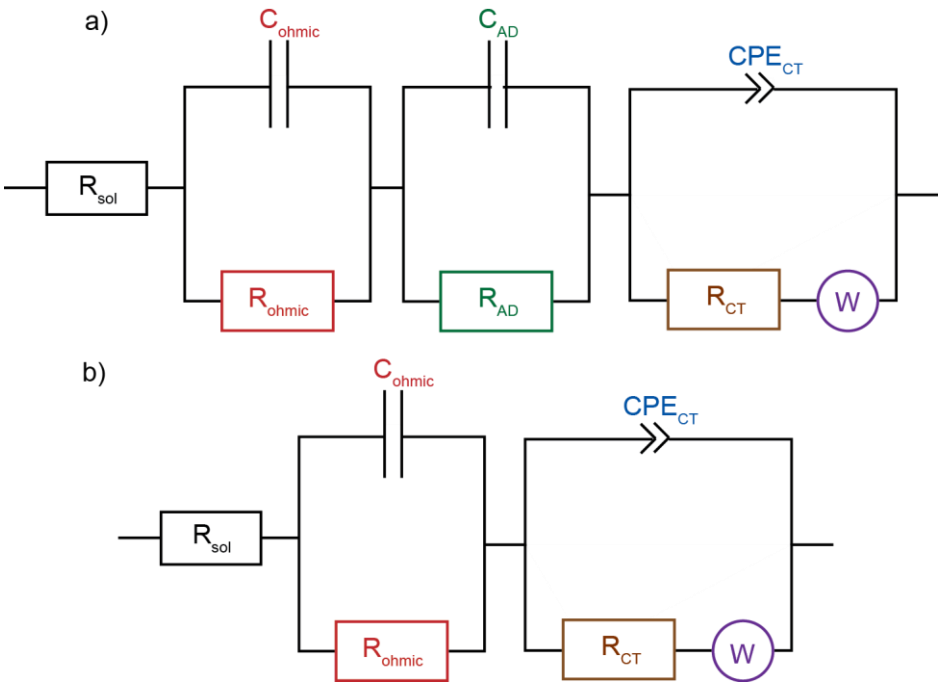

Figure 3.8. Illustrations of the a) 3RC and b) 2RC circuits.

Each capacitor-resistor time constant represents a different phenomenon; R_{ohmic}, adsorption resistance (R_{AD}), and R_{CT}. The Warburg element (W), the constant phase

element (CPE), and R_{sol} are featured in both circuits. W accounts for diffusional effects, such that it is an infinite array of resistors and capacitors.[26] CPE accounts for an unideal capacitance of the double layer, which may be due to non-uniform surface area or charging and results in the imperfect semicircle.[27] The only difference in circuit design, is that the 3RC accounts for an adsorption phenomenon and the 2RC does not. This resembles the two possible electrochemical events to clarify if there are two semicircles overlapping to give the appearance of one for Sn and Pb. Therefore, circuit analysis will reveal which circuit best mimics the ET event. For example, if the circuit simulation suggests better fitting to the 3RC, the material is likely to experience an adsorption phenomenon. If the circuit simulation shows better fitting to the 2RC, it is unlikely to experience an adsorption phenomenon.

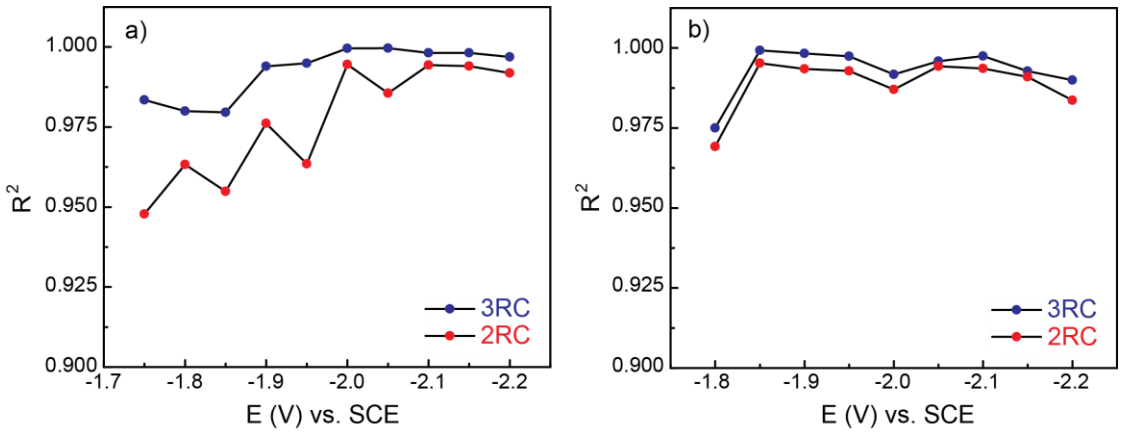

Figure 3.9. R-squared plots for the a) Sn and b) Pb cathodes for the 3RC (blue trace) and 2RC (red trace) circuit fittings.

The circuit fittings for Sn and Pb are shown in Figure 3.9a and b respectively, with R-squared (R^2) values with respect to applied potential for the 3RC (blue trace) and 2RC (red trace) simulation. The R^2 values for Sn prior to –2.0 V showed a strong correlation to the 3RC circuit, suggesting that Sn experiences an adsorption phenomenon and therefore has overlapping semicircles. Pb does not demonstrate a greater correlation to either circuit, implying that the 2RC is appropriate in portraying the redox reaction without R_{AD}. This suggests that the impurity adsorption may disrupt adsorption of IL.

Because the 3RC and 2RC are nearly identical for Pb, it was curious to observe how a simple 1RC circuit would compare. As illustrated in Figure 3.10a, the 1RC represents R_{CT} but is more complicated than the simple Randles circuit, such that diffusion and unequal charge distribution are accounted for via W and CPE respectively.

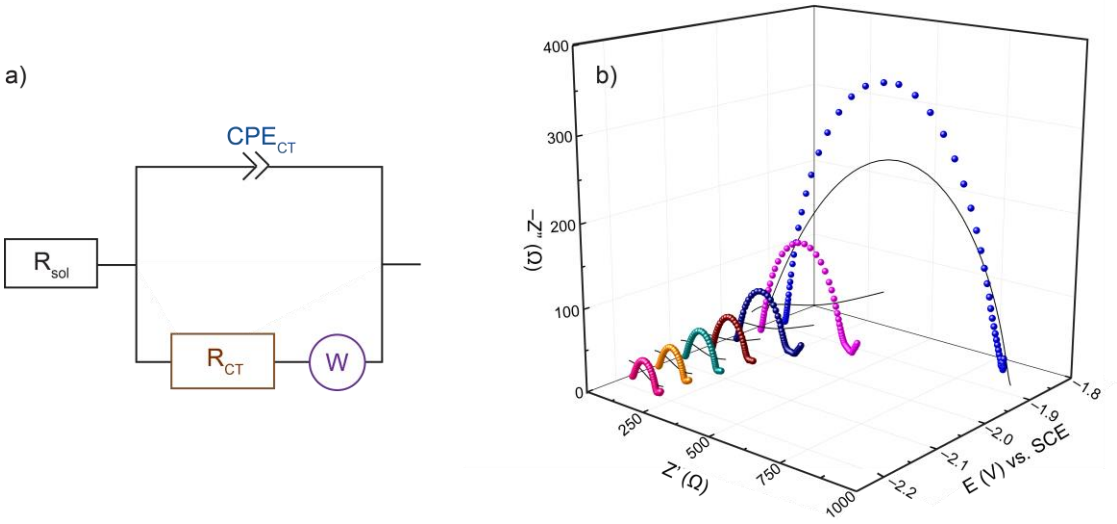

Figure 3.10. The 1RC circuit is illustrated in a). The 1RC simulation (black lines) and experimental impedance responses (colored dots) are summarized in the 3D Nyquist plot in b) for Pb.

It was clearly observed in Figure 3.10b that the 1RC poorly simulates the rate determining ET event. This suggests that R_{ohmic}, in the 2RC circuit, plays a significant role in the mechanism. This stresses the importance on the cathode material and its unique interaction with intermediates, i.e. blocking or facilitating ET events. It is therefore not surprising to see changes in catalysis upon impurity adsorption, such that efficient charge transfer is highly dependent on surface resistance.

Interestingly for both Sn and Pb, neither the 3RC nor 2RC showed a stronger correlation when –2.0 V was exceeded. Because the adsorption phenomenon is due to the adsorption of IL, this result implies that the stability of the adsorbed IL is jeopardized when approaching more negative potentials. Because Sn and Bi show similar catalytic behaviors, it was curious to see if the loss of the adsorption phenomenon also exists for Bi.

The impedance response for Bi was studied for the same range of potentials as executed for Sn. Because Bi had very defined fused semi-circles, these responses were summarized visually in a Nyquist plot (Figure 3.11) in lieu of calculating R^2. This allows for a clear visualization on the relationship between adsorption and applied potential.

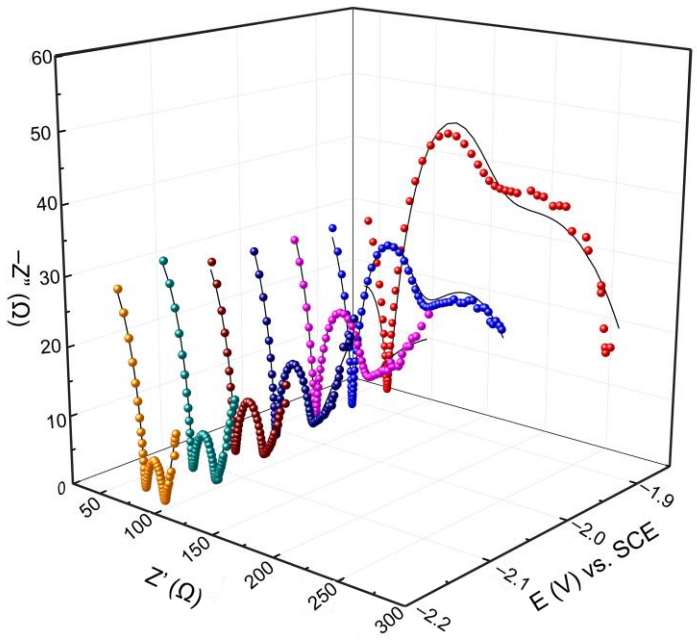

Figure 3.11. 3D Nyquist plot for the Bi cathode at varying applied potentials.

As shown in Figure 3.11, Bi demonstrated fused-semicircles between potential ranges of –1.85 to –1.95 V. Once exceeding these potentials, the adsorption phenomenon no longer existed. More negative applied potentials (≤ –2.05 V) result in a single semicircle followed by a linear response signifying diffusion into the bulk of solution.

Here, Bi is showing similar behavior to what was observed for the Sn cathode and highlights the interplay between the cathode and IL. More negative potentials, approaching the reduction potential of imidazolium may jeopardize the cathode/IL interface. There is merely a 100 mV difference between the optimal reduction potential for Pb and the reduction potential for imidazolium IL. This may contribute to rapid film passivation for the Pb cathode at –2.05 V.

Observing that Pb is not dependent on an adsorption time constant, there is now a distinction between how the catalytic mechanisms differ. The electronic differences suggest that the IL is not interacting with the cathode surfaces in the same manner. Thermodynamic formation of an impurity for Pb may discourage adsorption of IL and ultimately discourage its benefits towards effective catalysis. It was therefore of interest to next identify the composition of the adsorbate via XPS to gain greater mechanistic information on how the impurity may form.

3.3.1.4 Clarifying Adsorbate Identity via XPS

As a complimentary technique to EIS, XPS was used to characterize the adsorbing species for each cathode surface after electrolysis. Because the imidazolium IL is responsible for the adsorption phenomenon detected from EIS, the N 1*s* high resolution region was of greatest interest. Like the XPS surface studies performed for the active metal (Figure 3.3), the evolution of the N 1*s* high resolution region was observed by characterizing the surface before electrolysis (pre) and after (post). This provided a clear description of how the adsorbing species for Pb evolves and compares to Bi and Sn.

In characterizing the N 1*s* high resolution region, an understanding of the different nitrogen components was first necessary. From previous mechanistic study, 1,3-dialkylimidazolium ILs are believed to donate protons towards the $2H^+/2e^-$ redox reaction. Specifically, the acidic C2 proton is donated to $CO_2^{\bullet-}$ to yield the resulting carbene and carboxyl, as illustrated in Scheme 1.1. The imidazolium and carbene will both be detected in the N 1*s* high resolution spectrum.

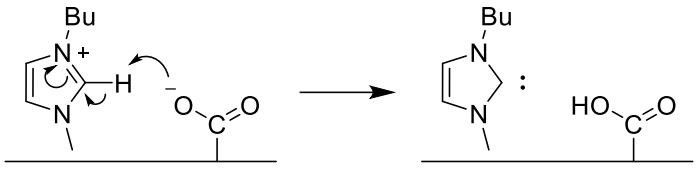

Scheme 3.1. Arrow pushing mechanism for the formation of the carbene and carboxyl upon the first H^+ transfer step.

The NCN^+ imidazolium nitrogens have an oxidative environment that is unique from the NCN carbene nitrogens. This results in characteristic binding energies (BEs) observed at 402.1 and 400.3 eV respectively. Additionally, supporting electrolyte ($TBAPF_6$) is also detected in this region and has a unique BE of 402.4 eV. The 0.3 eV difference between TBA^+ and imidazolium is stated with confidence upon multiple standards acquired.

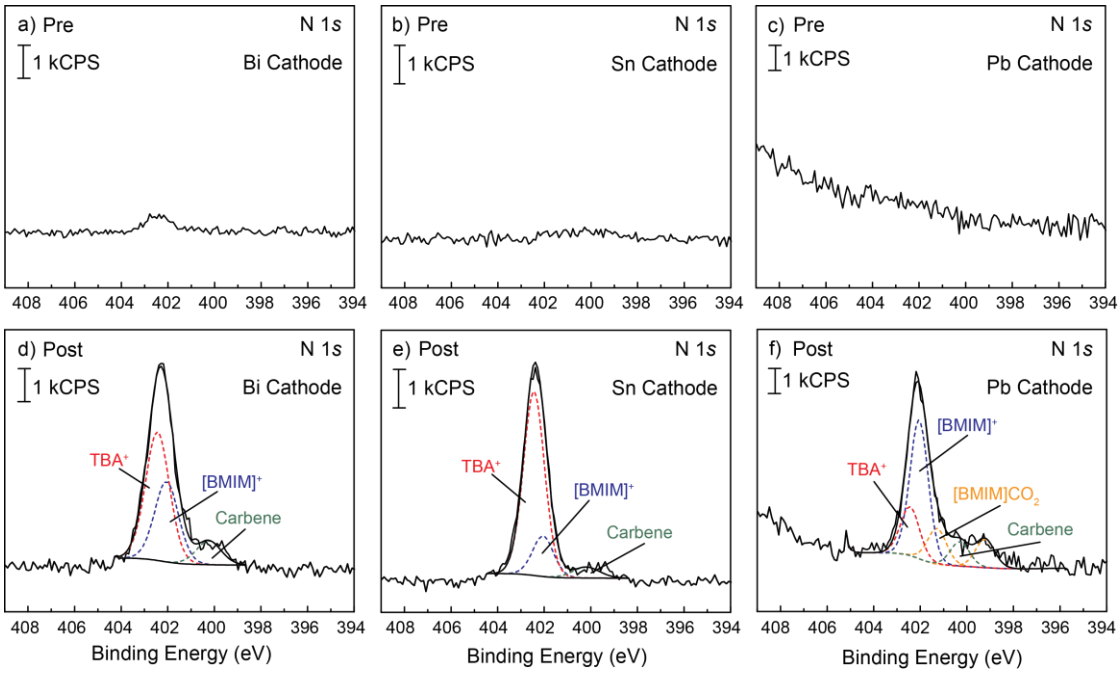

Figure 3.12. N 1*s* high resolution spectra for Bi, Sn, and Pb cathodes pre (a, b, and c respectively) and post (d, e, and f respectively) electrolysis.

Upon analyzing the surfaces after electrodeposition for Bi, Sn, and Pb (pre, Figure 3.12a, b, and c respectively), there was little to no nitrogen contribution. Any nitrogen detection would be residual from the electrodeposition bath ($TBAPF_6$). Post electrolysis, the N 1*s* region now showed components for TBA^+ (red trace), $[BMIM]^+$ (blue trace), and carbene (green trace) for all cathodes.

The N 1*s* high resolution spectra post electrolysis for Bi and Sn were nearly identical (Figure 2.12d and e respectively). Interestingly, Pb demonstrated a more complicated surface and had an inverse relationship between the amount of $[BMIM]^+$ and TBA^+ on the surface compared to Bi and Sn. The greater contribution of $[BMIM]^+$ may signify complications during catalysis to prevent proton transfer events. The two additional components contributing to the complicated spectrum (Figure 2.12f, orange

trace), are likely the source of impurity adsorption as previously suggested by Tafel analysis and EIS. The BE for the two new components are 401.3 and 399.3 eV. The 401.3 eV component has a nitrogen oxidation environment that is less electropositive than imidazolium and less electronegative than carbene. To match this electronic environment, the C2 position is likely bound to a separate species in solution to form an imidazolium-based adduct. If this represents the impurity for Pb, the theorized adduct (imidazolium-carboxylate) may prove to be irreversibly formed, thus creating a thermodynamic sink. The 399.3 eV component lies in a more electronegative environment than carbene. This suggests that C2 is bound to an electron donating substituent, such as oxygen, to yield 1-butyl-3-methylimidazolone. This would provide an electronic environment analogous to urea. It is curious to observe if this species is electrochemically generated during electrolysis, or if it simply the decomposition of the 401.3 component when exposed to air.

It was previously stated that Pb can thermodynamically form an imidazolium-carboxylate species when exposed to imidazolium and CO_2 at negatively applied potentials. This is illustrated in Scheme 3.2, where the reactive carbene performs a nucleophilic attack on neutral CO_2 that saturates the system to yield imidazolium-carboxylate.

.

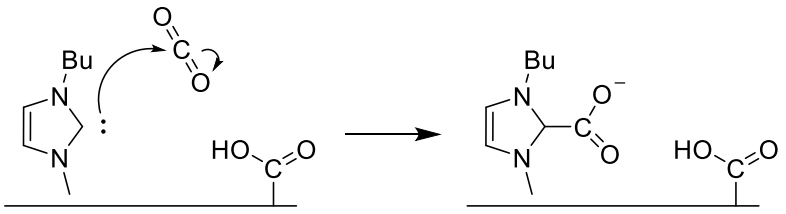

Scheme 3.2. Arrow pushing mechanism for the thermodynamic imidazolium-carboxylate adduct.

Experimental results via Tafel, EIS, and XPS now support the probable formation and adsorption of this adduct; there is an impurity adsorbed which blocks charge transfer and increases resistivity, and the adduct offers an ideal oxidative environment for the 401.3 eV component. To confirm that the identity of the 401.3 eV, surface characterization of the adduct itself was necessary. Characterization required the synthesis and subsequent BE standards obtained via XPS to confirm the nitrogen oxidation environment for imidazolium-carboxylate. Further, this will also provide insight on if the 399.3 eV component is from decomposition or if it is its own entity.

3.3.1.5 Synthesis and Characterization of Imidazolium-Carboxylate

To confirm the identity of the 401.3 eV component featured in the N 1*s* high resolution region for the Pb cathode, imidazolium-carboxylate was synthesized from a known literature procedure.[28] ^{1}H and ^{13}C NMR characterized the isolated adduct and XPS identified its BE, in addition to any decomposition products (399.3 eV). NMR was not only beneficial in describing the purity of the isolated product, but also in providing a solution standard. This will allow for adduct detection in the cathode solution after electrolysis. This is expected to elaborate on if the adduct only forms and adsorbs to the

surface, if it adsorbs to the surface and diffuses into the solution bulk, or if it only exists in solution without adsorbing to the surface.

3.3.1.5.1 ^{1}H and ^{13}C NMR Standards

The ^{1}H and ^{13}C NMR spectra were obtained in dCD_3CN. ^{1}H NMR revealed signature structural characteristics for successful transformation of imidazolium to imidazolium-carboxylate in the aromatic region in Figure 3.13a and b respectively; (1) A loss of the C2 proton at 9.16 ppm and (2) a shift of the doublet (C4 and C5 protons) at 7.46 and 7.42 ppm to 7.17 and 7.13 ppm respectively.

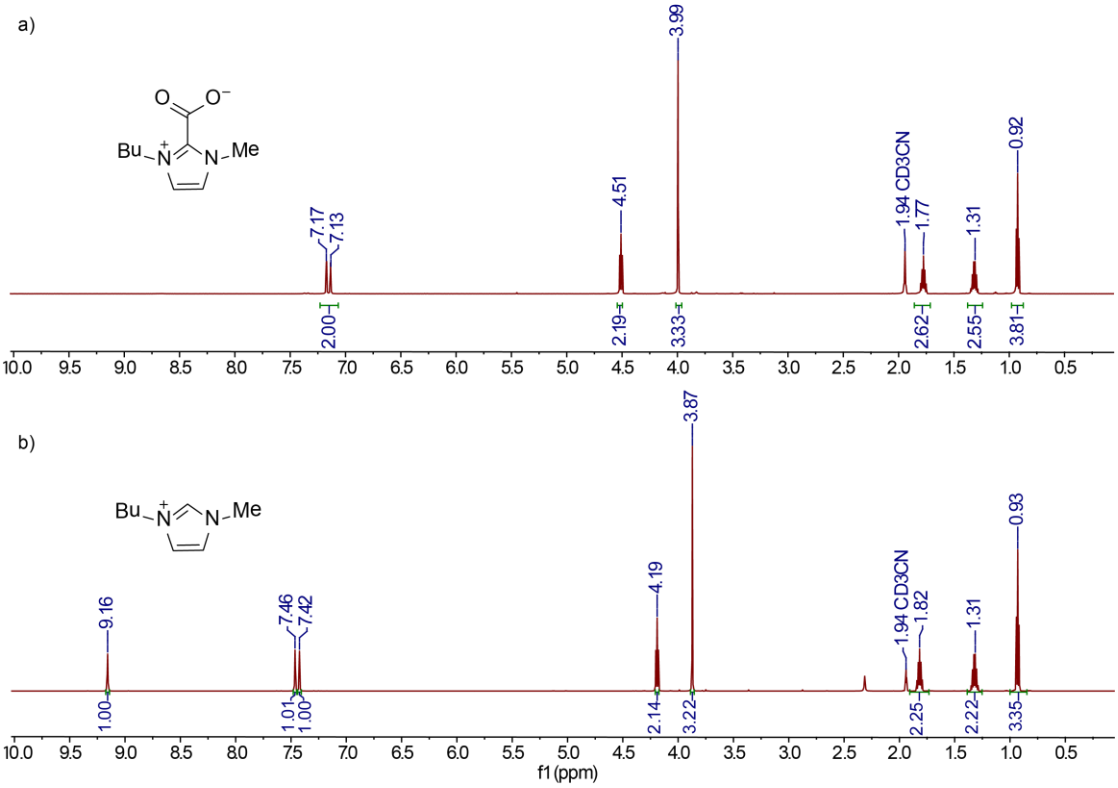

Figure 3.13. ^{1}H NMR of the a) $[BMIM]CO_2$ product and the b) [BMIM]Br starting material. NMRs obtained in dCD_3CN at 25 ºC.

Likewise, the ^{13}C NMR showed the appearance of a new C resonance at 155.34 ppm for the reaction product; 9 carbons for imidazolium-carboxylate and 8 carbons for imidazolium IL (Figure 3.14a and b respectively). This also represents a successful transformation of imidazolium to imidazolium-carboxylate.

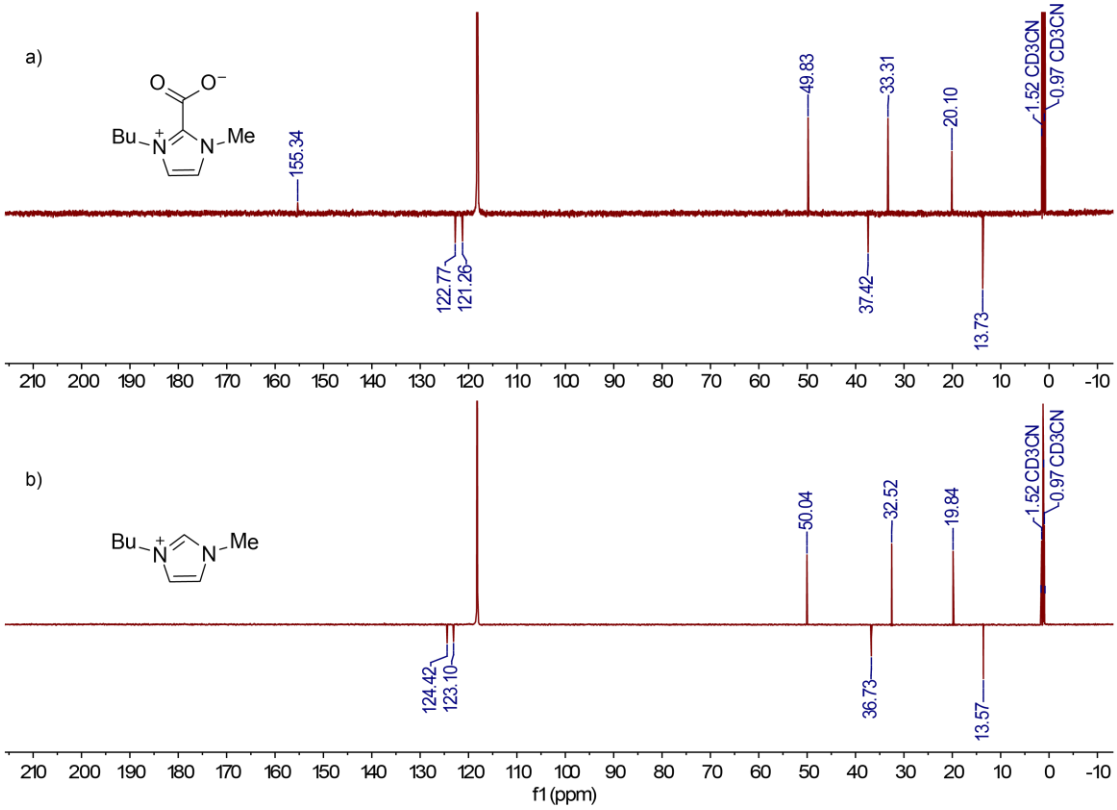

Figure 3.14. ^{13}C NMR of the a) [BMIM]CO_2 product and the b) [BMIM]Br starting material. NMRs obtained in dCD_3CN.

3.3.1.5.2 Detecting Imidazolium-Carboxylate in Cathode following Electrolysis

Having NMR standards of the imidazolium-carboxylate adduct encouraged investigation of the cathode compartment to observe if the adduct exists in solution for Bi and Sn, yet not adsorbing to the cathode surface. Additionally, it was of interest to

observe if the adduct exists in the solution for Pb, in addition to likely adsorbing onto the cathode. This study required surface modification to be performed on either glassy carbon plates (Bi and Pb) or Ni foil (Sn) opposed to the glassy carbon or Ni disk electrode. A greater surface area (0.07 cm^2 (GCE) vs. 0.7 cm^2 (plate/foil)) encourages greater quantities of product to form for heightened detection of solution products. For comparison, the cathode solution before electrolysis is shown (Figure 3.15a). The ^1H NMRs were obtained after 1 hour of electrolysis and are illustrated for Bi, Sn, and Pb in Figure 3.15b, c, and d respectively.

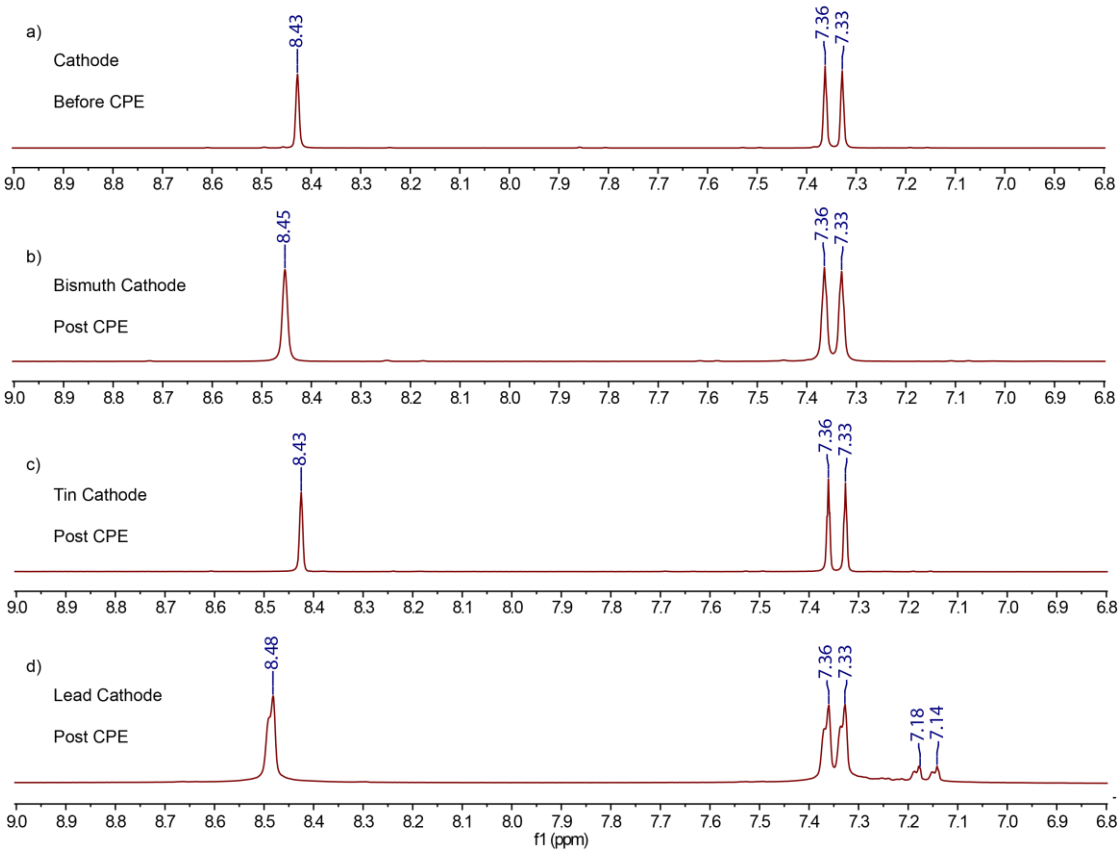

Figure 3.15. ^1H NMR of the cathode compartment after electrolysis at –1.95 V for Bi and Sn, and –2.05 V for Pb.

Bi and Sn overlaid well with the catholyte solution before electrolysis; a doublet resonance at 7.36 and 7.33 ppm (C4 and C5 protons) and a singlet with a resonance of ~8.44 ppm (C2 proton). There were no characteristic doublet resonances at 7.17 and 7.13 ppm, supporting that Bi and Sn do not favor the thermodynamic production of the adduct, neither in solution nor on the surface. Additionally, the IL does not show any signs of decomposition. The Pb cathode, however, showed a mixture of imidazolium and imidazolium-carboxylate in solution. This suggests that imidazolium-carboxylate may complicate diffusion of IL and reactants (CO_2) in the bulk, thus to further effect mass transport. This is supported by the intense decrease in current density during electrolysis.

Identifying the adduct in solution for only Pb further supports that its surface chemistry is unique. Therefore, it is critical to now observe if this adduct contributes to the complicated N 1*s* high resolution spectrum at 401.3 eV for Pb. This was studied by obtaining the XPS standard of the isolated imidazolium-carboxylate product.

3.3.1.5.3 XPS standards for the Complex N 1*s* Spectrum for Pb

The isolated imidazolium-carboxylate product (stored in N_2-filled glove box) was transferred to the XPS intro chamber using a vacuum transfer module. As illustrated in Figure 3.16a, the resulting N 1*s* spectrum showed a BE of 401.3 eV which correlates appropriately to the unidentified higher BE component for the Pb cathode (Figure 3.13f, orange trace). Detecting imidazolium-carboxylate on the Pb cathode suggested that adsorption of this species blocks charge transfer events that result in film passivation. This is the first report of imidazolium-carboxylate inhibiting CO_2 to CO heterogeneous electrocatalysis.

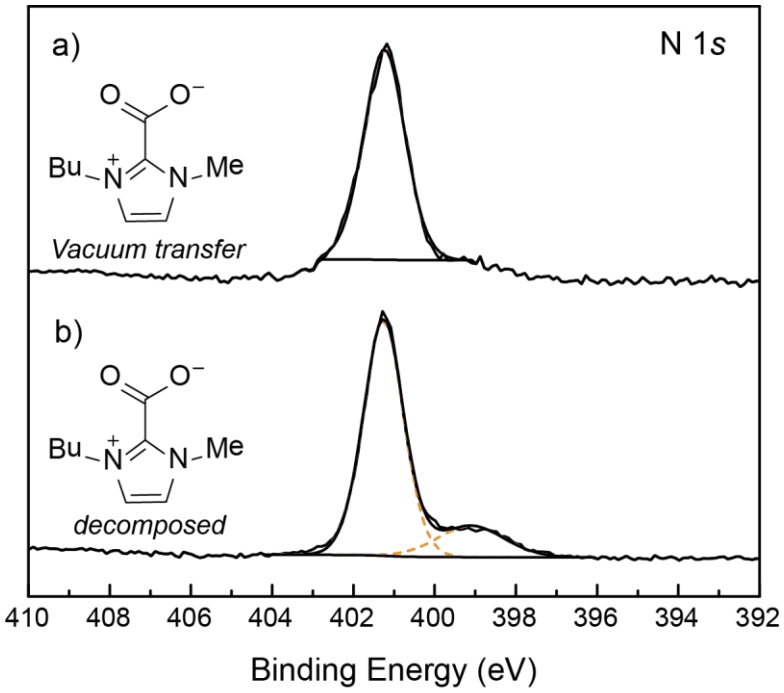

Figure 3.16. N 1*s* high resolution spectra for the synthesized imidazolium-carboxylate adduct a) when stored in a N_2 environment and b) when it is exposed to air.

To detect if the 399.3 eV component is the decomposition product of imidazolium-carboxylate, the isolated product was exposed to atmosphere and transferred to the XPS intro chamber ex situ. Two components were observed in the N 1*s* high resolution spectrum at 401.3 and 399.3 eV (Figure 3.16b). These components overlay with the observed N 1*s* components featured on the Pb cathode (Figure 3.13f, orange traces).

The 399.3 eV decomposition component is believed to have an oxidation environment like urea, such that its electronic structure suggests an electron rich environment for the nitrogen oxidation environment. This complex would likely form

through the proposed decomposition mechanism in Scheme 3.3. When the air-sensitive imidazolium-carboxylate adduct is exposed to moisture in the atmosphere, water can do a nucleophilic attack at the C2 position to ultimately remove CO_2 to yield CO, water, and 2-imidazolone.

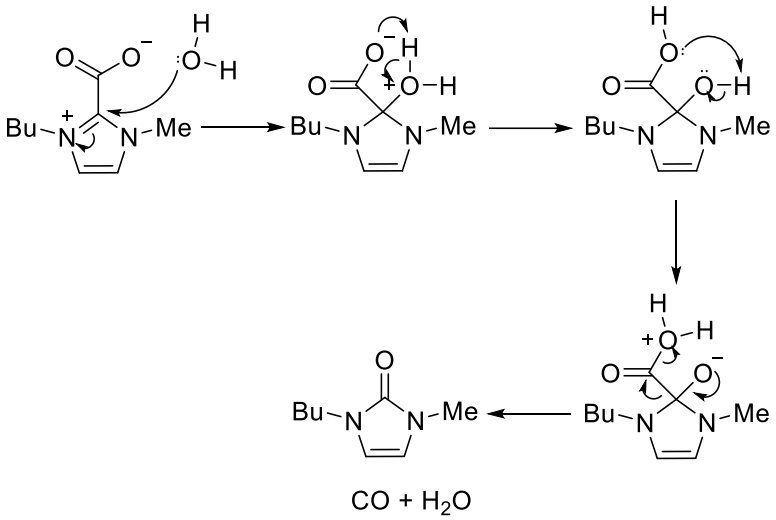

Scheme 3.3. Arrow pushing mechanism for the decomposition of imidazolium-carboxylate to urea when exposed to air

To test this theory, the 2-imidazolone complex was synthesized by known literature techniques.[29,30]. This procedure is a facile single oxidative deprotonation of imidazolium.[31] Upon developing a protocol for isolating and purifying this product, the 2-imidazolone species was characterized via NMR and XPS to obtain resonance (ppm) and BE standards respectively.

^{1}H and ^{13}C NMR were first performed to obtain the purity of the synthesized imidazolone. The ^{1}H NMR spectra illustrated a shift in resonances between the 1-butyl-

3-methyl-2-imidazolone product and the 1-butyl-3-methylimidazolium bromide starting material in Figure 3.17a and b respectively.

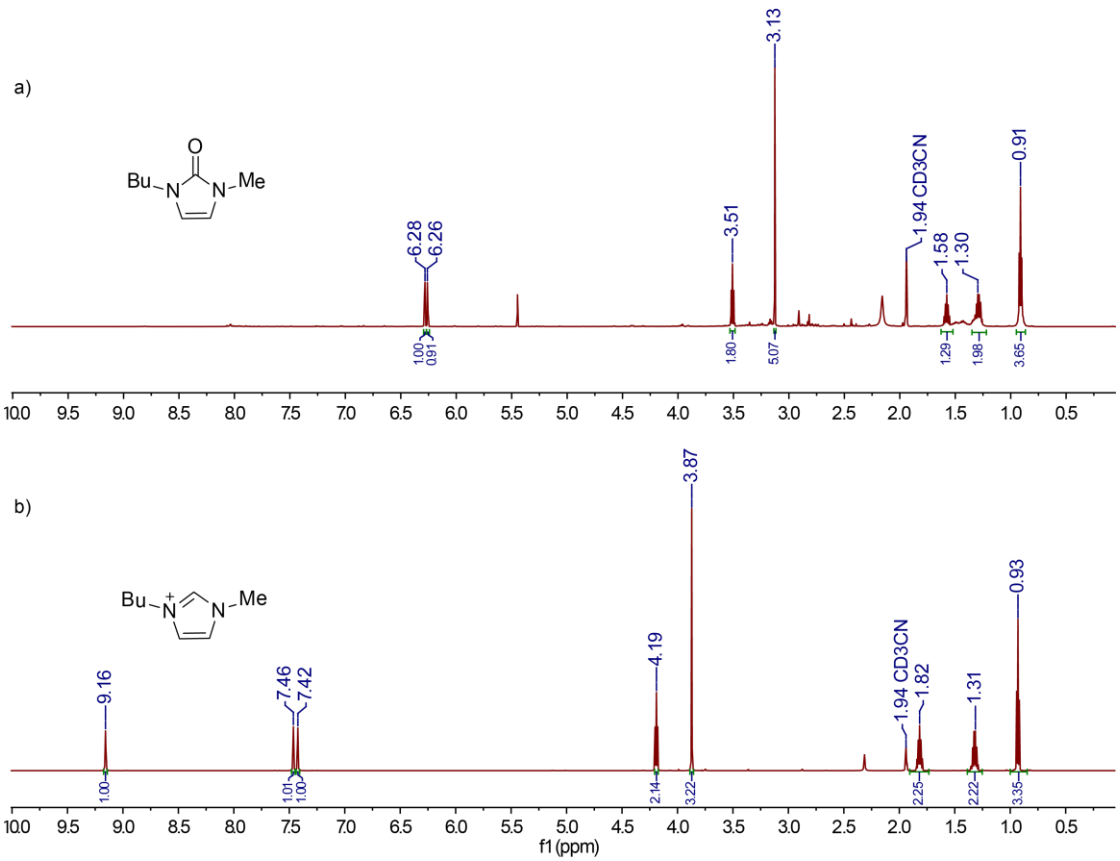

Figure 3.17. ^{1}H NMR of the a) 1-butyl-3-methyl-2-imidazolone product and the b) 1-butyl-3-methylimidazolium bromide starting material.

Importantly, the 2-imidazolone product does not show a proton resonance for the C2 proton at 9.16 ppm. The backbone C4 and C5 protons are shifted upfield to 6.28 and 6.26 ppm. Likewise, the methyl and C1 protons in the butyl chain are also shifted upfield due to the greater electron density in the ring. These shifts are also illustrated in

the ^{13}C NMRs for the 2-imidazolone product and imidazolium starting material in Figure 3.18a and b respectively.

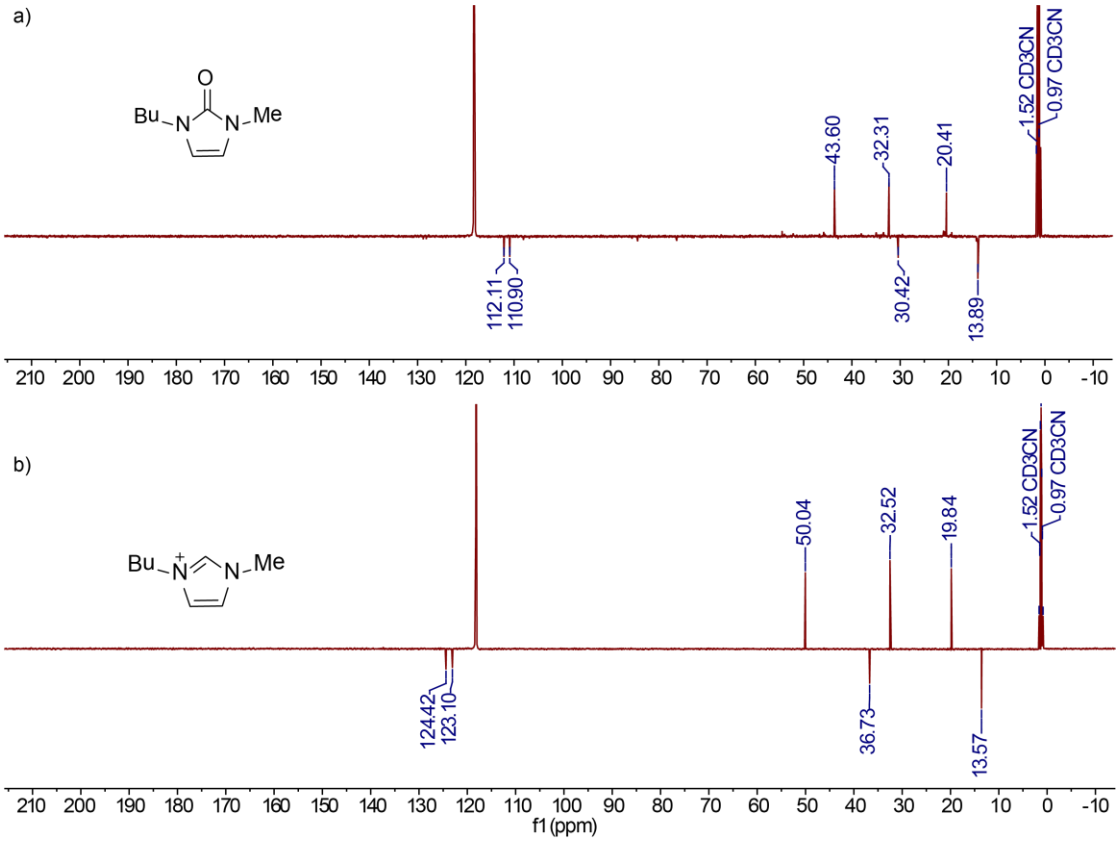

Figure 3.18. ^{13}C NMR of the a) 1-butyl-3-methyl-2-imidazolone product and the b) 1-butyl-3-methylimidazolium bromide starting material.

Having made and isolated the imidazole product with high purity, XPS was performed. Figure 3.19a illustrates the N 1*s* high resolution spectra for 2-imidazolone and its comparison to the decomposed imidazolium-carboxylate adduct (Figure 3.19b).

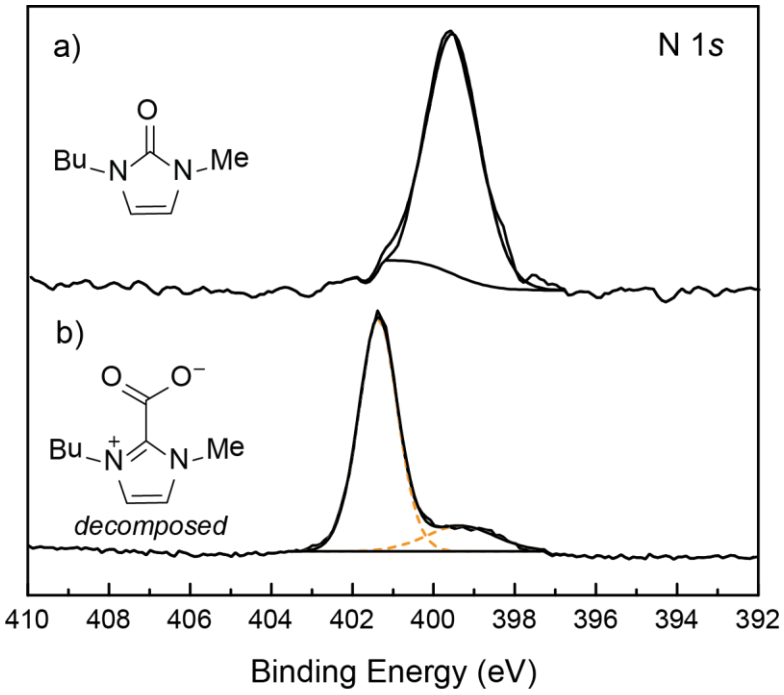

Figure 3.19. N 1*s* high resolution spectra overlay of the a) synthesized 1-butyl-3-methyl-2-imidazolone and the b) decomposed 1-butyl-3-methylimidazolium-carboxylate.

Figure 3.19a revealed a BE of 399.5 eV for the 2-imidazolone product. This BE is within error of the XPS capabilities (±0.3 eV). Decomposition was only observed after the conclusion of electrolysis and therefore does not play a role during the CO_2 to CO redox reaction. However, it is fascinating to uncover the instability of the imidazolium-carboxylate adduct into its subsequent decomposition complex.

3.3.2 Unique Mechanistic Pathway for Pb

The difference in surface adsorbates between Pb and the efficient Bi and Sn cathodes suggested that their mechanistic pathways deviate. To appreciate the differences in mechanistic pathways, it was important to first understand the $2H^+/2e^-$

mechanism for the Bi-CMEC. The following mechanism in Scheme 3.4a and b was proposed based on Tafel analysis and MD simulation performed in collaboration with the University of Michigan. The simulations and Tafel analysis supported that the first ET event is the RDS (Scheme 3.4a) to reduce surface bound CO_2 to $CO_2^{\bullet-}$. The simulations also revealed that the RDS is influenced by the addition of IL, such that the kinetic barrier was mitigated by the addition of imidazolium IL. The decrease in the kinetic barrier was suggested to be the result of IL stabilizing the electrode bias and the highly energetic $CO_2^{\bullet-}$ intermediate by Van der Waals non-bonding interactions. Therefore, the IL adsorbed on the surface (purple trace) does not participate in H^+/e^- transfers.

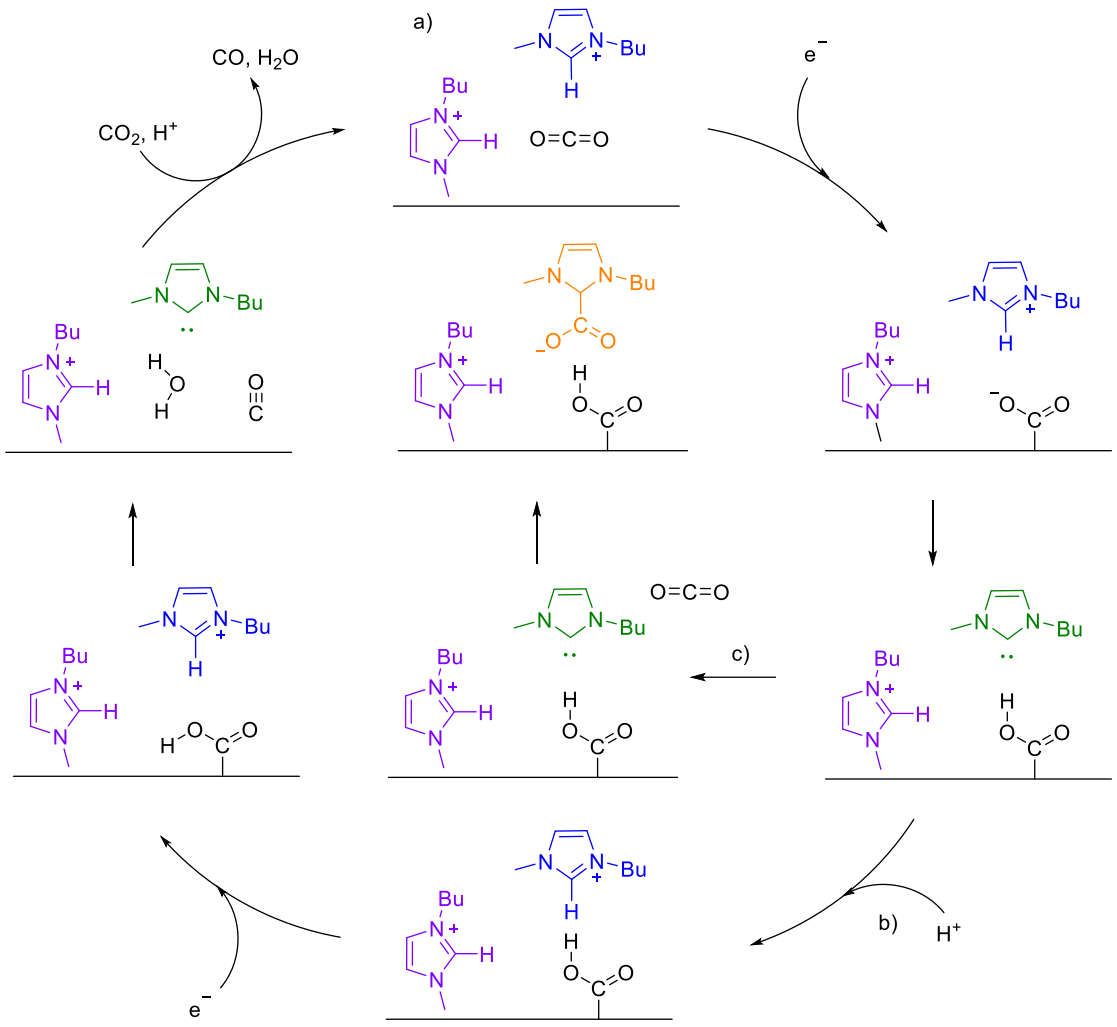

Scheme 3.4. Proposed mechanism and mechanistic deviations leading to film passivation (c) for the $2H^+/2e^-$ redox reaction for CO_2 reduction to CO for Bi, Sn, and Pb.

Following the RDS and the first proton transfer to form carboxyl and carbene, the mechanism proceeds to pathway b where IL becomes reprotonated from other nearby ILs in the solution bulk, or by protons migrating through the proton permeable Nafion membrane. The IL in the bulk (blue trace) have been calculated to have a pKa

of ~32 suggesting that these species are ideal to participate in Lewis acid/ Lewis base activity and will participate in the $2H^+/2e^-$ redox reaction.

After reprotonation of the carbene to regenerate the IL, the second H^+/e^- transfer event takes place, which are believed to occur in a similar manner. Because Bi and Sn produce similar metrics, their mechanisms are thought to be analogous. Importantly, simulations did not detect the generation of imidazolium-carboxylate in solution or on the surface.

Because Pb became passivated after only producing high CO efficiencies (83 %) for short durations, it likely proceeds through pathways a and b for minimal catalytic cycles efficiently. Because impurity adsorption of imidazolium-carboxylate was detected for Pb, film passivation likely deviates after pathway a to proceed through pathway c (Scheme 1.4c). Here, carbene nucleophilically attacks a nearby neutral CO_2 species to form the stable acid-base adduct and unaltering carboxyl. Carboxyl now exists on the surface for longer and may undergo additional surface chemistry to be transformed into more reduced carbon species not detectable within our GC detection limits.

The deviation from pathway a to c is largely influenced by the stability of the carbene.[32] After imidazolium donates a proton to yield carbene, it is sensitive/reactive and eagerly wants to alleviate the divalent C2. If the surface environment is preventing carbene from becoming reprotonated, it will capture CO_2. Formation due to limited proton availability is further enhanced by the detection of imidazolium-carboxylate in solution via ^{1}H NMR, such that the adduct in solution negatively effects mass transport.

This irreversible adsorption impurity leading to the restriction of charge transfer and reduced surface active sites was first suggested by Tafel analysis for Pb (Figure

3.2c). Here, we have identified the source of the impurity and revealed a mechanism for likely formation which deviates from efficient catalytic pathways. Impurity adsorption is likely influenced by Pb inherently binding to intermediates more strongly than Bi and Sn, and due to having a more negative applied bias to effect diffusion.[33] This is the first report for identifying the controversial behavior of imidazolium-carboxylate that deviates from what has been "accepted" in the literature.

3.4 Conclusions

The development of the general organic electrodeposition procedure contributed significantly to the existing drive to develop electrocatalysts for the CO_2 to CO redox reaction. This procedure was easily modified to incorporate a variety of inexpensive p-block metals (Bi, Sn, Pb, and Sb) in lieu using expensive transition metal catalysts. Initial electroanalytical studies via CV illustrated that while Sb was found to not be active towards CO_2 reduction, Sn and Pb demonstrated activity towards CO_2 reduction and were potential platforms for the organic electroreduction of CO_2 to CO. CPE later illustrated that Sn was nearly identical to Bi with respect to rate, energy efficiency (~70 %) and CO evolution (~80 %). Pb required a 100 mV greater overpotential to match the rate and production of CO for Bi and Sn, but the current density and CO selectivity was found to drop substantially after the first 5 minutes of electrolysis. When CPE was performed at the same overpotential as Bi and Sn, the current density was negligible (<1 mA/cm^2) and CO production was reduced by half. It was curious to understand why the Pb cathode became passivated so quickly, and why Pb required a greater overpotential than Sn and Bi.

Tafel analysis was performed to first observe if Pb goes through the same rate determining ET event as Bi and Sn. The first linear sweep revealed a Tafel slope of 126

mV dec^{-1} suggesting that the RDS is the first ET to reduce CO_2 to $CO_2^{\bullet-}$, which matches the Tafel studies performed with Bi. Continuous LSV sweeps were performed on the same Pb-modified electrode and revealed that the Tafel slope was growing larger to exceed the maximum 120 mV dec^{-1} for a two ET redox reaction. Exceeding 120 mV dec^{-1} indicates impurities adsorbing to the surface to block charge transfer events in an irreversible fashion.

EIS studies suggested that an IL adsorption phenomenon existed for Bi and Sn, but not for Pb. This suggests that the surface impurity, presented by Tafel analysis for Pb, complicates the necessary adsorption of IL to satisfy the cathode/IL interaction. Because the impurity adsorption phenomenon is not detected via EIS, the surface impurity is likely not electrochemically generated. Rather, it is a thermodynamic product that favorably forms and adsorbs only to the Pb cathode under these conditions.

XPS monitored the N 1*s* high resolution regions for Bi, Sn, and Pb surfaces both before and after electrolysis to observe the evolution of adsorbates for each cathode. All cathodes demonstrated adsorption of supporting electrolyte, imidazolium, and carbene. Interestingly, the imidazolium atomic% for Pb was greater than Bi or Sn, which implies that something is prevent IL from participating in the surface chemistry and being strongly bound to the surface. Additionally, Pb demonstrated a more complicated spectrum which included two new components located at 401.3 and 399.3 eV. XPS provided identity to these species as being imidazolium-carboxylate and 2-imidazolone (adduct decomposition product) respectively.

In addition to surface adsorption, the adduct was also identified in the Pb-cathode after electrolysis via ^{1}H NMR. Neither Bi nor Sn demonstrated the two signature resonances for this adduct at 7.18 and 7.14 ppm. For Pb, this discovery further

supported the thermodynamic formation of the adduct and identified it as being adsorbed to the surface while also existing in the solution bulk. Like complicated charge transfer events at the surface, the adduct in the cathode solution likely interferes with diffusion and contributes to poor proton transfer events. Limited proton transfer likely encourages additional adduct formations.

Based on the detection of the adduct with the passivation of the Pb cathode, the validity of current knowledge regarding the imidazolium-carboxylate adduct was questionable. These studies point towards the adduct being a thermodynamic sink, such that it is stable and irreversible within our redox potentials. Despite confidently identifying the adsorption impurity, a thorough investigation on the electrochemical behavior of the adduct itself was necessary. Understanding its electrochemical behavior will provide clarity to the previously discussed experiments and will support if the adduct truly complicates catalysis. Now having a method to synthetically prepare the adduct, in addition to having XPS and NMR standards to allow for precise identification during experimentation, electroanalytical studies can be performed on the adduct itself to probe for its true behaviors during the CO_2 to CO heterogeneous electrocatalysis, i.e. effect on current density, CO evolution, onset potential, etc. Screening the electrochemical behavior of the adduct would be a significant contribution for electrocatalyst design and provide valuable insight on the CO_2 to CO mechanistic pathway.

REFERENCES

(1) Kumar, B.; Brian, J. P.; Atla, V.; Kumari, S. Bertram, K. A.; White, R. T.; Spurgeon, J. M. *Catalysis Today*. **2016**, *270*, 19—30.

(2) Whipple, D. T.; Kenis, P. J. A. *Journal of Physical Chemistry Letters*. **2010**, *1*, 3451—3458.

(3) Morris, A. J.; McGibbon, R. T.; Bocarsly, A. B. *ChemSusChem*. **2011**, *4*, 191—196.

(4) Sun, L.; Ramesha, G. K.; Kamat, P. V.; Brennecke, J. F. *Langmuir*. **2014**, *30*, 6302—6308.

(5) Cheek, G. T.; Roeper, D. F.; Pearson, W.; O'Grady, W. E. *ECS Transactions*. **2014**, *64*, 161—160.

(6) Medina-Ramos, J.; DiMeglio, J. L.; Rosenthal, J. *Journal of the American Chemical Society*. **2014**, *136*, 8361–8367.

(7) Medina-Ramos, J.; Pupillo, R. C. Keane, T. P.; DiMeglio, J. L.; Rosenthal, J. *Journal of the American Chemical Society.* **2015**, *137*, 5021—5027.

(8) Noel, M.; Vasu, K. I. *Cyclic Voltammetry and the Frontiers of Electrochemistry*; Oxford & IBH: Janpath, New Delhi, 1990.

(9) Rosen, B. A.; Haan, J. L.; Mukherjee, P.; Braunschweig, B.; Zhu, W.; Salehi-Khojin, A.; Dlott, D. D.; Masal, R. I. *Journal of Physical Chemistry C*. **2012**, *116*, 15307—15312.

(10) Sun, L.; Ramesha, G. K.; Kamat, P. V.; Brennecke, J. F. *Langmuir*. **2014**, *30*, 6302—6308.

(11) Hollingsworth, N.; Taylor, S. G. R.; Galante, M. T.; Jacquemin, J.; Longo, C.; Holt, K. B.; de Leeuw, N. H.; Hardacre, C. *Angewandte Chemie International Edition.* **2015**, 54, 14164—14168.

(12) Lim, H.; Kim, H. *Molecules*. **2017**, *22*, 536.

(13) Benson, E. E.; Kubiak, C. P.; Sathrum, A. J.; Smieja, J. M. *Chemical Society Reviews*. **2008**, *38*, 89−99.

(14) Matsubara, Y.; Grills, D. C.; Kuwahara, Y. *ACS Catalysis*. **2015**, *5*, 6440—6452.

(15) Maeda, C.; Miyazaki, Y.; Ema, T. *Catalysis Science and Technology*. **2014**, *4*, 1482—1497.

(16) Shinagawa, T.; Garcia-Esparza, A. T.; Takanabe, K. *Nature*. **2015**, *5*, 13801.

(17) DiMeglio, J. L.; Rosenthal, J. *Journal of the American Chemical Society.* **2013**, *135*, 8798–8801.

(18) Gattrell, M.; Gupta, N.; Co, A. *Journal of Electroanalytical Chemistry*. **2006**, *594*, 1.

(19) Town, J. L.; MacLaren, F.; Dewald, H. D. Rotating Disk Voltammetry Experiment. *Journal of Chemical Education.* **1991**, *68*, 352—354.

(20) Kellogg, H. H. *Journal of Metals*. **1951**, *191*, 137—141.

(21) Wuttig, A. Liu, C.; Peng, Q.; Yaguchi, M.; Hendon, C. H.; Motobayashi, K.; Ye, S.; Osawa, M.; Surendranath, Y. *ACS Central Science.* **2016**, *2*, 522—528.

(22) Standard Thermodynamic Properties of Chemical Substances. CRC Press LLC, 2000.

(23) Salimon, J.; Hamzah, S.; Mohamad, M.; Ibrahim, H. N.; Yamin, B. M. *Science International*. **2003**, *14*, 325—329.

(24) Højberg, J.; McCloskey, B. D.; Hjelm, J.; Vegge, T.; Johansen, K.; Norby, P.;Luntz, A. C. *ACS Applied Materials and Interfaces*. **2015**, *7*, 4039.

(25) Brug, G. J.; Van Den Eeden, A.; Sluyters-Rehbach, M.; Sluyters, J. H. *Journal of Electroanalytical Chemistry*. **1984**, *176*, 275—295.

(26) De Levie, R.; Pospíšil, L. *Journal of Electroanalytical Chemistry*. **1969**, *22*, 277—290.

(27) Jorcin, J.; Orazem, M. E.; Pébère, N.; Tribollet, B. *Electrochimica Acta.* **2006**, *51*, 1473—1470.

(28) Zhou, H.; Zhang, W.Z.; Liu, C. H.; Qu, J. P.; Lu, X. B. *Journal of Organic Chemistry*. **2008**, *73*, 8039—8044.

(29) Islam, M. M.; Imase, T. Okajima, T.; Takahashi, M.; Niikura, Y.; Kawashima, N.; Nakamura, Y.; Ohsaka, T. *Journal of Physical Chemistry A.* **2009**, 113, 912—916.

(30) AlNashef, I. M.; Hashim, M. A.; Mjalli, F. S.; Al-haj Ali, M. Q.; Hayyan, M. *Tetrahedron Letters*. **2010**, *51*, 1976—1978.

(31) Liu, B. Zhang, Y.; Xu, D.; Chen, W. *Chemical Communications.* **2011**, *47*, 2883—2885.

(32) Feroci, M.; Chiarotto, I.; Forte, G.; Ciprioti, S. V.; Inesi, A. *ChemElectroChem Articles*. **2014**, *1*, 1407—1414.

(33) Kortlever, R.; Shen, J.; Scouten, K. J. P. Calley-Vallejo, F.; Koper, M. T. M. *Journal of Physical Chemistry Letters*. **2015**, *6*, 4073—4082.

Chapter 4

UNCOVERING THE TRUE CATALYTIC BEHAVIOR FOR THE MISINTERPRETED IMIDAZOLIUM-CARBOXYLATE ADDUCT

4.1 Introduction

Fossil fuels have dominated our global energy profile for decades and are a major contributor towards the rising atmospheric CO_2 levels.[1] Environmental warning signs, i.e. extreme weather, climate change, and encroaching oceans, have become prevalent and suggest that we are at a critical tipping point to make the switch from fossil fuels to renewables.[2] Heterogeneous CO_2 to CO electrocatalysis has received much attention due to being a promising carbon-neutral platform for lessening our rising atmospheric CO_2 contributions.[3,4] Electrochemically transforming CO_2 to CO is a simple $2H^+/2e^-$ redox reaction where CO is a versatile product to produce a slew of more reduce hydrocarbon synthetic fuels via the Fischer-Tropsch process. The Fischer-Tropsch process is an established reaction leaving most research towards catalyst development for this endergonic transformation.

A key feature in developing an efficient catalyst, is understanding the mechanistic pathway by which catalysis proceeds.[5] Ideally for heterogeneous redox reactions, the catalyst satisfies the Sabatier principal where it will bind to the reactants and products optimally. Understanding how the catalyst binds to those intermediates, and what those intermediates are, is critical for appropriate catalyst design.[6]

Our work recently explored the mechanistic differences between three cathode materials; Bi-, Sn-, and Pb-modified electrodes.[7] These catalytic systems were mediated

by the incorporation of imidazolium-based ionic liquids (ILs). While Bi- and Sn-carbon monoxide evolving catalysts (CMECs) were promising platforms for CO_2 to CO electrocatalysis, Pb demonstrated film passivation that sacrificed CO evolution, current density, and energy efficiency. Vigorous surface and solution phase studies were performed to understand the mechanistic differences leading to the deviated metrics for Pb. Ultimately, an adsorption impurity was found for Pb, but not for the Bi or Sn cathodes (See Chapter 3), which was believed to be the source of film passivation. Interestingly, the impurity was identified as the same intermediate highlighted in literature to decrease the overall kinetic energy barrier, an imidazolium-carboxylate adduct (Chapter 3, Figure 3.1). This contradiction triggered further study to understand this discrepancy between our experimental results and published literature accounts.

Imidazolium-carboxylate is believed to be an essential intermediate for CO_2 to CO electrocatalysis.[8] Literature hypotheses state that the adduct forms when imidazolium bound to the surface stabilizes the high-energy CO_2 radical anion ($CO_2^{\bullet-}$) after the first electron transfer (ET) rate determining step (RDS).[2,9] This is illustrated in Scheme 4.1. Published work documented this adduct as being an essential intermediate towards encouraging enhanced efficiency and activity towards CO_2 reduction to CO.[10,11] The hypotheses in the literature also state that if the $CO_2^{\bullet-}$ species does not form a complex with imidazolium, thus to lower the activation energy, catalysis will not occur.

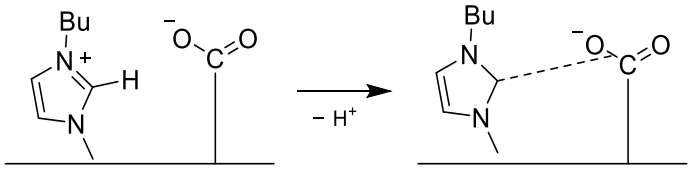

Scheme 4.1. General literature scheme for the essential formation of imidazolium-carboxylate.[8,10]

The stabilization of the $CO_2^{\bullet-}$ intermediate is critical towards catalysis. However, initial mechanistic studies for Bi-CMEC found fault with the proposed adduct formation in regards the surface bound imidazolium participating in surface chemistry to form the adduct. MD calculations performed in collaboration with the University of Minnesota suggested that the surface bound imidazolium serves two purposes; (1) to neutralize the negative applied bias and (2) to stabilize the high-energy $CO_2^{\bullet-}$ by Van der Waals interactions. Despite the surface bound imidazolium acting as a Lewis acid to stabilize $CO_2^{\bullet-}$, it does not lose its C2 proton. This is based on its high calculated pKa value. Therefore, it is suggested that only imidazolium in the solution bulk or near the electrode surface (pKa of ~32 in MeCN) can donate protons towards the $2H^+/2e^-$ redox reaction. Further, MD calculations provided no evidence of the resulting carbene nucleophilically attacking $CO_2^{\bullet-}$ on the surface for Bi-CMEC under typical electrolysis conditions.

Regardless of this mechanistic discrepancy for the formation of surface bound imidazolium, prior publications also stated that there is a reversible exchange between carbene and imidazolium-carboxylate, shown in Scheme 4.2, to allow for such a stabilization.[10,11]

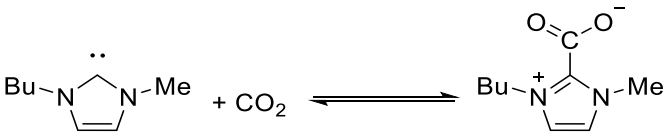

Scheme 4.2. Reversible reaction scheme of the carbene and imidazolium-carboxylate adduct proposed by previous literature.[10,11]

In contrast to the proposed equilibria, our previous electroanalytical studies performed with Pb, i.e. Tafel analysis, suggested that the adduct is irreversible and

thermodynamically stable. Tafel revealed that the formation of this impurity is favored based on non-ideal ET ($\alpha < 0.5$) events, where upon formation creates a thermodynamic sink (See Chapter 3).[12] As Tafel analysis suggested, the adsorption of this impurity interferes with charge transfer events and ultimately leads to film passivation. Therefore, if imidazolium were to form a stabilizing bond to $CO_2^{\bullet-}$, this species would not be reduced back unless more negative potentials are applied. Further, this would now jeopardize the energy cost of catalysis.

Our studies advocate adduct formation only when the carbene cannot become readily protonated as a means for stabilization, i.e. low proton availability, poor diffusion, etc. For example, if the highly reactive carbene cannot readily become reprotonated near the electrode surface (where the chemistry occurs), it will likely interact with neutral CO_2 which saturates the solution to form the robust imidazolium-carboxylate adduct. This is illustrated in Scheme 4.3. Catalytic conditions where diffusion or proton availability is poor can occur when a more negative bias is applied to result in a greater interaction between intermediates and substrate, in that these are potential dependent interactions.[13] Additionally, the greater attraction can also occur when the cathode material inherently binds to intermediates more strongly, such as for Pb.[14] Here, activating the intermediate to leave the surface limits the rate of reaction for catalysis, and ultimately charge transfer.[6] Therefore, when testing materials for heterogeneous catalysis, it would be ideal to find a catalyst that does not stabilize intermediates so strongly, yet is not limited by desorption of intermediates. This observation is critical for progressing catalyst design.

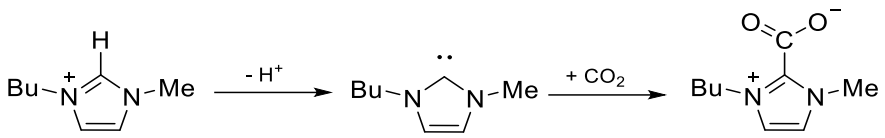

Scheme 4.3. Scheme describing imidazolium donating its proton to form carbene where upon Lewis acid/base chemistry the carbene reacts with CO_2 to form imidazolium-carboxylate.

Based on these conflicting hypotheses, it was imperative to discover the true mechanistic behavior of this adduct. To study the behavior of this adduct for our electrocatalytic system, a series of electrochemical studies were performed to understand its reversibility, effect on current density (rate) and activity for CO_2 reduction, and ultimately its effect on the RDS. These studies were performed with our Bi, Sn, and Pb platforms. Additionally, we were also curious if the adduct can exist in solution while remaining inert towards the surface redox events, specifically for the Bi and Sn systems.

4.2 Experimental Method

4.2.1 Materials and Methods

Reagents and solvents were purchased from Sigma Aldrich, Alfa Aesar, Acros or Fisher. Bismuth(III) trifluoromethanesulfonate was purchased from Aldrich, and tin(II) trifluoromethanesulfonate and lead(II) oxide 99.999 % puratrem were purchased from Strem Chemicals. Imidazolium ionic liquid 1-butyl-3-methylimidazolium trifluoromethanesulfonate ([BMIM]OTf) ≥ 98 % was purchased from Sigma Aldrich. Tetrabutylammonium hexafluorophosphate ($TBAPF_6$) was purchased from TCI

America and purified by recrystallization with ethanol. Carbon dioxide (CO_2) was purchased from Keen Compressed Gas Company.

Platinum gauze (99 %) was purchased from Sigma Aldrich. The bare glassy carbon disc electrode, bare Ni disc electrode, and the Ag/AgCl reference electrode were purchased from CHI Instruments. Graphite plates were purchased from Ohio Carbon and Ni foil was purchased from Sigma Aldrich.

4.2.2 Instrumentation

4.2.2.1 Electrochemical Measurements

Electrochemical studies were conducted using a CHI-620D potentiostat/galvanostat or a CHI-720D bipotentiostat. Electrochemical apparatus consisted of a three-electrode system; working (bare glassy carbon disc (3.0 mm diameter), bare nickel disc (3.0 mm diameter), bare graphite plate (~1 cm x 1.0 cm x 0.1 cm), bare Ni foil (~1 cm x 1cm x 0.00125 cm)), counter (platinum gauze), and a reference electrode (Ag/AgCl (1.0 M KCl)). Cyclic voltammetry and linear voltammetry experiments were performed with iR drop compensation with 100 mV s^{-1} scan rate. Ag/AgCl reference was converted to SCE referencing by the equation, $E_{SCE} = E_{Ag/AgCl} + 0.044$ V.

4.2.2.2 Electrochemical Impedance Spectroscopy

Electrochemical impedance spectroscopy (EIS) was performed using a CHI-720D bipotentiostat. Electrochemical apparatus consisted of a three-electrode system; working (bare glassy carbon disc (3.0 mm diameter), bare nickel disc (3.0 mm diameter), Ni foil (~1 cm x 1 cm x 0.00125 cm), graphite plate (~1 cm x 1 cm x 0.1

cm)), counter (platinum gauze), and a reference electrode (Ag wire)). Frequency ranged from 0.1 Hz to 100 000 Hz.

4.2.2.3 X-ray Photoelectron Spectroscopy

XPS analysis was performed using a Thermo Scientific K-alpha^{+} spectrometer with monochromatic Al Kα X-ray (1486.7 eV) and 72 W of power (12 kV, 6 mA) equipped with a 128 CCD detector plate. Operating vacuum pressure in the main chamber was less than $1x10^{-8}$ torr. XPS survey scans were collected with a step size of 1.0 eV and a pass energy of 100 eV. High resolution spectra were collected with a step size of 0.1 eV and a pass energy of 20 eV. The X-ray spot size was an elliptical shape with a semi-major axis of approximately 400 μm.

4.2.2.4 CO_2 Reduction Electrolysis and Headspace Analysis

Current densities were obtained by performing controlled potential electrolysis (CPE) on a sealed two-compartment electrochemical cell with the cathode and anode separated by a proton permeable Nafion membrane (NRE-212). The anode and cathode compartment both contained 20 mL of electrolyte solution; 0.1 M ionic liquid and/or 0.1 M $TBAPF_6$ that was dissolved in CO_2 saturated MeCN. The solution was sparged for 30 minutes.

During CPE, the cathode was stirred at a steady rate while there was a continuous flow of CO_2 into the headspace (5 mL min^{-1}). The cathode was vented directly into a flow gas chromatograph (SRI Instruments, SRI-8610C). A chromatograph was obtained every 15 min throughout the duration of electrolysis by placing the sampling loop in line with a packed HayeSep D column and a packed mole Sieve 13X column. The columns led directly to a thermal conductivity detector (TCD)

and a flame ionization detector (FID) equipped with a methanizer to quantify hydrogen and carbon monoxide production respectively. The gas carrier was Argon (Keen, 99.999 %).

4.2.2.5 Solvent Suppression ^{1}H NMR

Solvent suppression ^{1}H NMR was performed with aliquots from the cathode solution to detect any solution products from electrolysis and/or decomposition of electrolyte solution. The acetonitrile resonance was suppressed at 1.96 ppm. Formic acid production was monitored at 8.1 ppm and imidazolium-carboxylate adduct was monitored at 7.17 and 7.13 ppm. Samples were prepared in d-MeCN (purchased from Alfa Aesar).

4.2.3 Synthetic Protocols

4.2.3.1 Lead (II) trifluoromethansulfonate

Lead(II) oxide was reacted with excess triflic acid in correspondence to a modified literature procedure. A Schlenk flask, equipped with lead oxide (2.0029 g), triflic acid (4 mL) and 40 mL dry toluene. The mixture was heated at 110 ºC under N_2 for 5 hrs. The Schlenk flask was transferred to a N_2-filled glove box upon the removal of solvent and a slightly reduced pressure. The crude product was dissolved in acetonitrile and filtered through celite. The filtrate was then concentrated under vacuum to yield the resulting off-white powder in a 62 % yield. ^{19}F NMR (376 MHz, dCD_3CN, 25 ºC) δ/ ppm= –78.67.

4.2.3.2 1-butyl-3-methaneimidazolium carboxylate

In a N_2-filled glove box, we suspended 1-methyl-3-butylimidazolium bromide ([BMIM]Br; purchased from Alfa Aesar) in dried toluene and let it react with sodium hexamethyldisilizane (NaHMDS; purchased from Sigma Aldrich) for 2 hrs. This solution was filtered through celite and the filtrate, carbene, was sparged with CO_2 gas for 0.5 hr. This solution underwent a second filtration step where the product was collected as a white precipitate in a 78 % yield.

4.2.4 Electrodeposition of Bi, Sn, and Pb

Prior to electrodeposition, the nickel disc electrode (3.0 mm diameter), carbon disc electrode (3.0 mm diameter), or graphite plate (~1 cm x 1.0 cm x 0.1 cm) was polished with 0.05 micron alumina powder in Millipore water and then sonicated in Millipore water for five minutes to remove residual powder. If starting with Ni foil (~1 cm x 1.0 cm x 0.00125 cm), it was sonicated in water, acetone, and lastly acetonitrile for 20 minutes for each step to remove excess oils. The substrate was then submersed in an acetonitrile organic electrolyte solution containing 0.02 M of the respective triflate metal and 0.1 M $TBAPF_6$ saturated with N_2. A series of cyclic voltammetry sweeps (10 cycles, 100 mV s^{-1}) were performed with applied potentials ranging from –0.25 to –2.25 (V) vs. SCE. Following the electrode conditioning, the GCE/Ni disc was agitated to remove exfoliated material formed on the electrode surface. Using the same electrolyte solution, controlled potential electrolysis (CPE) applied a constant potential of –1.35 for $Bi(OTf)_3$, –0.55 V for $Sn(OTf)_2$, and –1.35 (V) vs. SCE for Pb until a total of ~1 C cm^{-2} was passed. The modified electrode was rinsed with acetonitrile followed by a drying step consisting of a gentle N_2 flow over the modified surface.

4.3 Results and Discussions

Imidazolium-carboxylate was synthesized using known literature techniques to effectively characterize its catalytic behavior.[15,16] Having a method to prepare the adduct synthetically and having XPS and NMR standards allowed for precise identification upon experimentation. The adduct was incorporated into electroanalytical studies via titrations, as an added component in the electrolyte solution (1:1 equivalent to imidazolium, 0.1 M), and as a substitute for imidazolium (no [BMIM]OTf). The range of experimental conditions are anticipated to provide a clear understanding of its behavior during electrolysis to either confirm or discredit published theories.

Specifically, the reversibility of the adduct was investigated with linear sweep voltammetry (LSV), its effects on electrolysis were studied with controlled potential electrolysis (CPE), the evolution of adsorbates on the cathode surface was monitored with X-ray photoelectron spectroscopy (XPS), and deviations in charge transfer events were monitored via electrochemical impedance spectroscopy (EIS) for the Bi, Sn, and Pb cathodes.

4.3.1 Observing the Reversibility of Imidazolium-Carboxylate

The reversibility of the adduct was studied with LSV to observe its experimental redox potential. The literature states that the adduct exists in equilibrium with carbene. Based on the thermodynamic stability for the adduct, however, the adduct would need to be electrochemically reduced for this equilibrium to hold true. If the potential applied for CPE is not at the appropriate overpotential to encourage the reduction of imidazolium-carboxylate, the complex will remain stable during electrolysis.

For these studies, the electrolyte solution consisted of 100 mM imidazolium-carboxylate and 100 mM supporting electrolyte ($TBAPF_6$) in CO_2 saturated MeCN.

Potentials ranged from –1.55 to –2.95 (V) vs. SCE (all potentials will be referred to this reference) for Bi (black trace), Sn (red trace), and Pb (blue trace) as shown in Figure 4.1. Here, imidazolium is absent from the electrolyte solution. The reduction of CO_2 is not likely to occur without a proton source. Therefore, the only cathodic feature expected within this spectral window should be the reduction of the adduct.

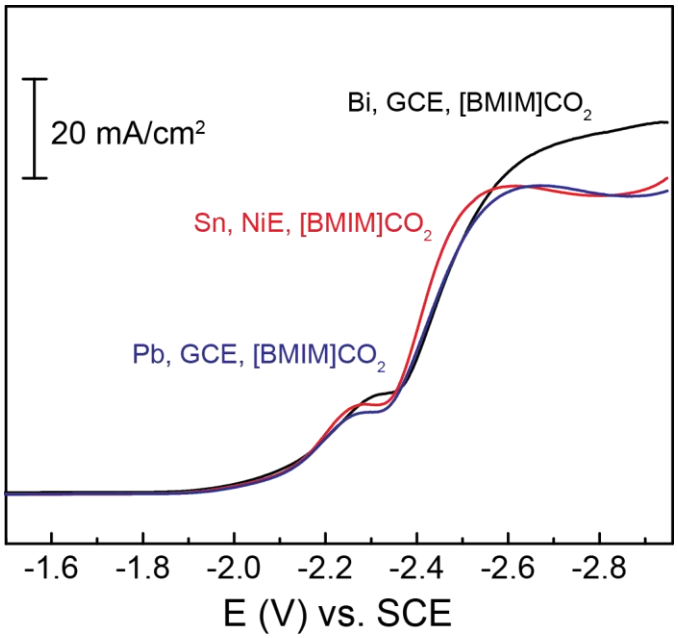

Figure 4.1. Overlaid linear sweep voltammograms for the Bi, Sn, and Pb cathodes in CO_2 saturated MeCN with 0.1 M $TBAPF_6$ and 0.1 M $[BMIM]CO_2$.

The current responses for each cathode showed negligible current from –1.5 to –2.05 V. This suggested that CO_2 reduction does not occur without the imidazolium proton source. The first cathodic peak has an onset potential of ~ –2.1 V and a peak maximum of ~ –2.3 V. This is the observed redox event for the adduct.

The cathodic feature at ~ –2.55 V is reduction of solvent, as the electrochemical window for MeCN is exceeded.

The first observed redox event is significant such that it discredits the adduct existing in an equilibrium with carbene. There is ~300 mV difference between the applied potential for catalysis and the potential at which the adduct is reduced. This is a significant overpotential and suggests that the formation of the adduct is irreversible during catalysis for our applied potentials. The irreversibility of the adduct is critical, such that upon formation it will act as a thermodynamic sink. Additional adduct formations will decrease imidazolium concentration because its formation shifts the equilibria towards its formation (See Chapter 3). Fewer imidazolium protons results in the lower current densities observed: lower proton availability for the $2H^+/2e^-$ redox reaction.

4.3.2 Detecting the Influence of the Adduct for CO_2 Reduction Activity

Understanding that the adduct formation is irreversible during electrolysis, it was curious to observe if its presence in the electrolyte solution has a direct effect on CO_2 reduction activity. Specifically, it was of interest to observe if additions of imidazolium-carboxylate will shift the equilibrium to favor further adduct formations, thus to lower the imidazolium concentration and ultimately reducing CO_2 reduction activity. Alternatively, it was curious if adduct additions would have no effect (inert) or a positive effect (enhancement) for CO_2 reduction activity. A positive effect would suggest that the adduct plays a role in the mechanism for the stabilization the intermediate ($CO_2^{\bullet-}$), as suggested by the literature.

LSV was used to probe for deviations in CO_2 reduction activity. Bi-, Sn-, and Pb-modified electrodes were submersed in 100 mM imidazolium and 100 mM $TBAPF_6$

in CO_2 saturated MeCN. Aliquots of imidazolium-carboxylate were titrated into the electrolyte solution up to 1 equivalent (100 mM). Deviations in current response, in addition to shifts in onset potential were monitored.

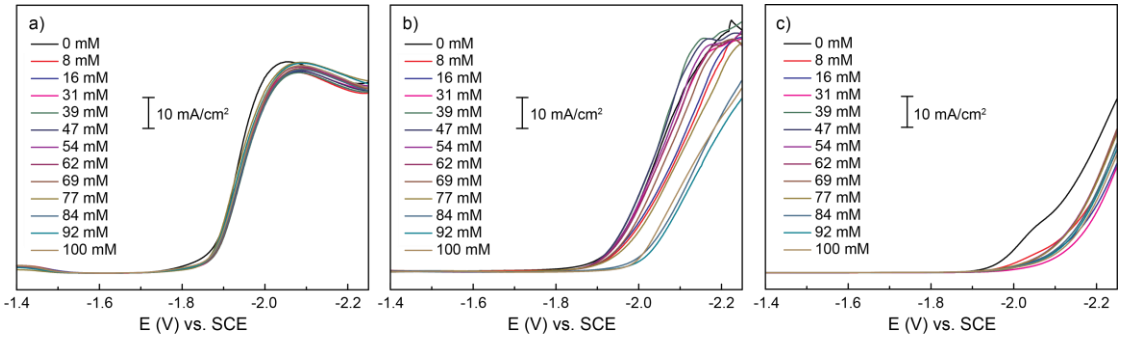

Figure 4.2. Linear sweep voltammograms for a) Bi, b) Sn, and c) Pb upon titrations of imidazolium carboxylate into 100 mM [BMIM]OTf and 100 mM $TBAPF_6$ in CO_2 saturated MeCN.

The LSV titrations are summarized in Figure 4.2. The voltammogram in Figure 4.2a illustrates the adduct titration for Bi, which suggested that the adduct is inert towards CO_2 reduction activity. The polarization curve retains its shape and the onset potential at ~ –1.85 V. Sn showed greater deviation in its current response compared to Bi (overpotential shift of ~150 mV), but still maintains high CO_2 reduction activity (Figure 4.2b). The polarization curve for Sn demonstrated that the adduct is slightly jeopardizing CO_2 reduction activity, but not so much as to poison catalysis. Pb displayed the most extreme deviation in current response (Figure 4.2c), such that upon the first addition of the adduct (8 mM, red trace) catalysis shut down. There was no longer a cathodic feature indicative of CO_2 reduction. This demonstrated how the cathode material significantly influences adsorbate interactions during catalysis. Importantly,

neither cathode demonstrated enhanced reduction activity due to greater concentrations of imidazolium-carboxylate in solution.

These observations discredit the belief that the adduct plays a stabilizing role during catalysis to lowering the kinetic barrier for the rate determining ET step. While the adduct was relatively inert towards the Bi cathode, it resulted in complete cathode passivation for Pb and demonstrated a slightly greater energy cost for Sn. Unlike Pb, Bi and Sn must therefore preserve active sights for the adsorption of imidazolium to promote catalysis. If the adduct were to stabilize the $CO_2^{\bullet-}$, a rise in current or a decrease in overpotential would be observed once the complex was added via titrations. This insinuated that the adduct does not function as it is believed to in the literature. Notably, this belief assumed that imidazolium-carboxylate was in a reversible exchange with the carbene, which was previously discredited (Figure 4.1).

Ultimately, these titrations suggested that imidazolium-carboxylate does not favorably adsorb to the Bi- or Sn-modified surfaces to interfere with charge transfer events. This surface interaction would later be studied via XPS. In correspondence with reduction activity, however, it was curious if the adduct effects electrolysis (CO selectivity, current density, etc.) upon the reduction of CO_2 despite appearing inert towards CO_2 reduction activity for Bi and Sn cathodes.

4.3.3 Monitoring Deviations in CPE with Intentional Adduct Incorporation

Noting how imidazolium-carboxylate remained relatively inert towards CO_2 reduction activity for Bi and Sn, while completely suppressing reduction activity for Pb, it was of interest to see if these behaviors persist during electrolysis. The literature states that the adduct will enhance the catalytic rate and efficiency of CO evolution during electrolysis.[17] Therefore, the product distribution and current density were monitored

specifically. To observe the true behavior during electrolysis, a series of CPE experiments were performed where the adduct was added to the cathode compartment during electrolysis. Here, it would be clear if CO efficiency is enhanced or reduced, or if there is an abrupt change in the steady current densities upon the addition of the adduct.

CPE began with 100 mM imidazolium and 100 mM $TBAPF_6$ in CO_2 saturated MeCN with an applied potential of –1.95 V for all cathodes. Pb was run at the less negative potential so film passivation was not the primary cause of rate loss. After the rate and CO production plateaued at its published CO Faradaic efficiencies (FEs) and current densities after ~120 minutes, one equivalent (100 mM) of the adduct was added via syringe to the cathode compartment. The current densities (black traces) and CO FEs (blue traces) for Bi, Sn, and Pb are summarized in Figure 4.3a, b, and c respectively.

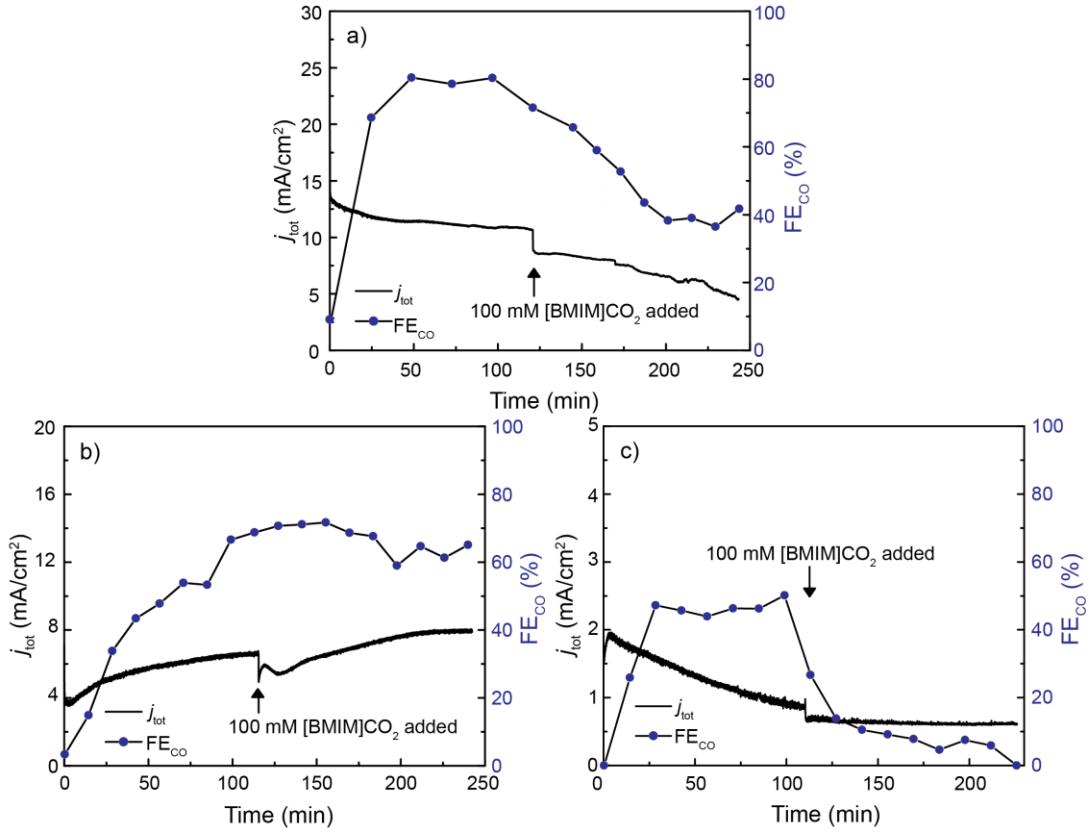

Figure 4.3. Current density plots and analogous CO FEs during CPE when 0.1 M [BMIM]CO_2 was added to the cathode after 120 minutes of electrolysis time with an applied potential of –1.95 (V) vs SCE for a) Bi, b) Sn, and c) Pb.

The rate for Bi and Sn remained steady for the first 120 minutes, signifying strong ohmic strength between the cathode and substrate. Even at a less negative potential applied for Pb (–1.95 V), cathode passivation occurred just minutes into electrolysis. Nevertheless, the CO FEs for Bi, Sn, and Pb plateaued at ~ 78, 75, and 45 respectively.

When the adduct was added after 120 minutes, the rate dropped instantly (between 2-3 mA/cm^2) for both Bi and Sn. At this point during electrolysis, the current

for Pb was already negligible so the decrease in rate was not as extreme. Upon further catalysis (up to ~250 minutes), the current density for Bi continued a steady decline whereas Sn reestablished its original rate (8 mA/cm^2). As expected for Pb, current densities remained negligible nearing 0.5 mA/cm^2. Decrease in current density signified complications with diffusion, such that the rate is sacrificed with additions of the adduct. The adduct likely interferes with mass transport of reagents and products moving to and from the electrode surface respectively. Because Sn reestablishes its current density, this material is likely to be less affected by the adduct in terms of diffusion.

For all metal cathodes, CO evolution was sacrificed, which discredits published theories that the adduct encourages a greater CO yield,[5,18] with Pb showing the most extreme deviation and Sn showing the least. CO production for Bi and Sn gradually declined, whereas Pb dropped nearly 30 % within a matter of minutes.

The loss in CO was supplemented with a slight increase in H_2 production. No other gaseous or solvated products were detected. H_2 production is normally suppressed due to the formation of an imidazolium IL monolater that forms upon applying the negative bias.[19,20] Therefore, analyzing of the cathode surface following these CPE experiments was of interest. Specifically, it was curious to detect if there was a loss of surface bound imidazolium IL. Alternatively, it was curious if the adduct now adsorbs to the surface when intentionally added to the cathode for Bi and Sn. This was of greatest interest for the Bi and Sn cathodes since there had been no detection of the adduct on the surface thus far.

4.3.3.1 Detecting Surface Adsorption of Adduct via XPS

Following the previous CPE studies where the adduct was intentionally to the cathode during electrolysis, the electrode surface was studied via XPS. As stated

previously, it was curious to observe if the adduct would now appear on the cathode surface for Bi and Sn, or alternatively, if there is a deviation in the amount of imidazolium on the surface to ultimately effect H_2 production.

Previous LSV titration studies suggested that the adduct was not adsorbing onto the Bi or Sn surface because the CO_2 reduction activity remained relatively unchanged (up to 100 mM). This implied that charge transfer events were not jeopardized as severely from the adduct as it was for Pb. Interestingly, the previous CPE studies showed an initial drop in current density upon addition of the adduct, which was accompanied by a decrease in CO evolution for all p-block cathodes. These results suggested that the adduct may act to disrupt the necessary interplay between the modified cathode and imidazolium without necessarily formally adsorbing to the surface.

To gain clarity on the possible events, the Bi-, Sn-, and Pb-modified electrodes were removed from the cathode and directly placed into the XPS intro chamber for surface analysis. No rinsing or conditioning steps were performed on the modified electrodes once removed from the cell.

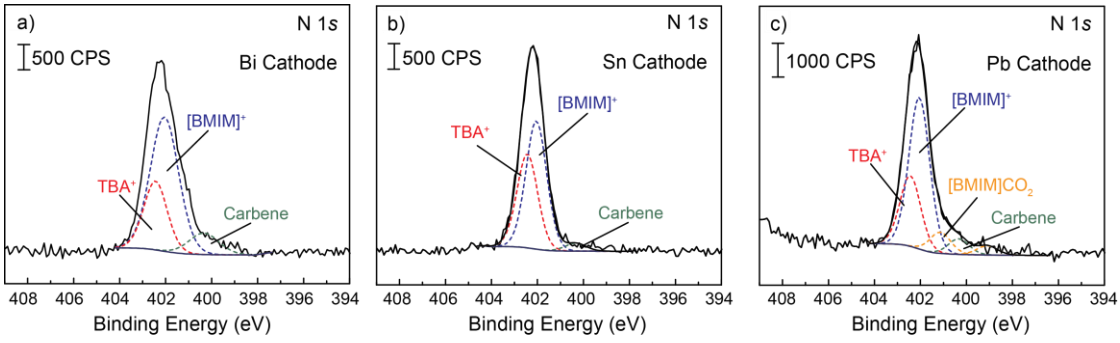

Figure 4.4. N 1*s* high resolution spectra for a) Bi, b) Sn, and c) Pb cathodes after CPE with addition of 0.1 M [BMIM]CO_2 at –1.95 (V) vs. SCE.

The N 1*s* high resolution regions were analyzed to reveal adsorption information and are summarized in Figure 4.4a, b, and c for the Bi, Sn, and Pb respectively. All cathodes showed the anticipated adsorption of supporting electrolyte (TBA^+, red trace, 402.4 eV), imidazolium ($[BMIM]^+$, blue trace, 402.1 eV) and carbene (green trace, 400.3 eV). It was found that regardless of the adduct added to the cathode solution, it did not adsorb onto Bi or Sn. Imidazolium-carboxylate therefore showed no thermodynamic stability towards these cathodes. Pb still demonstrated a complicated N 1*s* spectrum with adsorption of the adduct (401.3 eV, yellow trace) and its decomposition product (399.3 eV, yellow trace).

Because Bi and Sn surfaces do not interact directly with the adduct, it is possible that imidazolium-carboxylate offers diffusional effects that interferes with mass transport. This would affect the rate of catalysis, as observed previously with the drop in current density upon addition of the adduct. Reduced CO selectively is likely the result of the adduct altering the IL monolayer without formally adsorbing. The relative atomic percentage of IL on the cathode surface is greater than typical electrolysis experiments and is reminiscent of the surface at open circuit potential (OCP). At OCP, the modified electrode is submersed in the electrolyte solution where TBA^+ and $[BMIM]^+$ loosely adsorb to the electrode surface, as shown by the N 1*s* high resolution spectra in Figure 4.5a, b, and c for Bi, Sn, and Pb respectively.

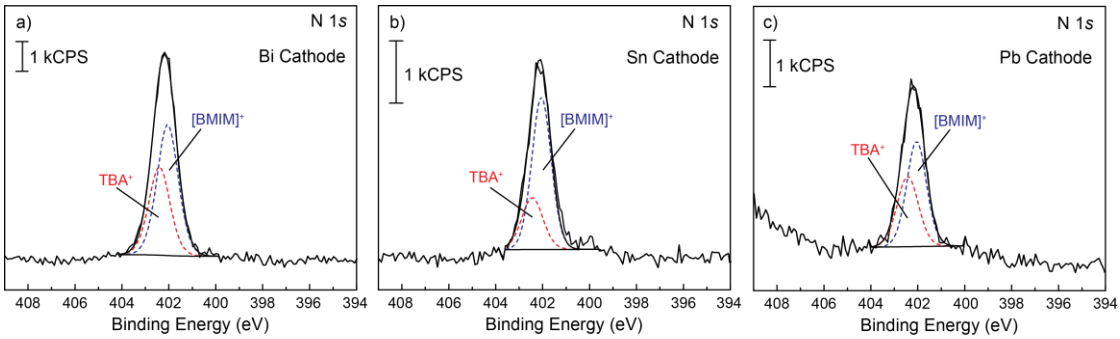

Figure 4.5. N 1*s* high resolution spectra for the a) Bi, b) Sn, and c) Pb cathodes after soaking the modified electrode at OCP in 100 mM [BMIM]OTf and 100 mM $TBAPF_6$ in CO_2 saturated MeCN.

These N 1*s* high resolution spectra showed high imidazolium atomic percentages, which resemble the N 1*s* spectra in Figure 4.4 (without the carbene component). Typically, when a negative bias is applied during CPE, IL will strongly adsorb to the electrode surface to stabilize the bias to create the IL monolayer, while ILs in the solution near the double layer will donate protons towards the $2H^+/2e^-$ redox reaction. With this, a decrease in imidazolium and an increase in carbene atomic percent are observed (See Chapter 3, Figure 3.12). Because this was not observed after CPE when the adduct was added during CPE, concern was raised regarding the behavior of the IL co-catalyst and the cathode/IL interface. Further, if the IL monolayer is now being detected by the X-ray photons via XPS more easily to result in greater detection (higher atomic percent), then it may no longer be hidden beneath the other N 1*s* components, thus loosely adsorpbed. To carefully compare these surfaces, the atomic percentages for TBA^+, $[BMIM]^+$, and carbene are summarized in Table 4.1 for the surface exposed 3 different environments: (1) soaked at OCP, (2) electrolyzed without the adduct added, and (3) electrolyzed with the adduct.

Table 4.1. N 1*s* atomic percentages for soaked, electrolyzed, and electrolyzed + adduct environments. Electrolysis performed at –1.95 V (Bi and Sn) and –2.05 V (Pb).

electrode	environment	400.3 eV	402.1 eV	402.4 eV
Bi	soaked	---	55.2 ± 6.4	44.8 ± 6.4
	electrolyzed	8.4 ± 5.5	26.2 ± 1.6	65.4 ± 3.9
	electrolyzed + adduct	6.7 ± 1.5	58.0 ± 7.0	35.4 ± 5.7
Sn	soaked	---	67.2 ± 6.5	32.8 ± 6.5
	electrolyzed	11.1 ± 1.6	7.3 ± 1.8	81.6 ± 3.3
	electrolyzed + adduct	3.3 ± 0.2	55.5 ± 0.3	41.2 ± 0.5
Pb	soaked	---	60.1 ± 2.8	39.9 ± 2.8
	electrolyzed	9.9 ± 1.7	40.67 ± 7.1	21.7 ± 1.5
	electrolyzed + adduct	6.2 ± 0.5	48.6 ± 11.0	32.5 ± 8.6

Because similar atomic percentages for $[BMIM]^+$ and TBA^+ are observed for the "soaked" and "electrolyzed + adduct" stages, the adduct is likely interfering with the cathode/IL interface. If imidazolium is loosely adsorbed to the surface, intermediate stabilization may be challenged to ultimately effect CO selectivity. Additionally, the ability for imidazolium to act as a proton source for the $2H^+/2e^-$ redox reaction may be challenged, as suggested by the decrease in carbene atomic percent. Figure 4.6 describes the relationship between the imidazolium atomic percent when soaked, electrolyzed without the adduct, and electrolyzed with the adduct added for Bi, Sn, and Pb in the maroon, blue and green traces respectively.

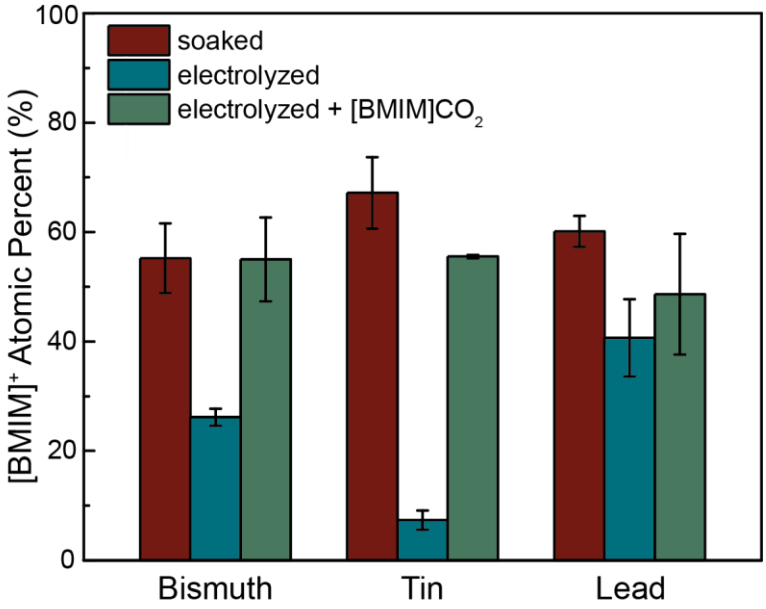

Figure 4.6. Atomic percentages of imidazolium ($[BMIM]^+$) on the Bi-, Sn-, and Pb-modified surfaces after soaking (maroon), electrolysis without imidazolium-carboxylate (blue), and electrolysis with imidazolium-carboxylate (green). Electrolysis was performed at –1.95 V for Bi and Sn and –2.05 V for Pb.

Figure 4.6 clearly illustrates the similarities between IL atomic percent after soaking and after electrolyzing with the adduct added. Because the only difference between the two electrolysis experiments is the addition or absence of the adduct, the adduct was likely the cause of poor catalysis, specifically to disrupt the cathode/IL interaction. This interference impacts the formation of the IL monolayer and provides reason for why H_2 production is no longer suppressed.

4.3.4 Investigating Electronic Effects with Addition of Adduct

We know from the previous CPE and XPS studies that despite the adduct not adsorbing onto the cathode surface for Bi or Sn, consequential decrease in CO evolution

was observed. XPS suggested that the addition of the adduct during CPE creates a poor cathode/IL interface to generate the switch from CO to H_2 production. It was curious if the poor electrode/IL interface can be confirmed with electrochemical impedance spectroscopy (EIS), specifically the investigation of an adsorption phenomenon (R_{AD}).

If IL no longer demonstrates a strong interaction with the surface, the R_{AD} would no longer be an essential component when simulating the impedance response via circuit analysis (See Chapter 3). If there is no adsorption phenomenon, it is likely that the imidazolium-carboxylate adduct is interfering and blocking imidazolium interaction at the surface. If an adsorbate acts as a blocking layer on the surface to negatively affect ET in the double layer, an increase in surface resistivity (decrease in conductance) would be observed.[21] This would complement XPS and Tafel results, such that the IL would now be loosely coordinated to the cathode to participate in surface chemistry.

In addition to observing deviations in R_{AD}, the resistance to charge transfer (R_{CT}) may compliment the N 1*s* surfaces after CPE when the adduct was added. If the R_{CT} remains unchanged after the adduct is added to the electrolyte solution, the adduct is not adsorbing to the surface to block charge transfer events. Complicated charge transfer events would result in a larger R_{CT} due to impurity adsorption to block active sites. Here, the system would be experiencing additional kinetic challenges due to the presence of the adduct. The enhanced kinetic barrier relates directly to the ability for imidazolium to stabilize the $CO_2^{\bullet-}$, which is generated upon first rate determining ET step. If $CO_2^{\bullet-}$ is not stabilized, the likelihood of further transformation to the CO production is challenged and the redox reaction may favor a more mechanistically feasible one step approach, i.e. H_2 production. EIS provides the electronic behavior for the RDS and should clearly describe the changes in R_{CT} upon adduct additions.

4.3.4.1 Elucidating Deviations in Charge Transfer Events

These EIS experiments were performed like the previous LSV adduct titration studies where the electrolyte solution initially consisted of 100 mM imidazolium and 100 mM $TBAPF_6$ in CO_2 saturated MeCN. Aliquots of imidazolium-carboxylate were titrated into this solution where upon each addition, an impedance response was obtained. Figure 4.7 shows the impedance responses for Bi, Sn, and Pb (–1.95 V and –2.05 V) for imidazolium-carboxylate concentrations up to 100 mM.

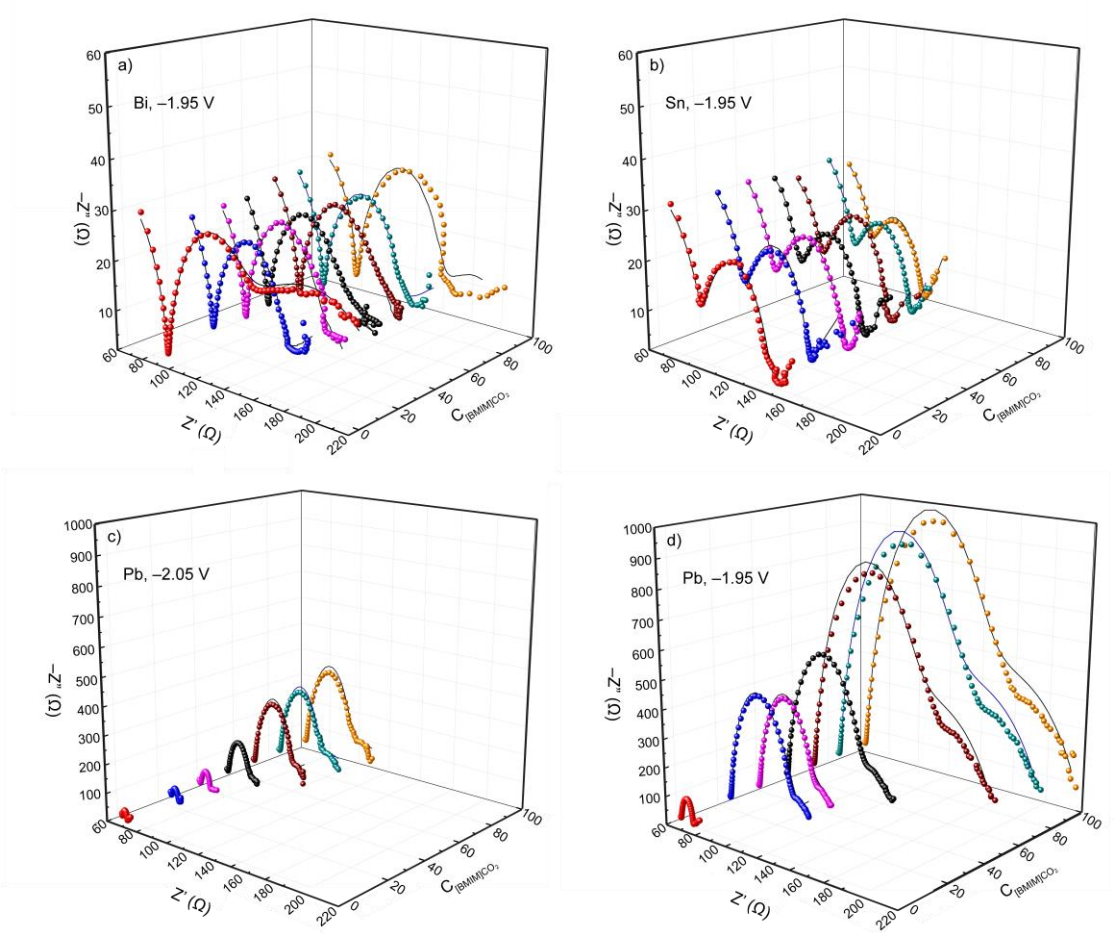

Figure 4.7. Overlaid 3D Nyquist plots for a) Bi, b) Sn, and c) Pb at –2.05 V and d) –1.95 V upon titrations of imidazolium-carboxylate. Bi and Sn were performed at –1.95 (V) vs. SCE.

Impedance responses revealed that even upon additions of imidazolium-carboxylate, the R_{CT} remained relatively constant for Bi and Sn (–1.95 V). There were no significant deviations in resistive (real, Z´) or capacitive (imaginary, Z″) components. This complimented the LSV titration results, in that the electronic behavior for the rate determining ET event (CO_2 reduction to $CO_2^{\bullet-}$) is unaffected by the adduct. This corresponds to the N 1*s* high resolution spectra post CPE such that the adduct does not

adsorb onto the surface to displace IL and complicate charge transfer events. Contrastingly, Pb showed significant deviations in the R_{CT} upon increasing adduct concentrations. Regardless of applying –1.95 or –2.05 V, the adduct provided additional resistivity to reduce CO_2. Increased R_{CT} corresponds to blocking of charge transfer upon impurity adsorption.

For Bi and Sn, it was clear from Figure 4.7a and b that there is a strong ohmic interaction between the film and electrode ("L" feature) at high frequencies. However, taking a close look at Figure 4.7a for Bi specifically, a fused semi-circle (red trace, 0 mM adduct) no longer exists upon additions of the adduct. If there is no adsorption phenomenon, it is likely that the imidazolium participating in surface chemistry has a poor interaction with the surface, supporting results from XPS studies (Figure 4.4). Sn inherently has more diffuse overlapping semi-circles, thus circuit analysis will help to determine if there is or is not an adsorption phenomenon.

4.3.4.2 Circuit Analysis for Adsorption Phenomenon Elucidation

Circuit analysis using the 3RC and 2RC circuits (Figure 4.8a and b respectively), was used to simulate the impedance responses from the EIS imidazolium-carboxylate titrations. The only difference between the two circuits is that the 3RC circuit accounts for an adsorption phenomenon (R_{AD}) whereas the 2RC does not.

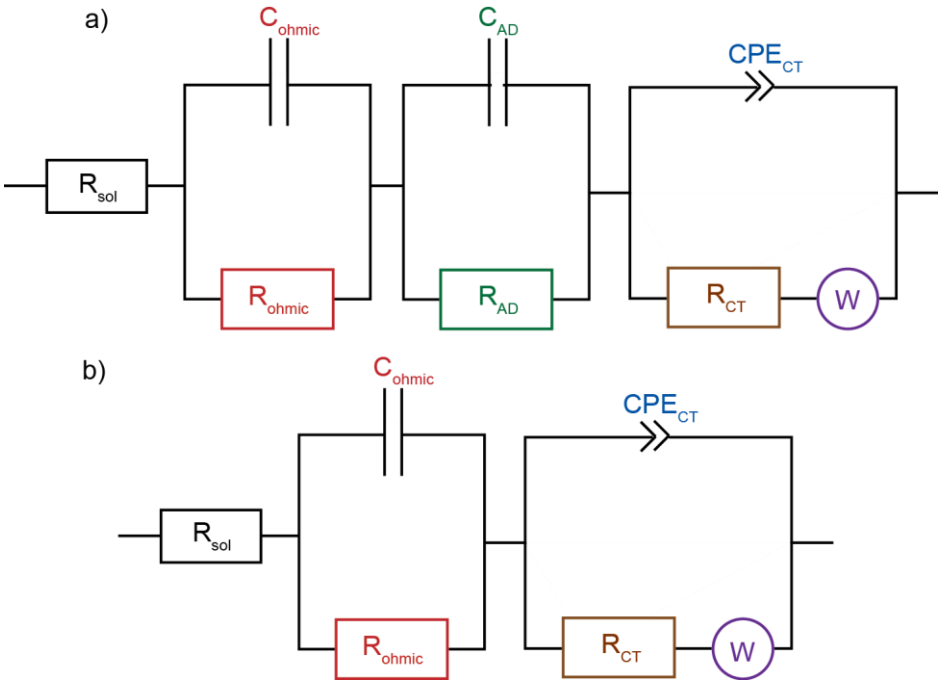

Figure 4.8. Circuit design for the a) 3RC and b) 2RC circuits.

R^2 values were subsequently obtained from the circuit fittings to reveal which circuit best simulates the electrochemical events. If the 3RC circuit demonstrates a better fit to the impedance data, an adsorption phenomenon is likely to occur. Alternatively, if the 2RC circuit demonstrates a better fit, an adsorption phenomenon is unlikely. The R^2 values for Sn are summarized in Figure 4.9.

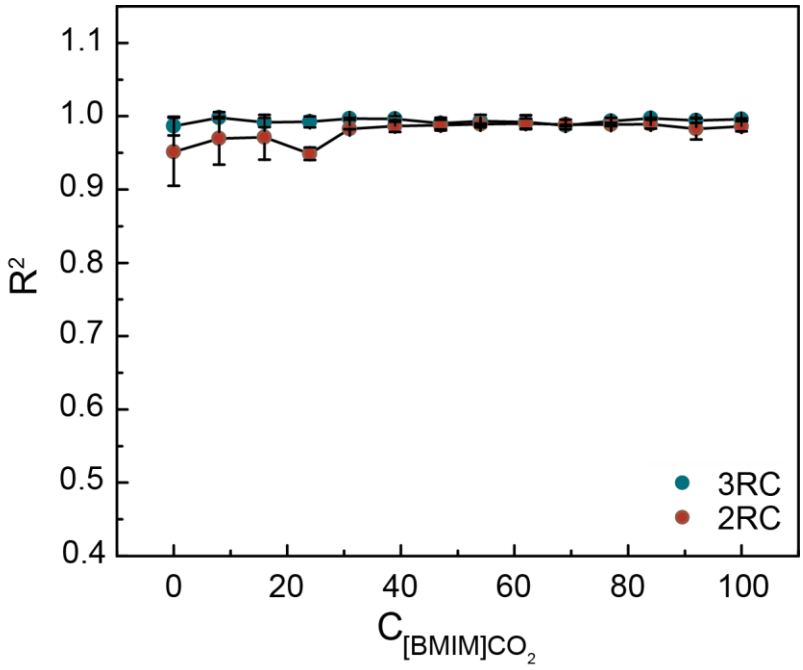

Figure 4.9. R-squared values for 3RC (blue trace) and 2RC (red trace) for Sn-CMEC for varying amounts of imidazolium-carboxylate in solution.

Under typical electrolysis conditions when the adduct is not added, Bi and Sn have illustrated better fittings to the 3RC circuit. This was true up until the applied potential exceeded –2.05 V, where it was believed that more negative potentials could be jeopardizing the durability of the catalytic functions of imidazolium to adsorb onto the surface efficiently (See Chapter 3). Interestingly, when imidazolium-carboxylate was added to the cathode, the R^2 values now suggested otherwise. No major deviations between the 3RC or 2RC simulations were evident. This suggested that an adsorption phenomenon was unlikely. These studies support why Pb never experienced an adsorption phenomenon.

These experiments truly advocate the negative effects of imidazolium-carboxylate towards CO_2 to CO electrocatalysis for our catalytic system, i.e., poor electrode/IL interface, increased R_{CT}, and reduced current density and CO selectivity. This provides reasons to question existing literature emphasizing the significance of this intermediate.

4.4 Observing the Catalytic Behavior Without Imidazolium

Thus far, imidazolium-carboxylate has been incorporated into our electroanalytical studies via titrations or in a starting 1:1 equivalence with imidazolium (100 mM) in the electrolyte solution. To find absolute confidence in discrediting literature claims for the catalytic behavior of the adduct, electroanalytical experiments were performed by substituting imidazolium with imidazolium-carboxylate during electrolysis. Here, these experiments will emphasize that the adduct is irreversible upon formation, such that it does not become reduced back to imidazolium during catalysis. Because there is no starting imidazolium, the proton source would be from the anode through the proton permeable Nafion membrane.

4.4.1 Electrolysis Deviations with Imidazolium-Carboxylate

CPE was performed with now 100 mM imidazolium-carboxylate and 100 mM $TBAPF_6$ in CO_2 saturated MeCN. Upon applying the negative bias, it was found that the current density dropped significantly (Table 4.2) by ~8-10 mA/cm^2 from normal electrolysis conditions performed with protonated imidazolium. This was demonstrated for all cathodes. The negligible rates suggested that that there is no driving force great enough (potential) to reduce the adduct to undergo the redox reaction. This further supports that this adduct is thermodynamically stable under these electrolysis

conditions. Unless the energy cost of the system is sacrificed, such as to apply a more negative potential, the adduct will unlikely be reduced to the carbene. A higher kinetic barrier now exists for these imidazolium-carboxylate systems, as illustrated by the absence of a CO_2 cathodic feature (Figure 4.1).

Table 4.2. CPE metrics for 100 mM imidazolium-carboxylate and 100 mM $TBAPF_6$ in CO_2 saturated MeCN.

electrode	overpotential (η)	FE_{CO} (%)	FE_{H2} (%)	j_{tot} (mA cm^{-2})
Bi	200 mV	---	12 ± 2	0.54 ± 0.13
Sn	200 mV	---	14 ± 5	0.28 ± 0.03
Pb	300 mV	---	5 ± 2	0.58 ± 0.24

As expected, Table 4.2 shows that there was no measurable CO production when monitoring the gaseous products with GC. Trace amounts of H_2 were produced, but because the measured current density is <1 mA/cm^2, much charge likely went to stabilizing the film/substrate interface. These current density values relate to electrolysis when no imidazolium is added.[22] Ultimately, these CPE experiments suggested that the catalytic benefits of the cathode/imidazolium-carboxylate interface are not comparable to the cathode/imidazolium interface.

For the trace amounts of H_2 produced, the necessary protons were likely from the anode compartment. This, however, creates a new electrolysis system with low proton availability. This system may follow a different mechanistic route (Scheme 4.4) to reduce CO_2 via a $2e^-$ pathway to yield CO and carbonate.

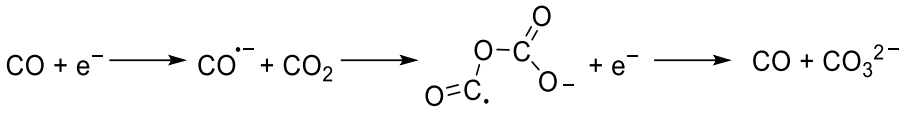

Scheme 4.4. Mechanism for low proton availability CO_2 to CO heterogeneous electroreduction.

Scheme 4.4 still relies on the formation of the rate determining $CO_2^{\bullet-}$. Therefore, the stabilization of if this species will strongly influence the energy cost (low or high proton availability). More negative and energy costing potentials are necessary to match the greater overpotential. Additionally, this further supports that imidazolium-carboxylate species near the electrode surface cannot become reduced to stabilize the $CO_2^{\bullet-}$ to lower the kinetic energy barrier and support favorable catalysis for our system.

4.4.2 EIS Charge Transfer Effects

Previous CPE studies demonstrated reduced current densities with 100 mM imidazolium-carboxylate in the absence of imidazolium. In addition to the inability to stabilize $CO_2^{\bullet-}$, the reduced rates can be the result of poor mass transport.[23] This is common for when the C2 position on imidazolium is blocked to prevent transformation to the carbene.[24] Inability to break the C2 bond has been found to complicate use with CO_2 and ultimately increase viscosity.[24] Additionally, it is possible that the poor rates are linked to greater resistivity at the surface. This would be demonstrated by EIS, specifically R_{CT}. Previous EIS carboxylate-imidazolium titrations revealed that Bi and Sn had negligible deviations in R_{CT} even in a 1:1 ratio of imidazolium to the adduct. However, it was curious to observe if there would be an observable deviation now in the absence of imidazolium, as is suggested by the reduced current density.

The EIS studies were performed in 100 mM imidazolium-carboxylate and 100 mM $TBAPF_6$ in CO_2 saturated MeCN. Bi, Sn, and Pb were studied at –1.95 V. Pb was also studied at –2.05 V for comparison.

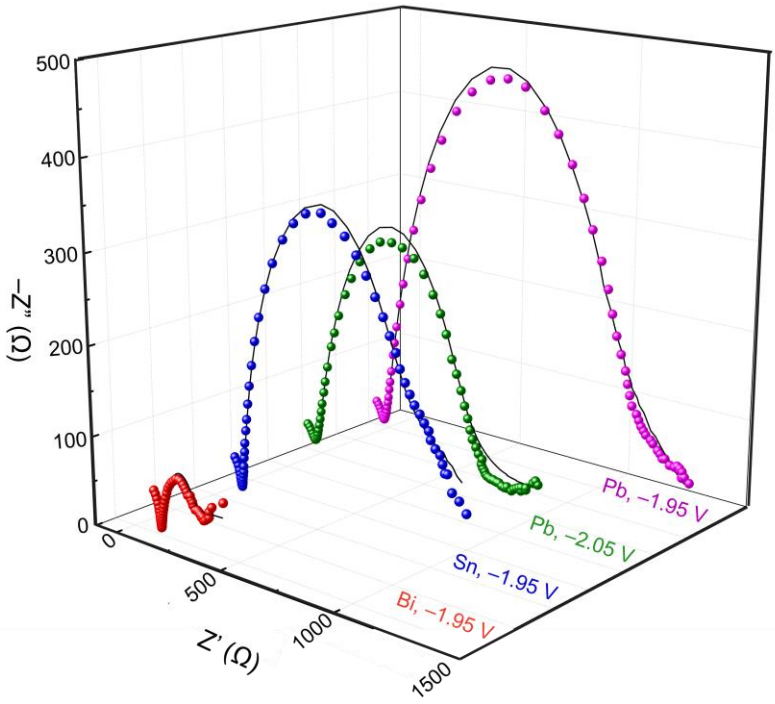

Figure 4.10. Overlaid 3D Nyquist plot for Bi (red trace), Sb (blue trace), and Pb (green trace, –2.05 V; pink trace, –1.95 V) for 100 mM imidazolium-carboxylate and 100 mM $TBAPF_6$ in CO_2 saturated MeCN. Black lines represent 3RC simulations.

Like EIS studies performed with 100 mM imidazolium, Bi demonstrated the smallest R_{CT} (Figure 4.10, red trace) and Pb demonstrated the largest R_{CT}, (Figure 4.10 pink trace, –1.95 V). Sn (Figure 4.10 blue trace) and Pb (Figure 4.10 green trace, –2.05 V) still demonstrated similar R_{CT} values. Despite lacking the acidic C2 proton, a

complete semicircle is observed because EIS is sensitive to the electrochemical behavior for the rate determining ET step, not for proton transfers.

To provide greater significance to these results, the impedance response for these studies were overlaid with the impedance responses for typical electrolysis conditions where there is no incorporation of the adduct. Here, direct comparisons were made regarding the R_{CT} for the first ET event.

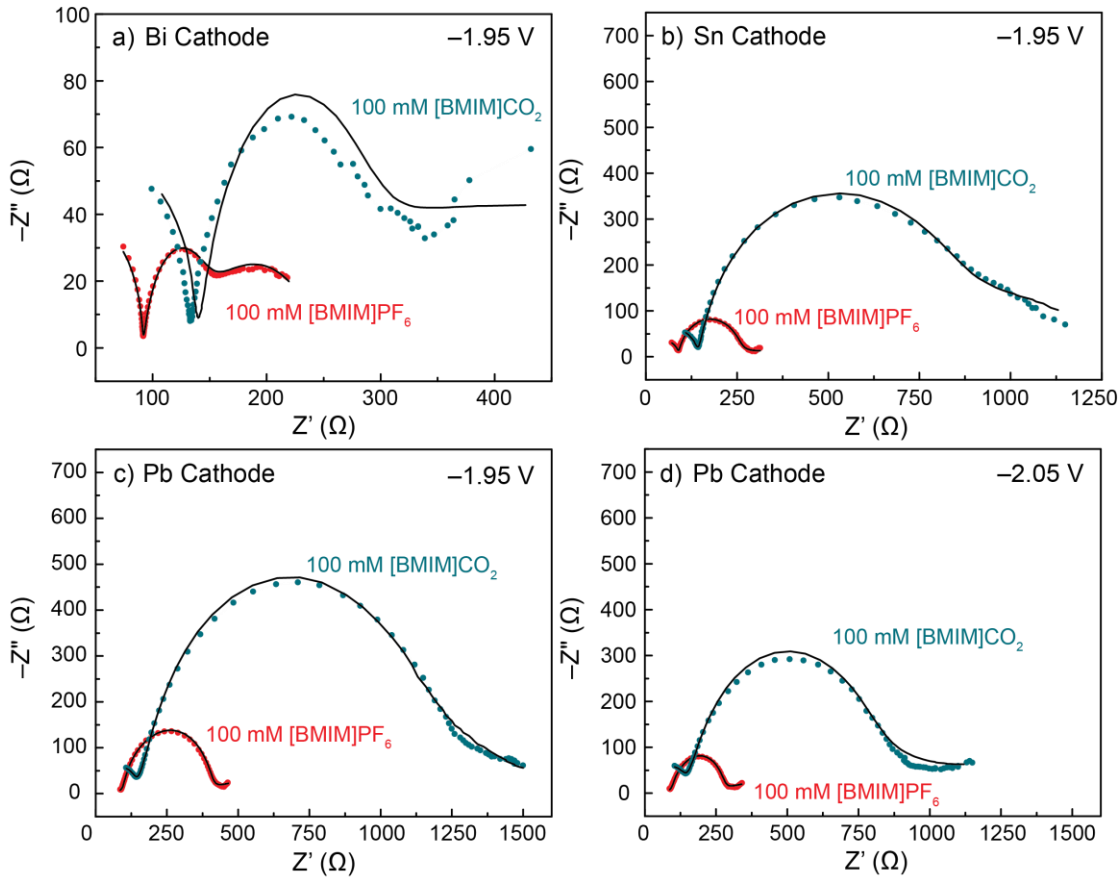

Figure 4.11. Nyquist plots for a) Bi, b) Sn, and c) Pb at –1.95 V and d) –2.05 V for electrolyte solution with 100 mM imidazolium (red dots) or 100 mM imidazolium-carboxylate (blue dots). Black lines represent 3RC simulations.

As illustrated in Figure 4.11, the R_{CT} increases for all cathodes when imidazolium-carboxylate is used in substitution for imidazolium. When imidazolium was in a 1:1 mixture with the adduct in previous EIS studies, the R_{CT} remained relatively unchanged likely due to imidazolium still being able to participate in surface charge stabilization. Imidazolium-carboxylate is an overall neutral species (zwitterion) that is not capable of stabilizing surface charges as efficiently.

In addition to the R_{CT} increasing, the resistance of solution (R_{sol}) was also increased. This signifies that the imidazolium-carboxylate is not only effecting stabilization, but is also interfering with the electrolyte solution itself. This supports that the imidazolium-carboxylate complicates diffusion and encourages poor mass transport by increasing the viscosity of the solution.

This provides clarity on why the current density decreases during electrolysis upon adduct formation. With increased viscosity, the mass transport for reactants and products is reduced. This results in an environment with low proton availability, such that the carbene (upon proton donation) cannot become readily protonated and will favorably react with CO_2 to form the adduct. This domino effect likely causes gradual film passivation.

4.5 Conclusions

The formation of imidazolium-carboxylate is a widely accepted intermediate for describing the mechanism for CO_2 to CO heterogeneous electrocatalysis mediated by imidazolium-based ILs.[25] Despite no evidence to validate this claim,[20,26] it was theorized to stabilize the $CO_2^{\bullet-}$ intermediate, thus lowing the potential barrier to make this a likely redox event. The validity of these statements was questioned when performing initial studies on the mechanistic deviations between the promising Bi and

Sn platforms and the Pb platform, which can produce high efficiencies of CO for only short periods of time before it becomes passivated.

During our initial studies with characterizing mechanistic differences, a significant discovery was made when analyzing the surface adsorbates for these cathodes. Bi and Sn both demonstrated appropriate adsorption energies of the supporting electrolyte, imidazolium, and carbene. In addition to these components, Pb also revealed adsorption of two additional components. Upon synthesis and elemental analysis of standards, these two components were identified as imidazolium-carboxylate and its decomposition product, 1-butyl-3-methyl-2-imidazolone.

Because there were no previous publications describing the negative catalytic effects of imidazolium-carboxylate, rigorous experimentation of its electrochemical behavior was critical towards this field of research. Specifically, the proposed equilibria that the adduct is claimed to exist in, and its claim to enhance CO_2 reduction activity and CO efficiency were our primary research concerns.

The effects on CO_2 reduction activity was demonstrated via LSV when the adduct was slowly titrated into an electrolyte solution consisting of imidazolium and supporting electrolyte. Bi and Sn demonstrated negligible effects in the structure of their polarization curves, whereas the activity for Pb dropped significantly. This not only demonstrated the negative effects that the adduct has on CO_2 reduction activity, but also on the importance of the cathode material itself. Electrochemical responses to the adduct are unique with respect to the specific material. Specifically, Pb offers greater thermodynamic stability for the adduct over Bi and Sn and therefore has greater interplay with the adduct to effect CO_2 reduction activity.

The effects that imidazolium-carboxylate has on rate for Bi and Sn was more prevalent during long CPE studies. When the adduct was added to the cathode compartment of the electrocatalytic cell, the current density dropped between 2-3 mA/cm^2 and was accompanied with a decrease in CO production. Loss of CO production was reasoned by enhanced overall resistivity and loosely coordinated IL via EIS and XPS. Heightened resistivity comes from poor surface and intermediate stability. Without stability, the kinetic barrier increases and the likelihood of further transformation is reduced, thus switching product distribution to the simple on step H_2 evolution reaction. The cathode surface after CPE did not suggest favorable thermodynamic adsorption of the adduct for Bi or Sn, but revealed a poor imidazolium-cathode interaction. This surface resembled the cathode surface when just soaking in electrolyte solution without an applied potential. Additionally, there was no longer an IL adsorption phenomenon for Bi or Sn. With the imidazolium-carboxylate present, there is no driving force to strongly adsorb imidazolium. Additionally, the reduced amount of carbene signified that the ability of imidazolium to function as a proton donor was challenged.

These studies suggest that the catalytic benefit of incorporating IL no longer exists when incorporating the adduct. This was further supported when the R_{CT} and R_{sol} became more resistive when the adduct was present. When the imidazolium C2 proton is blocked, viscosity increases and results in increased R_{sol}. This led to a cascade of events where mass transport was reduced to make it challenging for carbene to diffuse away from the surface to become reprotonated in the solution bulk. Reduced mass transport results in the carbene reacting with nearby neutral CO_2 to form the adduct.

Further, CPE and LSV studies revealed a substantial drop in rate when imidazolium-carboxylate was used in substitution of imidazolium. These rates were no better than when imidazolium was eliminated from the electrolyte solution completely. LSV studies for Bi, Sn, and Pb provided significant information on the reduction potential for imidazolium-carboxylate. Imidazolium-carboxylate is reduced at ~ –2.3 V. Having a reduction potential this negative would make it unlikely for the adduct to exist the hypothesized equilibria. Our studies demonstrate that once it is formed, it exists in solution as a thermodynamic sink.

Clarifying the role of imidazolium-carboxylate was critical for developing a larger library of CO evolving catalysts. A false understanding of intermediates can slow the process for further advancements in the field of CO_2 to CO heterogeneous electrocatalysis. Now understanding that the formation of imidazolium-carboxylate can enhance viscosity, and ultimately effect diffusion, it is curious to study more viscous systems to monitor if high viscosity truly encourages formation of the adduct in imidazolium IL-based solutions.

REFERENCES

(1) Gu, X.; Carneiro, J. S. A.; Nikolla, E. *Catalysis*. **2017**, *29*, 94—121.

(2) Sharma, P. P.; Zho, X. D. *WIREs Energy and Environment* **2017**, e239.

(3) Whipple, D. T.; Kenis, P. J. A. *Journal of Physical Chemistry Letters*. **2010**, *1*, 3451—3458.

(4) Gustavsson, L.; Börjesson, P.; Johansson, B.; Svenningsson, P. *Energy*. **1995**, *20*, 1097—1113.

(5) Rosen, B. A. Haan, J. L.; Mukherjee, P.; Braunschweig, B.; Zhu, W.; Salehi-Khojin, A.; Dlott, D. D.; Masel, R. I. *Journal of Physical Chemistry C.* **2012**, *116*, 15307—15312.

(6) Medford, A. J.; Vojvodic, A.; Hummelshøj, J. S.; Voss, J.; Abild-Pedersen, F.; Studt, F.; Bligaard, T.; Nilsson, A.; Nørskov, J. K. *Journal of Catalysis*. **2015**, *328*, 36—42.

(7) Medina-Ramos, J.; Pupillo, R. C. Keane, T. P.; DiMeglio, J. L.; Rosenthal, J. *Journal of the American Chemical Society*. **2015**, *137*, 5021—5027.

(8) Bocarsly, A. B.; Gibson, Q. D.; Morris, A. J.; L'Esperance, R. P.; Detweiler, Z. M.; Lakkaraju, P. S.; Zeitler, E. L.; Shaw, T. W. *ACS Catalysis*. **2012**, *2*, 1684—1692.

(9) Yang, D.; Li, Q.; Shen, F.; Wang, Q.; Li. L.; Song, N.; Dai, Y.; Shi, J. *Electrochimica Acta*. **2016**, *189*, 32—37.

(10) Matsubara, Y. Grills, D. C.; Kuwahara, Y. *ACS Catalysis*. **2015**, *5*, 6440—6452.

(11) Cheeck, G. T.; Roeper, D. F.; Pearson, W.; O'Grady, W. E. *ECS Transactions*. **2014**, *64*, 161—169.

(12) Noel, M.; Vasu, K. I. *Cyclic Voltammetry and the Frontiers of Electrochemistry*; Oxford & IBH: Janpath, New Delhi, 1990.

(13) Blum, L.; Legault, M. D.; Huckaby, D. A. *Interfacial Electrochemistry: Theory, Experiment, and Applications*. Marcel Dekker, Inc. New York, NY, 1999.

(14) Kortlever, R.; Shen, J.; Scouten, K. J. P. Calley-Vallejo, F.; Koper, M. T. M. *Journal of Physical Chemistry Letters*. **2015**, *6*, 4073—4082.

(15) Zhou, H.; Zhang, W.Z.; Liu, C. H.; Qu, J. P.; Lu, X. B. *Journal of Organic Chemistry*. **2008**, *73*, 8039—8044.

(16) Van Ausdall, B. R.; Glass, J. L.; Wiggins, K. M.; Aarif, A. M.; Louie, J. *Journal of Organic Chemistry*. **2009**, *74*, 7935—7942.

(17) Wang, S.; Wang, X. *Angewandte Chemie International Edition*. **2016**, *55*, 2308—2320.

(18) Sun, L.; Ramesha, G. K.; Kamat, P. V.; Brenneke, J. F. *Langmuir*. **2014**, *30*, 6302—6308.

(19) Lim, H.; Kim, H. *Molecules*. **2017**, *22*, 536.

(20) Hollingsworth, N.; Taylor, S. G. R.; Galante, M. T.; Jacquemin, J.; Longo, C.; Holt, K. B.; de Leeuw, N. H.; Hardacre, C. *Angewandte Chemie International Edition.* **2015**, *54*, 14164—14168.

(21) Salimon, J.; Hamzah, S.; Mohamad, M.; Ibrahim, H. N.; Yamin, B. M. *Science International*. **2003**, *14*, 325—329.

(22) DiMeglio, J. L.; Rosenthal, J. *Journal of the American Chemical Society.* **2013**, *135*, 8798–8801

(23) Xu, D.; Carbonell, R. G.; Kiserow, D. J.; Roberts, G. W. *Industrial and Engineering Chemistry Research*. **2003**, *42*, 3509—3515.

(24) Brennecke, J. F. *Journal of Chemical Engineering Data*, **2008**, *53*, 2112—2119.

(25) Girard, A.; Simon, N.; Zanatta, M.; Marmitt, S.; Conçalves, P.; Dupont, J. *Green Chemistry*. **2014**, *16*, 2815—2825.

(26) Shiflett, M. B.; Yokozeki, A. *Journal of Chemical Engineering Data*. **2009**, *54*, 108—114.

Chapter 5

MASS TRANSPORT EFFECTS FOR PURE IONIC LIQUID SYSTEMS

5.1 Introduction

Room temperature 1,3-dialkylimidazolium ionic liquids (RTILs) are multifunctional in that they possess a wide range of applications; sensing, chromatography, electroanalytical chemistry, extraction, organic synthesis, etc.[1,2] ILs have increasingly been used for industry as reaction solvents because they have tunable miscibility, they are non-flammable and reusable, and they can replace conventional toxic or volatile organic solvents.[3,4] ILs have also found utility in electrolysis. They are ideal for electroanalytical studies because they have an impressive range of electronic properties; large electrochemical window, multifunction as electrolyte and a proton source, and have high thermal and chemical stability.[5,6] Because of these fascinating properties and their seemingly complex nature of behaving both as a salt and organic liquid, much work in the literature has been devoted to understanding the physical behavior of ILs in greater detail.[7,8] This has been a challenging endeavor because the behavior for ILs has suggested to be unique for the specific environment and reaction condition, i.e. temperature, admixtures, and applied potential, which results in discrepancies in the literature.[3] Because of these discrepancies, it was curious to directly observe how ILs behave for our electrocatalytic studies in detail. Specifically, the IL interactions between Bi-, Sn-, and Pb-carbon monoxide evolving catalysts (CMEC) were investigated.

ILs have been an essential contributor for promoting our heterogeneous CO_2 to CO electrocatalytic redox reaction for Bi, Sn, and Pb platforms, owing to the cathode/IL interface.[9,10] Incorporating IL into electrocatalysis has shown significant enhancements in the rate of reaction (current density, j_{tot}), CO selectivity (Faradaic efficiency, FE), activity for CO_2 reduction, and a decrease in the overall energy cost (overpotential, η). Further, MD calculations detected multiple purposes and functions of 1-3-dialkylimidazolium ILs during catalysis which included: stabilizing adsorbed intermediates ($CO_2^{\bullet-}$), forming an IL monolayer over the catalyst film to suppress H_2 evolution, and acting as a Lewis acid to contribute protons to the $2H^+/2e^-$ redox reaction. It was found that in high IL concentrations (300 mM), supporting electrolyte was no longer necessary for the electrolyte solution, such that the IL is plentiful enough to be conducting yet still participate in the surface chemistry. To emphasize the cathode/IL interface, catalysis was performed in the absence of IL where it was found that neither high CO selectivity nor appreciable rates were achieved.

The catalytic benefits of having the cathode/IL interface is remarkable. This inspired curiosity for how catalysis will function in neat IL systems, such that supporting electrolyte and acetonitrile (MeCN) would no longer be present. Here, IL would be functioning as solvent, supporting electrolyte, and a Lewis acid. The primary concern would be the inherent properties of pure RTILs. Most RTILs have high viscosity (>50 cP) and therefore have low self-diffusion (~0.1 $x10^{-9}$ m^2 s^{-1}) with modest conductivity (~1 S m^{-1}).[11]

Thus far, RTILs have been used in small concentrates as an admixture to MeCN to impressively co-catalyze the reduction of CO_2 to CO for the Bi, Sn, and Pb platforms. Investigating the role of RTILs as solvent for electrocatalytic reactions would be a

significant contribution to the field of IL mediated electrolysis. Based on the increasing amount of RTIL publications, these solvents are likely to become a permanent feature for analytical chemistry.[1] Additionally, this would encourage chemistry involving "greener" solvents in lieu of using volatile and wasteful organic solvents.[1,7,12]

Two RTILs selected for this study were 1-butyl-3-methylimidazolium hexafluorophosphate ([BMIM]PF_6) and 1-butyl-3-methylimidazolium trifluoromethanesulfonate ([BMIM]OTf). Both RTILs have encouraged high current densities and CO selectivity when used in dilute concentrations in MeCN in previous study.[10,13] [BMIM]PF_6 and [BMIM]OTf have different physical properties, i.e. viscosity, symmetry, thermal stability, steric environment.[14] Varied RTIL properties will afford a thorough study for understanding what physical properties will encourage an ideal electrolyte solvent for catalysis.

5.2 Experimental Method

5.2.1 Materials and Methods

Reagents and solvents were purchased from Sigma Aldrich, Alfa Aesar, Acros or Fisher. Bismuth(III) nitrate pentahydrate (99.999 %) was purchased from Alfa Aesar and tin(II) trifluoromethanesulfonate was purchased from Strem Chemicals. Imidazolium ionic liquids; 1-butyl-3-methylimidazolium hexafluorophosphate ([BMIM]PF_6), 1-butyl-3-methylimidazolium trifluoromethanesulfonate ([BMIM]OTf were purchased from Alfa Aesar and Sigma Aldrich respectively. Electrochemistry grade potassium bromide (KBr), and hydrochloric acid (36.5—38.0 % in H_2O) were purchased from Sigma Aldrich. Tetrabutylammonium hexafluorophosphate ($TBAPF_6$) was purchased from TCI America and purified by recrystallization with ethanol. Carbon

dioxide (CO_2) was purchased from Keen Compressed Gas Company grade 4.0 high purity.

Platinum gauze (99 %) was purchased from Sigma Aldrich. The bare glassy carbon disc electrode, bare Ni disc electrode, and the Ag/AgCl (1.0 M KCl) reference electrode were purchased from CHI Instruments. Ag wire was used as a pseudo reference for the neat RTIL electroanalytical studies and was assembled in a glass casing filled with [BMIM]OTf or [BMIM]PF_6 equipped with a frit. Ag/AgCl reference was used for the electrodeposition of Bi-CMEC and Sn-CMEC.

Graphite plates were purchased from Ohio Carbon and Ni foil was purchased from Sigma Aldrich.

5.2.2 Single-Compartment Electrochemical Cell

CPE was performed in a single-compartment cell (made in house) to accommodate a smaller volume of RTILs to be used (2 mL). The RTIL was stirred at a steady rate with a stir bar. It consisted of a typical three-electrode system with a working (nickel plate electrode (~1 cm x 1.0 cm x 0.00125 cm) or graphite plate (~1 cm x 1.0 cm x 0.1 cm)), auxiliary (Pt mesh), and pseudo reference (Ag wire cast in RTIL).

5.2.3 Temperature Regulation

Temperature was regulated by a stir/heat plate (purchased from Chemglass) with a temperature probe with a digital reading. Silicone oil was used at the heat bath.

5.2.4 Instrumentation

5.2.4.1 Electrochemical Measurements

Electrochemical studies were conducted using a CHI-620D potentiostat/galvanostat or a CHI-720D bipotentiostat. Electrochemical apparatus consisted of a three-electrode system; working (bare glassy carbon disc (3.0 mm diameter), bare Ni disc (3.0 mm diameter), Ni foil (~1 cm x 1.0 cm x 0.00125 cm), or graphite plate (~1 cm x 1.0 cm x 0.1 cm)), counter (platinum gauze), and a reference electrode (Ag wire)). Cyclic voltammetry and linear voltammetry experiments were performed with iR drop compensation with 100 mV s^{-1} scan rate.

5.2.4.2 Electrochemical Impedance Spectroscopy

Electrochemical impedance spectroscopy (EIS) was performed using a CHI-720D bipotentiostat. Electrochemical apparatus consisted of a three-electrode system; working (bare glassy carbon disc (3.0 mm diameter), bare Ni disc (3.0 mm diameter), Ni foil (~1 cm x 1.0 cm x 0.00125 cm), or graphite plate (~1 cm x 1.0 cm x 0.1 cm)), counter (platinum gauze), and a reference electrode (Ag wire)). Frequency ranged from 0.1 Hz to 100 000 Hz.

5.2.4.3 X-ray Photoelectron Spectroscopy

XPS analysis was performed using a Thermo Scientific K-alpha^{+} spectrometer with monochromatic Al Kα X-ray (1486.7 eV) and 72 W of power (12 kV, 6 mA) equipped with a 128 CCD detector plate. Operating vacuum pressure in the main chamber was less than $1x10^{-8}$ torr. XPS survey scans were collected with a step size of 1.0 eV and a pass energy of 100 eV. High resolution spectra were collected with a step

size of 0.1 eV and a pass energy of 20 eV. The X-ray spot size was an elliptical shape with a semi-major axis of approximately 400 μm.

5.2.4.4 Gas Chromatography and CO_2 Headspace Analysis

Current densities were obtained by performing controlled potential electrolysis (CPE) on a single-compartment electrochemical cell made in house. The compartment was filled with 2 mL of either CO_2 saturated [BMIM]PF_6 or [BMIM]OTf. The solution was sparged for 30 minutes before the start of CPE.

During CPE, the solution was stirred at a steady rate while there was a continuous flow of CO_2 into the headspace (5 mL min^{-1}). The cathode was vented directly into a flow gas chromatograph (SRI Instruments, SRI-8610C). A chromatograph was obtained every 15 min throughout the duration of electrolysis by placing the sampling loop in line with a packed HayeSep D column and a packed mole Sieve 13X column. The columns led directly to a thermal conductivity detector (TCD) and a flame ionization detector (FID) equipped with a methanizer to quantify hydrogen and carbon monoxide production respectively. The gas carrier was Argon (Keen, 99.999 %).

5.2.4.5 Electrodeposition of Sn-CMEC

Prior to electrodeposition, the nickel disc electrode (3.0 mm diameter) was polished with 0.05 micron alumina powder in Millipore water and then sonicated in Millipore water to remove residual powder. If starting with Ni foil (~1 cm x 1.0 cm x 0.00125 cm), it was sonicated in water, acetone, and lastly acetonitrile for 20 minutes each to remove excess oils. The Ni substrate was then submersed in an organic electrolyte solution containing 0.02 M $Sn(OTf)_2$ and 0.1 M $TBAPF_6$ saturated with N_2.

A series of cyclic voltammetry sweeps (10 cycles, 100 mV s^{-1}) were performed with applied potentials ranging from –0.25 to –2.25 (V) vs. SCE. Following the electrode conditioning, the Ni substrate was agitated to remove exfoliated material formed on the electrode surface. Using the same electrolyte solution, controlled potential electrolysis (CPE) applied a constant potential of –0.55 (V) vs. SCE until a total of ~1 C cm^{-2} was passed. The now Sn-modified electrode was rinsed with acetonitrile followed by a drying step consisting of a gentle N_2 flow over the modified surface.

This consisted of a three-electrode system; working bare Ni disc (3.0 mm diameter) or nickel foil (~1 cm x 1.0 cm x 0.00125 cm), counter (platinum gauze), and a reference electrode (Ag/AgCl (1.0 M KCl)).

5.2.4.6 Electrodeposition of Bi-CMEC

Prior to electrodeposition, the working bare carbon disc electrode (3.0 mm diameter) or graphite plate (~1 cm x 1.0 cm x 0.1 cm) was first polished with 0.05 micron alumina powder in Millipore water and then sonicated in Millipore water to remove residual powder. This electrode was later submersed in an aqueous electrolyte solution containing 0.02 M bismuth(III) nitrate ($Bi(NO_3)_3$), 1.0 M hydrochloric acid (HCl), and 0.5 M potassium bromide (KBr) where a series of cyclic voltammetry sweeps (10 cycles, 100 mV s^{-1}) were performed with applied potentials ranging from 0.05 to –0.55 (V) vs. SCE. Following the electrode conditioning, the GCE was agitated to remove exfoliated material formed on the electrode surface. Using the same electrolyte solution, controlled potential electrolysis (CPE) applied a constant potential of –0.21 (V) vs. SCE until a total of 3 C cm^{-2} was passed. The now Bi-modified electrode was rinsed with hydrochloric acid (HCl), Millipore water, then acetonitrile (MeCN), followed by a drying step consisting of a gentle N_2 flow over the modified surface.

This consisted of a three-electrode system; working bare carbon disc electrode (3.0 mm diameter) or graphite plate (~1 cm x 1.0 cm x 0.1 cm), counter (platinum gauze), and a reference electrode (Ag/AgCl (1.0 M KCl)).

5.2.4.7 ^{1}H NMR

^{1}H NMR was performed with aliquots from the cathode solution to detect any solution products from electrolysis and/or decomposition of electrolyte solution. Samples were run in dCD_3CN. Formic acid production was monitored at 8.1 ppm and imidazolium-carboxylate adduct was monitored at 7.17 and 7.13 ppm.

5.3 Results and Discussions

In exploring the electrochemical properties of neat RTILs during electrolysis, our pioneering Bi-CMEC platform prepared via acid aqueous electrodeposition was used for these initial studies. The published metrics for Bi-CMEC will act as a reference for possible deviations in catalysis upon changing the electrolytic environment. To study the electrocatalytic behavior of neat RTIL electrolyte systems, cyclic voltammetry (CV) and controlled potential electrolysis (CPE) were performed.

5.3.1 Exploring the Electrocatalytic Properties of RTIL Electrolyte

CV was used to observe the cathodic features upon scanning through potential ranges of –1.0 to –2.25 (V) vs. SCE (all potentials will be referred to this reference) under CO_2 and N_2 saturated [BMIM]OTf and [BMIM]PF_6, as shown in Figure 5.1a.

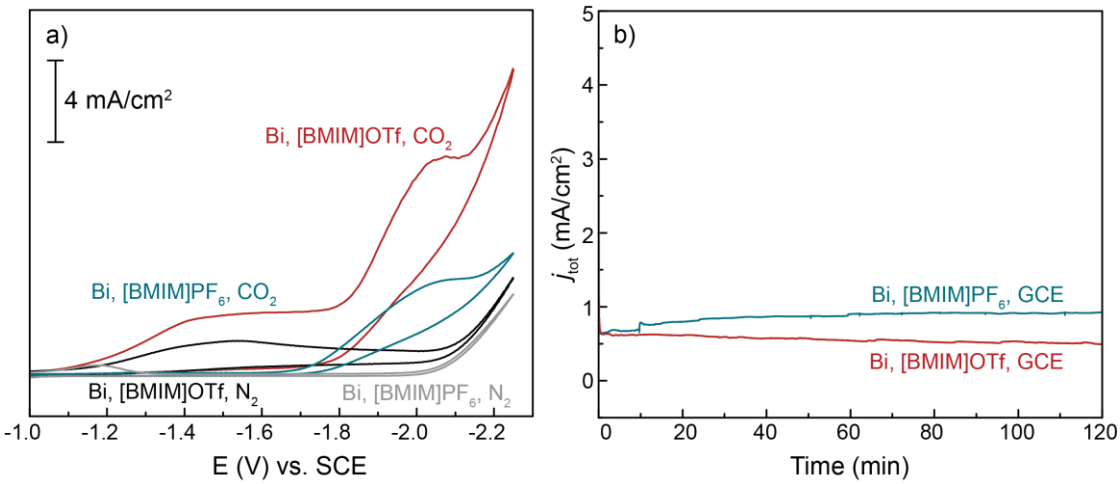

Figure 5.1. Cyclic voltammograms a) for [BMIM]OTf under CO_2 and N_2 (red black traces respectively) and [BMIM]PF_6 under CO_2 and N_2 (blue and gray traces respectively). Plot b) illustrates the current density for [BMIM]OTf (red trace) and [BMIM]PF_6 (blue trace).

[BMIM]OTf and [BMIM]PF_6 both showed polarization curves with a cathodic rise at ~ –1.8 V and a peak maximum at ~ –2.0 V under CO_2. The current enhancements were not present when the RTIL was saturated with N_2, suggesting that these features are due to CO_2 reduction specifically. When applying a constant potential at the peak maximum, the current densities for these RTILs were steady over time and showed no signs of passivation (Figure 5.1b). Possible types of passivation would include IL decomposition or film deterioration. [BMIM]PF_6 surprisingly demonstrated slightly faster kinetics than the less viscous [BMIM]OTf. This may in part be to the heightened capacitive feature observed in Figure 5.1a for [BMIM]OTf (–1.2 to –1.8 V). However, these current densities are comparable and deviate only by 0.3 mA/cm^2.

Table 5.1. CPE metrics for neat [BMIM]OTf and [BMIM]PF_6 with Bi-CMEC/GCE at –1.95 (V) vs. SCE at room temperature.

electrode	IL	FE_{CO} (%)	FE_{H2} (%)	j_{CO} (mA cm^{-1})	j_{H2} (mA cm^{-2})
Bi-CMEC	[BMIM]OTf	82 ± 4	10 ± 4	0.41 ± 0.01	0.05 ± 0.02
Bi-CMEC	[BMIM] PF_6	86 ± 8	4 ± 2	0.77 ± 0.11	0.04 ± 0.02

The amount of CO evolved using Bi-CMEC was comparable to CO production for organic electrolyte systems using dilute concentrations of 1,3-dialkylimidazolium RTILs (100 mM), as summarized in Table 5.1. The selectivity for CO was comparable for both RTILs and was accompanied with trace H_2 production and no side products, i.e. formic acid. Unfortunately, the current densities for both RTILs were <1 mA/cm^2. This was found to be the major drawback to using RTILs as solvent, such that substantially lower rates are achieved from their high viscosities. Bi-CMEC typically has rates ~5x faster when it is submersed in acetonitrile (MeCN) with dilute IL (100 mM) and supporting electrolyte.

Because electrolyte conductivity is a measure of the available ion charge carriers and their mobility, it was intriguing to observe how low the current densities were with RTIL electrolyte. High conductivities may be expected for ILs since they are composed solely of charged ions, however, their degree of ion pairing is so large (likely form ion aggregates, that they experience reduced mobility.[8] In keeping with RTIL as the solvent, methods to establish faster rates were explored to further our study of understanding the physical properties of RTILs during electrocatalysis.

5.3.2 Exploring Methods for Rate Enhancement

Two variables that affect the rate of an electrochemical reaction are the applied potential and temperature. The drawback to changing the potential is that the product

selectivity is jeopardized.[15,16] Additionally, applying more negative potentials risks reducing the RTIL itself and can affect the binding affinities for adsorbates to no longer satisfy the Sabatier principle. Therefore, altering the temperature at which catalysis takes place was the ideal method for initiating the movement of species in solution. Temperature effects were studied via variable temperature linear sweep voltammetry (VT LSV) where deviations in the cathodic peak maxima in the polarization curve were monitored.

5.3.2.1 Promoting Rate with Temperature Elevation

The VT electrochemical experiments were performed with a carbon plate electrode in lieu of a carbon disc electrode. Disc electrodes can only withstand gentle heating (≤ 60 ºC) and were therefore not compatible for the following experiments.

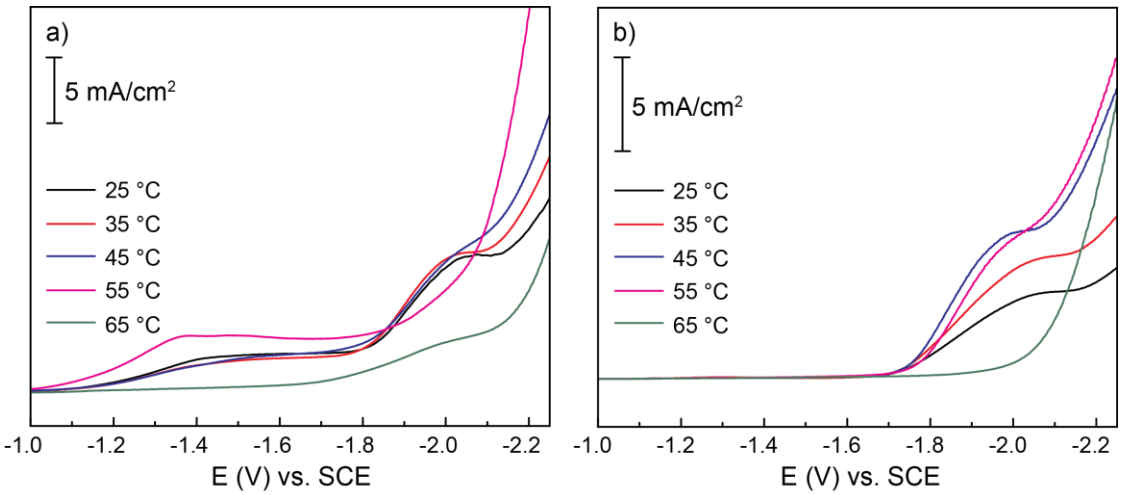

Figure 5.2. Variable temperature cyclic voltamograms are shown for Bi-CMEC in CO_2 saturated a) [BMIM]OTf and b) [BMIM]PF_6.

VT LSV was used to detect the current responses for the CO_2 reduction activity of Bi-CMEC in neat RTIL when the temperature was incremented by 10 ºC, starting from room temperature (RT, 25 ºC). The solution sat at each temperature for 5 minutes prior to collecting the voltammogram to assure accurate activity readings.

Interestingly [BMIM]OTf showed no appreciable changes in activity up to 45 ºC. [BMIM]PF_6 showed a current density enhancement of ~ 2 mA/cm^2, with 45 ºC being the optimal temperature. Both RTILs demonstrated a loss in activity at 55 ºC and a complete drop in activity at 65 ºC. These similarities ignited curiosity on the durability of the RTILs or of Bi-CMEC at elevated temperatures.

At this point, decomposition of the RTILs was unlikely due to their high published decomposition temperatures. Therefore, the likely cause for the current drop was due to the film itself. Despite being robust at RT, the ohmic strength for Bi-CMEC was suggested to weaken at elevated temperatures. In pursuing VT electrocatalysis on RTILs, a more robust catalyst was used (Sn-CMEC).

5.3.3 Pursuing a More Robust Catalyst Platform

Previous study demonstrated how impressively similar the Bi- and Sn-CMEC platforms are in terms of electrocatalytic activity for the reduction of CO_2 to CO. When studied in dilute RTIL solutions, their selectivity for CO was analogous, nearing 80 %, and both demonstrated current densities approaching 10 mA/cm^2.[10] When Sn was electrodeposited onto Ni electrodes, the film was not found to lose its ohmic connect with the substrate. These factors contributed to Sn-CMEC being an appropriate substitute for the VT electroanalytical studies.

5.3.3.1 CO_2 Reduction Activity for Sn-CMEC at Variable Temperatures

Polarization curves for Sn-CMEC via VT LSV were obtained in a similar manner as done previously with Bi-CMEC. The key differences being the Sn-modified Ni plate electrode. As illustrated in Figure 5.3, the starting temperature was 25 ºC and each consecutive segment was incremented by 10 ºC.

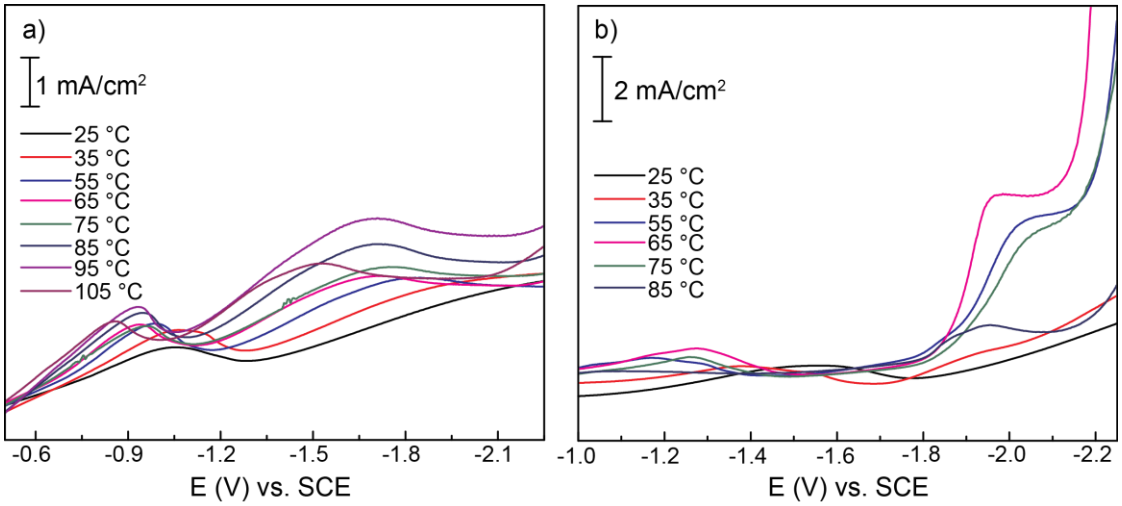

Figure 5.3. Variable temperature linear sweep voltammetry for Sn-CMEC/Ni foil in CO_2 saturated a) [BMIM]OTf and b) [BMIM]PF_6.

Here, current enhancements were now observed for both neat [BMIM]OTf and [BMIM]PF_6 with the introduction of heat as shown in Figure 5.3a and b respectively. Approaching higher temperatures while obtaining more appreciable current responses suggests the Sn/Ni ohmic interaction can withstand these more aggressive electrolysis conditions. Further, a gray lustrous film was observed on the Ni foil electrode after these experiments were performed.

[BMIM]OTf and [BMIM]PF_6 demonstrated greatest activity for CO_2 reduction at 95 ºC and 65 ºC respectively. This difference may be due to the intrinsic properties of the RTILs, i.e. viscosity, binding modes. Importantly, the durability of each RTIL must also be considered. Although these temperatures do not approach their published decomposition temperature, RTILs have been found to decompose below their onset temperature.[17] Decomposition is triggered by either the cation or the anion of the IL.[18] Because these are both 1-butyl-3-methylimidazolium ILs, the anion is the likely source of instability. For instance, [BMIM]PF_6 has a greater durability risk than [BMIM]OTf because it can slowly hydrolyze during electrolysis.[19] These physical changes may not have been present in previous study because the RTILs were only used in small concentrations (100 mM). Because of this risk in decomposition, the solution will be monitored by ^{1}H NMR after electrolysis studies.

These results, in comparison to the electrochemical results for Bi-CMEC, stresses the importance of the catalyst and substrate interaction. Each catalyst possesses unique behaviors that respond to reaction environments differently. Because the Sn/Ni foil platform demonstrated greater durability than Bi/GCP, Sn will therefore act as the optimal catalyst platform to the remainder of this study exploring the catalytic effects for RTIL electrolyte at elevated temperatures.

5.3.4 Electrolysis with Sn-CMEC at Variable Temperature

Observing that higher current densities were achieved at elevated temperatures for both RTILs, VT CPE was performed to further observe the stability of the Sn cathode and the RTIL durability for the duration of electrolysis. CPE was performed at 25, 55, and 100 ºC for [BMIM]OTf and [BMIM]PF_6 at an applied potential of –1.95 V. In

addition to monitoring the stability of the solution and Sn electrode, the gaseous products were detected with inline gas chromatography (GC).

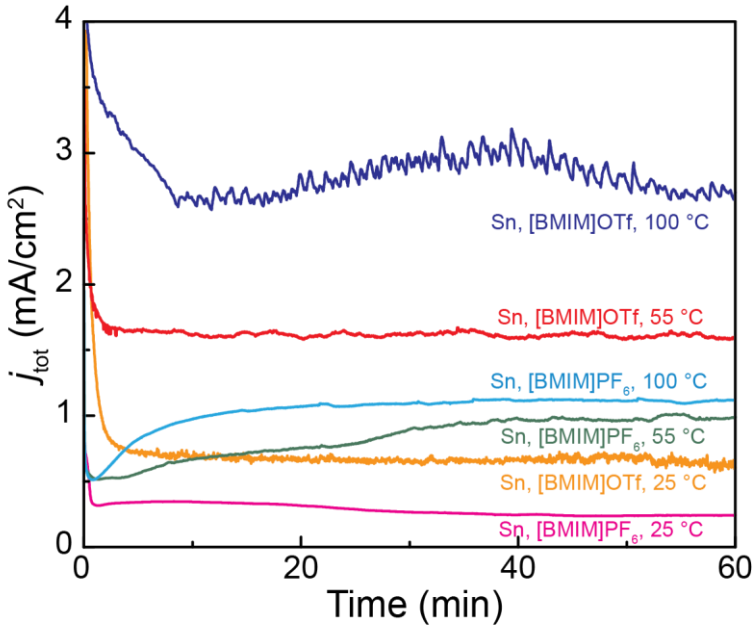

Figure 5.4. Current density plot for Sn-CMEC in neat [BMIM]OTf and [BMIM]PF_6 at 25, 55, and 100 ºC at –1.95 (V) vs. SCE.

The current density plot in Figure 5.4 summarizes the VT CPE experiments for [BMIM]OTf and [BMIM]PF_6 performed at 25, 55, and 95 ºC using Sn-CMEC/Ni foil. Importantly, the current density plot revealed steady current over the duration of electrolysis for both RTILs. This suggested that the ohmic contact remains robust at all temperature ranges.

Additionally, the current density was found to increase with every temperature increment, as summarized in Table 5.2. Interestingly, [BMIM]OTf was found to have

faster rates at each temperature studied than [BMIM]PF_6. This is likely the result of varied viscosity between the RTILs and its effect on diffusion; [BMIM]OTf and [BMIM]PF_6 have a viscosity of 90 and 450 cP respectively.[14] Because [BMIM]OTf is one of the least viscous imidazolium ionic liquids and is not surprising to see a greater enhancement in current in comparison to [BMIM]PF_6.

Table 5.2. VT CPE metrics for Sn-CMEC performed at –1.95 (V) vs. SCE.

IL	ºC	FE_{CO} (%)	FE_{H2} (%)	j_{tot} (mA cm^{-2})
[BMIM]PF_6	25	3 ± 1	63 ± 14	0.3 ± 0.1
	55	2 ± 1	68 ± 3	1.0 ± 0.2
	100	1 ± 1	99 ± 4	2.3 ± 0.2
[BMIM]OTf	25	58 ± 3	46 ± 9	0.6 ± 0.01
	55	61 ± 3	34 ± 2	1.4 ± 0.3
	100	71 ± 3	7 ± 1	2.2 ± 0.1
	125	---	92 ± 7	6.8 ± 0.4
	150	---	97 ± 6	14.3 ± 0.4
	175	---	48 ± 4	32.3 ± 0.2

When monitoring the product distribution via GC analysis, it was fascinating to find that [BMIM]PF_6 was not selective for CO evolution at any temperature range, whereas [BMIM]OTf was. The difference in electrochemical behavior sparked interest because Bi-CMEC showed no deviations in CO selectivity for the two RTILs when used in dilute concentrations. This emphasizes the significance of the cathode and substrate conditions.

From 25 ºC to 100 ºC for [BMIM]OTf, the temperature enhancement suppressed H_2 production and promoted CO selectivity. This correlation between temperature enhancement and CO evolution enhancement was promising. This observation encouraged more elevated temperatures to be investigated in hopes of obtaining even

greater CO selectivity and current densities. Upon doing so, the current density continued to increase, however, it was interesting to observe an abrupt switch is product selectivity to favor H_2 evolution with no co-production of CO. Figure 5.5a and b illustrates the deviations in product selectivity for [BMIM]OTf and [BMIM]PF_6 respectively.

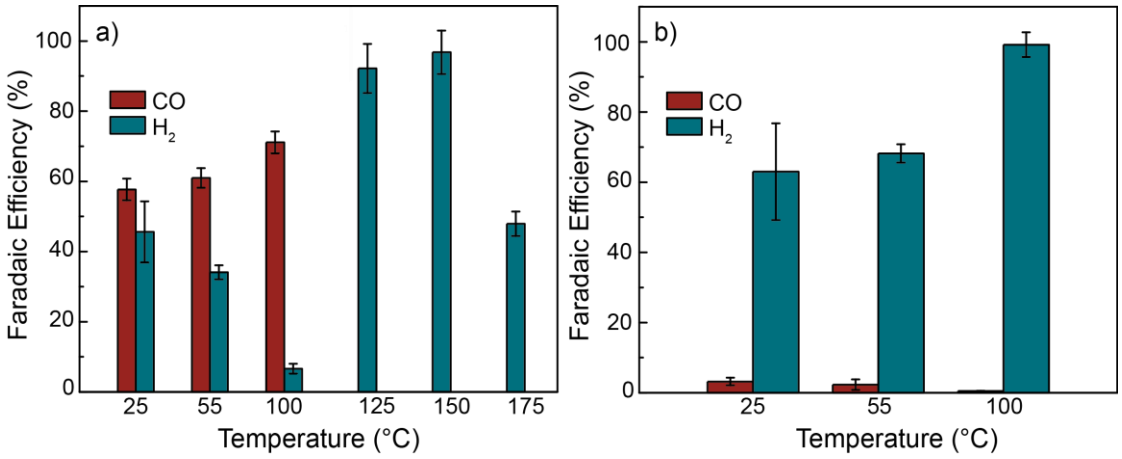

Figure 5.5. Bar graphs summarizing the evolution of CO (red) and H_2 (blue) for CO_2 saturated a) [BMIM]OTf and b) [BMIM]PF_6 using the Sn/Ni foil electrode at –1.95 (V) vs. SCE.

It was fascinating to observe a continued rise in current density despite a shutdown in catalysis and CO production. Therefore, control studies were performed via CPE in the absence of Sn-CMEC to observe if the rise in current was due to the Sn/RTIL interaction, or the RTIL's physical response to temperature enhancement. The metrics from the control CPE experiments are summarized in Table 5.3. No observable gaseous products were detected within our GC detection limits and ^{1}H NMR after CPE revealed no detection of solution products.

Table 5.3. VT CPE metrics for control studies with unmodified Ni foil at –1.95 (V) vs. SCE.

electrode	IL	ºC	FE_{CO} (%)	FE_{H2} (%)	j_{tot} (mA cm^{-2})
none	$[BMIM]PF_6$	25			0.20 ± 0.01
		55			0.48 ± 0.09
		100			0.83 ± 0.05
none	[BMIM]OTf	25			0.19 ± 0.01
		55			0.61 ± 0.12
		100			1.70 ± 0.10

As shown in the Table 5.3 and the overlaid current density plots in Figure 5.6a and b for [BMIM]OTf and $[BMIM]PF_6$ respectively, the current density still increases with respect to temperature even in the absence of Sn-CMEC. This suggested that the RTIL ion dissociation for rate enhancement (ion movement) is highly dependent on temperature, but does not necessarily have a direct effect on the rate for electron transfer (ET) events. Regardless, it is important to note that the current density is overall greater with Sn-CMEC.

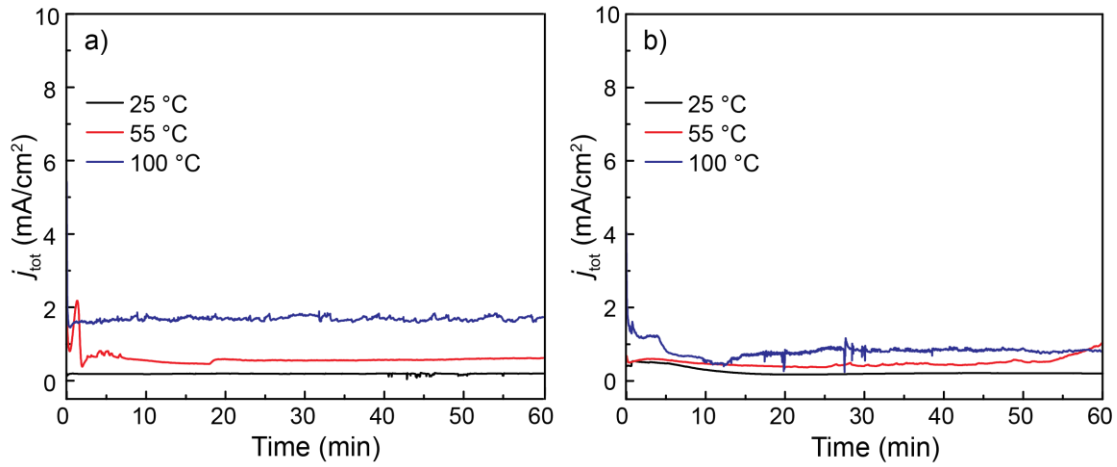

Figure 5.6. Current Density plots for CO_2 saturated a) [BMIM]OTf and b) $[BMIM]PF_6$ without Sn-CMEC. –1.95 (V) vs. SCE.

When comparing the total current density for [BMIM]OTf and [BMIM]PF_6 with and without the Sn-modified Ni foil at the varied temperature ranges, it was fascinating to observe that the rate enhancement for [BMIM]PF_6 with Sn-CMEC was equivalent to the rate enhancement for [BMIM]OTF without Sn-CMEC (within standard deviations). This relationship is illustrated in Figure 5.7.

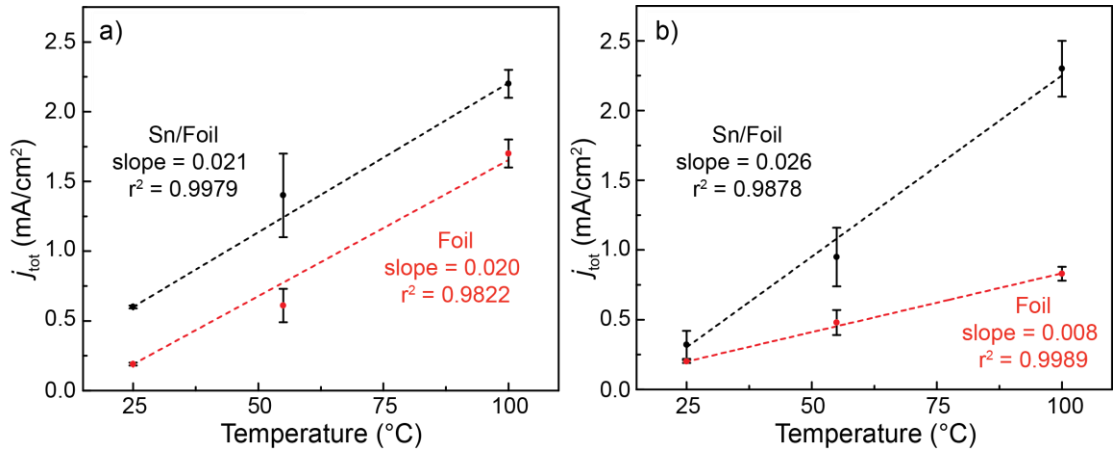

Figure 5.7. Total current density correlation to temperature enhancement for neat a) [BMIM]OTf and b) [BMIM]PF_6 for the Sn/Ni foil electrode (black trace) and the bare Ni foil electrode (red trace).

The current density enhancement for [BMIM]OTf with and without the Sn-modified electrode was not found to be dependent on the catalyst. Importantly, and as previously emphasized, the overall kinetics are greater when Sn is present. Conversely, [BMIM]PF_6 demonstrated a greater dependence on the Sn catalyst, shown by the higher slope for Sn/foil compared to the bare unmodified Ni foil. Based on these deviations, and understanding that catalysis does not occur without the Sn/IL interface, this supports

that an increase in current due to an increase in temperature does not directly relate to enhancements in ET events for the CO_2 to CO transformation.

Now understanding why current density (rate of reaction) increases despite demonstrating poor product selectivity, it was of interest to investigate why [BMIM]OTf and [BMIM]PF_6 behave so differently during catalysis. This is critical for understanding the electrochemical properties of RTIL solvent for CO_2 to CO electrocatalysis. Specifically, it is curious as to why [BMIM]PF_6 does not evolve CO regardless of the temperature condition, and why product selectivity switches from CO to H_2 evolution for [BMIM]OTf (T >100 ºC).

5.3.5 Investigation of RTIL Electrocatalytic Behavior

To clarify the differences in catalytic behaviors between these RTILs, their electrochemical behavior was probed with electrochemical impedance spectroscopy (EIS) and circuit analysis.

5.3.5.1 Temperature Effects on Electrochemical Behavior of RTILs

Electrochemical impedance spectroscopy measures the resistive (Z′″, real) and capacitive (–Z″, imaginary) components of the rate determining step (RDS) of an electrochemical reaction. The relationship between these components are reported in a Nyquist plot. The RDS has experimentally been suggested to be the first electron transfer to form $CO_2^{\bullet-}$. MD simulation suggested that IL stabilizes the $CO_2^{\bullet-}$ on the surface thus lowing the kinetic energy barrier. This is observed in Nyquist plots by the resistance to charge transfer (R_{CT}). The smaller the R_{CT}, the more favorable the electrochemical transformation and the smaller the kinetic barrier.

The Nyquist plot in Figure 5.8 summarizes the electrochemical behavior for [BMIM]OTf (red trace) and [BMIM]PF_6 (blue trace) at 25 ºC.

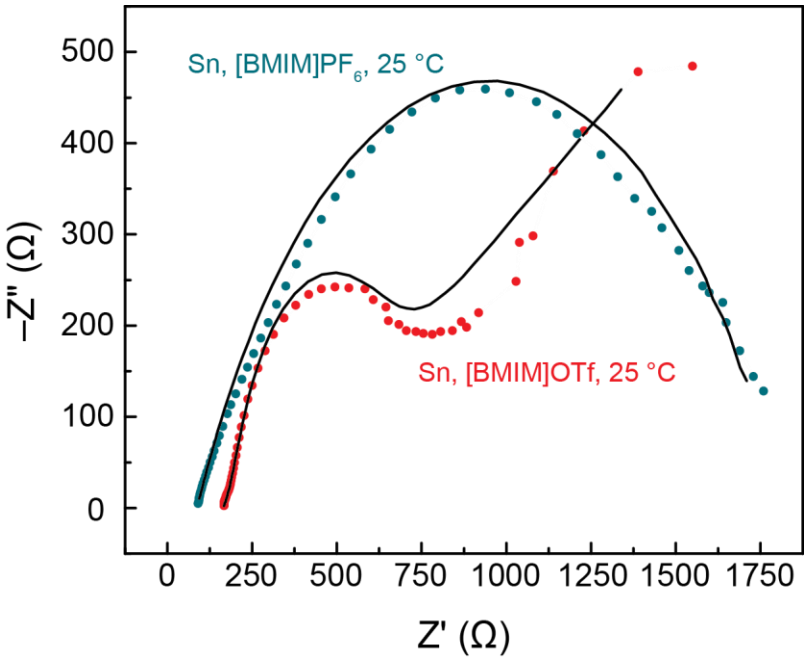

Figure 5.8. Nyquist plot for CO_2 saturated [BMIM]OTf (red dots) and [BMIM]PF_6 (blue dots) at 25 ºC. Dots represent experimental data and black lines represent 2RC simulations.

There are observable deviations in R_{CT} and diffusion behavior for the two RTILs. Specifically, [BMIM]OTf had an R_{CT} of ~500 Ω and demonstrated a single semicircle followed by a linear region with a slope of ~0.5. This linear region represents diffusion into the solution bulk at lower frequencies. [BMIM]PF_6, however, only displayed a large diffuse semicircle with an R_{CT} >1,600 Ω and no observed diffusion region. This suggests an explanation for the varied metrics between the two RTILs. [BMIM]PF_6 at 25 ºC appears to be too viscous to encourage diffusion from the electrode

surface to the solution bulk. With poor diffusion, reactants (CO_2) will find difficulty migrating to the surface active sites, and products (CO) will find difficulty diffusing away from the electrode surface. Difficulty leaving the electrode surface jeopardizes further reduction to more reduced hydrocarbon species to result in poor CO selectivity.

Understanding how the electrochemical behavior for the RDS compares at 25 ºC for [BMIM]OTf and [BMIM]PF_6, it was of interest to observe if this behavior is consistent or if it deviates at elevated temperatures. EIS was performed at 25, 55, 100, 125, 150, and 175 ºC for each RTIL in a CO_2 saturated environment. The results are summarized in Figure 5.9a and b for [BMIM]OTf and [BMIM]PF_6 respectively.

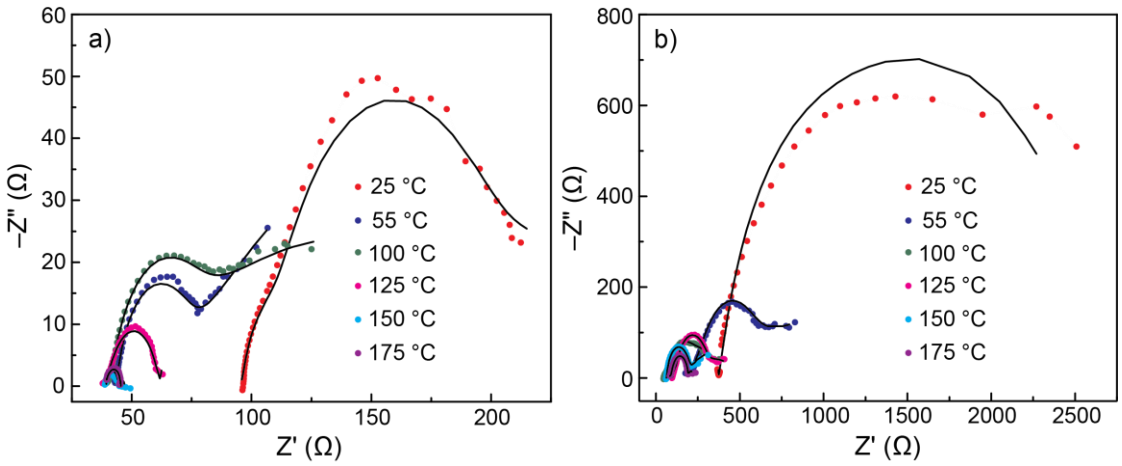

Figure 5.9. Nyquist plots for CO_2 saturated a) [BMIM]OTf and b) [BMIM]PF_6 for Sn/Ni foil at 25 (red dots), 50 (navy dots), 100 (green dots), 125 (pink dots), 150 (cyan dots), and 175 ºC (purple dots) at –1.95 (V) vs. SCE. Dots represent experimental data and black lines represent 2RC simulated data.

The VT EIS studies elucidated information on the resistance of solution (R_{sol}) and R_{CT}. R_{sol} is detected at high frequencies. It is seen in the Nyquist plot at the start of

the semicircle impedance response. For both [BMIM]OTf and [BMIM]PF_6, R_{sol} is most resistive at 25 ºC, ~95 Ω and ~375 Ω respectively. This suggested that the RTILs are most viscous at RT. The R_{sol} was immediately reduced when the temperature was incremented 30 ºC for both RTILs. For [BMIM]OTf, R_{sol} was reduced to ~25 Ω at 55 ºC and remained unperturbed for the following temperature increments. [BMIM]PF_6 maintained its lowest R_{sol} (~80 Ω) at temperatures ≥100 ºC. The decrease in R_{sol} for both RTILs corresponds to the observed increase in current density with increasing temperature (Figure 5.4). With a lower R_{sol}, reactants and products can diffuse to and from the electrode surface more easily.

R_{CT} is the resistance associated with the rate determining ET step. For all temperature ranges, [BMIM]OTf demonstrated a smaller R_{CT} than [BMIM]PF_6. The R_{CT} for [BMIM]OTf continuously decreased until 175 ºC. Interestingly at ≥125 ºC, the impedance response no longer demonstrated a linear diffusion feature at lower frequency inputs. [BMIM]PF_6 showed minimal deviations in R_{CT} at ≥100 ºC, yet showed no diffusion feature at any temperatures. The lack of, or sudden absence of this region may be due to complications with the RTIL composition at harsh temperatures.

To detect if the RTIL composition was being jeopardized, the Sn/RTIL interface after electrolysis was studied via XPS and the RTIL electrolyte solution was studied via ^{1}H NMR. Importantly, the mechanisms for both RTIL systems were elucidated with circuit analysis for the varied temperature ranges.

5.3.5.2 Circuit Analysis for Mechanistic Elucidation

Pairing impedance responses with circuit analysis allowed for mechanistic information on the RDS to be elucidated. Circuits are typically composed of a capacitor (C) and resistor (R) in parallel to form a time constant (RC). Each time constant

represents an electrochemical phenomenon. When multiple time constants are arranged in series with one another, multiple electrochemical phenomenon are described.

Sn-CMEC in dilute RTIL organic electrolyte solutions have been successfully modeled with the 3RC circuit illustrated in Figure 5.10a.

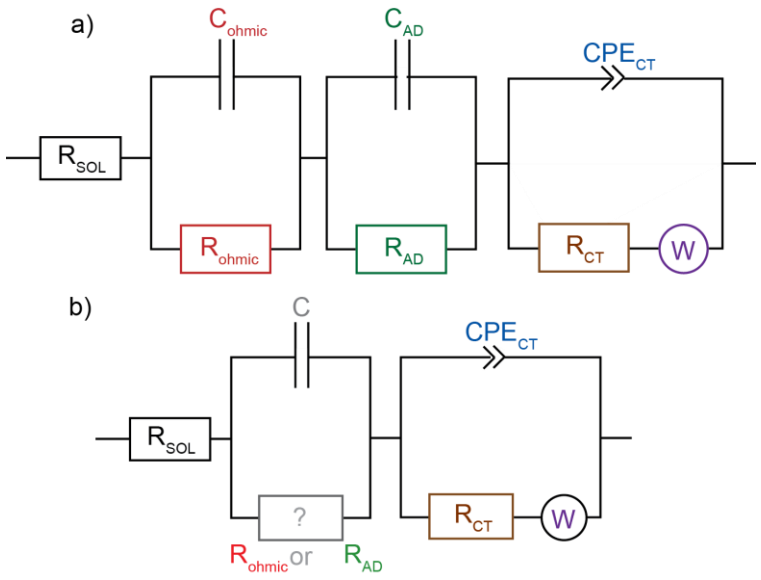

Figure 5.10. The 3RC and 2RC circuits are illustrated in a) and b) respectively.

The 3RC circuit consists of three RCs representing three different electrochemical phenomena: ohmic resistance (R_{ohmic}), adsorption resistance (R_{AD}), and R_{CT}. To account for diffusion, demonstrated by the linear region at low frequencies, a Warburg element (W) was implemented in the circuit design which is composed of an infinite array of resistors and capacitors. A constant phase element (CPE) was used to account for unideal charging of the double layer, such as ununiform film surfaces or charge accumulation. R_{ohmic} is the resistance between the substrate and electrodeposited

Sn film. R_{AD} is sometimes observed in the Nyquist plot as two conjoined semicircles, which we have found in previous study to be representative of adsorption of imidazolium-based ILs. Sn has been shown to experience an adsorption event, but the two semicircles are broad and overlap to give the appearance of one semicircle. The two overlapping semicircles were discovered by simulating its impedance response with both the 3RC and 2RC (Figure 5.10a and b respectively). The 2RC, which lacks an adsorption phenomenon (R_{AD}), was found to poorly simulate the experimental data comparison to the 3RC (See Chapter 4), as represented by a smaller R-squared (R^2) value.

Curious if the 3RC still mimics the mechanism for Sn in RTIL electrolyte, the impedance responses at varied temperatures were fit to the 3RC and 2RC circuits. Their least squares fittings with respect to applied temperature are shown in Figure 5.11.

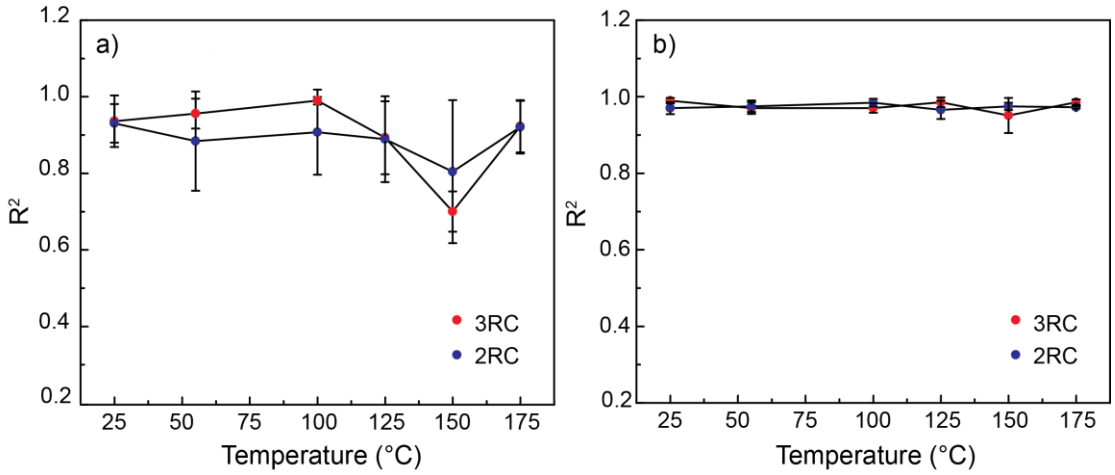

Figure 5.11. R-squared values for the 3RC (red trace) and 2RC (blue trace) fittings for a) [BMIM]OTf and b) [BMIM]PF_6 at 25, 50, 100, 125, 150, and 175 ºC using the Sn/Ni foil at –1.95 (V) vs. SCE

The R^2 results demonstrate deviations from what was found for Sn-CMEC in dilute RTIL systems. The 3RC and 2RC circuit show minimal discrepancies, such that the mechanisms can be described with the simpler 2RC model. Because Sn is known to have overlapping semicircles for R_{AD}, it was curious if the first RC for the 2RC circuit represents R_{ohmic} or R_{AD}. Therefore, the high frequency region in the Nyquist plot was investigated to clarify the first electrochemical phenomenon.

R_{ohmic} is represented by an "L" feature ("elbow") at high frequency. When there is minimal resistance to facilitate the ET from the substrate through the film, this ohmic feature will be a pronounced. The ohmic region at 25, 55, and 100 ºC is illustrated in Figure 5.12a and b for [BMIM]OTf and [BMIM]PF_6 respectively.

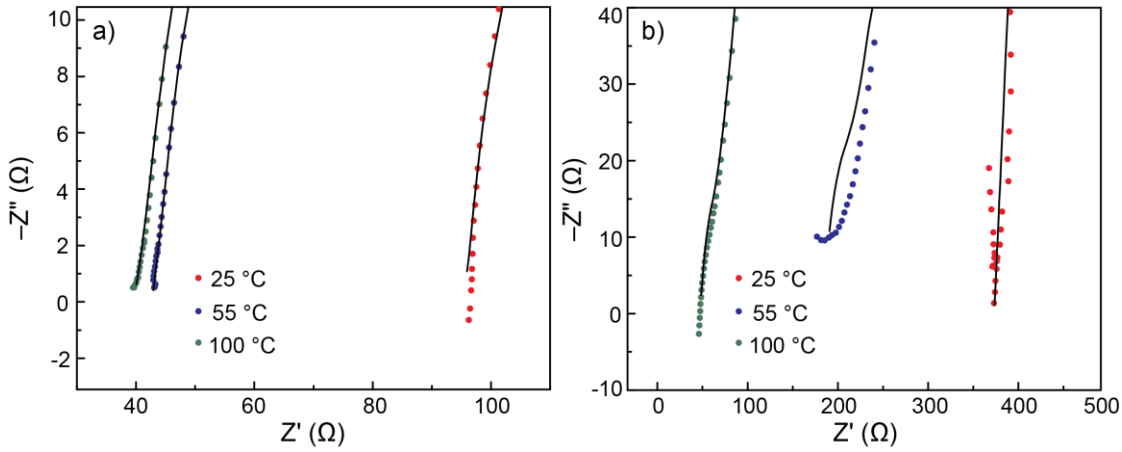

Figure 5.12. Nyquist plot high frequency regions for CO_2 saturated a) [BMIM]OTf and b) [BMIM]PF_6 using Sn/Ni foil electrode at –1.95 (V) vs. SCE.

Interestingly, there was no ohmic feature for either RTIL at any temperature. Because there is no high frequency feature, this electrochemical phenomenon is

insignificant for the circuit design and suggested that the first RC in the 2RC circuit represents R_{AD}. It was intriguing, however, to observe no ohmic phenomenon between the substrate and film for Sn-CMEC. A highly resistive surface suggests that the enhanced viscosity of the RTIL solvent is making charge transfer events challenging at the surface.

Circuit analysis aided to elucidate mechanistic information for RTIL solvent for electrocatalysis for Sn-CMEC. In comparison to dilute IL systems in MeCN, IL adsorption remains an essential phenomenon for facilitating charge transfer processes. This suggested that despite having greater resistivity at the surface (R_{ohmic}), the mechanisms for concentrated and dilute RTIL systems appears analogous. With added resistivity, however, it was curious to detect more directly how the solution resistivity effects the movement of ions. This was performed by Bode analysis to calculate the capacitance of the double layer (C_{DL}).

5.3.5.3 Bode Analysis for the Elucidation of C_{DL}

Bode plots are derived from Nyquist plots to obtain information on the ion movement specifically by the C_{DL}. C_{DL} provides information on surface area and the speed of ion movement, which is stressed to be largely dependent on the surface chemistry.[20] Specifically, C_{DL} is influenced by electrode potential, ion types, surface roughness, temperature, and impurity adsorption.[21] Therefore, any deviation in these variables will affect the solution mobility. Here, the applied potential was constant (–1.95 V) and the surface roughness is constant (Sn-modified Ni foil was cut into two identical pieces (0.5 cm x 1.0 cm x 0.00125 cm) for [BMIM]OTf and [BMIM]PF_6 EIS experiments). C_{DL} will now be largely influenced by temperature, anion, and possible impurity adsorptions (imidazolium-carboxylate).

For Bode plots, impedance and frequency values are manipulated into log |Z| (y-axis) and log ω (x-axis) respectively. Z is the absolute impedance and is calculated by equation 5.1. In the Nyquist plot, Z´ is the real component (resistive) and Z˝ is the imaginary component (capacitive). ω is the frequency in radians and is calculated by equation 5.2, where *f* is the frequency applied during EIS.

$$|Z| = \sqrt{Z'^2 + Z''^2} \qquad (5.1)$$

$$\omega = 2\pi f \qquad (5.2)$$

$$|Z| = 1/C_{DL} \qquad (5.3)$$

The Bode plot for neat [BMIM]OTf at 25 ºC is illustrated in Figure 5.13a. C_{DL} information was obtained by performing a linear regression on the first frequency break for the first limiting step.[22] The y-intercept will give the value for log |Z|. Deriving log |Z| for the value for Z, equation 5.3 can be used to calculate C_{DL}. C_{DL} values for both RTILs were calculated for the same temperature range studied previously via EIS. Figure 5.13b and c illustrate the C_{DL} value with respect to temperature for [BMIM]OTf and [BMIM]PF_6 respectively.

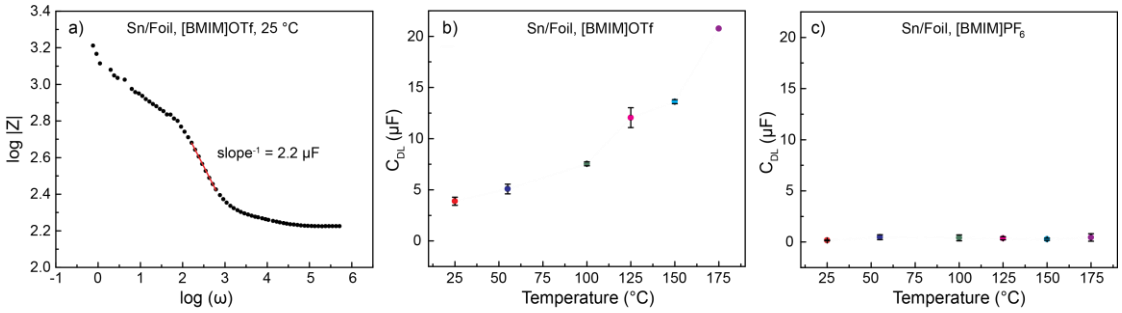

Figure 5.13. Figure a) features the Bode plot for Sn/foil in CO_2 saturated [BMIM]OTf at 25 ºC. The C_{DL} with respect to temperature (ºC) for b) [BMIM]OTf and c) [BMIM]PF_6 are shown for Sn/foil at –1.95 (V) vs. SCE.

Drastic differences were observed for the C_{DL} for [BMIM]OTf and [BMIM]PF_6. [BMIM]OTf demonstrated a positive correlation between C_{DL} and temperature. As expected, 25 ºC showed the lowest C_{DL}, and in turn, the slowest movement of ions. According to the classic Walden rule, the IL should follow typical Arrhenius behavior such that there should be a linear relationship between conductivity and temperature.[23] Up until 100 ºC, this rule holds true. At T ≥100 ºC, the conductivity exponentially increases. This deviation from linearity has been attributed to when the glass transition temperature of the IL is approached.[23,24]

Conversely, the C_{DL} for [BMIM]PF_6 was inert with temperature elevation. This suggested that the current enhancements observed via VT CPE for [BMIM]PF_6 were not from an enhancement in the rate determining ET event. Previous reports which investigated the durability of [BMIM]PF_6 at elevated temperatures found that it became more viscous with increasing temperature.[14,23] Figure 5.13c generally supports that viscosity is not decreasing to enhance ion mobility. This instills greater curiosity for understanding the differences in IL behavior at the electrode surface to recognize how their unique physical properties (i.e. viscosity, stability, cation/anion interaction) effect catalysis.

5.3.6 Detecting RTIL Decomposition

One of the fascinating properties of RTILs is their high decomposition temperature and low volatility. It was previously stated, however, that the decomposition of these RTILs have occurred at temperatures lower than their published onset temperatures. For example, [BMIM]PF_6 and [BMIM]OTf have onset temperatures of 433 and 409 ºC respectively,[25] but their experimental degradation for when 1% of the RTIL decomposes for a given time was found to be 248 and 159 ºC

respectively.[17] Additionally, applying a negative bias during electrolysis and having water in trace amounts ($2H^+/2e^-$ transfer yields CO and H_2O) can further jeopardize the durability of the RTILs.[26] The applied potential for electrolysis (–1.95 V) does not exceed the electrochemical windows for [BMIM]OTf and [BMIM]PF_6 (>4 and >6 V respectively) in that the possible decomposition is from water. These are moisture-sensitive ILs.[27] Possible RTIL decomposition for the cation and anions were investigated by XPS and ^{1}H NMR. Additionally, the metal catalyst high resolution spectra, Sn 3*d*, was also monitored to support that the catalyst is not experiencing degradation (Appendix D.2). The Sn 3*d* high resolution spectra showed no deviation upon varying the temperature. The Sn $3d_{5/2}$ components mimic the composition for the Sn cathode after CPE with a –1.95 V applied potential with dilute IL concentrations (See Chapter 3).

It is important to note that even though there is an abundance of imidazolium species in solution, the chemistry is happening at the surface. If surface imidazolium ILs are decomposing, replenishing these species would be slow and unrealistic if the decomposed IL species strongly adsorbs to the surface to block charge transfer events. RTIL decomposition would likely contribute to the poor catalytic efficiencies and would be a profound discovery because RTIL decomposition was not detected for dilute RTIL systems.

5.3.6.1 Detecting Anion and Cation Decomposition via XPS

XPS is a surface sensitive technique that characterizes a material's elemental composition based on oxidative environments represented by binding energies (BEs). The regions of interest were F 1*s*, P 2*p*, and S 2*p*. These elements appear in the RTIL anions (PF_6^- and OTf^-) for the two RTILs. The anion is the only difference between the

1-butyl-3-methlimidazolium ILs, thus, the stability of the anion was of significant interest. The N 1*s* high resolution region was also investigated to detect the durability of the cation itself.

The F 1*s*, P 2*p*, and S 2*p* high resolution regions are shown in Figure 5.14 for CPE performed at 25, 100, and 175 ºC for [BMIM]OTf, and 25 and 100 ºC for [BMIM]PF_6. The OTf^- and PF_6^- standards are shown at the bottom of the high resolution overlays for F 1*s*, S 2*p*, and P 2*p* regions.

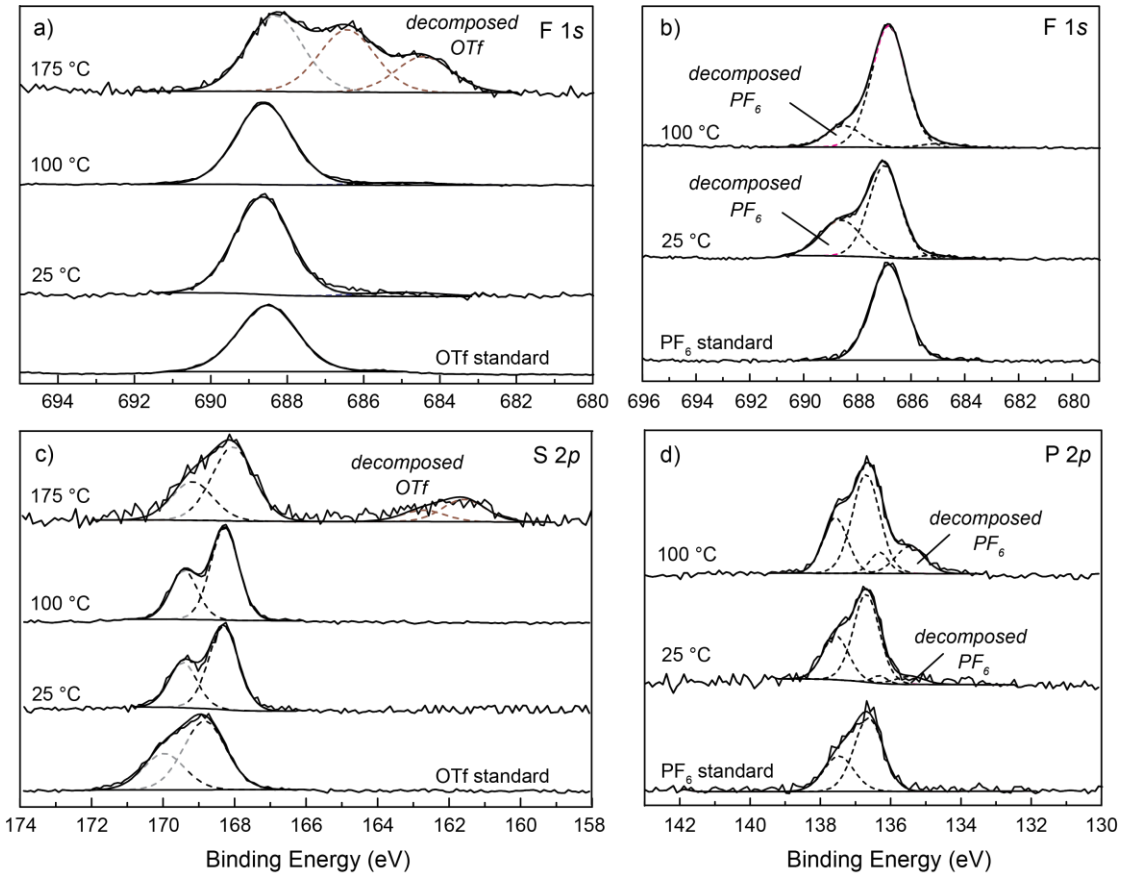

Figure 5.14. F 1*s* high resolution spectra for CO_2 saturated a) [BMIM]OTf and b) [BMIM]PF_6. S 2*p* high resolution spectra for [BMIM]OTf, c). P 2*p* high resolution spectra for [BMIM]PF_6, d). Spectra acquired after CPE at 25, 100, and 175 ºC at –1.95 (V) vs. SCE.

[BMIM]OTf suggested anion thermal stability up until 100 ºC; the F 1*s* and S $2p_{3/2}$ high resolution spectra reveal similar oxidative environments to the OTf^- standard at 688.7 eV and 168.5 eV respectively. At the most extreme temperature (175 ºC), a new oxidative environment is present at 161.6 eV for the S $2p_{3/2}$ high resolution spectrum. The F 1*s* high resolution spectrum also showed a more complicated region

with a shift in the OTf^- component to 688.3 eV and the emergence of two additional components at 686.4 and 684.4 eV.

[BMIM]PF_6 demonstrated signature PF_6^- components for the F 1*s* and P $2p_{3/2}$ high resolution spectra at 686.8 and 136.7 eV respectively at 25 and 100 ºC. At these temperatures, however, there were also signs of PF_6 decomposition. The P $2p_{3/2}$ spectrum showed an emerging component at 135.5 eV and the F 1*s* spectrum showed a growth of a feature at 688.6 eV. It was surprising to observe decomposition of [BMIM]PF_6 at room temperature. [BMIM]PF_6, however, is less robust than [BMIM]OTf and has been observed to decompose at temperatures as low as 120 ºC.[28,29] [BMIM]PF_6 has also been demonstrated to slowly hydrolyze in the presence of water and metal catalysis to form HF and PO_4^{3-} which can dramatically alter the catalytic reaction.[14,30] Its ease in decomposition under non-harsh conditions and inability to tolerate catalysis is significant for the chemical industry looking to use this RTIL as solvent.

In addition to the anion demonstrating poor durability under these reaction conditions, it was curious if the cation was also demonstrating signs of decomposition. Decomposition for imidazolium ILs may involve dealkylation or C2 deprotonation and sequential C2 substitution to prevent further proton transfers.[31] As discussed in Chapter 4, C2 substitution likely occurs with low proton availability and poor diffusion to form the imidazolium-carboxylate adduct. Therefore, detection of this species was monitored.

Signature components in the N 1*s* high resolution region are 1-butyl-3-methylimidazolium ($[BMIM]^+$), carbene, and imidazolium-carboxylate and its decomposition product at 402.1, 400.3, and 401.3 and 399.3 eV respectively. Ideal

catalysis will not show the adsorbed adduct. It is a thermodynamic sink for catalysis and leads to poor CO selectivity and reduced current density.

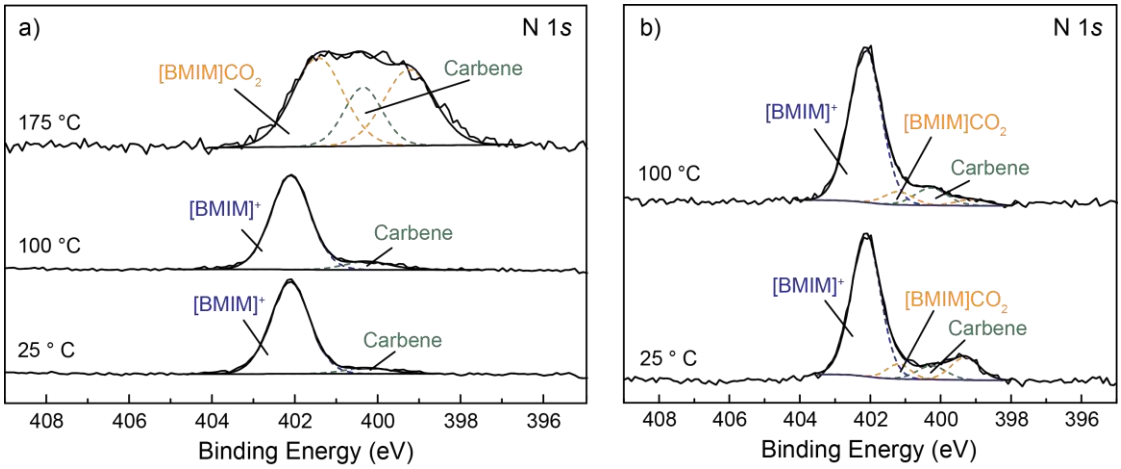

Figure 5.15. N 1*s* high resolution spectra for a) [BMIM]OTf and b) [BMIM]PF_6 after CPE at –1.95 (V) vs. SCE.

Figure 5.15a showed imidazolium stability up to 100 ºC for [BMIM]OTf; like the observed anion stability. At the most elevated temperature (175 ºC), presence of the adduct was now observed with complete suppression of imidazolium at the surface. This suggested that [BMIM]OTf loses stability at T >100 ºC. Because imidazolium-carboxylate is thermodynamically stable, it is not surprising that the adduct will dominate the surface with additions of heat.

Like the anion XPS spectra for [BMIM]PF_6, evidence for cation decomposition was shown at 25 and 100 ºC (Figure 5.15b). [BMIM]PF_6 is highly viscous, such that its mass transport is slower than the less viscous [BMIM]OTf (Table 5.2). With highly

viscous solutions, proton transfer is jeopardized. Therefore, it is not alarming to observe decomposition of imidazolium at room temperature via C2 substitution which is influenced by the nature of the anion.[32]

Observing that an impurity formed and adsorbed to the cathode surface, it was curious if decomposed imidazolium also existed in the bulk. ^{1}H NMR was used to monitor this decomposition.

5.3.6.2 Detecting RTIL Decomposition via ^{1}H NMR

Certain types of cation decomposition for imidazolium ILs at T <160 ºC are: the formation of imidazolium carboxylate, elimination of the 1-butyl side-chain, transalkylation, and retroalkylation (Scheme 5.1a, b, and c respectively).[28] Removal of the alkyl substituent will alter the electronics in the imidazolium ring which will result in a deshielded system and a shift to a slightly higher resonance (C2 proton at ~9.3 ppm).[33]

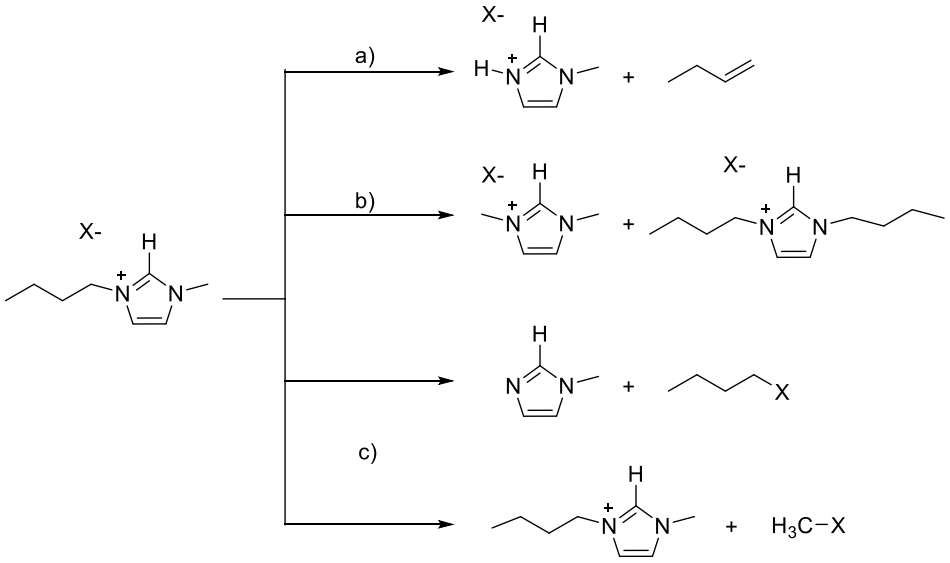

Scheme 5.1. Decomposition types for 1-butyl-3-methylimidazolium: a) elimination, b) transalkylation, c) retroalkylation.[28] X^{-} represents the anion.

^{1}H NMR spectra were obtained after 1 hour of electrolysis. The ^{1}H NMRs for [BMIM]PF_6 are illustrated in Figure 5.16a, b, c, and d for the RTIL standard before CPE and the RTIL solution after CPE at 25, 55, and 100 ºC respectively. At 25 ºC, the aromatic region resembled that of the RTIL standard. At 55 and 100 ºC, a resonance emerged at ~9.4 ppm. This was featured downfield, thus a less shielded system. It is likely that the alkyl substituents are lost on the imidazolium ring, while still existing in solution.

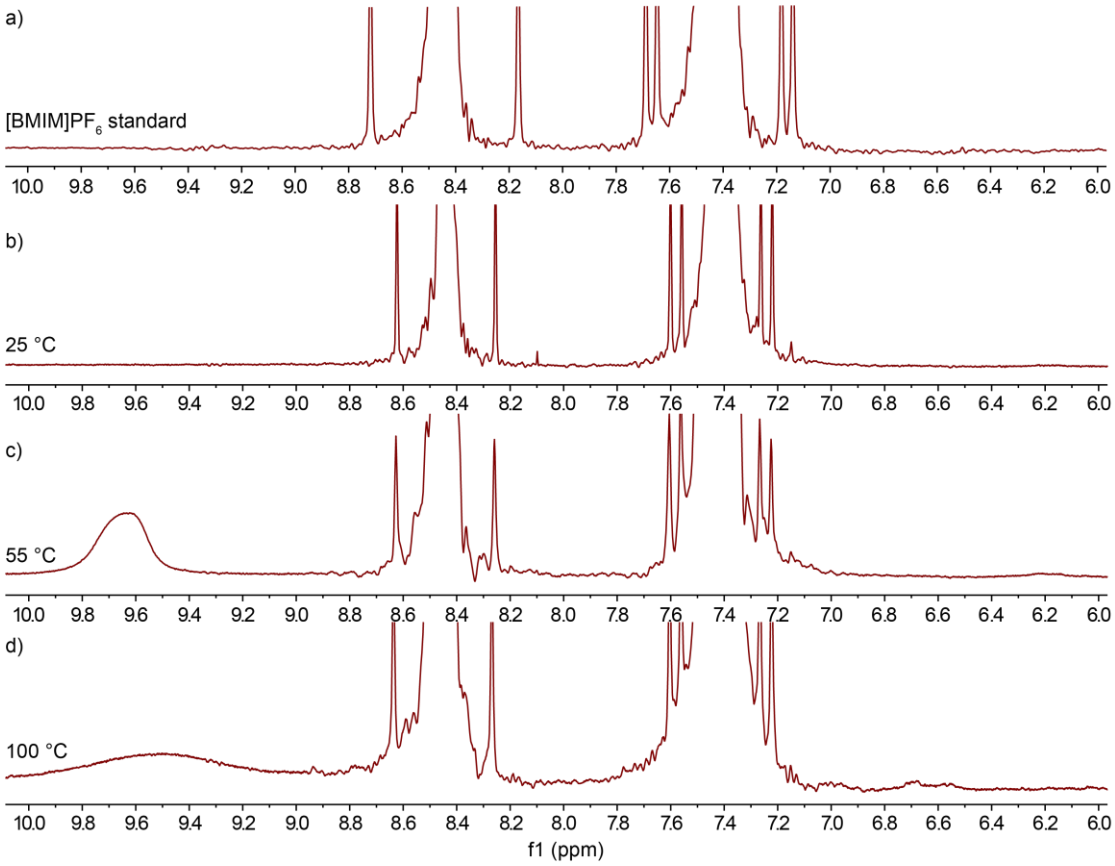

Figure 5.16. ^{1}H NMR for the a) [BMIM]PF_6 standard and the [BMIM]PF_6 solution after CPE at b) 25, c) 55, and d) 100 ºC.

The ^{1}H NMR for the [BMIM]OTf standard, and the RTIL after CPE for 25, 55, 100, 125, 150, and 175 ºC are illustrated in Figure 5.17a, b, c, d, e, f, and g respectively. [BMIM]OTf did not show the same resonance growth as [BMIM]PF_6, but it did show an emergence of a broad resonance at ~7.15 ppm that grew in intensity from 125 to 175 ºC. The ^{1}H NMR for T ≤100 ºC resembled the [BMIM]OTf standard before CPE. This suggested that [BMIM]OTf was resistant to decomposition during catalysis at T ≤100 ºC. The first appearance of this resonance at 125 ºC correlates to the product selectivity switch from CO to H_2 and the detection of imidazolium-carboxylate via XPS. This resonance growth corresponds to the resonance for imidazolium-carboxylate (See Chapter 3).

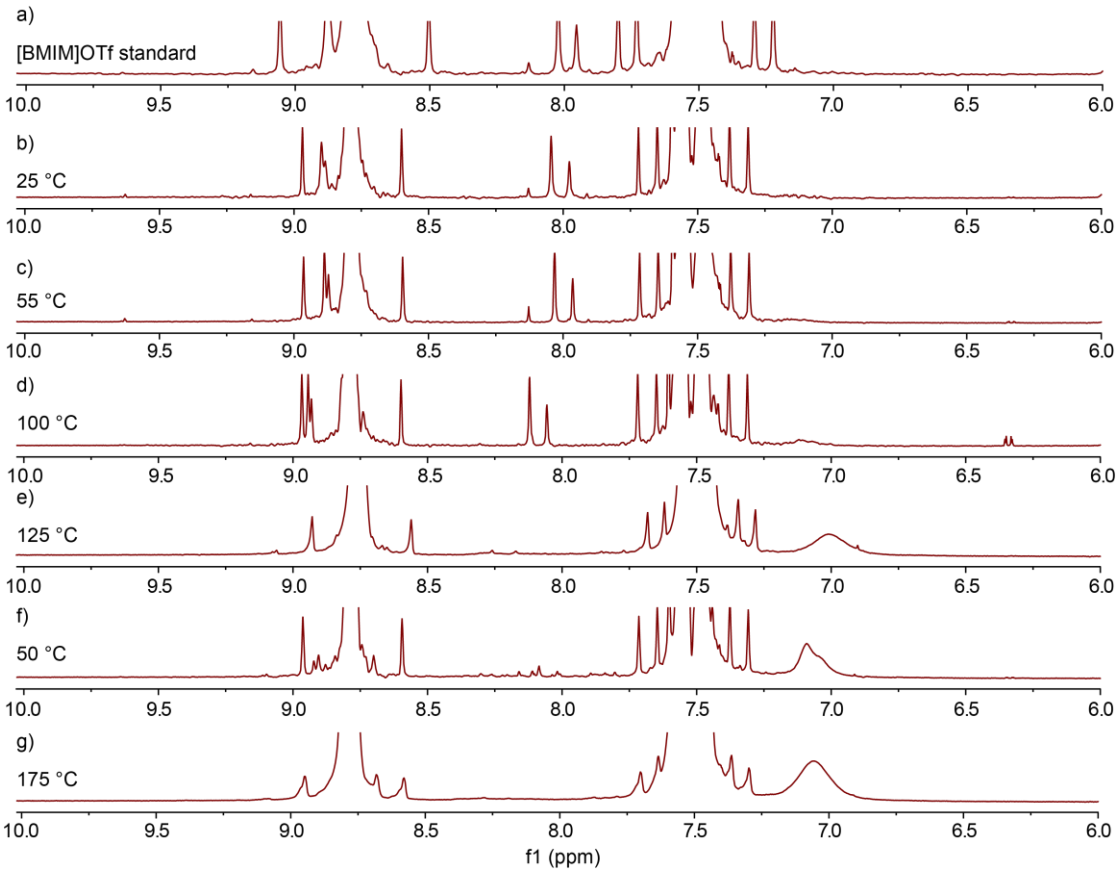

Figure 5.17. ^{1}H NMR for the a) [BMIM]OTf standard and the [BMIM]OTf electrolyte after CPE at b) 25, c) 55, d) 100, e) 125, f) 150, and g) 175 ºC.

The difference in decomposition temperatures for [BMIM]OTf and [BMIM]PF_6 highlights how their unique physical properties depend simply on the counter anion. XPS and ^{1}H NMR demonstrated that [BMIM]PF_6 is overall less stable during catalysis than [BMIM]OTf. Decomposition of the anion resulted in reduced ability to stabilize the imidazolium cation and had a direct effect on cation decomposition.[31]

5.3.7 Understanding how Substrate Size Effects Catalytic Outcomes

It was fascinating to observe that Bi-CMEC and Sn-CMEC offered different electrocatalytic outcomes for catalysis in a neat RTIL environment. For dilute IL organic solutions, the metrics for Bi and Sn were nearly analogous. The only difference between the Bi and Sn study for neat RTIL systems, was the catalyst size and inert substrate; glassy carbon disc electrode (3.0 mm diameter) and Ni foil (~1 cm x 1.0 cm x 0.00125 cm) for Bi and Sn respectively. This led to investigation regarding how the electrode size effects catalysis. This resulted in studying the electrochemical behavior for a Sn-modified Ni disc and foil electrodes. This will elaborate on how the substrate effects catalysis and will impact industries using RTIL solvents under scaled conditions.

To determine if the size of the electrode effects the electronics at the surface, EIS was performed with a Ni disc electrode, an area ~30x smaller than Ni foil used previously. A comparison of impedance responses using a Ni disc electrode and Ni foil for [BMIM]OTf and [BMIM]PF_6 are shown in Figure 5.18a and b respectively for Sn-CMEC.

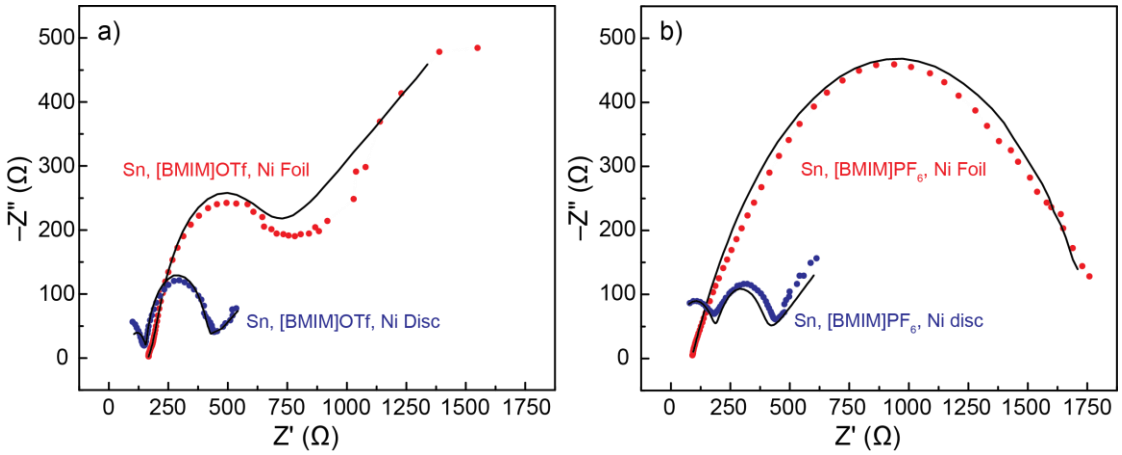

Figure 5.18. Nyquist plots for CO_2 saturated a) [BMIMOTf and b) [BMIM]PF_6 for Sn electrodesposited on Ni foil (red dots) and Ni disc (blue dots). Black line represents 2RC simulated data.

These comparisons showed a clear distinction in electrochemical behavior between a smaller disc electrode and a larger foil electrode. Unlike the larger Ni foil, the Ni disc electrode for both RTILs show a distinct ohmic feature (elbow) at high frequency. This suggested that the smaller Ni disc electrode can more easily facilitate ET events at the surface. Additionally, the larger electrode surface area may require greater stabilization, thus exhibiting greater resistance to carry on catalysis efficiently.

Greater resistance is also demonstrated by the greater R_{CT} for Ni foil over the Ni disc electrode. Seeing that the disc electrode has a less resistive R_{CT} and R_{ohmic}, it was curious to observe how these properties effect the metrics for CO_2 to CO conversion. This study was performed at 25 and 55 ºC (cannot exceed this temperature due to disc electrode temperature restraints). The metrics are summarized in Table 5.4 for Sn-CMEC at an applied potential of –1.95 V.

Table 5.4. VT CPE metrics for CO_2 saturated [BMIM]OTf and [BMIM]PF_6 with a Sn-modified Ni disc electrode at –1.95 (V) vs. SCE.

electrode	IL	ºC	FE_{CO} (%)	FE_{H2} (%)	j_{tot} (mA cm^{-2})
Sn-CMEC	[BMIM]PF_6	25	40 ± 3	13 ± 10	0.35 ± 0.004
		55	67 ± 2	12 ± 10	0.51 ± 0.14
Sn-CMEC	[BMIM]OTf	25	10 ± 1	21 ± 13	0.35 ± 0.03
		55	23 ± 1	5 ± 3	1.21 ± 0.17

The metrics for Sn/Ni disc are similar to the initial CPE study performed with Bi-CMEC using a small GCE (3.0 mm diameter). With increasing temperature, the current density also showed an increase in rate. Interestingly with the smaller disc electrode, [BMIM]PF_6 now evolved CO. Further, [BMIM]PF_6 produced CO with greater selectivity than [BMIM]OTf. These resembled the initial Bi-CMEC/GCE results (Table 5.1). [BMIM]PF_6 may interact more at the surface due to having less steric restraint than [BMIM]OTf, despite being more viscous. This can encourage greater stabilization of intermediates to facilitate charge transfer. This is supported in Figure 5.18, such that the R_{CT} for [BMIM]PF_6 is slightly smaller than [BMIM]OTf.

Regardless of temperature enhancement encouraging CO selectivity for both systems, the current density is still ~1 mA/cm^2. Based on the temperature limitations of disc electrodes, they are not appropriate substrates for neat RTIL electrolyte despite evolving CO. These studies were beneficial in providing insight on the stability of the ohmic interaction for larger substrates.

5.4 Conclusions

Understanding the physical aspects of RTILs is important for industries looking to make the switch from organics to these innovative solvents for chemical reactions or catalysis. ILs encourage lower volatility and toxicity than organics, but a primary factor effecting this switch is the degradation temperature of the RTILs, specifically from their

moisture sensitivity.[28] Work has been dedicated towards determining the decomposition temperature for a variety of RTILs, but the results are convoluted, such that there is poor agreement for any specific RTIL.[28,34] In considering the degradation of RTIL as solvent, variables other than their inherent physical properties must be considered. The decomposition of RTILs is largely dependent on reaction temperature, reaction time, and the substrate.[35] Little is currently understood about RTIL durability as solvent during catalysis. Here, RTILs were investigated for their compatibility as solvent for the electrocatalytic reduction of CO_2 to CO. It was ultimately revealed that the imidazolium anion significantly influences catalysis, in that it greatly effects the overall thermal stability of the RTIL. This observation was supported by previous reports.[36]

Because the anion and cation have a strong influence over the physical properties of the RTIL, ILs can be tailored specifically to meet criteria for the desired chemistry.[5,37] Here, the RTIL behavior was controlled by the different physical properties of the anion, which varies in symmetry and interionic interactions. There is increased symmetry from the organic anion (OTf^-, *C3v*) compared to the inorganic anion (PF_6^-, *Oh*) which ultimately impacts their relative viscosities.[14] Fluorinated anions generally enhance viscosity, but their specific symmetries influence their intermolecular interaction with the imidazolium cation.[38] Specifically, OTf^- experiences strong negative charge delocalization. The fluorines on OTf^- distort the electron density on the imidazolium ring to encourage hydrogen bonding. PF_6^- experiences more Van der Waals forces over hydrogen bonding, which have been shown to increase viscosity.[38] This allows [BMIM]OTf to have overall greater conductively and diffusion coefficients than [BMIM]PF_6.[5] Additionally, it was found that the thermal stability of ILs increase with

increasing anion size.[39] OTf^- is a larger anion than PF_6^- and can therefore add more theral stability to the imidazolium IL.

[BMIM]PF_6 was found to degrade relatively easily, which is in correspondence with previous reports.[35,40] [BMIM]PF_6 is known to decompose in the presence of a metal catalyst and trace amounts of water.[14,30] The $2H^+/2e^-$ reduction of CO_2 yields an equivalent of CO and H_2O. The trace amount of water produced likely encouraged facile decomposition of this RTIL. Even at room temperature and vigorously dry conditions, PF_6^- anions can hydrolyze to produce decomposition products.[39] The suspected decomposition products, PO_4^{3-} and HF can significantly affect the outcome of catalysis and deviate the product distribution.

[BMIM]OTf was experimentally shown to be more robust than [BMIM]PF_6. It demonstrated structural stability for T ≤100 ºC with CO evolution approaching 80 % and a 2 mA/cm^2 current density enhancement. T ≥100 ºC resulted in a switch in product selectivity from CO to H_2. ^{1}H NMR and XPS revealed this likely to be due anion and cation decomposition.

Degradation of the RTILs during electrolysis at elevated temperatures is suspected to discourage the IL monolayer that forms on the cathode when the negative bias is applied. With the disruption of the monolayer (the cathode/IL interface), it is anticipated to no longer discourage the competitive H_2 production pathway.

Based on C_{DL}, the movement of ions in response to temperature was drastically different for the two RTILs. Interestingly, temperature enhancements were found to have no effect on ion movement for [BMIM]PF_6, suggesting that temperature does not demonstrate enhancement towards ET events for this RTIL. Seeing as temperature poorly effects catalysis and further destabilizes [BMIM]PF_6, an alternate method for

improving current densities while discouraging RTIL decomposition was of interest. A promising method is through incorporating admixtures of MeCN, which has demonstrated to effect diffusion, ionic conductivity, and viscosity for various 1,3-dialkylimidazolium ionic liquids.[41] It is curious if [BMIM]PF_6 will no longer be prone to degradation during catalysis with MeCN admixtures.

REFERENCES

(1) Pandey, S. *Analytica Chimica Acta*. **2006**, *556*, 38—45.

(2) Han, Q.; Wang, X.; Byrne, N. *ChemCatChem*. **2016**, *8*, 1551—1556.

(3) Vakili-Nezhaad, G.; Vatani, M.; Asghari, M.; Ashour, I. *Journal of Chemical Thermodynamics*. **2012**, *54*, 148—154.

(4) Montaliban, M. G.; Bolivar, C. L.; Banos, G. D.; Villora, G. *Journal of Chemical Engineering.* **2015**, *60*, 1986—1996.

(5) Ramya, K. R.; Kumar, P.; Venkatnathan, A. *Journal of Physical Chemistry B.* **2015**, *119*, 14800—14806.

(6) Hagiwara, R. Ito, Y. *Journal of Fluorine Chemistry*. **2000**, *105*, 221—227.

(7) De Francesco, M.; Simonetti, E.; Gorgi, G.; Appetecchi, G. B. *Challenges*. **2017**, *8*, 11.

(8) Chaban, Vitaly V., and Oleg V. Prezhdo. "Mixtures of 1-butyl-3-methylimidazolium tetrafluoroborate ionic liquid and acetonitrile: a molecular simulation." *arXiv preprint arXiv:1108.3607* (2011).

(9) DiMeglio, J. L.; Rosenthal, J. *Journal of the American Chemical Society.* **2013**, 135, 8798–8801.

(10) Medina-Ramos, J.; Pupillo, R. C. Keane, T. P.; DiMeglio, J. L.; Rosenthal, J. *Journal of the American Chemical Society.* **2015**, *137*, 5021—5027.

(11) Chaban, V. V.; Voroshylova, I. V.; Kalugin, O. N.; Prezhdo, O. V. *Journal of Physical Chemistry B*. **2012**. *116*, 7719—7727.

(12) Welton, T. *Chemical Reviews*. **1999**, *99*, 2071—2083.

(13) Medina-Ramos, J.; DiMeglio, J. L.; Rosenthal, J. *Journal of the American Chemical Society*. **2014**, *136*, 8361–8367.

(14) Huddleston, J. G.; Visser, A. E.; Reichert, W. M.; Willaeur, H. D.; Broker, G. A.; Rogers, R. D. *Green chemistry*. **2001**, *3*, 156—164.

(15) Fry, A. J.; Singh, A. H. *Journal of Organic Chemistry*. **1994**, *59*, 8172—8177.

(16) Wrighton, M. S.; Ellis, A. R.; Wolczanski, P. T.; Morse, D. L.; Abrahamson, H. B.; Ginley, D. S. *Journals of the American Chemical Society*. **1976**, *98*, 2774—2779.

(17) Cao, Y.; Mu, T. *Industrial and Engineering Chemistry Research.* **2014**, *53*, 8651—8664.

(18) Prechtl, M. H. G.; Campbell, P. S.; Scholten, J. D.; Fraser, G. B.; Machado, G.; Santini, C. C.; Dupont, J.; Chauvin, Y. *Nanoscale*. **2010**, *2*, 2601—2606.

(19) Freire, M. G.; Neves, C. M. S. S.; Marrucho, I. M.; Coutinho, J. A. P.; Fernandes, A. M. *Journal of Physical Chemistry A.* **2010**, *114*, 3744.

(20) Lozano-Castello, D.; Cazorla-Amoros, D.; Linares-Solano, A.; Shiraishi, S.; Hurihara, H.; Oya, A. *Carbon*. **2003**, *41*, 1765—1775.

(21) Singh, M.; Manoli, K.; Tiwari, A.; Ligonzo, T.; Di Franco, C.; Cioffi, N.; Palazzo, G.; Scamarcio, G.; Torsi, L. *Journal of Materials Chemistry C.* **2017**, *5*, 3509—3518.

(22) Basics of Electrochemical Impedance Spectroscopy: Application Note AC-1. Princeton Applied Research.

(23) Chaban, V. V.; Prezhdo, O. V. *Journal of Physical Chemistry Letters*. **2013**, *4*, 1423—1431.

(24) MacFarlane, D. R.; Sun, J.; Golding, J.; Meakin, P.; Forsyth, M. *Electrochimica Acta*. **2000**, *45*, 1271—1278.

(25) Tokuda, H.; Hayamizu, K.; Ishii, K.; Susan, M. A. B. H.; Watanabe, M. *Journal of Physical Chemistry B.* **2004**, *108*, 16593−16600.

(26) Kroon, M. C.; Buijs, W.; Peters, C. J.; Witkamp, G. *Green Chemistry*. **2005**, *8*, 241—245.

(27) Suarez, P. A. Z.; Selbach, V. M.; Dullius, J. E. L.; Einloft, S.; Piatnicki, C. M. S.; Azambuja, D. S.; de Souze, R. F.; Dupont, J. *Electrochimica Acta*. **1996**, *42*, 2533-2535.

(28) Mein, N.; Benedito, F. Rinaldi, R. *Green Chemistry*. **2010**, *12*, 1711—1714.

(29) Freire, M. G.; Neves, C. M. S. S.; Marrucho, I. M.; Coutinho, J.A. P.; Fernandes, A. M. *Journal of Physical Chemistry A*. **2010**, *114*, 3744.

(30) Advances in Catalysis. Gates, B.C.; Knozinger, H., Eds; Elsevier: California, 2006.

(31) Chambreau, S. D.; Schenk, A. C.; Sheppard, A. J.; Yandek, G. R.; Vaghjani, G. L.; Maciejewski, J.; Koh, C. J.; Golan, A.; Leone, S. R. *Journal of Physical Chemistry A*. **2014**, *118*, 11119—11132.

(32) Feroci, M.; Chiarotto, I.; Forte, G.; Ciprioti, S. V.; Inesi, A. *ChemElectroChem Articles*. **2014**, *1*, 1407—1414.

(33) Reich, H. J. Proton Chemical Shifts. 2017. Univ. Wisc. http://www.chem.wisc.edu/areas/reich/nmr/h-data/hdata.htm

(34) Scammells, P. J.; Scott, J. L.; Singer, R. D. *Australian Journal of Chemistry.* Aust. J. Chem., **2005**, *58*, 155–169.

(35) Duan, Z. Y.; Zhang, H. Xiang, X. M.; Xian, L.; Wang, Y. B. *Asian Journal of Chemistry*. **2012**, *24*, 261—263.

(36) Villanueva, M.; Coronas, A.; Garcia, J.; Salgado, J. *Industrial and Engineering Chemistry Research*. **2013**, *52*, 15718—15727.

(37) Payagala, T.; Huang, J.; Breitbach, Z. S.; Sharma, P. S.; Armstrong, D. W. *Chemistry of Materials*. **2007**, *19*, 5848−5850.

(38) Bonhote, P.; Dias, A. P.; Papageorgiou, N.; Kalyanasundaram, K.; Gratzel, M. *Inorganic Chemistry*. **1996**, *35*, 1168—1178.

(39) Fredlake, C. P.; Crosthwaite, J. M.; Hert, D. G.; Aki, S. N. V. K.; Brennecke, J. F. *Journal of Chemical and Engineering Data.* **2004**, *49*, 954—964.

(40) Kroon, M. C.; Buijs, W.; Peters, C. J.; Witkamp, G. *Thermochimica Acta*. **2007**, *465*, 40—47.

(41) Chaban, V. V.; Voroshylova, J. V.; Kalugin, O. N.; Prezhdo, O. V. *Journal of Physical Chemistry B*. **2012**, *116*, 7719—7727.

Chapter 6

ACETONITRIL ADMIXTURES TO PROMOTE THE ELECTROCATALYTIC CAPABILITIES OF [BMIM]PF_6 SOLVENT

6.1 Introduction

There has been a growing interest in using room temperature ionic liquids (RTILs) as innovative solvents for industrial use.[1,2] RTILs are attractive due to their recyclability, lower toxicity, and reduced volatility compared to typical wasteful organic solvents.[3,4,5] Therefore, RTILs have been classified as a "greener" solvent option. A challenge with using RTILs as solvent, however, is the possibility of decomposition and reduced reaction kinetics.[6] Decomposition is dependent on reaction conditions (temperature, applied potential, pressure, etc.) in addition to the cation/anion combination which effects the strength of their intermolecular attraction.[7,8] Decomposition temperatures have been reported for a slew of RTILs, but agreement lacks between the varied publications, such that decomposition has been reported to occur below the published values.[9] The published range of high decomposition temperatures for ILs (>400 ºC) has been deemed "overrated" and there is new belief that long-term thermal stability of ILs is unlikely.[10] Further, in considering the reaction rate for RTILs, there is a strong inverse correlation with solvent viscosity. RTILs are highly viscous molten salts that impede mass transport of reactants and products for heterogeneous reactions. Much study has been devoted to developing a cation/anion combination with low viscosity, while still demonstrating high current density, selectivity, and low toxicity to bypass these challenges and to improve industrial RTIL conditions.[11]

In lieu of varying the cation/anion combinations, one method to enhance the rate of reaction is by increasing the reaction temperature to encourage molecular movement. This was studied specifically for the heterogeneous electrocatalytic reduction of CO_2 to CO (See Chapter 5). Temperature enhancement was shown to have varied effects on ionic transport which was based on the degree of ion pairing electrostatic forces, and ultimately, the stability of the cation/anion interaction.[8] For example, when the IL cation/anion combination experienced more hydrogen bonding forces, 1-butyl-3-methylimidazolium trifluoromethanesulfonate ([BMIM]OTf), there was a positive correlation between temperature and rate ($T \leq 100$ ºC). When the IL combination experienced more Van der Waals forces, 1-butyl-3-methylimidazolium hexafluorophosophate ([BMIM]PF_6), a negative correlation was observed ($T \geq 25$ ºC).

It was fascinating to observe the stability of [BMIM]PF_6 experimentally, such that even at mild temperatures (25 ºC), X-ray photoelectron spectroscopy (XPS) and ^1H NMR revealed degradation of the PF_6^- anion and cation. The addition of temperature further jeopardized its structural stability. Interestingly, when [BMIM]PF_6 was used as a dilute admixture in organic acetonitrile (MeCN) electrolyte, there was no observable anion or cation degradation.[12] Additionally, further studies supported that temperature enhancements for [BMIM]PF_6 have a negative effect on viscosity.[8,13] Because temperature enhancements were ineffective in enhancing the rate by means of lowing the viscosity, this inspired further study to explore a new method for enhancing the current density for [BMIM]PF_6 without jeopardizing its composition. The ability to lower the viscosity for the traditional [BMIM]PF_6 IL would be advantageous for scientist and industries, such that it is widely used for catalysis, synthesis, and chemical separations.[14,15]

An alternate method for reducing the viscosity and enhancing the current density for [BMIM]PF_6 solvent would be to introduce admixtures of a co-solvent (MeCN) to encourage ion movement by lessening ion aggregation. The IL cation and anion have a strong electrostatic interaction which results in their high viscosity. Incorporating a co-solvent is expected to help shield this interaction to encourage greater charge dissociation.[16,17] Co-solvents have been shown to decrease viscosity of ILs by nearly 50 % when used in just a 20 mol%.[8] Conductivity is inversely related to viscosity and is therefore highly dependent on the diffusion of ion pairs, whereas the ion movement is independent. The addition of solvent will help to stabilize those ion pairs by the new anion-solvent and cation-solvent interactions.[17]

Although organic solvent would still be incorporated as a co-solvent, only trace amounts will be used. RTILs are considered safer solvents for the future because of their negligible toxicity.[18] Although MeCN is a volatile and toxic solvent capable of forming highly toxic species, i.e. cyanogen, the RTIL-based solution will maintain its low toxicity. RTILs have been shown to substantially lower the volatility of MeCN to reduce its hazardous effects.[19] Further, with trace amounts of MeCN, there will not be a surplus of wasteful and toxic organics. Therefore, this would be a significant contribution for industries currently using RTIL solvents, or for those transitioning from traditional organics to using green RTIL solvents. If MeCN admixtures demonstrate success, much study would be devoted to uncovering an optimal ratio of RTIL to co-solvent to facilitate chemical reactions with high efficacy and mass transport, while maintaining a green mindset.

The ability to reduce the viscosity of [BMIM]PF_6 would be advantageous because it is amongst the most viscous RTILs (from the larger electron density at the

anion) which may have discouraged further applications with this solvent.[8] Additionally, it is curious to compare catalytic deviations between dilute [BMIM]PF_6 concentrations in MeCN, and when MeCN is used in small concentration in neat [BMIM]PF_6. Admixtures of MeCN have been reported to enhance mass transport, ionic conductivity, and reduce viscosity to a variety of 1,3-dialkylimidazolium ionic liquids.[20] Because it has not yet been demonstrated for CO_2 to CO heterogeneous catalysis, it would be a valued contribution for this field of redox chemistry.

6.2 Experimental Method

6.2.1 Materials and Methods

Reagents and solvents were purchased from Sigma Aldrich, Alfa Aesar, Acros or Fisher. Tin(II) trifluoromethanesulfonate was purchased from Strem Chemicals. Imidazolium ionic liquids; 1-butyl-3-methylimidazolium hexafluorophosphate ([BMIM]PF_6) was purchased from Alfa Aesar. Tetrabutylammonium hexafluorophosphate ($TBAPF_6$) was purchased from TCI America and purified by recrystallization with ethanol. Carbon dioxide (CO_2) was purchased from Keen Compressed Gas Company grade 4.0 high purity.

Platinum gauze (99 %) was purchased from Sigma Aldrich. The bare nickel disc electrode and the Ag/AgCl (1.0 M KCl) reference electrode were purchased from CHI Instruments. Nickel foil was purchased from Sigma Aldrich. Ag wire was used as a pseudo reference for the neat RTIL electroanalytical studies and was assembled in a glass casing filled with [BMIM]PF_6 equipped with a frit. Ag/AgCl reference was used for the electrodeposition of $Sn(OTf)_2$.

6.2.2 Single-Compartment Electrochemical Cell

CPE was performed in a single-compartment cell (made in house) to accommodate a smaller volume of RTILs used (~2 mL). The RTIL was stirred at a steady rate with a stir bar. The single cell consisted of a typical three-electrode system with a working (Ni plate electrode (~1 cm x 1.0 cm x 0.00125 cm), auxiliary (Pt mesh), and pseudo reference (Ag wire cast in RTIL). (See Chapter 5, Appendix D.1.)

6.2.3 Instrumentation

6.2.3.1 Electrochemical Measurements

Electrochemical studies were conducted using a CHI-620D potentiostat/galvanostat or a CHI-720D bipotentiostat. Electrochemical apparatus consisted of a three-electrode system; working (bare Ni disc (3.0 mm diameter) or Ni foil (~1 cm x 1.0 cm x 0.00125 cm)), counter (platinum gauze), and a reference electrode (Ag/[BMIM]PF_6 or Ag/AgCl (1.0 M HCl))). Cyclic voltammetry and linear voltammetry experiments were performed with iR drop compensation with 100 mV s^{-1} scan rate. (See single cell diagram in Appendix D.1.)

6.2.3.2 Electrochemical Impedance Spectroscopy

Electrochemical impedance spectroscopy (EIS) was performed using a CHI-720D bipotentiostat. Electrochemical apparatus consisted of a three-electrode system; working (bare nickel disc (3.0 mm diameter) or nickel foil (~1 cm x 1.0 cm x 0.00125 cm)), counter (platinum gauze), and a pseudo reference electrode (Ag wire)). Frequency ranged from 0.1 Hz to 100 000 Hz. The frequencies were generated by alternating potentials

The impedance responses were summarized in a Nyquist plot with imaginary (–Z″, capacitive) vs. real (Z´, resistive) components as the y- and x- axis.

6.2.3.3 X-ray Photoelectron Spectroscopy

XPS analysis was performed using a Thermo Scientific K-alpha^{+} spectrometer with monochromatic Al Kα X-ray (1486.7 eV) and 72 W of power (12 kV, 6 mA) equipped with a 128 CCD detector plate. Operating vacuum pressure in the main chamber was less than $1x10^{-8}$ torr. XPS survey scans were collected with a step size of 1.0 eV and a pass energy of 100 eV. High resolution spectra were collected with a step size of 0.1 eV and a pass energy of 20 eV. The X-ray spot size was an elliptical shape with a semi-major axis of approximately 400 μm.

6.2.3.4 Gas Chromatography and CO_2 Headspace Analysis

Current densities were obtained by performing controlled potential electrolysis (CPE) on a single-compartment electrochemical cell made in house. The compartment was filled with 2 mL [BMIM]PF_6 + MeCN%. The solution was sparged for 30 minutes before the start of CPE.

During CPE, the solution was stirred at a steady rate while there was a continuous flow of CO_2 into the headspace (5 mL min^{-1}). The cathode was vented directly into a flow gas chromatograph (SRI Instruments, SRI-8610C). A chromatograph was obtained every 15 min throughout the duration of electrolysis by placing the sampling loop in line with a packed HayeSep D column and a packed mole Sieve 13X column. The columns led directly to a thermal conductivity detector (TCD) and a flame ionization detector (FID) equipped with a methanizer to quantify hydrogen

and carbon monoxide production respectively. The gas carrier was Argon (Keen, 99.999 %).

6.2.3.5 Electrodeposition of Sn-CMEC

Prior to electrodeposition, the Ni disc electrode (3.0 mm diameter) was polished with 0.05 micron alumina powder in Millipore water and then sonicated in Millipore water to remove residual powder. If starting with Ni foil (~1 cm x 1.0 cm x 0.00125 cm), it was sonicated in water, acetone, and lastly acetonitrile for 20 minutes each to remove excess oils. The Ni substrate was then submersed in an organic electrolyte solution containing 0.02 M $Sn(OTf)_2$ and 0.1 M $TBAPF_6$ saturated with N_2. A series of cyclic voltammetry sweeps (10 cycles, 100 mV s^{-1}) were performed with applied potentials ranging from –0.25 to –2.25 (V) vs. SCE. Following the electrode conditioning, the Ni substrate was agitated to remove exfoliated material formed on the electrode surface. Using the same electrolyte solution, controlled potential electrolysis (CPE) applied a constant potential of –0.55 (V) vs. SCE until a total of ~1 C cm^{-2} was passed. The now Sn-modified electrode was rinsed with acetonitrile followed by a drying step consisting of a gentle N_2 flow over the modified surface.

This consisted of a three-electrode system; working bare Ni disc (3.0 mm diameter) or Ni foil (~1 cm x 1.0 cm x 0.00125 cm), counter (platinum gauze), and a reference electrode (Ag/AgCl (1.0 M KCl)).

6.2.3.6 ^{1}H NMR

^{1}H NMR was performed with aliquots from the cathode solution to detect any solution products from electrolysis and/or decomposition of RTIL solution. Samples were run in dCD_3CN. The acetonitrile resonance was suppressed at 1.96 ppm. These

NMR studies detected formic acid production for some cathode conditions at 8.1 ppm and imidazolium-carboxylate adduct was monitored at 7.17 and 7.13 ppm.

6.3 Results and Discussion

6.3.1 Detecting Catalytic Enhancements with MeCN Admixtures

MeCN admixtures in viscous ILs have shown promise towards enhancing ionic conductivity, diffusion, and lowing viscosity.[8,20] Observing how admixtures correlate to CO_2 reduction activity, and ultimately CO selectivity and current density was essential. To elucidate these metrics, linear sweep voltammetry (LSV) and controlled potential electrolysis (CPE) were performed with [BMIM]PF_6 and MeCN admixtures. The Sn carbon monoxide evolving catalyst (Sn-CMEC) was used for these studies, in continuation of the variable temperature (VT) studies (See Chapter 5) for comparison.

6.3.1.1 Monitoring CO_2 Reduction Activity with MeCN Admixtures

LSV was used to monitor the deviations in polarization curves upon additions of MeCN into CO_2 saturated [BMIM]PF_6 (Figure 6.1a). After each addition of MeCN (100 μL), a LSV polarization curve was obtained (up to 400 μLs). Here, the cathodic peak maxima and overpotential shifts were monitored.

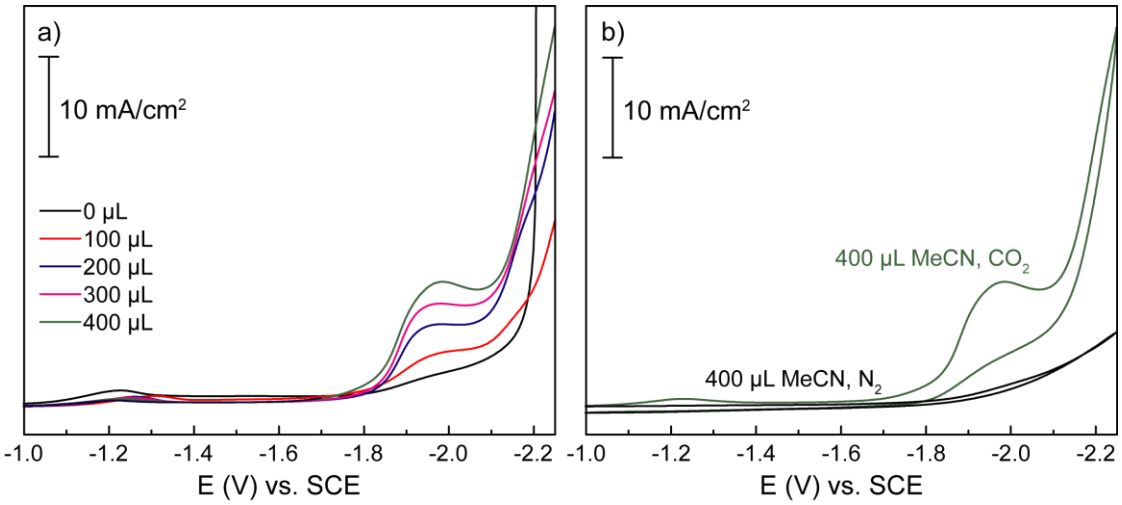

Figure 6.1. Linear sweep voltammograms for a a) MeCN titration into CO_2 saturated [BMIM]PF_6 and b) cyclic voltammograms for of 400 µL MeCN in CO_2 saturated (green trace) and N_2 saturated (black trace) [BMIM]PF_6.

When no MeCN was added, the activity for CO_2 reduction was negligible, as shown in the black trace in Figure 6.1a. Upon the first few additions of MeCN, a noticeable current enhancement was observed at –1.95 (V) vs. SCE (all potentials will be referred to this reference) with an onset potential of ~ –1.85 V. Importantly, the enhanced CO_2 reduction activity did not demonstrate shifts in overpotential. The increase in current response suggested the limiting electron transfer (ET) event for the rate determining step (RDS) is occurring at a faster rate. This observation was optimistic in achieving enhanced ion mobility for viscous IL reaction solutions. Further, the current response reached a substantial current enhancement with only 400 µL MeCN (Figure 6.1a, green trace). Therefore, 400 µL MeCN in [BMIM]PF_6 appeared as an optimal admixture to avoid using larger amounts of organic solvent. The rate will continue to enhance with increasing amounts of MeCN, as demonstrated by previous study with dilute concentrations of IL, but here we have found a potentially ideal volume ratio of

MeCN to IL (17 %) to obtain the benefits of achieving higher CO_2 reduction activity, without using harmful organic solvent. This ratio will be studied further with CPE to determine if it is optimal for encouraging mass transport and CO selectivity.

To support that CO_2 is responsible for the rise in activity, the IL with 400 μL MeCN was saturated with N_2 and compared with the observed activity under CO_2 (Figure 6.1b, black and green trace respectively). The current response was shown to be negligible under N_2 and no cathodic feature was observed at ~1.95 V. This suggested that the cathodic rise is due to the Sn/IL interface to promote CO_2 reduction.

It was remarkable to observe how trace amounts of MeCN can significantly impact CO_2 reduction activity for [BMIM]PF_6 by nearly 10 mA/cm^2. Observing that admixtures of MeCN can boost the activity for CO_2 reduction, it was curious if CO selectivity would also be enhanced.

6.3.2 MeCN Admixture Effects of Selectivity and Current Density

CPE was performed under a variety of electrolyte conditions which were dependent on the MeCN admixture. LSV demonstrated that the activity for CO_2 reduction varied with varying amounts of MeCN. It was curious if this behavior would also be evident with the current density and product distribution. To answer these question, CPE was performed with a 5, 10, 17, 33, and 50 % MeCN (v/v) to neat [BMIM]PF_6 by volume under CO_2 saturated conditions. 17 % MeCN (v/v) demonstrated optimal current enhancement via LSV. Here, metrics for %MeCN approaching and surpassing this value (17 %) will be of great interest to have a complete story of how the metrics evolve based on viscosity.

The chemistry took place in a single compartment cell tethered with inline analytics to a gas chromatograph (GC) for monitoring gaseous products. Solution products were monitored with ^{1}H NMR.

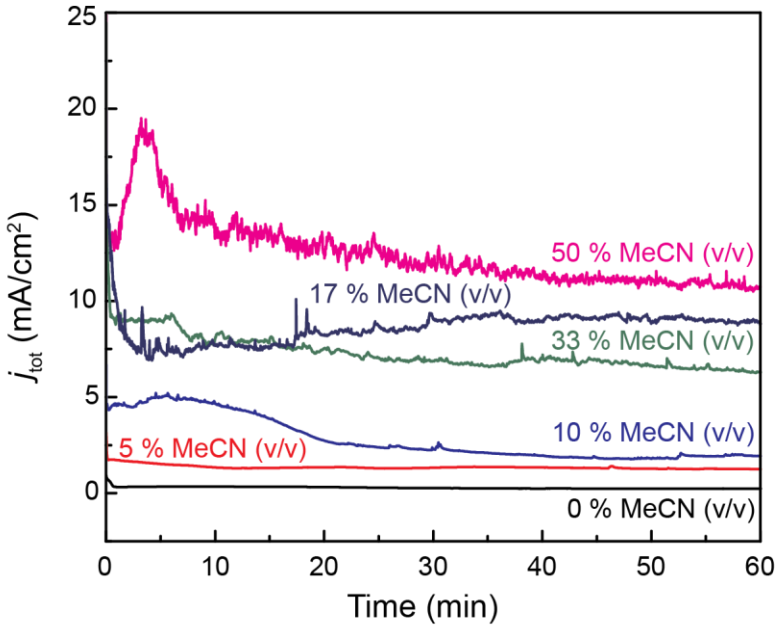

Figure 6.2. Current density plot for 0 (black trace), 5 (red trace), 10 (blue trace), 17 (navy trace), 33 (green trace), and 50 % MeCN (pink trace) in [BMIM]PF_6 by volume. Sn-CMEC/Ni foil acted as the working electrode with an applied potential of –1.95 (V) vs. SCE.

The current density plot in Figure 6.2 supported that the rate of reaction increases with increasing amounts of MeCN, as suggested by the LSV MeCN titration. The current density increased until the solution had 17 % MeCN (v/v). Surpassing 17 % MeCN (v/v) to 33 and 50 % demonstrated equally high rates that ranged between ~7 and ~13 mA/cm^2 These current densities are comparable within their standard

deviations. This compliments the LSV titration (Figure 6.1a), such that the cathodic peak maxima plateaued with MeCN admixtures of 17-20 %.

Table 6.1 summarizes the metrics associated with each MeCN admixture in [BMIM]PF_6. Upon analyzing the gaseous products, a positive correlation was also found for CO evolution, similarly, up to 17-50 % MeCN (v/v).

Table 6.1. CPE metrics for the reduction of CO_2 for MeCN admixtures in [BMIM]PF_6 using Sn-CMEC/Ni foil at an applied potential of –1.95 (V) vs. SCE.

electrode	(%) MeCN (v/v)	FE_{CO} (%)	FE_{H2} (%)	FE_{HCOOH} (%)	j_{tot} (mA cm^{-2})
Sn/Foil	0[†]	3 ± 1[†]	63 ± 14[†]	---	0.3 ± 0.1[†]
	5	28 ± 7	64 ± 6	12 ± 2	1.6 ± 0.3
	10	57 ± 4	12 ± 5	14 ± 1	3.0 ± 1.4
	17	47 ± 5	17 ± 4	14 ± 4	6.8 ± 2.8
	33	47 ± 6	16 ± 4	14 ± 3	5.8 ± 1.6
	50	54 ± 6	15 ± 6	11 ± 2	7.0 ± 2.1

[†]Reported in Chapter 5

Neat [BMIM]PF_6 produced trace amounts of CO and favored H_2 evolution. Upon addition of MeCN, H_2 evolution became suppressed and CO was now the primary product. Formic acid (FA, HCOOH) was also produced during electrolysis. This was not surprising because Sn-CMEC had been reported to co-produce FA during electrolysis when used in dilute concentrations in MeCN.[21] Sn-CMEC had also been reported to produce CO with ~80 % selectivity. These studies revealed CO efficiencies averaging ~ 50 %, however, a larger Ni substrate (Ni foil) was used for these studies to allow for accurate comparison between previous VT CPE studies (See Chapter 5). The Ni substrate is nearly 13x larger than the substrate used to report the previous metrics. Lower efficiencies have been observed experimentally with higher surface areas for catalysis. Much of the charge becomes devoted to stabilizing the film/substrate

interface. This variation in electrode performance was also observed for Pt electrodes and biological cathodes for fuel cells.[22,23]

The ability to tune product selectivity and rate of reaction with trace additions of MeCN is a significant contribution for IL solvents for chemical reactions or catalysis. Here, the structural integrity of the IL holds true based on the steady current densities over time (Figure 6.2). Additionally, we have demonstrated that ion dissociation can be controlled based on the tuning the viscosity of the solution. For MeCN admixtures in IL to resemble conventional electrolytes, the volume of MeCN would need to be $\geq$ 75 %.[20] When ILs were used in dilute concentrations in previous electrolysis experiments, the volume of MeCN was 97.5 %. At this volume, the added aprotic solvent would no longer be used in trace amounts and would void advancements in using green inovative solvents.

When [BMIM]PF_6 was used as a neat solvent for electrocatalysis, the structural durability of the IL was jeopardized significantly and resulted in termination CO production at ambient conditions. Studies have demonstrate an essential interplay between Sn-CMEC and IL to where in the absence of one component, CO evolution is sacrificed.[2112,21,] The metrics for neat [BMIM]PF_6 solvent mimicked those metrics; low current density and no CO production. This behavior suggested the breakdown of IL, thus a breakdown of the cathode/IL interface. This was supported by detecting decomposition of both the anion and cation via XPS and ^{1}H NMR. Now that neat [BMIM]PF_6 demonstrated enhanced CO production and an increase in current density, it was curious if the stability of the IL was also enhanced with trace MeCN. This was observed similarly with XPS and ^{1}H NMR to analyze the anion (PF_6^-) and cation (1-butyl-3-methylimidazolium, $[BMIM]^+$) respectively.

6.3.2.1 Detecting Cation/Anion Decomposition with MeCN Admixtures

XPS is a surface technique that identifies the elemental compositions based on oxidative environments reported in binding energies (BE). To detect possible anion decomposition, the F 1*s* and P 2*p* high resolution regions (Figure 6.3a and b respectively) were analyzed. Specifically, shifting in oxidative environments, elimination of the PF_6^- component (686.8 and 136.7 eV for F and P respectively), or for the emergence of a new component were monitored. If decomposition occurs, the F 1*s* and P $2p_{3/2}$ region will reveal new components at 688.6 and 135.5 eV respectively.

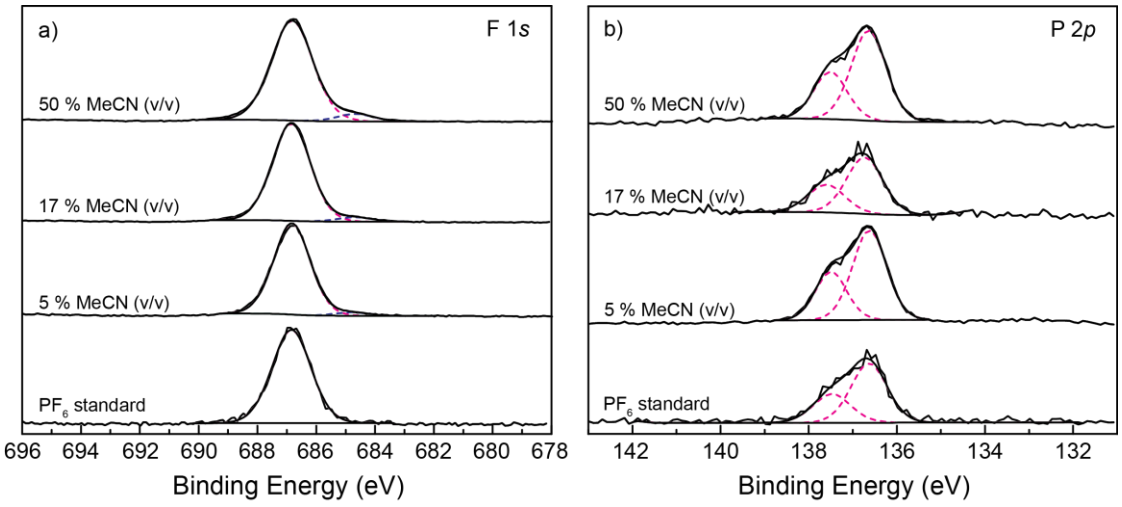

Figure 6.3. XPS high resolution spectra for a) F 1*s* and b) P 2*p* for the PF_6^- standard and the Sn cathode surfaces after CPE for 5, 17, 33, and 50 % MeCN (v/v) in [BMIM]PF_6.

The F 1*s* and P 2*p* showed no deviation from the PF_6^- BE standard. The anion stability with the MeCN admixture, as small as 5 % MeCN, was improved considerably. The additional F 1*s* component at ~684.6 eV corresponds to the fluorine BE for SnF_2.

SnF_2 has been identified previously as a Sn^{2+} component in the Sn 3$d_{5/2}$ high resolution spectrum for the Sn-modified surface both before and after electrolysis (See Chapter 3). The Sn 3*d* high resolution spectra are shown in Figure 6.4 for 5, 17, and 50 % MeCN (v/v) reaction conditions. Importantly, no BE shifts were observed in this region suggesting that the catalyst is robust during catalysis under the varied co-solvent conditions.

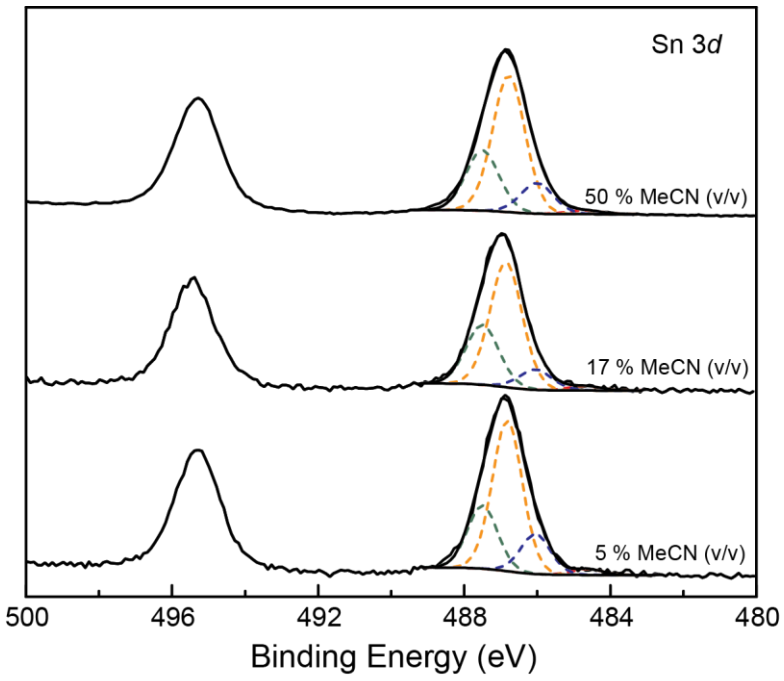

Figure 6.4. Sn 3*d* high resolution spectra for the Sn cathode after electrolysis with 5, 17, and 50 % MeCN (v/v) in CO_2 saturated [BMIM]PF_6. The Sn 3$d_{5/2}$ region is composed of Sn(0) (red trace), Sn(II) oxide (blue trace), Sn(IV) oxide (orange trace), and Sn(II) fluoride (green trace).

The durability of the imidazolium cation was also analyzed by XPS when monitoring the N 1*s* high resolution region. This region allowed for deviations in the

oxidative environment for the nitrogens in the imidazolium ring to be monitored. Repetitious study revealed imidazolium to have a BE of 402.1 eV. If there is decomposition of imidazolium, there will be a greater breath where carbene normally appears in the spectrum at 400.3 eV. The broadening of the spectrum is due to the emergence of two new components surrounding carbene, 401.3 and 399.3 eV, representing imidazolium-carboxylate and its decomposition product (1-butyl-3-methyl-2-imidazolone) respectively. C2 substitution is one possible decomposition for imidazolium.[24] The N 1*s* high resolution spectra for 5, 17, and 50 % MeCN (v/v) is illustrated in Figure 6.5.

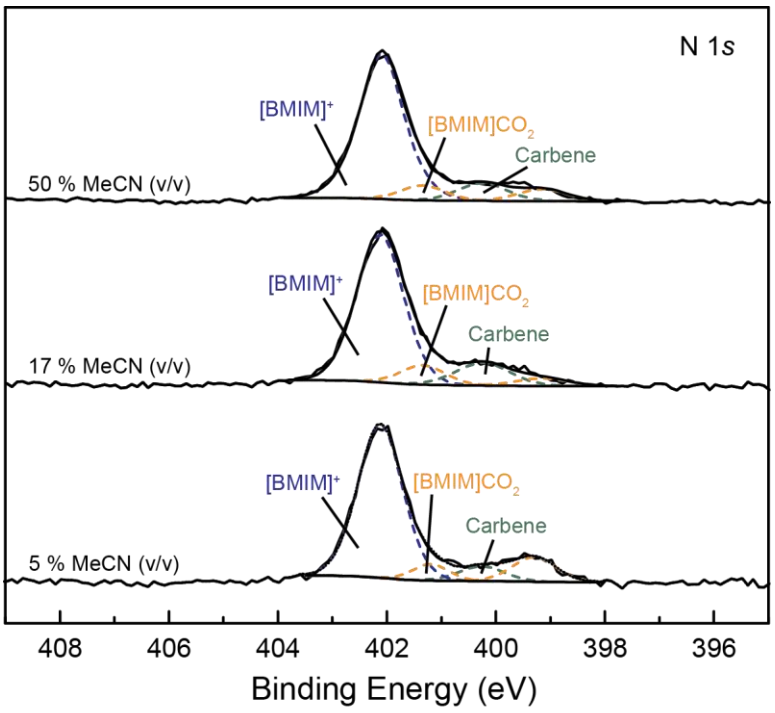

Figure 6.5. N 1*s* high resolution spectra for the Sn cathode after electrolysis with 5, 17, and 50 % MeCN (v/v) in CO_2 saturated $[BMIM]PF_6$.

The N 1*s* region was primarily composed of imidazolium (Figure 6.5, blue trace) with slight contribution from carbene (Figure 6.5, green trace) for 5, 17, and 50 % MeCN (v/v). Interestingly, there was evidence for cation decomposition at 401.3 and 399.3 eV, imidazolium-carboxylate ([BMIM]CO_2) and its decomposition product respectively. The relative amount of the adduct on the surface is trace in comparison to the amount of imidazolium on the surface. This suggested that despite some imidazolium cations undergoing C2 substitution, most of the imidazolium cations remain stable from interactions with the now non-decomposed counter anion.

Observing trace decomposition at the surface for imidazolium via C2 substitution, it was curious if degradation of the cation could be observed in the solution bulk by ^{1}H NMR. Specifically, it was of interest to observe if the decomposed cation only exists at the surface to interfere with charge transfer events, or if it also diffuses into the solution bulk to interferer further with diffusion of reactants and products. Additionally, other types of anion decomposition including alkyl elimination, transalkylation, or retroalkylation, were monitored by a resonance growth downfield in the aromatic region.[9,24] The aromatic region for the MeCN/IL solution after CPE is shown in Figure 6.6.

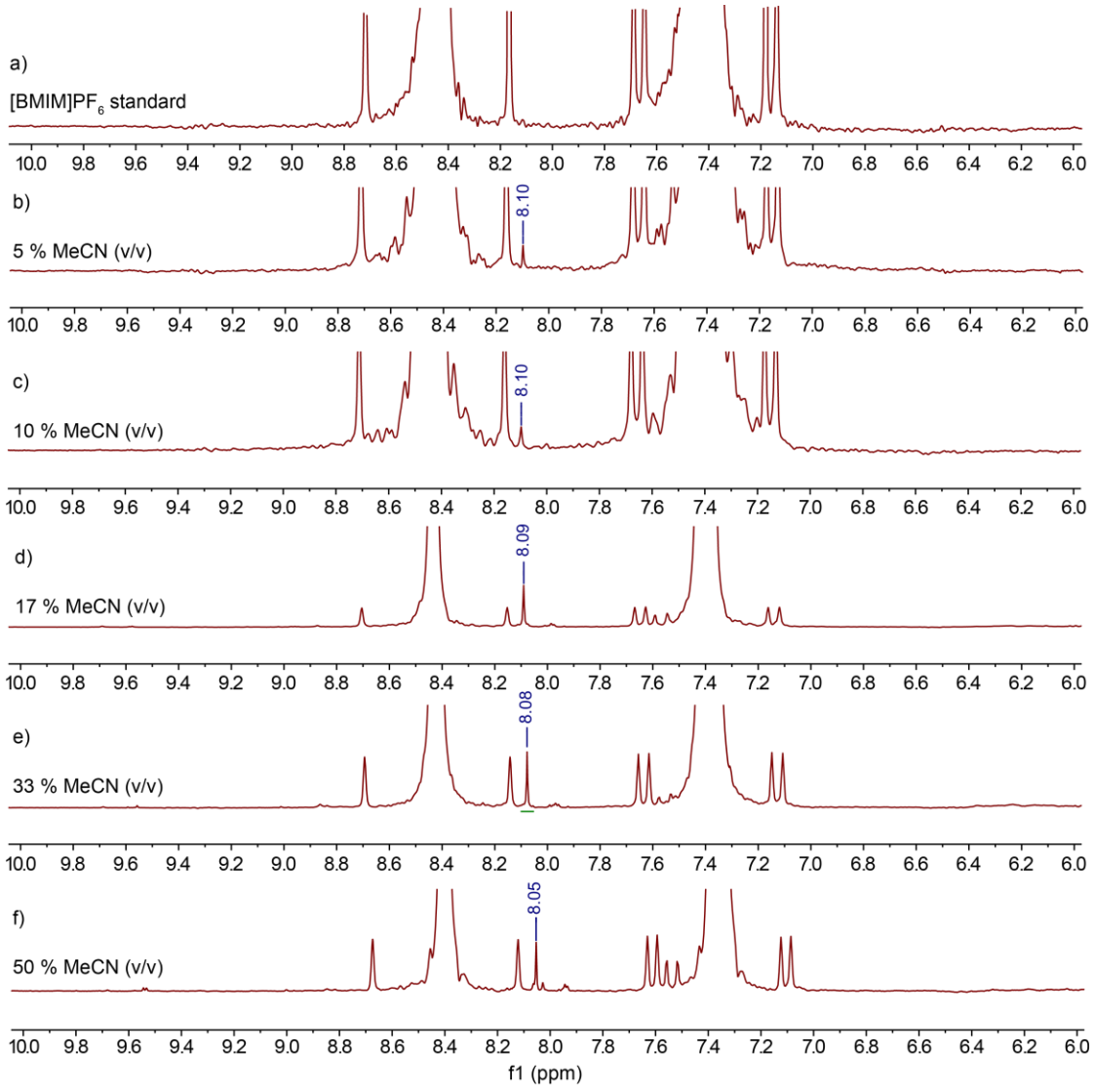

Figure 6.6. ^{1}H NMR for the MeCN/IL solution after electrolysis for a) the [BMIM]PF_6 standard, b) 5, c) 10, d) 17, e) 33, and f) 50 % MeCN (v/v).

The NMR illustrated no growth of downfield resonances at ~9.4 ppm to signify decomposition of alkyl groups. This region illustrated no observable deviations from the IL standard other than the growth of the FA resonance at 8.1 ppm. Because there is

no resonance at 7.13 and 7.17 ppm for the imidazolium-carboxylate, the adduct likely does not diffuse into the solution bulk once formed at the cathode surface.

The adduct was first detected on surfaces where it is thermodynamically stabilized (Pb-CMEC) in diluted IL concentrations (See Chapter 3). This adduct is stable within the potential applied for catalysis and behaves as a thermodynamic sink; Film passivation, lower CO evolution, etc. (See Chapter 4). The adduct was later identified on surfaces that were initially inert towards the adduct thermodynamically forming and adsorbing to the surface (Sn-CMEC) when the catalytic temperature was increased (See Chapter 5). Here, adduct formation and adsorption was directly related to the solution viscosity. This supports that the adduct forms with limited proton availability. With highly viscous systems, the mass transport is reduced and ultimately reduces the rate at which protons can be replenished near the surface. There is likely a viscosity threshold for when the adduct will form and when it will not. This relates to the notion that the adduct forms when the reactive carbene at the surface cannot readily diffuse away to the solution bulk to become reprotonated, and instead, forms a thermodynamically stable bond with CO_2. This adduct formation may hinder catalysis despite the abundance of IL.

To confirm that the adduct is thermodynamically forming under viscous conditions, LSV was performed for the Sn-modified electrode in 17% MeCN (v/v) and dilute IL electrolyte (100 mM IL). Separate electrodes were prepared for each study. The electrode was not re-plated after the potential sweeps. This was to observe deviations in polarization curves (activity for CO_2 reduction) upon possible formation of the adduct. The results are summarized in Figure 6.7a and b for 17% MeCN (v/v) and dilute IL solutions respectively.

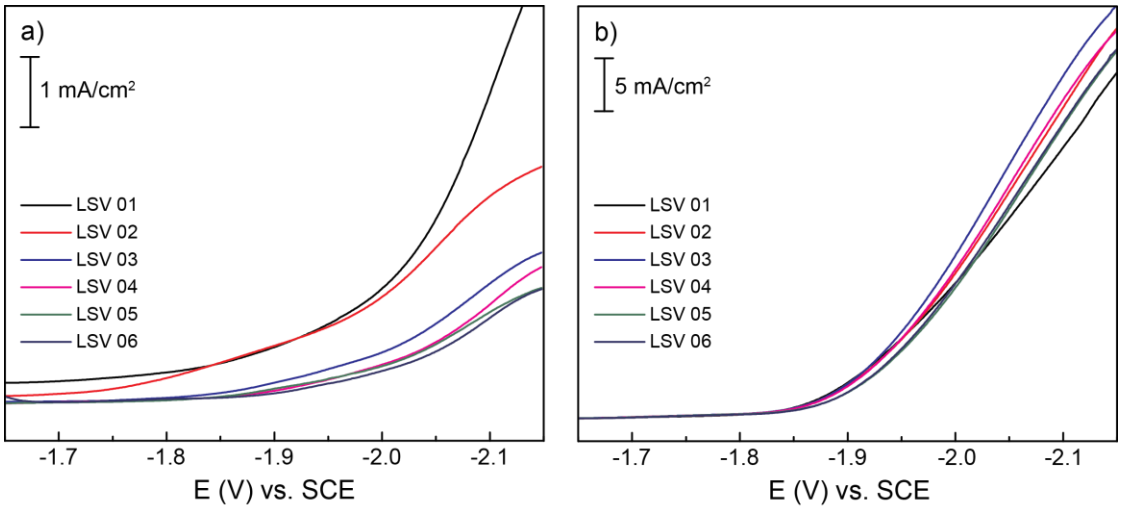

Figure 6.7. Overlaid linear sweep voltammetry polarization curves for a) 17% MeCN (v/v) in [BMIM]PF_6 and b) 100 mM [BMIM]PF_6 and 100 mM $TBAPF_6$ in MeCN. Performed under CO_2 saturated solutions with the Sn-modified electrode.

Figure 6.7a revealed that the activity for CO_2 reduction became subdued upon sequential potential sweeps using the same Sn-modified electrode for 17 % MeCN (v/v). This supports film passivation due to the formation of an impurity adsorption, imidazolium-carboxylate, to block charge transfer events.[25] This behavior was not observed for Sn-CMEC in dilute IL (Figure 6.7b). The polarization curve retained its steep cathodic feature and demonstrated no signs of film passivation. These results support that viscosity encourages formation of imidazolium-carboxylate.

Despite trace decomposition of the cation, it is important to note that the anion now shows no signs of degradation during catalysis which helps to maintain the structural integrity of the IL. It was remarkable to observe structural enhancement with merely 5% MeCN (v/v). Seeing how trace amounts of MeCN can suppress H_2 production and enhancement current density, it was curious if the electronics for this

deviation also show signs of improvement. This was studied through electrochemical impedance spectroscopy (EIS).

6.3.3 Electrochemical Behavior of MeCN/IL Admixtures

EIS is a sensitive technique in detecting the electronics involved in the rate limiting ET event. The rate determining step (RDS) for Sn-CMEC has been suggested to be the first ET to reduce surface bound CO_2 to the high-energy CO_2 radical anion ($CO_2^{\bullet-}$). This was suggested by Tafel analysis, for the analogous Bi-CMEC. The degree of stabilization for $CO_2^{\bullet-}$ is related to the kinetic barrier (energy cost) and significantly effects the outcome of electrolysis, i.e. product distribution and current density. Optimal stability, lowers the kinetic barrier and makes for a more facile ET event. Additionally, the viscosity of the solution impacts the overall resistivity of the ET event. It is curious how MeCN admixture can alter the resistance (viscosity) and the $CO_2^{\bullet-}$ stabilization to encourage CO evolution with increased current density. It was also of interest to observe how MeCN admixtures effect ion mobility by monitoring the capacitance of the double layer (C_{DL}).

6.3.3.1 Elucidating Resistivity of MeCN/IL Admixtures

Changes in resistivity can be monitored by the resistance to charge transfer (R_{CT}) and resistance of solution (R_{sol}). The relationship between R_{CT} and R_{sol} is described in equation 6.1.

$$R_{CT} = R_{sol} - (R_{sol} + R_{CT}) \qquad (6.1)$$

R_{CT} and R_{sol} values are obtained from the x-axis on the Nyquist plot (Z´, real) which describes resistive properties. This is when there is no capacitive (–Z″) contribution (y-axis, imaginary). Here, R_{sol} and R_{CT} can be measured. R_{sol} is measured

in the Nyquist plot by the start of the semicircle impedance response at higher frequencies. R_{CT} is located where the semicircle ends. The Nyquist plot in Figure 6.8 illustrates the deviations in R_{sol} and R_{CT} for when MeCN is titrated in $[BMIM]PF_6$.

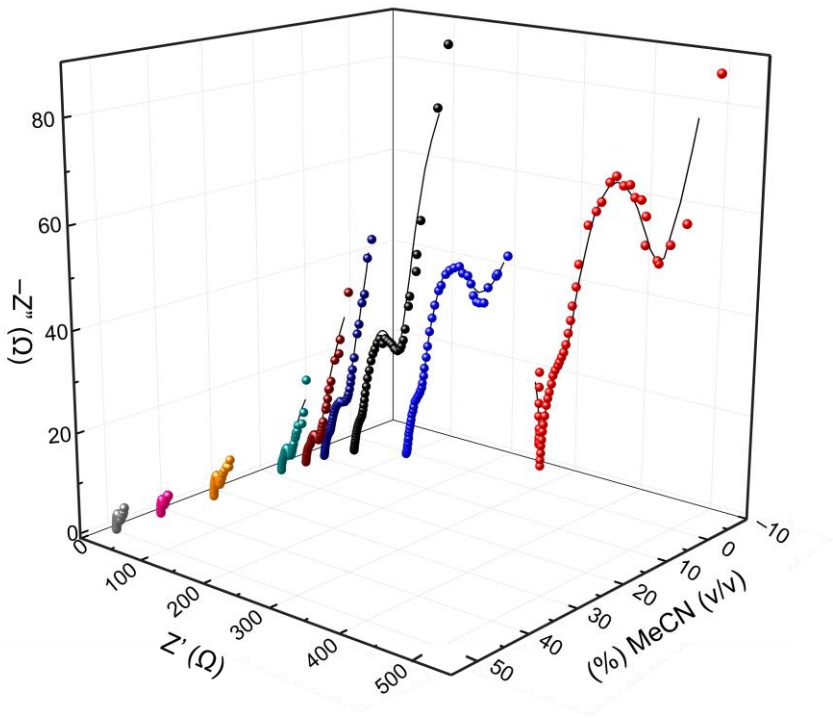

Figure 6.8. 3D Nyquist plot for MeCN titrated in to CO_2 saturated $[BMIM]PF_6$.

The Nyquist plot illustrates drastic changes in both R_{sol} and R_{CT} with admixtures of 0, 5, 13, 17, 20, 33, and 50 % MeCN (v/v). A smaller R_{CT} illustrates that the rate determining ET event experiences a smaller kinetic barrier. This suggested that the IL at the electrode surface can participate more with intermediate stabilization, such that the resistance at the electrode surface is reduced with additions of MeCN. The viscosity of the IL was studied specifically by deviations in R_{sol}. Reduced R_{sol} suggested that the

IL is less resistive and became less viscous with increasing amounts of MeCN. Deviations in R_{sol} and R_{CT} are illustrated more clearly in Figure 6.9a and b respectively.

Figure 6.9a shows that R_{sol} is significantly reduced with MeCN additions. Pure [BMIM]PF_6 demonstrated an R_{sol} of ~300 Ω. With only 5 % MeCN (v/v), this resistance dropped over 150 Ω. Upon further additions, up to 50 % MeCN (v/v), R_{sol} was reduced further to 15 Ω. This suggested that [BMIM]PF_6 is becoming less viscous to encourage a more facile ET event. The less resistive ET was also supported by the reduced R_{CT} with MeCN admixtures (Figure 6.9b).

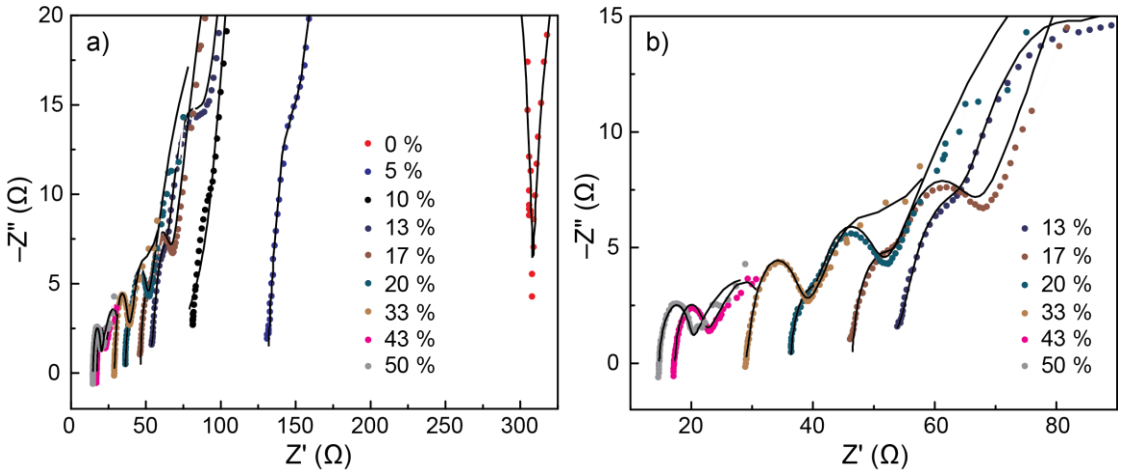

Figure 6.9. Nyquist plots highlighting a) R_{sol} for 0, 5, 10, 13, 17, 20, 33, 43, and 50 % MeCN (v/v) admixtures and b) R_{CT} for 13, 17, 20, 33, 43, and 50 % MeCN (v/v) admixtures in CO_2 saturated [BMIM]PF_6.

Figure 6.9b illustrates a significant decreased in R_{CT} with 17 % MeCN (v/v). Here, the R_{CT} has a value of ~20 Ω. This is roughly a 150 Ω decrease from neat [BMIM]PF_6. The R_{CT} continues to decrease slightly up to 43 % MeCN (v/v). Here, the

MeCN% is approaching conventional electrolyte conditions, which clarifies why the deviations in R_{CT} and R_{sol} become minimal. At 43 and 50 % MeCN (v/v), the R_{CT} is ~8 Ω. This value is comparable to the R_{CT} at 17 % MeCN (v/v) (~10 Ω). Therefore, when pursuing MeCN admixtures to reduce the viscosity of [BMIM]PF_6, 17 % MeCN (v/v) is appropriate to encourage the IL solution to resemble conventional electrolyte behavior. These studies clarify that the overall solution and charge transfer resistances are reduced with MeCN admixtures, and highlights why there is are deviation in current density and CO evolution with increasing amounts of MeCN.

6.3.3.2 Uncovering Ion Mobility Enhancements via C_{DL}

The decrease in R_{sol} illustrated by EIS and the current density enhancement from CPE suggested that ion mobility increased. Neat [BMIM]PF_6 systems have been shown previously to demonstrate an enhancement in current density in response to temperature elevation, however, the enhancement in current density was not related to ion mobility (See Chapter 5). This was demonstrated by deriving the C_{DL} value for each electrolysis condition and ultimately finding that the value was static. Therefore, to observe if MeCN has a positive correlation to ion mobility, the C_{DL} was calculated for the various MeCN admixtures.

EIS is an irreplaceable method for elucidating electrochemical phenomenon, and is largely useful for uncovering the dynamics for mobile charge at the interfacial or bulk regions.[26] C_{DL} is a phenomenon that occurs at the electrode-liquid interface and is directly related to ion mobility; if C_{DL} is high then the ion mobility is fast.[27] C_{DL} is calculated by manipulating the impedance responses (Z´ and –Z″) into a Bode plot, log |Z| vs. log ω, where Z is the absolute impedance and ω is the frequency in radians. Z

and ω are calculated by equation 6.2 and 6.3 respectively where *f* is the frequency applied during the EIS experiment.

$$|Z| = \sqrt{Z'^2 + Z''^2} \qquad (6.2)$$

$$\omega = 2\pi f \qquad (6.3)$$

$$|Z| = 1/C_{DL} \qquad (6.4)$$

Figure 6.10a illustrates overlaid Bode plots for the MeCN titration discussed previously in a Nyquist plot (Figure 6.8). Unlike the Nyquist plot, the log-log plot allows for all impedance responses to be viewed in one spectral window for a clear illustration of how the behaviors compare. For example, Figure 6.10b describes how R_{sol} and R_{CT} are identified and more easily compared. Additionally, this illustrated how the C_{DL} can be extrapolated, which is by taking the linear regression of the first break point in the Bode plot where the y-intercept value (log |Z|) is obtained. Deriving the y-intercept for |Z| and taking the inverse will give C_{DL} (equation 6.4). The C_{DL} for 0, 5, 13, 17, 20, 33, and 50 % MeCN (v/v) are summarized in Figure 6.9c.

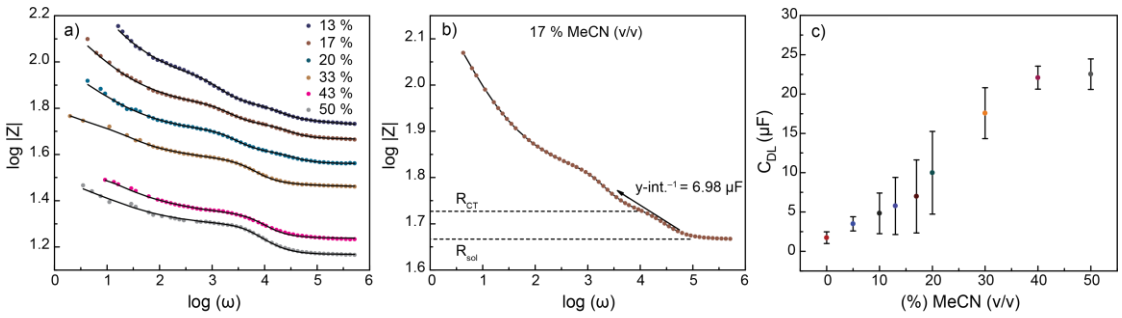

Figure 6.10. Bode plot illustrated in a) represents the impedance responses for MeCN titrated into [BMIM]PF_6. The Bode plot for 17 % MeCN (v/v) is highlighted in b) to elucidate how to extrapolate R_{CT}, R_{sol}, and C_{DL} information. C_{DL} with respect to MeCN (v/v) is illustrated in c.

Remarkably, an enhancement in ion movement was now observed for [BMIM]PF_6 with MeCN admixtures. From 0 to 50 %, the C_{DL} increased from 2 to 23 μF respectively. The IL mobility follows the Walden Rule (Arrhenius behavior) from 0 to 17 %, which states that molar conductivity and viscosity are proportional for the cation/anions in different solvent conditions.[8,28] The break in linearity at 20 % MeCN (v/v) exemplifies a switch from viscous conditions to conventional electrolyte conditions. The C_{DL} for dilute IL concentrations in MeCN is ~60 μF. Although the electronics are not up to par with dilute IL solutions, they demonstrated advanced ET events that were not achievable under neat conditions or with temperature elevations.

These studies revealed interesting behavioral interactions for catalysis, specifically with the dependency on the IL. For example, when undergoing catalysis in organic solvent in the absence of 1,3-dialkylimidazolium ILs, the selectivity for CO and current density was jeopardized substantially, 48 % and <1 mA/cm^2 respectively.[12] Now having an abundance of imidazolium IL, the CO efficiency and current density were jeopardized once again, suggesting that catalysis is not only dependent on IL, but also MeCN. Therefore, these studies are highly beneficial for discovering the optimal MeCN/IL dynamic to facilitate CO_2 to CO electroreduction with high efficacy.

6.3.4 Elucidating the Mechanistic Behaviors Influenced by MeCN Admixtures

Further characterization of MeCN admixtures in [BMIM]PF_6 involved elucidating the mechanism for the CO_2 to CO transformation. As mentioned previously, EIS characterizes the electronic behavior for the RDS and portrays that behavior in a Nyquist plot. Simulations were performed on the impedance responses to elucidate the electrochemical phenomenon occurring as represented by time constants (RCs). Simulations were modeled by circuits, 3RC and 2RC (Figure 6.11a and b respectively).

Each circuit was designed with RCs occurring in series to represent events including ohmic resistance (R_{ohmic}), adsorption resistance (R_{AD}), or R_{CT}. Sn-CMEC in dilute IL concentrations was best modeled by the 3RC circuit, which consists of R_{ohmic}, R_{AD}, and R_{CT}. Sn-CMEC in neat [BMIM]PF_6 was best modeled by the 2RC circuit, which lacked the R_{ohmic} time constant (See Chapter 5). It was curious to observe which circuit best portrays the electronic environment with MeCN admixtures. The impedance responses for 0, 5, 13, 17, 20, 33, and 50 % MeCN (v/v) were simulated by the 3RC and 2RC circuit and their R-squared values (R^2) for the 3RC (blue dots) and 2RC (red dots) are reported in Figure 4.11c.

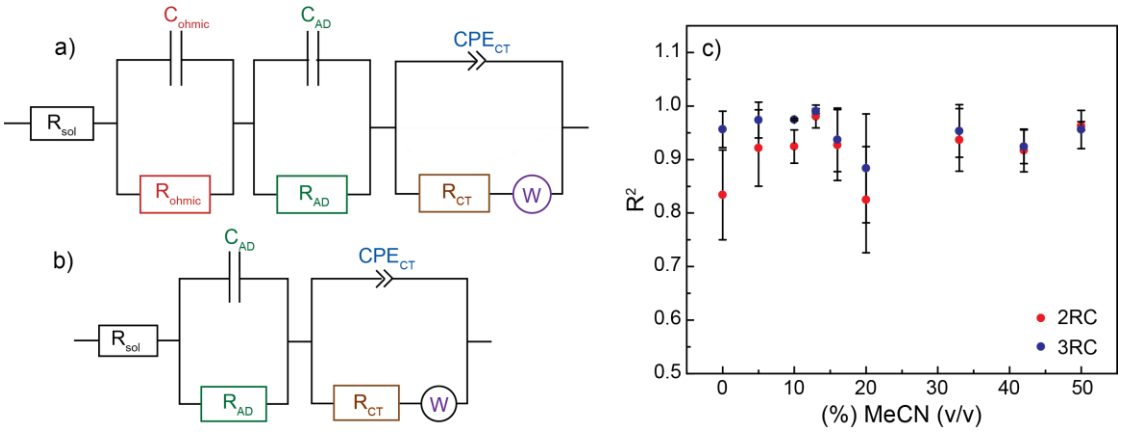

Figure 6.11. 3RC and 2RC circuits are illustrated in a) and b) respectively. The R-squared values for the 3RC (blue trace) and 2RC (red trace) simulations with respect to %MeCN (v/v) is illustrated in c).

The R^2 values summarized in Figure 6.11c demonstrated that there is essentially no difference between the 3RC and 2RC circuits. The lack of discrepancy between the

circuits suggested that these conditions mostly resemble the ET events for neat [BMIM]PF_6 catalysis (2RC).

The 2RC circuit simulates a mechanism that is highly dependent on adsorption and charge transfer events. R_{ohmic} was removed from the circuit design because there is no signature "L" feature at high frequency to highlight the interaction between the film and substrate (6.9b). It is fascinating to observe that high IL concentrations can increase surface resistance such that there is no longer a capacitive contribution to the RC. Ideally, there would be a 50/50 distribution of electrons traveling through the resistor and capacitor of an RC (Figure 6.12b). With high concentrations of IL, the electrons favor the path of the resistor (Figure 6.12a).

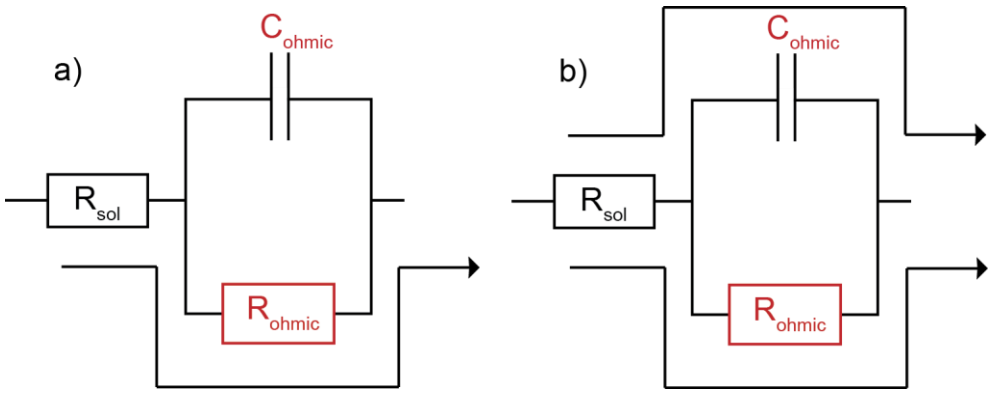

Figure 6.12. Electron pathway for a) a purely resistive system and a b) 50/50 distribution of electrons through the resistor and capacitor.

EIS demonstrated that neat ILs are highly resistive; large R_{CT} and R_{sol} values. The elevated resistivity jeopardized ET effects and ultimately disrupted the IL monolayer believed to suppress H_2 production (also in part due to the decomposition of IL). With addition of MeCN, the resistivity of the system decreased and mass transport

was improved. It is fascinating how changing the viscosity can alter the mechanistic pathway for facilitating the electron limiting transfer event.

6.4 Conclusions

RTILs are highly viscous (>50 cP) and by themselves, exhibit low self-diffusion (0.1 $x10^{-9}$ m^2 s^{-1}) and modest conductivity (1 S m^{-1}).[20] These properties posed complications for using innovative RTILs as solvents for chemical reactions or catalysis. These properties were exemplified with [BMIM]PF_6, one of the more viscous RTILs (450 cP).[20] To enhance diffusion and the overall conductivity, variable temperature (VT) CPE was performed, which unfortunately resulted in facile degradation of [BMIM]PF_6 with no enhancement in mass transport. Although the rate of reaction can also increase with increasing applied potential, this risks altering the product distribution and negatively impacting the selectivity for CO. Therefore, MeCN admixtures were then pursued to enhance ion mobility and ultimately lower solution viscosity while keeping with the ideals of using green recyclable RTILs solutions.

There was now a positive correlation between MeCN admixtures and the efficacy of catalysis. Importantly, XPS revealed that anion degradation no longer occurred, even with only 5 % MeCN (v/v). XPS revealed that there was trace cation decomposition via C2 substitution to yield imidazolium-carboxylate. This formation and adsorption to the surface was supported by LSV when adsorption of the adduct blocked charge transfer to result in reduced CO_2 reduction activity. Importantly, the adsorbed adduct was trace in comparison to the adsorbed imidazolium on the surface and did not demonstrate diffusion into the solution bulk to interrupt further with mass transport via ^{1}H NMR.

17 % MeCN (v/v) demonstrated an optimal admixture for CO_2 to CO electrocatalysis, as demonstrated by high CO selectivity, CO_2 reduction activity, and current density. This volume percent correlates to the reported ionic conductivity dependence on co-solvent being below 20 %.[29] This was the least amount of MeCN added to encourage a current density increase of ~7 mA/cm^2 and a switch in product distribution to suppress H_2 evolution and favor CO production. These metrics suggested that solution viscosity not only impacts mass transport and the rate of reaction, but also the product selectivity. Specifically, the behavior of surface bound imidazolium ILs.

The interplay between viscosity and catalysis was further demonstrated by EIS in monitoring its effects on the RDS. The overall solution resistance was reduced drastically with only 5 % MeCN (v/v) and the reduced R_{CT} signified stabilization of the $CO_2^{\bullet-}$. Both R_{sol} and R_{CT} showed minimal deviation at 43 and 50 % MeCN (v/v). These volumes start to approach conventional electrolyte conditions (75 %). 17 % MeCN (v/v) demonstrated similar resistive properties and was comparable to the higher MeCN volumes (43 and 50 %). The added co-solvent encouraged weaker anion/cation coordination to the IL to behave as conventional electrolyte.[30]

These viscosity studies contributed to understanding the physical properties for imidazolium-carboxylate in greater depth. This adduct was suggested to be a thermodynamic sink upon formation on surfaces where it is thermodynamically stabilized. It is believed to form when the carbene interacts with neutral CO_2 near the cathode surface. Previously, this was believed to occur when the carbene cannot diffuse from the surface to reprotonate, or when catalysis temperature is enhanced to favor the formation of the thermodynamic product. Here, formation is also suggested to occur with enhanced viscosity. Viscous solutions have low diffusion. With reduced mass

transport, protons near the surface cannot be replenished quickly to protonate carbene. The reactive carbene then reacts with CO_2 to become stabilized.

This work furthers the applicability of RTILs at solvent. It highlights the effects viscosity plays in chemical reactions and demonstrates how reaction solutions can be tuned with just trace amounts of organic solvent. Electrostatic interactions between the RTIL cation and anion are screened with the co-solvent to encourage dissociation by lessening their electrostatic attraction.[20] Greater ion mobility is influenced by ion dissociation. The percentage of co-solvent strongly influences the solution conductivity by changing the electrostatic interactions between the cation and anion to facilitate charge transfer.[20] These studies suggest optimal shielding with 17 % of the co-solvent.

REFERENCES

(1) Chun, S.; Dzyuba, S. V.; Bartsch, R. A. *Analytical Chemistry*. **2001**, *73*, 3737—3741.

(2) Singh, M.; Manoli, K.; Tiwari, A.; Ligonzo, T.; Di Franco, C.; Cioffi, N.; Palazzo, G.; Scamarcio, G.; Torsi, L. *Journal of Materials Chemistry C.* **2017**, *5*, 3509—3518.

(3) Montaliban, M. G.; Bolivar, C. L.; Banos, G. D.; Villora, G. *Journal of Chemical and Engineering Data*. **2015**, *60*, 1986—1996.

(4) Marsh, K. N.; Boxall, J. A.; Lichtenthaler, R. *Fluid Phase Equilibria*. **2004**, *219*, 93—98.

(5) Mizuuchi, H.; Jaitely, V.; Murdan, S.; Florence, A. T. *European Journal of Pharmaceutical Sciences*. **2008**, *33*, 326—331.

(6) P. Wasserscheid and T. Welton, Ionic Liquids in Synthesis, Wiley-VCH, Weinheim, Germany, 2003.

(7) Mohammad, A. *Green Solvents II: Properties and Applications of Ionic Liquids*. Springer Science and Business Media, New York, 2012.

(8) Chaban, V. V.; Prezhdo, O. V. *Journal of Physical Chemistry Letters*. **2013**, *4*, 1423—1431.

(9) Mein, N.; Benedito, F. Rinaldi, R. *Green Chemistry*. **2010**, *12*, 1711—1714.

(10) Kosmulski, M.; Gustafsson, J.; Rosenholm. J. B. *Thermochimica Acta*. **2004**, *412*, 47—53.

(11) Canales, R. I. Brennecke, J. F. *Journal of Chemical and Engineering Data*. **2016**, *61*, 1685—1699.

(12) DiMeglio, J. L.; Rosenthal, J. *Journal of the American Chemical Society*. **2013**, *135*, 8798—8801.

(13) Huddleston, J. G.; Visser, A. E.; Reichert, M.; Willauer, H. D.; Broker, G. A.; Rogers, R. D. *Green Chemistry*. **2001**, *3*, 156—164.

(14) Zhang, H.; Hong, K.; Mays, J. W. *Polymer Bulletin*. **2004**, *52*, 9—16.

(15) Zhou, Q.; Wang, L.; Chen, H. *Journal of Chemical Engineering*. **2006**, *51*, 905—908.

(16) Chaban, V. V.; Voroshylova, J. V.; Kalugin, O. N.; Prezhdo, O. V. *Journal of Physical Chemistry B*. **2012**, *116*, 7719—7727.

(17) Chaban, Vitaly V., and Oleg V. Prezhdo. "Mixtures of 1-butyl-3-methylimidazolium tetrafluoroborate ionic liquid and acetonitrile: a molecular simulation." *arXiv preprint arXiv:1108.3607* (2011).

(18) Samanta, A. *Journal of Physical Chemistry Letters*. **2010**, *1*, 1557—1564.

(19) Chaban, V. V.; Prezhdo, O. V. *Journal of Physical Chemistry Letters*. **2011**, *2*, 2499—2503.

(20) Chaban, V. V.; Voroshylova, J. V.; Kalugin, O. N.; Prezhdo, O. V. *Journal of Physical Chemistry B*. **2012**, *116*, 7719—7727.

(21) Medina-Ramos, J.; DiMeglio, J. L.; Rosenthal, J. *Journal of the American Chemical Society*. **2014**, *136*, 8361–8367.

(22) Green, R. A.; Toor, H.; Dodds, C. Lovell, N. H. *Sensors and Materials*. **2012**, *24*, 165—180.

(23) Song, H. L.; Zhu, Y.; Li, J. *Arabian Journal of Chemistry*. **2015**.

(24) Noack, K.; Schulz, P. S.; Paape, N.; Kiefer, J.; Wasserscheid, P.; Leipertz, A. *Physical Chemistry Chemical Physics*. **2010**, *12*, 14153—14161.

(25) Noel, M.; Vasu, K. I. *Cyclic Voltammetry and the Frontiers of Electrochemistry*; Oxford & IBH: Janpath, New Delhi, 1990.

(26) Barsoukov, E.; Macdonald, J. R. *Impedance Spectroscopy: Theory, Experiment, and Applications*; John Wiley & Sons, Inc: Hoboken, New Jersey, 2005.

(27) Wang, H.; Pilon, L. *Journal of Physical Chemistry C.* **2011**, *115*, 16711—16719.

(28) Schreiner, C.; Zugmann, S.; Hartl, R.; Gores, H. J. *Journal of Chemical Engineering Data*. **2010**, *55*, 1784—1788.

(29) Diaw, A.; Chagnes, A.; Carre, B.; Willmann, P. Lemordant, D. *Journal of Power Sources*. **2005**, *146*, 682—684.

(30) Bešter-Rogač, M.; Stoppa, A.; Buchner, R. *Journal of Physical Chemistry*. **2014**, *118*, 1426—1435.

Appendix A

CHAPTER 2: ADDITIONAL FLOW CELL DATA

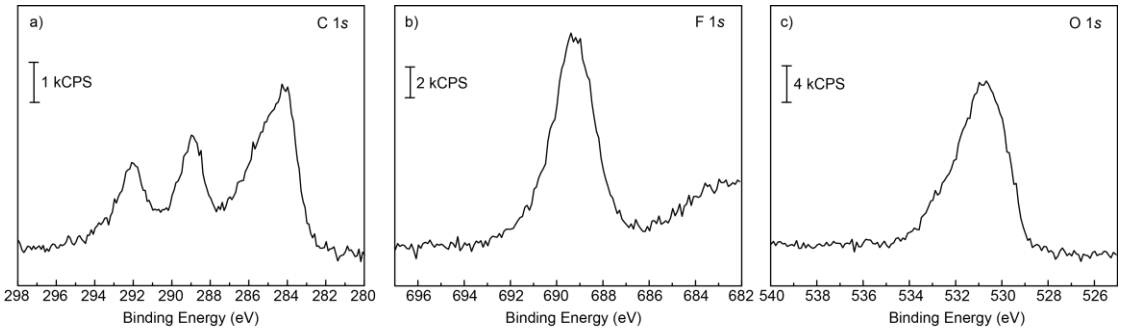

Figure A.1. XPS high resolution spectra for a) C 1*s*, b) F 1*s*, and c) O 1*s* for the bismuth(III) carbonate modified carbon paper.

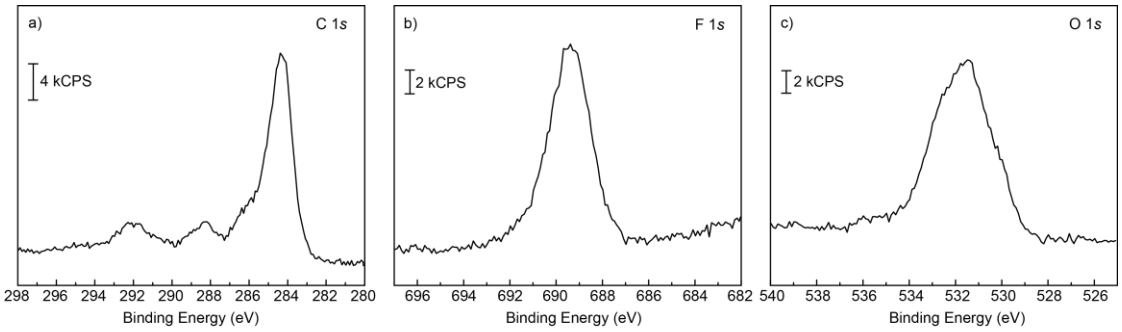

Figure A.2. XPS high resolution spectra for a) C 1*s*, b) F 1*s*, and c) O 1*s* for the bismuth(III) subsalicylate modified carbon paper.

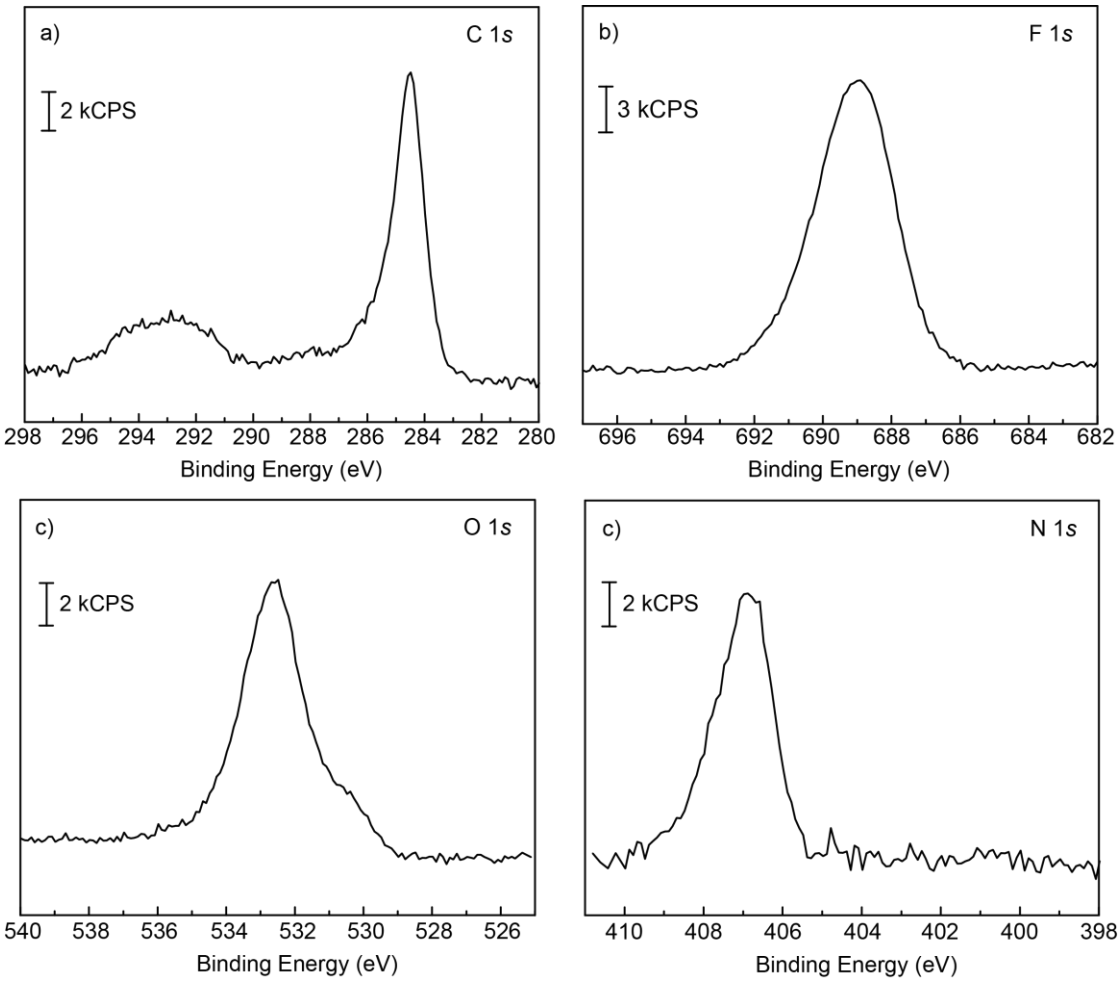

Figure A.3. XPS high resolution spectra for a) C 1*s*, b) F 1*s*, and c) O 1*s* for the bismuth(III) nitrate modified carbon paper.

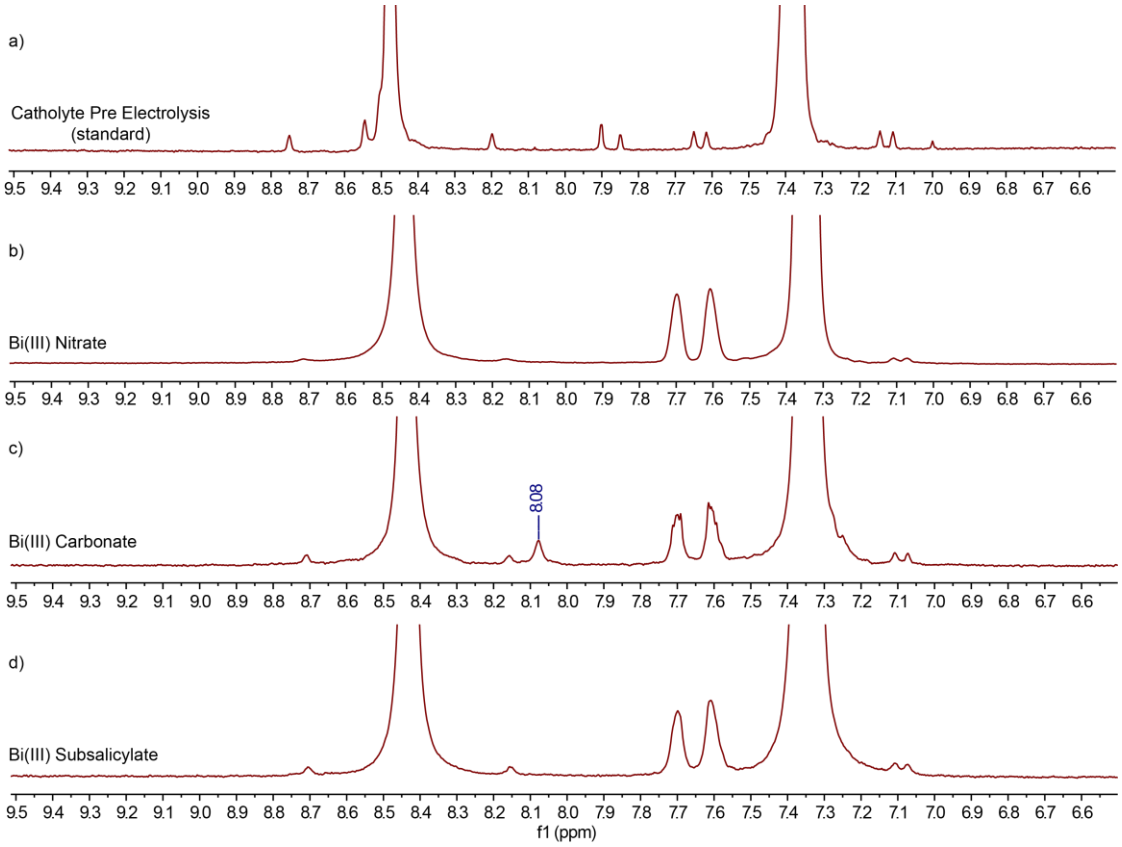

Figure A.4. ^{1}H NMR of the a) catholyte standard before electrolysis and the catholyte after electrolysis for b) bismuth(III) nitrate), c) bismuth(III) carbonate, and d) bismuth(III) subsalicylate. CPE performed at –1.95 (V) vs. SCE.

Appendix B

CHAPTER 3: ADDITIONAL P-BLOCK DATA

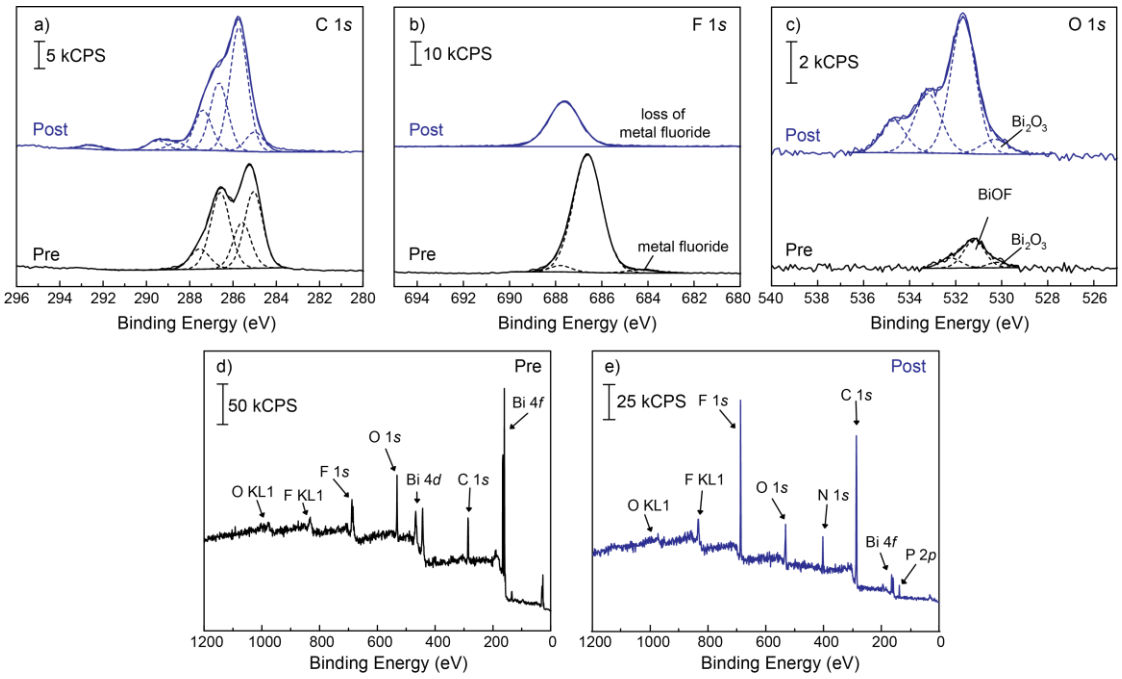

Figure B.1. a) C 1*s*, b) F 1*s*, and c) O 1*s* high resolution spectra for the bismuth cathode pre (black) and post (blue) electrolysis. The d) pre survey spectrum and e) post survey spectrum are also displayed.

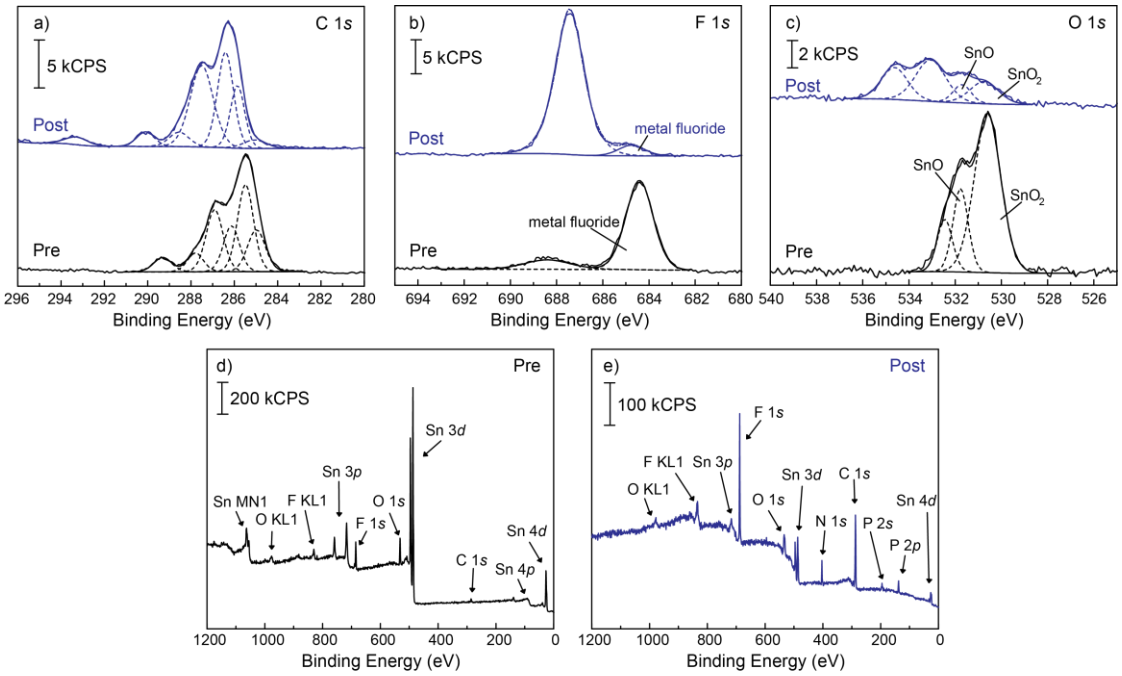

Figure B.2. a) C 1*s*, b) F 1*s*, and c) O 1*s* high resolution spectra for the tin cathode pre (black) and post (blue) electrolysis. The d) pre survey spectrum and e) post survey spectrum are also displayed.

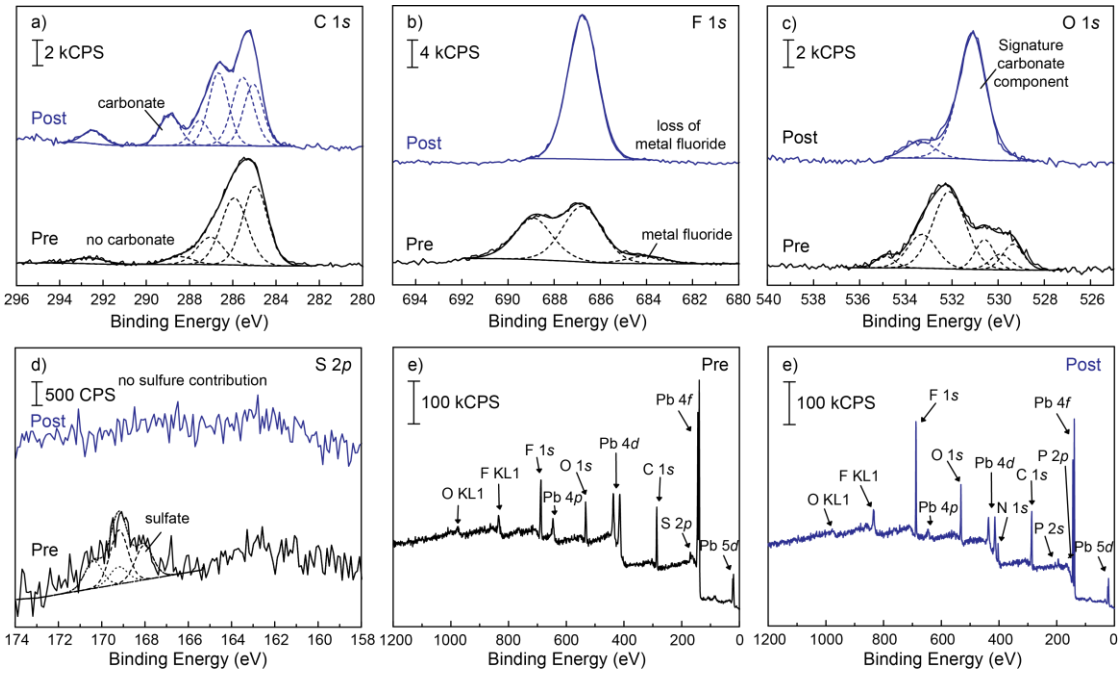

Figure B.3. a) C 1*s*, b) F 1*s*, c) O 1*s*, and S 2*p* high resolution spectra for the lead cathode pre (black) and post (blue) electrolysis. The e) pre survey spectrum and f) post survey spectrum are also displayed.

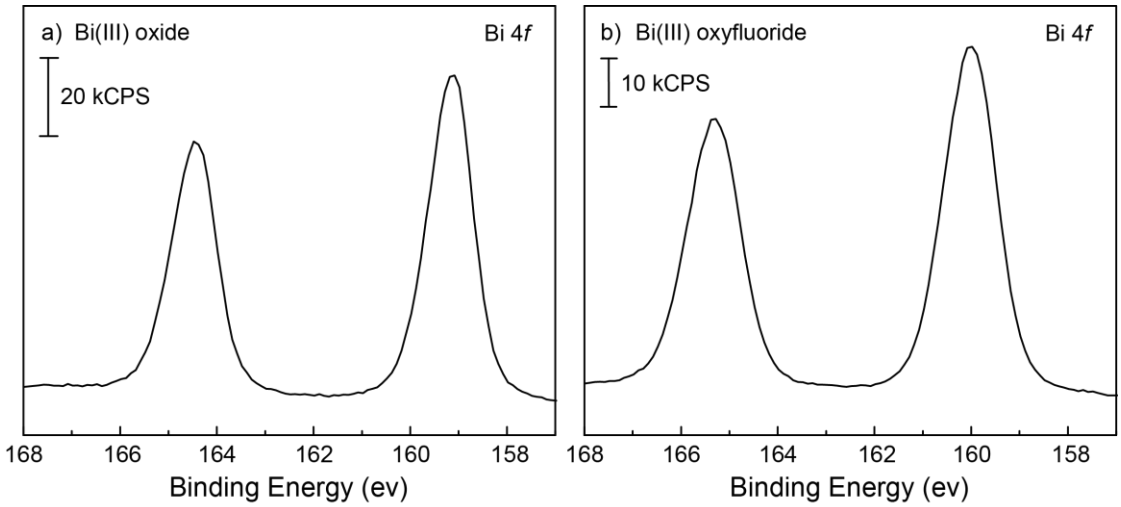

Figure B.4. Bi 4*f* high resolution spectra for a) bismuth(III) oxide and b) bismuth(III) oxyfluoride standards.

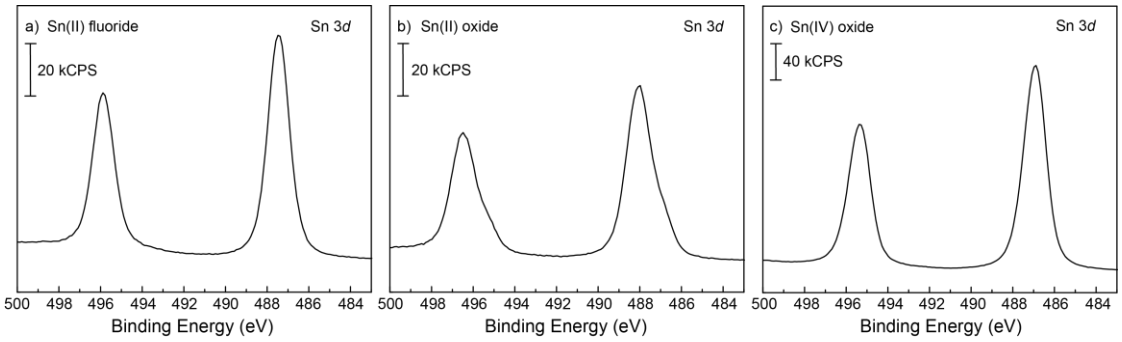

Figure B.5. Sn 3*d* high resolution spectra for a) tin(II) fluoride, b) tin(II) oxide, and c) tin(IV) oxide standards

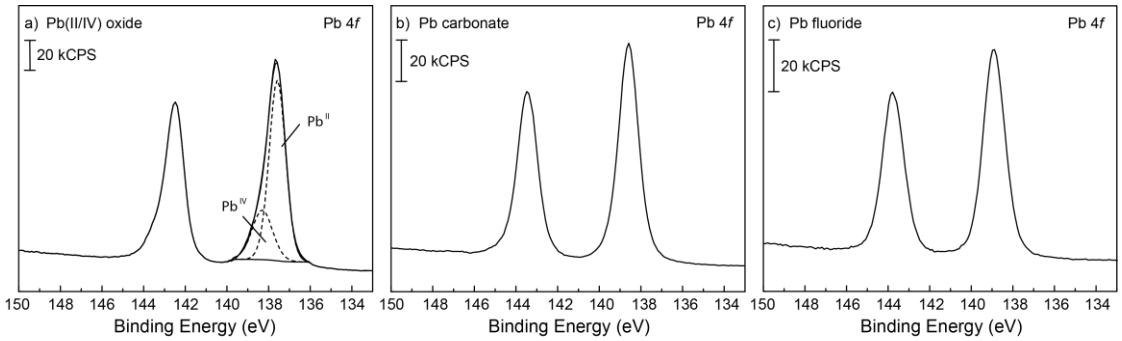

Figure B.6. Pb 4*f* high resolution spectra for a) lead(II/IV) oxide, b) lead(II) carbonate, and c) lead(II) fluoride standards.

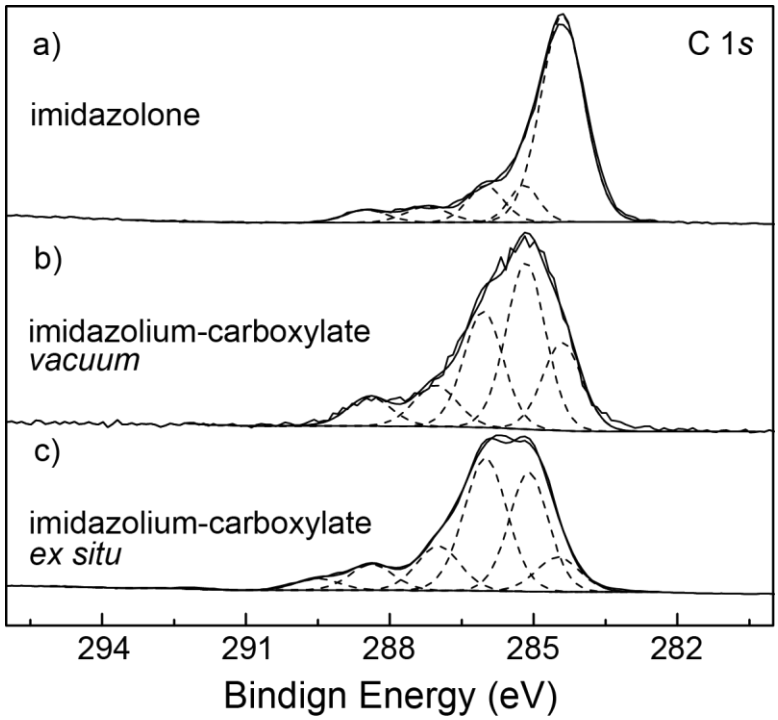

Figure B.7. Complimentary C 1*s* high resolution spectra for a) 1-butyl-3-methyl-2-imidazolone, b) imidazolium-carboxylate obtained via vacuum transfer, and c) imidazolium-carboxylate obtained via ex situ XPS.

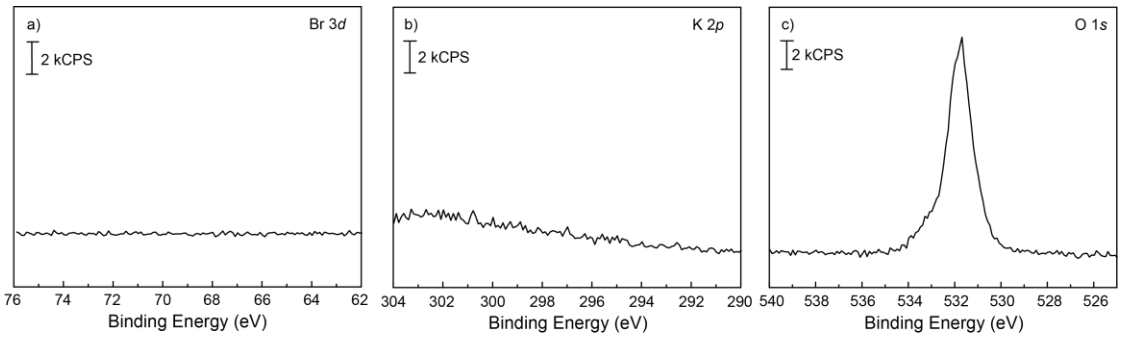

Figure B.8. a) Br 3*d*, b) K 2*p*, and c) O 1*s* high resolution XPS spectra for synthesized 1-butyl-3-methyl-2-imidazolone to further illustrate successful product formation synthetically.

Appendix C

CHAPTER 4: ADDITIONAL IMIDAZOLIUM-CARBOXYLATE DATA

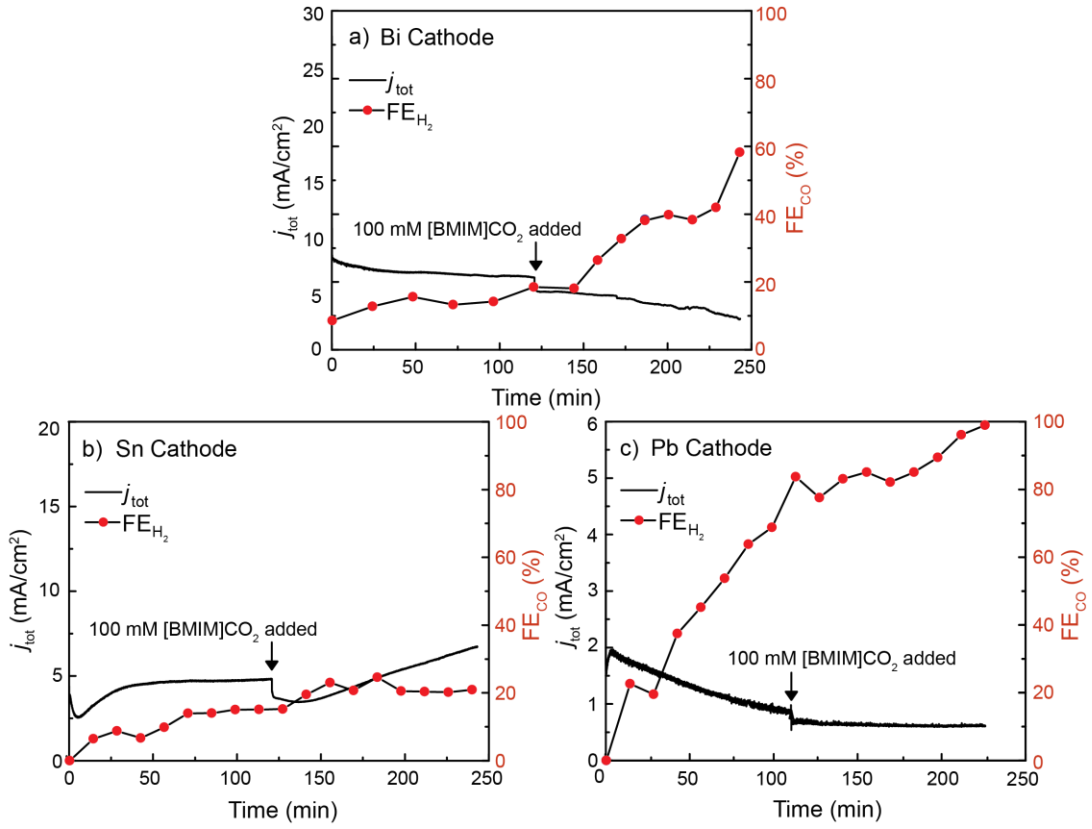

Figure C.1. Supporting H_2 FE and current density plots for a) Bi, b) Sn, and c) Pb for when imidazolium-carboxylate is added to the cathode after ~120 minutes of electrolysis.

Appendix D

CHAPTER 5: ADDITIONAL VT RTIL DATA

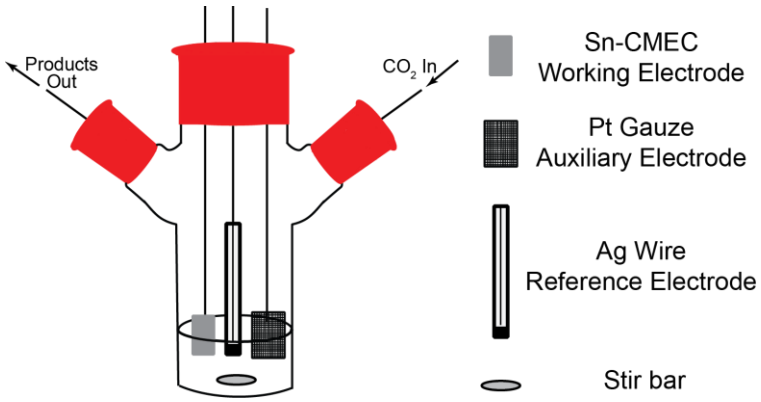

Figure D.1. Illustration of the single compartment cell used for controlled potential electrolysis.

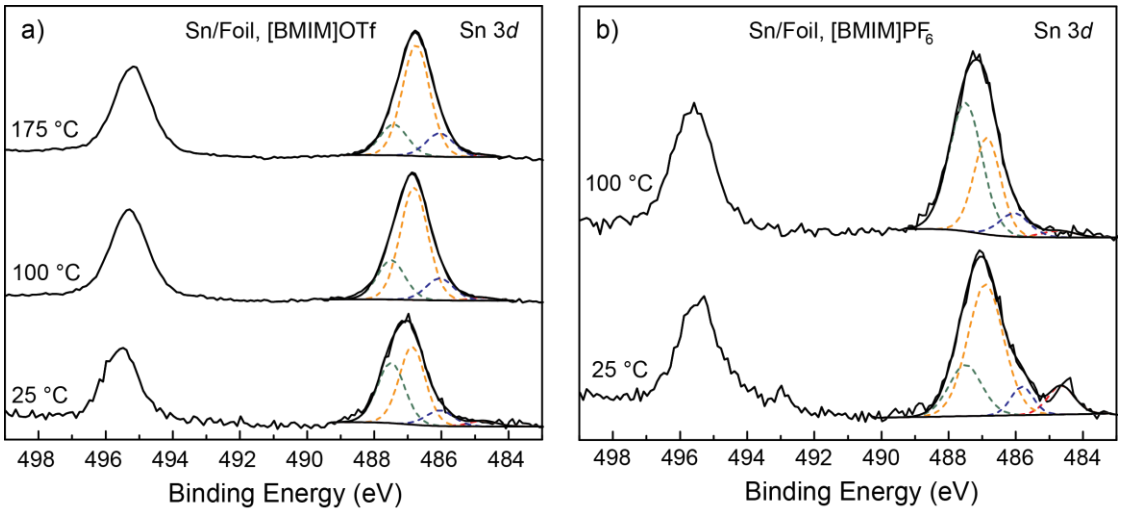

Figure D.2. Sn 3*d* high resolution spectra for a) [BMIM]OTf and b) [BMIM]PF_6 after CPE at –1.95 (V) vs. SCE.

Appendix E

CHAPTER 6: ADDITIONAL ACETONITRILE ADMIXTURE DATA

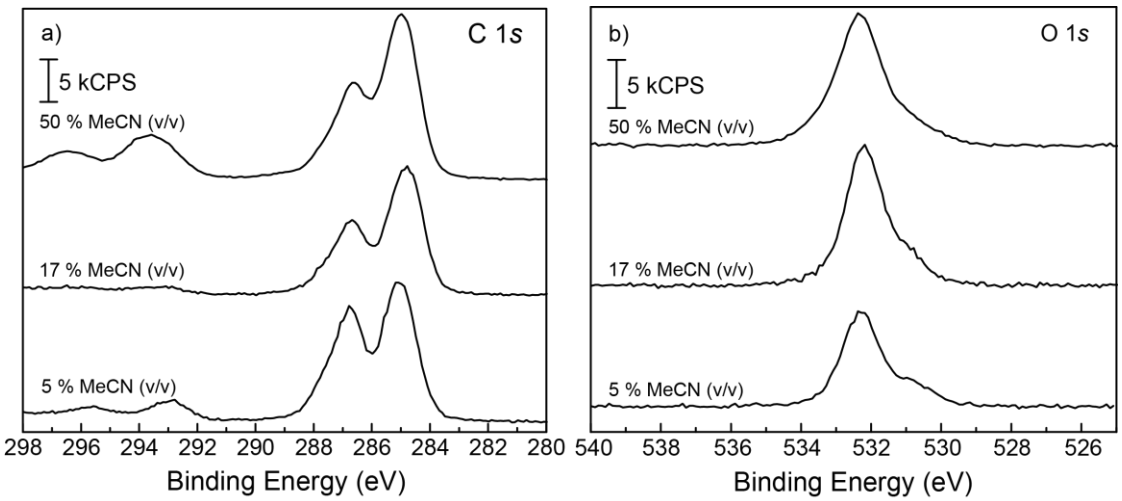

Figure E.1 Supporting C 1*s* and O 1*s* high resolution XPS spectra for 5, 17, and 50 % MeCN (v/v) in [BMIM]PF_6.